TECHNISCHE UNIVERSITÄT MÜNCHEN
Max-Planck-Institut für extraterrestrische Physik

Using γ-ray bursts as tools: prompt emission mechanism, host galaxy environment, and the cosmic star formation history connection

Jonathan Elliott

Vollständiger Abdruck der von der Fakultät für Physik der Technischen Universität München zur Erlangung des akademischen Grades eines

Doktors der Naturwissenschaften (Dr. rer. nat.)

genehmigten Dissertation.

<table>
<tr><td>Vorsitzende:</td><td></td><td>Univ.-Prof. Dr. Nora Brambilla</td></tr>
<tr><td>Prüfer der Dissertation:</td><td>1.</td><td>Priv.-Doz. Dr. Jochen Greiner</td></tr>
<tr><td></td><td>2.</td><td>Univ.-Prof. Dr. Laura Fabbietti</td></tr>
</table>

Die Dissertation wurde am 17.07.2013 bei der Technischen Universität München eingereicht und durch die Fakultät für Physik am 19.09.2013 angenommen.

Abstract

Gamma-ray bursts (GRBs) are, for a brief moment, the brightest objects in the Universe, easily reaching isotropic-equivalent luminosities as high as $10^{53}\,\mathrm{erg\,s^{-1}}$. The standard model envisages a relativistic e^-, e^+, γ fireball being released from a compact object, directed along its polar regions, while it accretes matter from a surrounding disc or torus. Fireball shells of varying Lorentz factors that cross one another result in internal shocks that accelerate electrons across the shock front and eventually cool via synchrotron emission in the form of a powerlaw. Later, the shells will collide with the interstellar medium, resulting in an afterglow emission, emitted as synchrotron radiation from the X-ray to radio wavelengths. Despite the effort that has gone into detecting GRBs and obtaining their γ-ray light curves and spectra, there is still no consensus on the underlying mechanism that causes the initial emission.

A sub-class of long duration GRBs are believed to be the beacon of the death of massive, rapidly rotating stars, most likely of the Wolf-Rayet type, as a result of their spectroscopically confirmed association with supernovae type-Ib/c. This standard model, named the collapsar model, is believed to only occur in low-metallicity environments as otherwise the stellar winds of the progenitor would stop the creation of a long GRB. Even though initial studies of host galaxy environments backed-up this claim, recent observations of solar/super-solar metallicity hosts galaxies has questioned the requirements of the collapsar model.

Their simple synchrotron spectra, in combination with their brightness, makes GRBs unique and simple tools to investigate the early years of the Universe. In addition, their association with the death of massive stars allows them to be used as star formation indicators at high redshifts. Long GRB samples have only just become large and complete enough to make such predictions, but despite this advance there are still a limited number of long GRBs above redshift of ~ 5. As a result, it is becoming more common to use simulations to make predictions instead, while we wait for high redshift number counts to increase.

This thesis uses long GRBs as tools in three different ways: (1) to investigate the prompt emission mechanism of GRBs, (2) to investigate the environmental and host galaxy preferences of long GRBs, and (3) to investigate the connection between cosmic star formation history and the long GRB rate, using statistically relevant samples and cosmological simulations. First, we overview the early discoveries of GRBs and the currently favoured ideas and models of GRBs and their phenomena, in Chap. 1. Following this, we introduce the main instruments we have used in our studies, primarily the *Swift* and *Fermi* satellites, and the Gamma-Ray Burst optical/Near-infrared Detector (GROND). We describe the operation of GROND, the data we obtained from all instruments and outline the models used and how they are fit to the data in Chap. 2.

In Chap. 3, we discuss the near-infrared (NIR) emission during a prompt emission period of GRB 121217A, which was observed simultaneously with GROND, *Swift*, and *Fermi*. The normal internal shock model cannot reproduce the observed spectrum unless self-absorption is included at frequencies of $\nu_\mathrm{a} > 5 \times 10^{12}\,\mathrm{Hz}$. Despite this, the large

quantity of host gas that is required, $N_{\mathrm{H,X}} \sim 10^{23}\,\mathrm{cm}^{-2}$, in combination with the poor best-fits, rules out the internal shock model. We show that the Band function can explain the features of the light curve and spectra during the prompt emission period.

GRB 110918A was one of the brightest long GRBs to be detected. In Chap. 4 we show it has the most massive ($M_* \sim 10^{11}\,\mathrm{M}_\odot$) host galaxy for $z < 2$, in comparison to the long GRB population and has one of the largest host metallicities ever detected, $\sim 1.0\,\mathrm{Z}_\odot$. The large quantity of metals rules out any cut-off in metallicity for host galaxies and questions again the environmental preferences of long GRB progenitors.

GROND has acquired a large and complete long GRB sample that we outline in Chap. 5. We utilise the high redshift completeness of this sample to investigate the connection of the cosmic star formation history (CSFH) to the long GRB rate. We find that metallicity constraints of the type $Z < 0.1\,\mathrm{Z}_\odot$ are the result of luminosity-cuts placed on samples to increase completeness and that the long GRB rate can be used to estimate the CSFH, without assuming any evolutionary dependence between the two.

To tackle the lack of high redshifts long GRBs, we utilise a high-resolution cosmological simulation, which includes advanced treatment of chemical evolution (Chap. 6). We populate long GRBs in the simulation using Monte-Carlo procedures and compare their rate to the CSFH of the simulation. We find that if a bias for low-metallicity environments was present, it would only become influential at redshifts of $z < 5$, and that the observed redshift dependence would not be reproducible by environmental effects alone.

Zusammenfassung

Gammablitze (Eng.: GRBs) sind, für einen kurzen Augenblick, die hellsten Objekte im Universum und erreichen äquivalent-isotrope Strahlungsleistungen von bis zu $10^{53}\,\mathrm{erg\,s^{-1}}$. Das Standardmodell sieht einen relativistischen e^-e^+,γ-Feuerball vor, der von einem kompakten Objekt, das Materie über eine Scheibe oder einen Torus akkretiert, entlang seiner Polarregionen freigesetzt wird. Diese Materieschalen, die unterschiedliche Lorentz-Faktoren aufweisen, kollidieren miteinander und resultieren in internen Schocks. Elektronen werden zunächst über diese Schockfronten hinaus beschleunigt, kühlen aber anschließend wieder, in Form eines Potenzgesetzes, ab. Anschließend kollidieren die Schalen mit dem interstellaren Medium, welches das typische Nachglühen in Form von Synchrotronstrahlung, beobachtbar in allen Wellenlängen von Röntgenstrahlen bis Radiowellen, verursacht. Trotz der Mühe, die in die Detektion von GRBs und der Beobachtung ihrer Lichtkurven und Spektren im Gamma-Bereich gesteckt wurde, gibt es nach wie vor keinen Konsensus über den zu Grunde liegenden Mechanismus, der für die Initialzündung der Gammablitze verantwortlich ist.

Man glaubt, daß der Tod von massereichen und schnell rotierenden Wolf-Rayet Sternen für die Unterklasse der langen Gammablitze verantwortlich ist, davon ihnen Supernovae des Typs Ib/c beobachtet wurden. Dieses Standardmodell, auch Kollapsar Modell genannt, tritt vermutlich nur in Umgebungen mit geringer Metallizität auf, da ansonsten der stellare Wind des Vorläufers eine Entstehung eines langen Gammablitzes unterdrücken würde. Obwohl erste Beobachtungen von Umgebungen in Wirtsgalaxien diese Behauptung unterstützen, haben neuere Beobachtungen von Wirtsgalaxien, die sonnenähnlicher oder sogar noch höherer Metallizitäten aufweisen, dieses Modell wieder in Frage gestellt.

Ihr einfaches Synchrotron Spektrum, in Zusammenhang mit ihrer Helligkeit, macht Gammablitze zu einem einzigartigen und einfachen Werkzeug, um die Entstehungsgeschichte des Universums zu untersuchen. Zusätzlich erlaubt die Verbindung zwischen den Gammablitzen und dem Tod von massereichen Sterne ihren Gebrauch als Sternentstehungsindikatoren bei hohen Rotverschiebungen. Die Stichprobe an langen Gammablitzen ist zwar erst kürzlich groß und vollständig geworden, um derartige Voraussagen zu treffen, aber trotzdem gibt es immer noch sehr wenig lange Gammablitze mit Rotverschiebung größer als 5. Deshalb verwendet man weiterhin Simulationen, um Voraussagen zu treffen.

Diese Arbeit verwendet lange Gammablitze auf drei verschiedene Arten: (1) um den Mechanismus der prompten Emission zu untersuchen, (2) um die Eigenschaften der Umgebung und der Wirtsgalaxien von langen Gammablitzen zu untersuchen und (3) um die Verbindung zwischen der kosmischen Sternentstehungsgeschichte und der Rate an langen GRBs, mittels statistisch signifikanter Stichproben und kosmologischen Simulationen, zu untersuchen. In Kapitel 1 verschaffen wir uns zunächst einen Überblick über die frühen Entdeckungen von Gammablitzen und die aktuell bevorzugten Ideen und Modelle, welche ihre Eigenschaften erklären. Anschließend führen wir die Hauptinstrumente ein, die wir in unseren Untersuchungen verwendet haben; hauptsächlich sind

dies die beiden Satelliten *Swift* und *Fermi* und der "Gamma-Ray Burst optical/Near-infrared" Dektektor (GROND). In Kapitel 2 beschreiben wir die Arbeitsweise von GROND, die Daten, die wir von unseren Instrumenten erhalten und umreißen die Modelle, die wir verwendet haben, und wie sie an die Daten angepasst werden.

In Kapitel 3 diskutieren wir die Nahinfrarot-Emission, die mit GROND während der andauernden prompten Emissionsphase des GRB 121217A beobachtet wurde, welcher durch *Swift* und *Fermi* entdeckt wurde. Das normale interne Schockmodell kann das beobachtete Spektrum nur dann reproduzieren, wenn Selbstabsorption bei $\nu_{\mathrm{a}} > 5 \times 10^{12}\,\mathrm{Hz}$ angenommen wird. Aber da selbst dann große Mengen an Gas in der Wirtsgalaxie notwendig wären ($N_{\mathrm{H,X}} \sim 10^{23}\,\mathrm{cm}^{-2}$), und die globalen besten Anpassungswerte nicht gut genug sind, kann das Standardmodell ausgeschlossen werden. Wir zeigen, dass die Band-Funktion die Eigenschaften der Lichtkurve und des Spektrums während der prompten Phase hinreichend erklären kann.

GRB 110918A war einer der hellsten Gammablitze, der je beobachtet wurden. In Kapitel 4 zeigen wir, dass die Wirtsgalaxie dieses Gammablitzes, im Vergleich zur Gesamtpopulation an langen Gammablitzen, die Massereichste bei $z < 2$ war und auch eine der größten Metallizitäten ($\sim 1.0\,\mathrm{Z}_{\odot}$) aufweist, die jemals entdeckt wurde. Die große Menge an Metallen spricht gegen einen rapiden Metallizitätsabfall für Wirtsgalaxien und stellt die Umgebungs-Vorlieben für die Erzeuger von langen Gammablitzen in Frage.

GROND hat eine sehr große und komplette Stichprobe von langen Gammablitzen gesammelt, welche wir in Kapitel 5 zeigen. Wir verwenden die Vollständigkeit der GRBs bei hohen Rotverschiebungen, um die Verbindung zwischen der kosmischen Sternentstehungsgeschichte (Eng.: CSFH) und der Rate an langen Gammablitzen zu untersuchen. Wir finden, dass die Metallizitätsbeschränkungen der Art $Z < 0.1\,\mathrm{Z}_{\odot}$ das Resultat eines Leuchtkraft-Schnittes ist, welcher an Stichproben angelegt wird, um die Vollständigkeit der Stichprobe zu erhöhen, und dass die Rate an langen Gammablitzen verwendet werden kann, um die CSFH abzuschätzen, ohne dass eine evolutionäre Verbindung zwischen den beiden angenommen werden muss.

Um das Problem der geringen Anzahl an GRBs bei hohen Rotverschiebungen zu lösen, verwenden wir eine hochauflösende kosmologische Simulation welche, detaillierte Aspekte der chemischen Entwicklung beinhaltet (Kapitel 6). Wir bevölkern lange Gammablitze in der Simulation mittels Monte-Carlo Prozeduren und vergleichen ihre Rate zu der kosmischen Sternentstehungsgeschichte der Simulation. Wir finden, dass wenn tatsächlich eine Tendenz für metallarme Umgebungen anwesend wäre, sie erst bei Rotverschiebungen $z < 5$ signifikant würde und dass die beobachtete Rotverschiebungs-abhängigkeit nicht ausschließlich durch Umgebungseffekte reproduzierbar wäre.

Contents

Chapter 1

Introduction

1.1 GRB discovery and overview

The discovery of γ-ray bursts (GRBs) from space was made by the military *Vela* satellites in 1973 (Klebesadel et al. 1973, also, see Fig. 1.1), which were initially used to ensure compliance with the nuclear test ban treaty. This discovery lead to many scientists to begin research with instruments on satellites that were already in orbit and allowed them to arrive at the following conclusions: (i) there was a bimodal distribution of the temporal duration of GRBs (Mazets et al. 1981), (ii) the GRB spectra were of a powerlaw shape (Cline et al. 1973), (iii) the GRBs were isotropically located in the sky (Mazets et al. 1981), and (iv) the GRBs did not follow the flux-intensity dependence that was expected from normal galactic sources (Vedrenne 1981). Unfortunately, these studies lacked number statistics and the method of selection was completely heterogeneous, thus making the conclusions not statistically reliable.

The favoured models to explain GRBs were usually of galactic origin, which made it difficult to reconcile with the claimed isotropic distribution. Along with many inconsistencies and the intrinsic problem of sample size and heterogeneous selection, a new instrument was required. All of these problems were alleviated by the launch of the Burst and Transient Source Experiment (BATSE; Fishman et al. 1989) and the satellite *BeppoSAX* (Scarsi 1997).

BATSE was able to detect 1 GRB per day, which facilitated the collection of a large homogeneous data set, as it identified and followed GRBs with a consistent set of criteria. First, it showed that the GRB population was clearly separated into two (Fishman et al. 1994) based on the duration of the burst (see Fig. 1.2). Now, they are separated into two classes, the short class with $T_{90} < 2\,\mathrm{s}$, and the long class with $T_{90} > 2\,\mathrm{s}$, where T_{90} is the time at which 90% of the GRB's flux has been emitted (we note that this time constraint is in the frame of the observer). The short duration bursts were seen to be more spectrally hard and the long duration bursts spectrally soft, therefore, they are now referred to as soft-hard and long-soft GRBs (Kouveliotou et al. 1993). Secondly, due to the positional accuracy of BATSE, the angular distribution of GRBs was compiled (Fig. 1.3) and it confirmed that GRBs were in fact distributed isotropically (Fishman
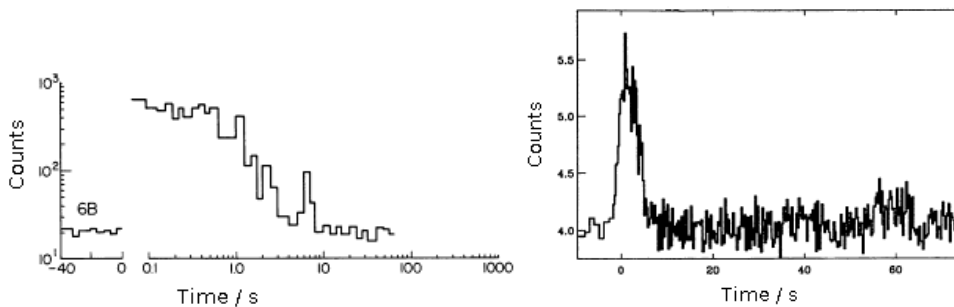
Figure 1.1 **Left**: Prompt emission light curve of the first ever GRB that was detected by the *Vela* satellites. Adapted from Klebesadel et al. (1973). **Right**: A typical prompt GRB light curve that was detected during the period of BATSE. Adapted from Fishman et al. (1994).

et al. 1994). For a consistency check, a comparison was made with the intensity distribution of GRBs. The argument is that for a spatially homogeneous distribution, the number of visible sources increases by a factor of R^3, but the total emitted flux would decrease by R^{-2}. Therefore, a plot of $\log N$-$\log S$, where S is the total fluence of the GRB and N is the total number of GRBs with that fluence, would have a powerlaw of slope $-3/2$, and any deviation would imply inhomogeneity. After correction of the detections based on the flux limitations of BATSE, a slope that differed to $-3/2$ was found due to the underlying lack of faint source detections (Fishman et al. 1994). Many models tried to explain the isotropic angular distribution, yet inhomogeneous $\log N$-$\log S$ distribution (Fig. 1.4). One of the solutions was that the lack of faint sources was due to cosmological effects (e.g., Prilutskii & Usov 1975).

The origin (Galactic or cosmological) of GRBs was eventually solved by the *BeppoSAX* satellite that was launched in 1996. It housed four sodium scintillator detectors and a wide-field X-ray camera. *BeppoSAX* could obtain positions with a precision of 3 arcminutes and on the 28th Febuary 1997 the first X-ray counterpart to a GRB was discovered (Costa et al. 1997). Further ground-based follow-up discovered the first optical counterpart (Cline et al. 1997). An underlying galaxy was also found and a spectrum of it taken (Djorgovski et al. 1999), which suggested a redshift of $z = 0.695$ (most likely the first ever measured host galaxy redshift). However, as there was no direct evidence it was the host galaxy, the cosmological origin was not completely accepted, until three months later when the spectrum of the optical afterglow of GRB 970508A resulted in a redshift of $z = 0.767 - 0.835$ based on metal absorption lines (Metzger et al. 1997a). The cosmological origin of GRBs was solidified and paved the way for a new set of standard models to explain the phenomena.

Throughout the thesis we are only interested in the GRB sub-class of long-soft and, therefore, do not include any details of the short-hard population.
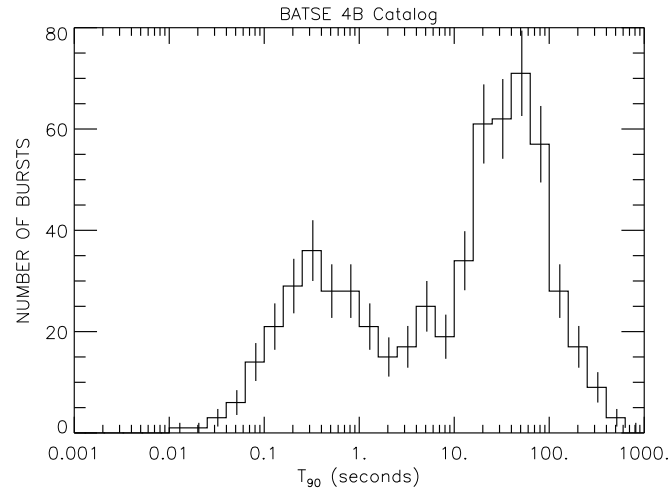
Figure 1.2 Distribution of T_{90} for all (soft-hard and long-soft) GRBs in the BATSE third data release, where T_{90} is the time at which 90% of the GRBs flux has been emitted. A bimodal distribution is easily seen, with the cross over of the two classes occurring at 2 s. Credit to NASA.
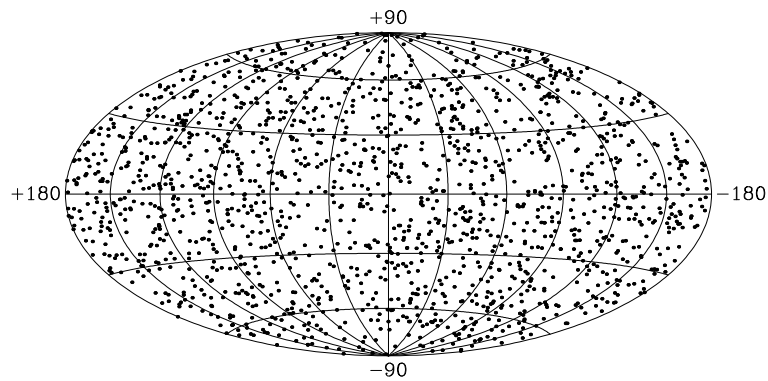
Figure 1.3 Angular distribution of the BATSE 4th GRB data sample release. The GRBs show no preference for the Galactic disc and it can be shown that this is an isotropic distribution. Taken from Paciesas et al. (1999).

3
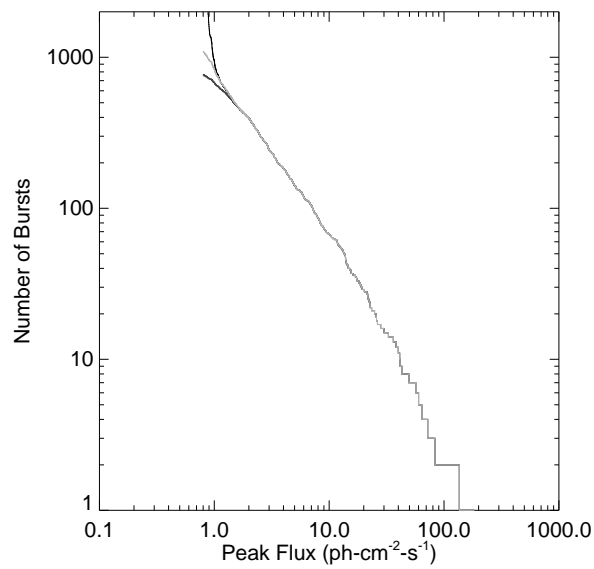
Figure 1.4 Log$N$ versus log$S$ plot of the BATSE 4th GRB sample release, used to investigate the homogeneous distribution of GRBs. The deviation from a straight line was the first sign that GRBs were of a cosmological origin. Taken from Paciesas et al. (1999).

1.2 Standard Models

1.2.1 Fireball Model

The estimated energy release of GRBs is of the order $E \sim 10^{53}$ erg and is released in a matter of milliseconds. This quantity corresponds to the total output of our Sun over its lifetime, i.e., $L_\odot \times \tau_\odot \sim 10^{47}$ erg, making it one of the most energetic and violent events in the Universe. Following standard astrophysical arguments; the time scales of processes that are shorter than the light crossing time of the object will be smeared out from the signal and so the observed variability can be used as a loose constraint on the size of the source, i.e., $R \lesssim \delta tc \sim 10^7$ cm (c.f. $R_\odot \sim 10^{10}$ cm) (Vedrenne & Jean-Luc 2009). Such a large energetic output in a small space and short amount of time would result in an e^-, e^+, γ fireball and thus the formation of the fireball model. The fireball model requires the following properties (for a full description, see Mészáros 2006):

1. Highly relativistic

   Photons in the fireball would be expected to create electron-positron pairs and, therefore, there would be a dampening of flux above 1 MeV, however, this has not been observed. This is easily reconciled by assuming that the fireball is moving relativistically with a Lorentz factor of Γ. Therefore, the fireball becomes opaque to the creation of electron-positron pairs as the scattering probability is reduced by: (i) the photons being blue shifted and their time scales shortened, (ii) the moving size of the fireball is increased by Γ^2 resulting in a small density, and (iii) we observe a smaller fraction of the emission, specifically $1/\Gamma$.

2. Baryonic contamination

   The equilibrium of electron-positron pairs in a relativistic fireball results in a high optical depth for the photons, until they eventually recombine at a co-moving temperature of $T \sim 17$ keV ($T \propto \frac{1}{R}$, where R is the radial distance of the fireball from the central engine). The photon spectrum at this photospheric radius is expected to be thermal, which is in contradiction to the observed non-thermal spectra of GRBs. Secondly, the time scales at which the photons escape are much too short in comparison to the observed emission periods. These major issues were reconciled by requiring that there was a contamination of baryons in the fireball. The baryons would retain the majority of the fireball energy in the form of kinetic energy, which could then be reconverted into the internal energy of the particles, by Fermi acceleration (Fermi 1949), if there existed relativistic shocks. These non-thermal particles would then radiate via synchrotron emission, resulting in the powerlaw spectrum observed from GRBs.

These two points lead to the current state of the fireball model, which has two types of shocks: internal and external. Internal shocks refer to shocks generated by the crossing of two different shells within the fireball and currently is the favoured model for prompt emission (discussed further in Sect. 1.2.2). External shocks are shocks generated

when the fireball interacts with the interstellar or surrounding wind-like media and is the favoured model of the afterglow emission, which is discussed thoroughly in Sect. 1.2.3.

1.2.2   Prompt Emission

The favoured model of prompt emission is the fireball internal shock model. As already noted, this envisages an engine that releases many shells with different Lorentz factors, which then cross one another, creating a relativistic shock. The relativistic shock forms a discontinuous boundary (shock front), which results in two distinct regions either side of the shock front. The gas in front of the shock (upstream) is heated and accelerated as the shock front passes through, leaving it behind the shock front (downstream). This boundary separates two sets of microphysical parameters, specifically: the Lorentz factor, particle number density, energy and magnetic fields. Particles have a finite chance of going upstream or downstream of the shock front, or escaping from the shock completely. Each time a particle crosses the shock front it has a fractional energy increase of $\frac{<E>}{E} = \frac{4V}{3c}$ where V is the particles velocity (e.g., Longair 1994). This process is also known as first order (type A/I) Fermi acceleration (Fermi 1949) and it can be shown that the energy spectrum is well described by a powerlaw of the form, $N(\gamma)\,\mathrm{d}\gamma \propto \gamma^{-p}\mathrm{d}\gamma$, where p is the photon index.

The shock front also amplifies the magnetic fields and so the electrons will then begin to cool via synchrotron radiation. The characteristic frequency ν_m is the mean (i.e., $<\gamma_e> \sim \gamma_m$) value determined from the γ distribution and places a lower limit on the optically thin emission of the system. Electrons that have energies larger than a critical value, γ_c, will rapidly radiate all their energy via synchrotron radiation at a corresponding frequency of ν_c. Below the characteristic frequency the shape of the spectrum is dominated by the synchrotron beam tail of the electrons, which is independent of the electron density. Usually below the ultra-violet regime the electrons can become optically thick (ν_a), such that they absorb emission when a photon interacts with the magnetic field. Also, a reverse process is possible, whereby photons are emitted at higher energies during the interaction (negative absorption). Finally, the rate at which these electrons cool (synchrotron cooling time scale $t_{\mathrm{sync}} \propto \frac{1}{\gamma_e \Gamma}$) in comparison to the dynamical time ($t_{\mathrm{dyn}} \propto \frac{R}{\Gamma}$) as the shell expands radially in R, changes the spectral shape between γ_c and γ_m, resulting in the following two spectral shapes (for a full derivation, see Sari et al. 1998):

1. Fast cooling ($t_{\mathrm{syn}} < t_{\mathrm{dyn}}$)

$$F_\nu \propto \begin{cases} \nu^{\frac{5}{2}} & \text{for} \quad \nu < \nu_{\mathrm{a}} \\ \nu^{\frac{1}{3}} & \text{for} \quad \nu_{\mathrm{a}} < \nu < \nu_{\mathrm{c}} \\ \nu^{-\frac{1}{2}} & \text{for} \quad \nu_{\mathrm{c}} < \nu < \nu_{\mathrm{m}} \\ \nu^{-\frac{p}{2}} & \text{for} \quad \nu > \nu_{\mathrm{m}} \end{cases} \qquad (1.1)$$

2. Slow cooling $(t_{\mathrm{syn}} > t_{\mathrm{dyn}})$

$$F_\nu \propto \begin{cases} \nu^{\frac{5}{2}} & \text{for} \quad \nu < \nu_{\mathrm{a}} \\ \nu^{\frac{1}{3}} & \text{for} \quad \nu_{\mathrm{a}} < \nu < \nu_{\mathrm{m}} \\ \nu^{-\frac{p-1}{2}} & \text{for} \quad \nu_{\mathrm{m}} < \nu < \nu_{\mathrm{c}} \\ \nu^{-\frac{p}{2}} & \text{for} \quad \nu > \nu_{\mathrm{c}} \end{cases} \qquad (1.2)$$

We have assumed self-absorption of the optically thick case $\nu^{\frac{5}{2}}$. For the optically thin case of negative absorption, the form would change to ν^2. The spectra for both cases can be seen in Fig. 1.5.

The internal shock model was favoured, primarily because it could explain the short time scales in the GRB prompt emission light curves and also the observed powerlaw spectra. However, the expected power law models do not always fit well the observed GRB spectra and, in addition, other non-physical models (Band (Band et al. 1993) or exponential cut-off (Kaneko et al. 2006)) have been found to replicate the data much better. This is especially prominent at the lower frequencies. Secondly, the efficiency of the internal shock model is so low ($\sim 10\%$), it would mean there is more energy for the afterglow phase and, therefore, an expected emission brighter than the prompt period (see, e.g., Piran 1999). However, this is not observed and usually the afterglow is a tenth of that observed in the prompt emission. These discrepancies have lead to many other proposed mechanisms:

1. Poynting flux dominated models (e.g., Drenkhahn & Spruit 2002)

   The magnetic fields of the compact object can reconnect through instabilities, which allows the magnetic potential to be converted into kinetic energy of the plasma or to create particles. These particles will then eventually radiate. If cooling of the plasma occurs outside the photosphere, it will proceed via synchrotron radiation because of the large magnetic fields of the compact object. The conversion of the magnetic potential to kinetic energy also accelerates the flow due to a magnetic pressure gradient. The only expected difference to the internal shock model is the afterglow emission. However, the differences are expected to be too small to be observed.

2. Dissipative photosphere (e.g., Beloborodov 2010)

   This considers a fireball that is contaminated with neutrons, in the same quantity as protons. During the fireballs expansion, while it is still optically thick, there are nuclear collisions of the neutrons and protons that create electron-position pairs that radiate their energy away before they become part of the plasma. Also, the protons are heated by the nuclear collisions. They, in turn, heat the plasma via Coulomb collisions. Eventually the fireball becomes optically thin and radiates a spectrum that is very similar to the empirical Band spectrum.

3. External shocks (e.g., Dermer et al. 1999)
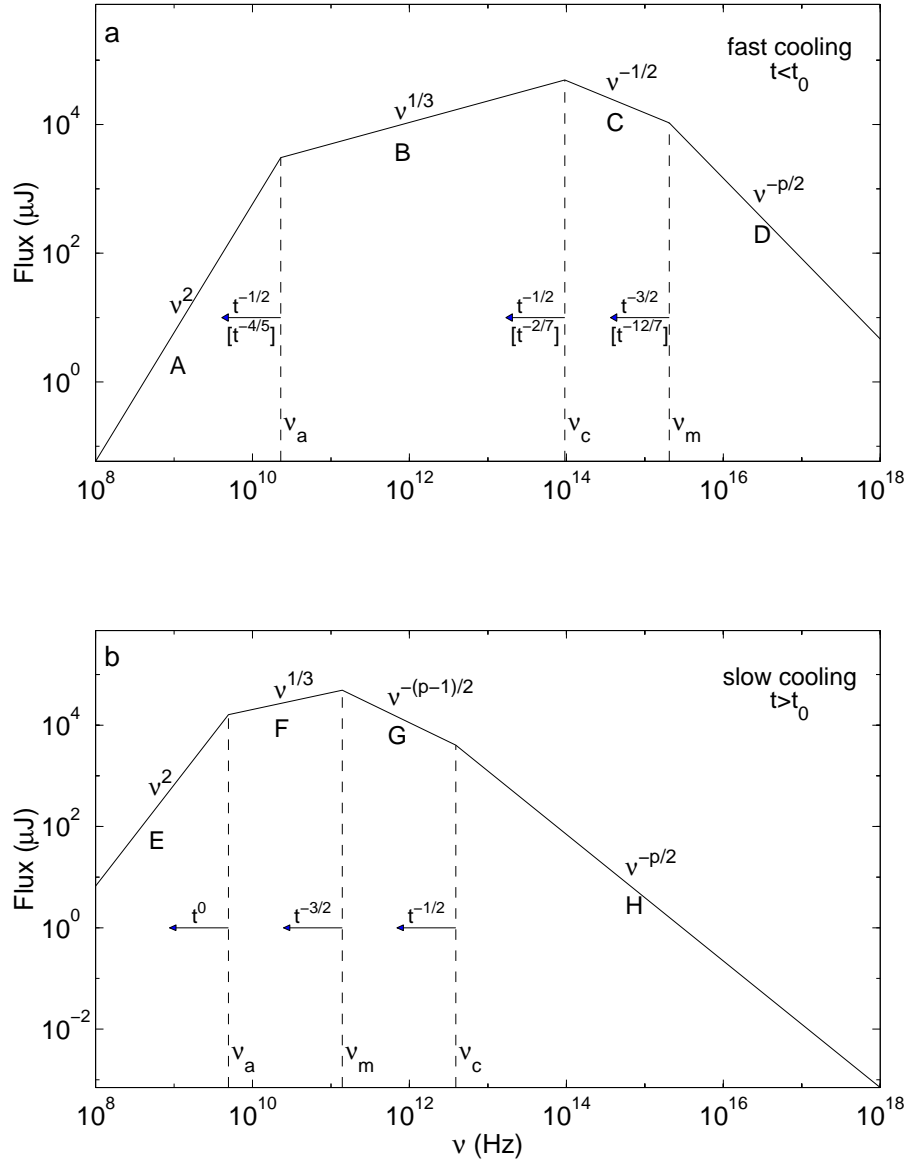
Figure 1.5 The spectra expected from a source cooling via synchrotron (the mechanism is explained thoroughly in Sect. 1.2.2). Panel (a) is the case for which the source is cooling faster than the dynamical time, whereas, (b) depicts the source when it is cooling slower than the dynamical time. Temporal indices describe the evolution of the frequencies for adiabatic cooling (radiative cooling values are within square braces). Adapted from Sari et al. (1998).

8

Initially, external shocks were not a favoured explanation for the prompt emission, as they would not be able to explain the variability seen in prompt emission light curves. However, if it is assumed that the interstellar medium consists of clumpy dust, then this could also reproduce the observed light curves. The current problem with this model is that it makes several assumptions that do not make it completely realistic (we discuss the use of the external shock model to explain afterglow emission in the next section).

4. Cannonball model (e.g., Dar & de Rújula 2004)

The cannonball model assumes that there is a release of several cannonballs or bullet-like objects of matter during a supernova that have a mass similar to that of the Earth. These cannonballs contain a plasma, which then inverse Compton scatters the supernova light into γ-rays, easily explaining the temporal variability of the observed light curves. However, there is currently no description of how these cannonballs are created.

5. Synchrotron self-Compton (e.g., Stern & Poutanen 2004)

In any model where synchrotron cooling occurs, it is also possible that the radiating electrons will up scatter the photons they emitted. This can drastically change the shape of the expected spectra, which could explain some of the features found to date.

1.2.3 Afterglow Emission

The widest accepted model to explain afterglow emission is the external shock scenario (Sari et al. 1998). The concept is the same as that outlined for the internal shock scenario in Sect. 1.2.2, but rather than relativistic shocks between two shells, it is when a single shell collides with the interstellar medium or stellar winds of the progenitor star. As the fireball ploughs into the ISM, a shock will form both in the direction of the fireball (forward shock) and in the opposite direction (reverse shock). Initially the fireball will coast along until it has swept up material that is equivalent to a fraction of its own mass-energy and then it decelerates. This is known as the deceleration radius R_{dec} (e.g., Mészáros 2006; Vedrenne & Jean-Luc 2009). Therefore, the afterglow component will rise in luminosity until it reaches the deceleration radius and then begin to decay like a powerlaw. As already noted, the Fermi acceleration at the contact discontinuity, in combination with magnetic fields, will result in the electrons cooling via synchrotron emission, as depicted in Fig. 1.5. The hydrodynamical evolution of the forward and reverse shocks, or light curves, depend on how the electron density, characteristic frequencies (ν_m, ν_c, ν_a), and the maximum flux change with time. In the adiabatic case, where energy is constant, one can show (Sari et al. 1998):

$$\nu_c \propto \epsilon_B^{-\frac{3}{2}} E_{52}^{-\frac{1}{2}} n^{-1} t^{-\frac{1}{2}} \quad \propto t^{-\frac{1}{2}} \tag{1.3}$$

$$\nu_m \propto \epsilon_B^{\frac{1}{2}} \epsilon_e^2 E_{52}^{\frac{1}{2}} n^{-1} t^{-\frac{3}{2}} \quad \propto t^{-\frac{3}{2}} \tag{1.4}$$

$$F_{\nu,\max} \propto \epsilon_B^{\frac{1}{2}} E_{52} n^{\frac{1}{2}} D_{28}^{-2} \quad \propto t^0 \tag{1.5}$$

where ϵ_B is the fraction of the internal energy behind the shock that has gone into the magnetic field, ϵ_e is the fraction of the electron internal energy, n is the ISM density, E is energy released assuming it is isotropic, and D is the luminosity distance (we have used the convention that $Q_x = 10^x Q$ and everything is in cgs units). However, if the expansion of the shock is radiative, the characteristic frequencies will evolve as:

$$\nu_c \propto \epsilon_B^{-\frac{3}{2}} E_{52}^{-\frac{4}{7}} \Gamma^{\frac{4}{7}} n^{-\frac{13}{14}} t^{-\frac{2}{7}} \quad \propto \Gamma(t)^{\frac{4}{7}} t^{-\frac{2}{7}} \tag{1.6}$$

$$\nu_m \propto \epsilon_B^{\frac{1}{2}} \epsilon_e^2 E_{52}^{\frac{4}{7}} \Gamma^{-\frac{4}{7}} n^{-\frac{1}{14}} t^{-\frac{12}{7}} \quad \propto \Gamma(t)^{-\frac{4}{7}} t^{-\frac{12}{7}} \tag{1.7}$$

$$F_{\nu,\max} \propto \epsilon_B^{\frac{1}{2}} E_{52}^{\frac{8}{7}} \Gamma^{-\frac{8}{7}} n^{\frac{5}{14}} D_{28}^{-2} t^{-\frac{3}{7}} \quad \propto \Gamma(t)^{-\frac{8}{7}} t^{-\frac{3}{7}} \tag{1.8}$$

where Γ is the Lorentz factor of the ejecta. These details make it possible to determine the flux at a given time at different frequencies (Fig. 1.6), viz., light curves.

Once the prescription of the spectrum and its evolution with time in an expanding fireball is known, a set of relations that the temporal and spectral indices must satisfy can be derived, called the closure relations. These can be seen in Fig. 1.7 and depend upon the frequency range with respect to the characteristic values (ν_c, ν_m, ν_a), the type of cooling (fast, slow), the medium it is moving through, and if there is a jetted outflow or not.

There is mounting evidence that the relativistic outflow is confined into jets (e.g., Wiersema et al. 2013 Nature in prep.), the two biggest clues are related to the energetic output and light curve breaks. Firstly, the isotropic-equivalent energies are as large as the binding energy of the Sun (10^{53} erg), such that it would be difficult to have such energetics from a stellar object, like a massive star (Vedrenne & Jean-Luc 2009). Therefore, if the outflow was collimated into a jet, the total energetic release would be reduced by a factor of ~ 100, as a result of the opening angle of the jet. For example, a jet with an opening angle of $\theta = 10°$ would have a correction of $f = 1 - \cos(\theta/2) \sim \frac{\theta^2}{2} \approx 0.01$ (Frail et al. 2001). A reduction in energy output of this amount would make it plausible for a massive star to create a GRB (this process is discussed in detail in Sect. 1.2.4).

Supporting evidence of collimation was obtained from the radio afterglow of a few GRBs. The expanding fireball becomes brighter in the radio bands at later times, as depicted in Fig. 1.6, as the frequencies of the spectrum move to lower frequencies over time, as shown in Fig. 1.5. The expanding fireball, that causes the afterglow emission, is also expected to expand transversely and eventually spherically after several weeks (see, e.g., Waxman et al. 1998). This allows the isotropic energy of the fireball to
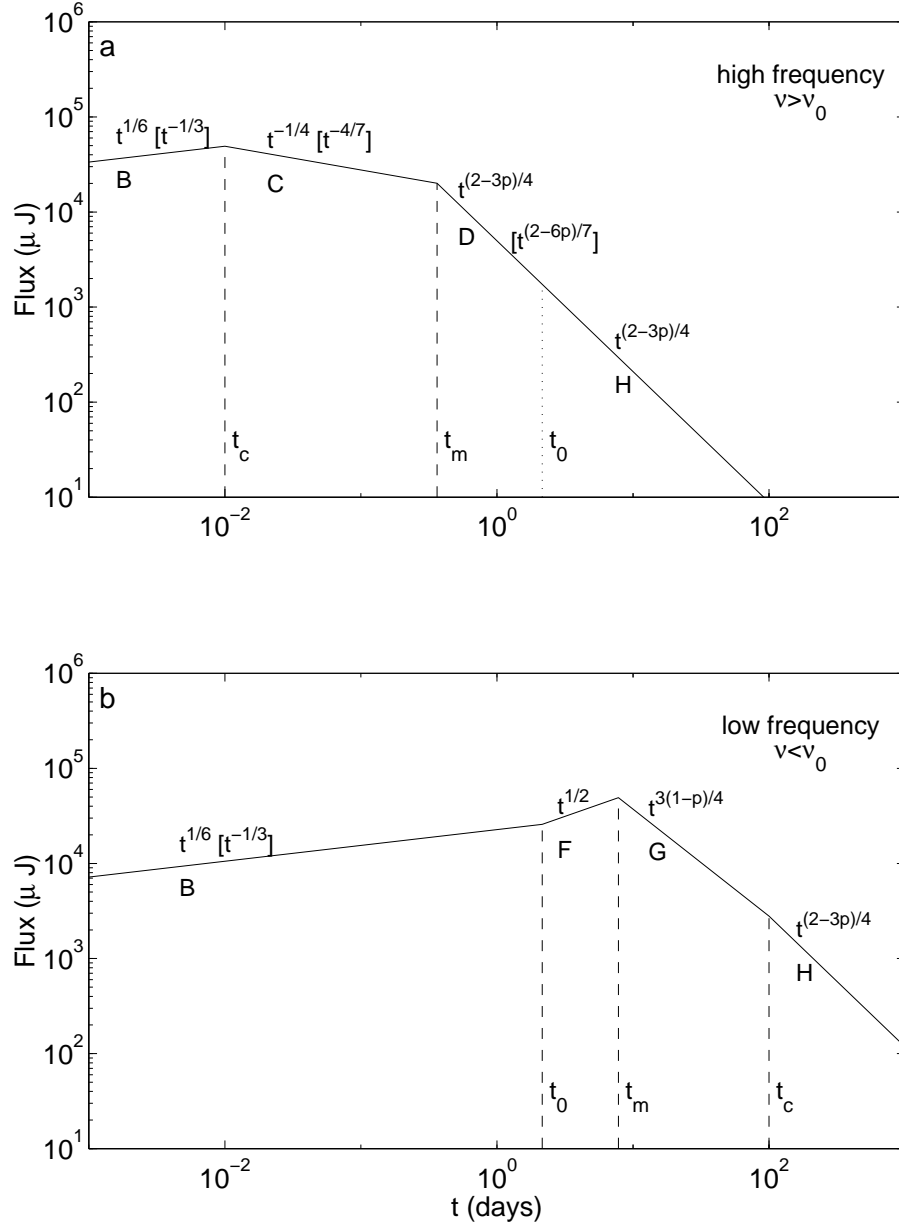
Figure 1.6 Light curves expected from a relativistically expanding fireball that is cooling via synchrotron radiation. **(a)** For the frequencies larger than $\nu = \nu_0 = \nu_c = \nu_m$, i.e., the time t_0 at which the typical frequency and critical frequency cross one another. **(b)** Light curve for frequencies less than ν_0. The temporal slopes are for adiabatic evolution and the square braces are for radiative evolution. The capitalised letters are the same spectral segments shown in Fig. 1.5. Adapted from Sari et al. (1998).

Closure Relations

		β	a No Energy Injection $\alpha(\beta)$ $(p>2)$	b $\alpha(\beta)$ $(1<p<2)$	c Energy Injection $\alpha(\beta)$ $(p>2)$
			ISM, Slow Cooling		
1	$\nu_m < \nu < \nu_c$	$\frac{p-1}{2}$	$\alpha = \frac{3\beta}{2}$	$\alpha = \frac{3(2\beta+3)}{16}$	$\alpha = (q-1) + \frac{(2+q)\beta}{2}$
2	$\nu > \nu_c$	$\frac{p}{2}$	$\alpha = \frac{3\beta-1}{2}$	$\alpha = \frac{3\beta+5}{8}$	$\alpha = \frac{q-2}{2} + \frac{(2+q)\beta}{2}$
			ISM, Fast Cooling		
3	$\nu_c < \nu < \nu_m$	$\frac{1}{2}$	$\alpha = \frac{\beta}{2}$	$\alpha = \frac{\beta}{2}$	$\alpha = (q-1) + \frac{(2-q)\beta}{2}$
4	$\nu > \nu_m$	$\frac{p}{2}$	$\alpha = \frac{3\beta-1}{2}$	$\alpha = \frac{3\beta+5}{8}$	$\alpha = \frac{q-2}{2} + \frac{(2+q)\beta}{2}$
			Wind, Slow Cooling		
5	$\nu_m < \nu < \nu_c$	$\frac{p-1}{2}$	$\alpha = \frac{3\beta+1}{2}$	$\alpha = \frac{2\beta+9}{8}$	$\alpha = \frac{q}{2} + \frac{(2+q)\beta}{2}$
6	$\nu > \nu_c$	$\frac{p}{2}$	$\alpha = \frac{3\beta-1}{2}$	$\alpha = \frac{\beta+3}{4}$	$\alpha = \frac{q-2}{2} + \frac{(2+q)\beta}{2}$
			Wind, Fast Cooling		
7	$\nu_c < \nu < \nu_m$	$\frac{1}{2}$	$\alpha = \frac{1-\beta}{2}$	$\alpha = \frac{1-\beta}{2}$	$\alpha = \frac{q}{2} - \frac{(2-q)\beta}{2}$
8	$\nu > \nu_m$	$\frac{p}{2}$	$\alpha = \frac{3\beta-1}{2}$	$\alpha = \frac{\beta+3}{4}$	$\alpha = \frac{q-2}{2} + \frac{(2+q)\beta}{2}$
			Uniform Jet (spreading), Slow Cooling		
9	$\nu_m < \nu < \nu_c$	$\frac{p-1}{2}$	$\alpha = 2\beta + 1$	$\alpha = \frac{2\beta+7}{4}$	$\alpha = 2\beta + 1 - \frac{2(1-q)(\beta+2)}{3}$
10	$\nu > \nu_c$	$\frac{p}{2}$	$\alpha = 2\beta$	$\alpha = \frac{\beta+3}{2}$	$\alpha = 2\beta - \frac{2(1-q)(\beta+1)}{3}$
			ISM, Uniform Jet (nonspreading)		
11	$\nu_m < \nu < \nu_c$	$\frac{p-1}{2}$	$\alpha = \frac{6\beta+3}{4}$	$\alpha = \frac{6\beta+21}{16}$	$\alpha = \frac{6\beta+3}{4} - \frac{(1-q)(2\beta+5)}{4}$
12	$\nu > \nu_c$	$\frac{p}{2}$	$\alpha = \frac{6\beta+1}{4}$	$\alpha = \frac{3\beta+11}{8}$	$\alpha = \frac{6\beta+1}{4} - \frac{(1-q)(2\beta+3)}{4}$
			Wind, Uniform Jet (nonspreading)		
13	$\nu_m < \nu < \nu_c$	$\frac{p-1}{2}$	$\alpha = \frac{3\beta+2}{2}$	$\alpha = \frac{2\beta+13}{8}$	$\alpha = \frac{3\beta+2}{2} - \frac{(1-q)(\beta+2)}{2}$
14	$\nu > \nu_c$	$\frac{p}{2}$	$\alpha = \frac{3\beta}{2}$	$\alpha = \frac{\beta+5}{4}$	$\alpha = \frac{3\beta}{2} - \frac{(1-q)(\beta+2)}{2}$
			ISM, Structured Jet		
15	$\nu_m < \nu < \nu_c$	$\frac{p-1}{2}$	$\alpha = \frac{3k+12\beta}{8-k}$		
16	$\nu > \nu_c$	$\frac{p}{2}$	$\alpha = \frac{12\beta+2k-4}{8-k}$		
			Wind, Structured Jet		
17	$\nu_m < \nu < \nu_c$	$\frac{p-1}{2}$	$\alpha = \frac{6\beta+k\beta+2}{4-k}$		
18	$\nu > \nu_c$	$\frac{p}{2}$	$\alpha = \frac{6\beta+k-k\beta-2}{4-k}$		

Figure 1.7 The closure relations that the temporal and spectral slopes of an external shock are expected to satisfy for the type of medium that it is moving through and the type of jet it has. Adapted from Racusin et al. (2009).

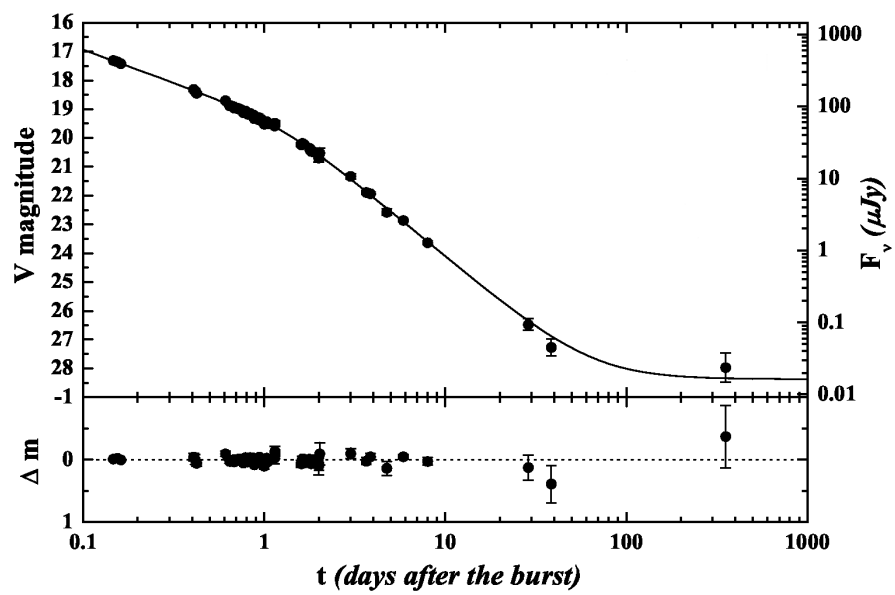Figure 1.8 The light curve of GRB 990510A, which shows a break in the light curve 1.3 days after the burst. This change in the temporal decay index of the light curve is usually considered to be a sign of a jet break. The flattening of the light curve around 400 days after the GRB is when the emission from the underlying host galaxy dominates over the afterglow. Adapted from Zeh et al. (2006).

be calculated directly. Many authors found that the calculated energetic output from the radio afterglow was much smaller than that measured by the prompt emission. This was consistent with the prompt emission originating from a collimated outflow (see, e.g., Waxman et al. 1998). Finally, many afterglows have been observed to have achromatic breaks in their light curves where the decay becomes steeper (Fig. 1.8). Such a break would occur when the beaming angle becomes large enough that the observer sees the entire emission from the flow (i.e, $\theta < 1/\Gamma$; Rhoads 1997). In addition, some GRB light curves that exhibit a rebrightening have attributed it to the fact that two jets exist with different opening angles (i.e., one inner jet and one outer jet with $\theta_{\mathrm{inner}} < \theta_{\mathrm{outer}}$) and Lorentz factors, arguing again for a collimated outflow (Filgas et al. 2011b). Current values of opening angles, obtained from the break time in the afterglow light curve, range from $0 - 10°$ (Frail et al. 2001). However, recent magnetic hydrodynamical simulations of collimated fireballs have shown that they cannot reproduce jet breaks at the same time periods as that observed, suggesting that what is seen is not actually a result of a collimated outflow (van Eerten & MacFadyen 2012).

Another way of ascertaining if the GRB emission is, in fact, collimated into a jet utilises polarimetry, viz., measure the polarisation of the emitted optical/near-infrared light (see Wiersema 2013 and references therein). Synchrotron electrons that cool within a collimated jet would give rise to polarised light. The amount of polarisation, how it changes with time, and its direction are all dependent upon the jet geometry, its structure, and the magnetic fields (see Fig. 1.9). As a result of the sensitivities achieved with the limited number of polarimetry observations, there is currently no consensus on the polarisation of the outflow (currently the polarisation is in the range of $\sim 1 - 10\%$; Wiersema et al. 2012; Wiersema 2013). The recent detection of a polarisation angle change during the jet break of an afterglow (GRB 121024A; Wiersema et al. 2013 Nature in prep.) undoubtedly supports the idea of a jetted outflow. However, the ratio of the expected circular polarisation to linear polarisation under predicts drastically what is observed and questions the external shock origin of afterglows or the assumption that the electron pitch angle is isotropic.

Sub-classes

Within the GRB community there exists a few sub-classes of afterglows, the most notable are the following:

1. Dark bursts

   Afterglows that have highly extincted or no detected optical counterpart are placed in the class of dark bursts (for a more detailed definition see Greiner et al. 2011a). The origin of this optical dampening is the result of two possible effects: (i) dust in the line-of-sight of the GRB emission, or (ii) the Lyman-break as a result of the redshift of the GRB. In the majority of cases ($\sim 75\%$) it is the result of dust absorption. We discuss more thoroughly the mechanics of these effects in Chapter 2.
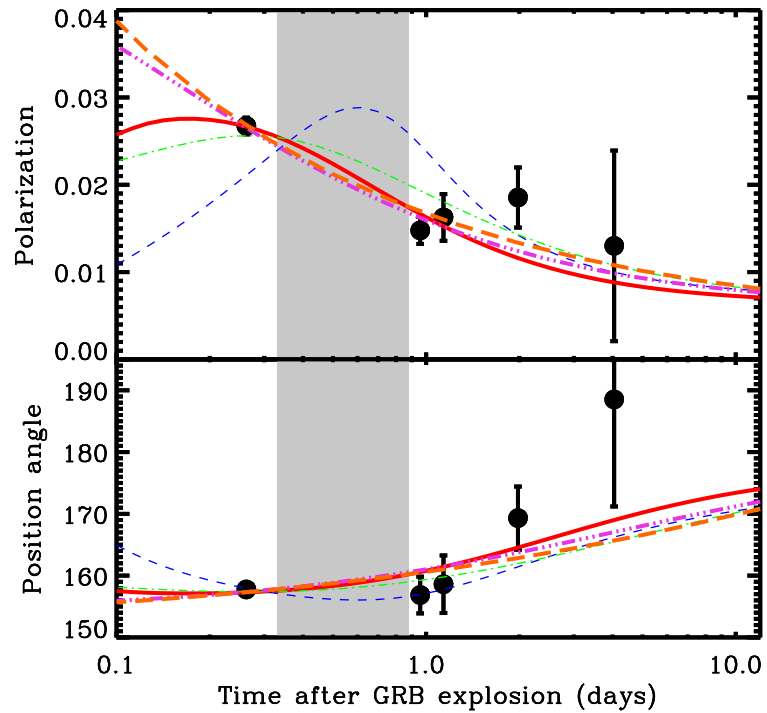
Figure 1.9 The top and bottom panels show the temporal evolution of the polarisation and position angle, respectively, for a set of models (coloured lines) and measurements of GRB 020813. The different colours refer to different jet geometries, structures and the media it is passing through (see Lazzati et al. 2004 and references therein for details about the different models). Adapted from (Lazzati et al. 2004).

2. Orphan afterglows

   An afterglow that has no associated prompt emission is called an orphan afterglow. This sub-class is expected to exist if the GRB emission is collimated, such that the beam axis is offset from the observer and the afterglow only becomes visible once the jet widens. Only one viable candidate has been found so far (Soderberg et al. 2010), but as it had no associated prompt emission only upper limits have been placed on the opening angle of the jet.

Short comings and alternatives

The fireball model is favoured because of its ease of use in comparing it with observations and, in the majority of cases, it can reproduce what is observed. However, there are several problems still not settled (Vedrenne & Jean-Luc 2009). Firstly, for most GRBs, the best-fit light curve models are in ISM environments rather than stellar wind environments ($\sim \frac{2}{3}$ show a preference for a constant density medium; Schulze et al. 2011), which is not consistent with the picture of a Wolf-Rayet-like progenitor (see Sect 1.2.4). Secondly, the microphysical parameters are not always constant (see, e.g., Filgas et al. 2011a, 2012) and so the simple fireball picture no longer applies, as the simplest case assumes these to be constant. Thirdly, the purported observations of jet breaks cannot be reproduced in magnetohydrodynamic simulations with the same characteristics.

The cannon ball model is the only other competitor to explain the observed afterglow, as noted in Sect. 1.2.2, whereby the cannon ball sweeps up electrons in the surrounding medium and accelerates them within itself, resulting in synchrotron emission. Despite its problems, the fireball model is still the favoured model of explaining both the prompt and afterglow emission.

1.2.4   GRB Progenitors

Collecting information about the progenitor of a GRB is one of the most daunting, if not completely impossible, tasks in the GRB field. The prime reason for this is that the progenitor cannot be directly observed and even if the field has been observed prior to the prompt emission of the GRB, we are limited to low redshifts, such that the progenitor could still be resolved with current instrumentation. As a result of these limitations, most of the progenitor models are inferred from observations of the different properties of the GRB, e.g., the environment that surrounds it, which is ascertained from absorption lines in spectroscopy or closure relations, environments of the hosting galaxies, energetic output and many other things.

The only contender that is able to produce the huge energetic output of a GRB, at cosmological scales, is the gravitational collapse of a massive star to a neutron star or black hole (Woosley 1993), or even mergers of these events (see, e.g., Narayan et al. 1992), and is called the collapsar model. Woosley (1993) suggested that big enough black holes could form via a failed type Ib supernovae. This involves the collapse of a massive

star's iron core, which does not explode in a supernovae as a result of angular momentum (or other reasons) and it would continue to feed the black hole. This would result in the formation of a disc around the black hole (there are many possible avenues for creating a black hole with an accretion disc, as outlined in Fig. 1-13 of Fryer et al. (1999), however, we stick to the original concept throughout the discussion). The disc would then feed onto the black hole at a rate of $\sim 0.1\,\mathrm{M_\odot yr^{-1}}$ (MacFadyen & Woosley 1999), which would then be radiated as neutrinos in all three flavours at a rate of $10^{52}\,\mathrm{erg\,s^{-1}}$ (Woosley 1993). Once the accretion disc forms (~ 10 s) and the polar regions become clear, the emitted neutrinos will recombine in the process $\nu + \bar{\nu} \to e^+ + e^-$ (Eichler et al. 1989) and will be directed in polar directions as a result of the disc shape (see Fig. 1.10). The magnetic fields must also not be neglected, which grow in size through viscous shear within the disc to field strengths of $B \sim 10^{17}\,\mathrm{G}$ and could result in the ejection of field lines through Parker-like instabilities (Narayan et al. 1992). These field lines have little baryonic contamination, required by the fireball model, and multiple flare-like reconnections would explain the prompt emission variability. Another avenue of creating a jet like structure from magnetic fields is via the Blandford-Znajek mechanism. The magnetic field lines within the disc thread the event horizon of the rotating black hole (more correctly, the ergosphere), which are then dragged by the rotation of the black hole, that in turn, will generate a cascade of electron-positron pairs (Blandford & Znajek 1977). Regardless of the mechanism which creates the jetted material (currently there is no consensus), the electron-positron fireball will propagate out of the stellar envelope and exit after $\sim 10s$. The final constraint is that there should be no hydrogen envelope left over from the progenitor star, as the outflowing jet would be slowed by the hydrogen layer to such low Lorentz factors that it would no longer be relativistic (MacFadyen & Woosley 1999). These collapsar models also predict that a supernova will also be observed, which is believed to result from the winds coming from the disc of the black hole, associated to the same progenitor as the GRB (for a review, see, e.g., Woosley & Bloom 2006).

The first observational hint that GRBs were caused by the death of massive stars was the association of the supernovae 1998bw with GRB 980425, such that both of the objects occurred at a similar time ($\Delta t = 1^{+0.7}_{-0.2}$ days) and a similar direction in the sky (Kulkarni et al. 1998; Galama et al. 1999). It took another five more years until the association was confirmed by spectroscopy for GRB 030329 and SN 2003dh (see Fig. 1.11; Stanek et al. 2003; Matheson et al. 2003; Hjorth et al. 2003). Many other associations have been confirmed through spectroscopy or inferred from bumps in the afterglow's light curves (see, e.g., Zeh et al. 2004; Olivares E. et al. 2012). The GRB supernovae population are usually of type Ib/c (Hjorth et al. 2012), as their spectra lack hydrogen and helium, which usually has a Wolf-Rayet-like progenitor (Filippenko 1997).

All of these properties are in support of the collapsar model, however, simulations showed that a GRB would only form if enough angular momentum would be retained ($3 < j/10^{16}\mathrm{cm^2s^{-1}} < 20$; MacFadyen & Woosley 1999). Given the large stellar winds expected from Wolf-Rayet stars during their lifetime the angular momentum
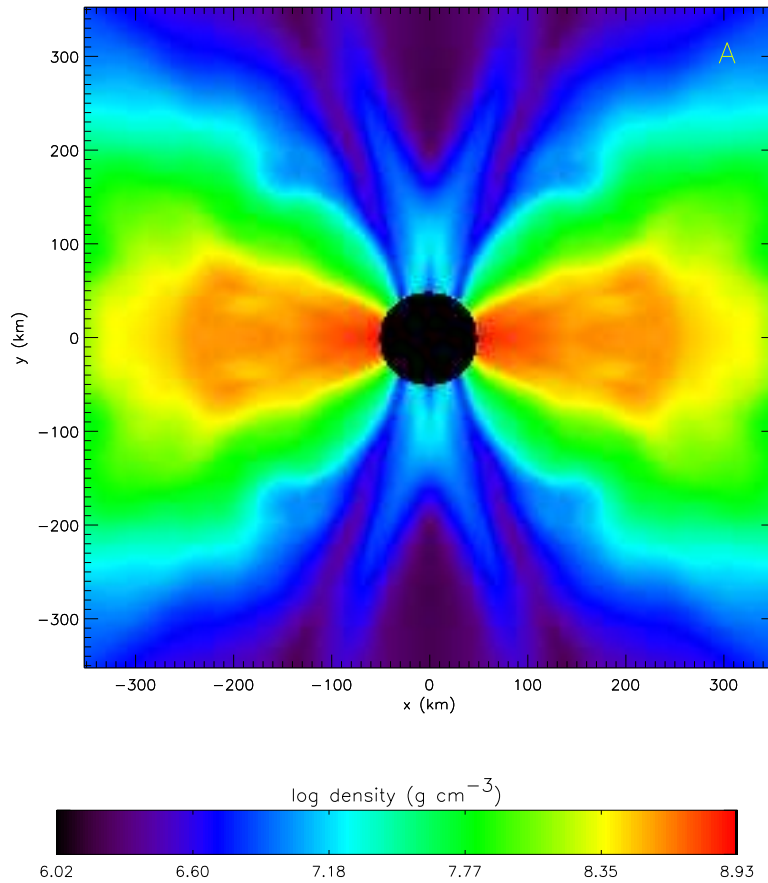
Figure 1.10 Density map of gas around an accreting, rotating, black hole. The contours show that because of angular momentum conservation or lack of centrifugal forces a disc has formed and has left the polar regions empty. Such a schematic shows the possibility of creating jetted material in the polar directions if energy is released. Adapted from MacFadyen & Woosley (1999).
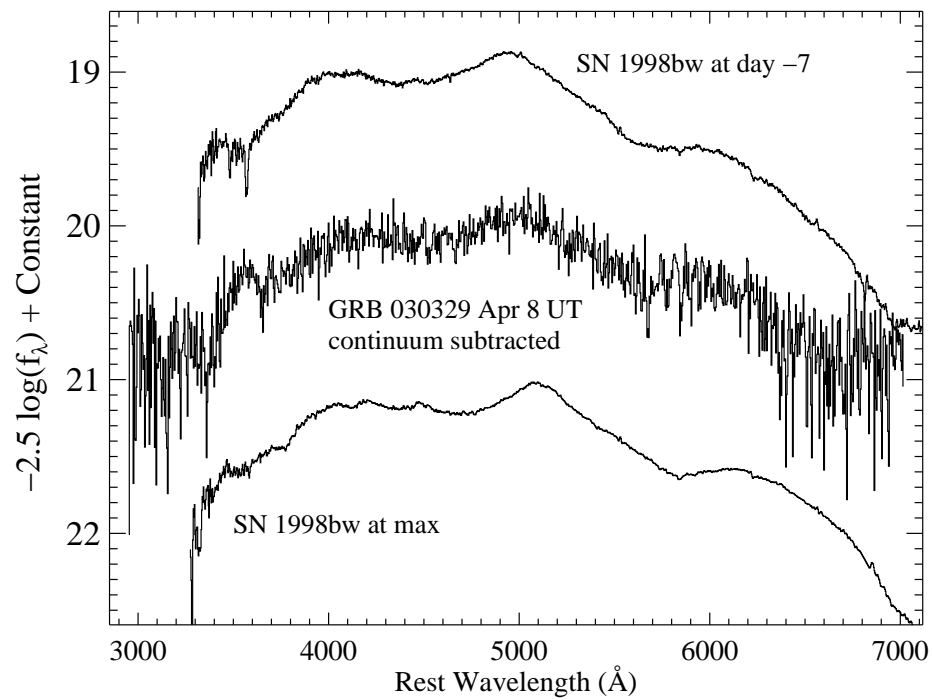
Figure 1.11 Spectrum of GRB 030329 (middle) has had the afterglow continuum subtracted. The remaining spectral shape is very similar to that of 1998bw, which is shown above and below for different time periods of its evolution. This is the first spectroscopically confirmed SN association with a GRB. Adapted from Stanek et al. (2003).
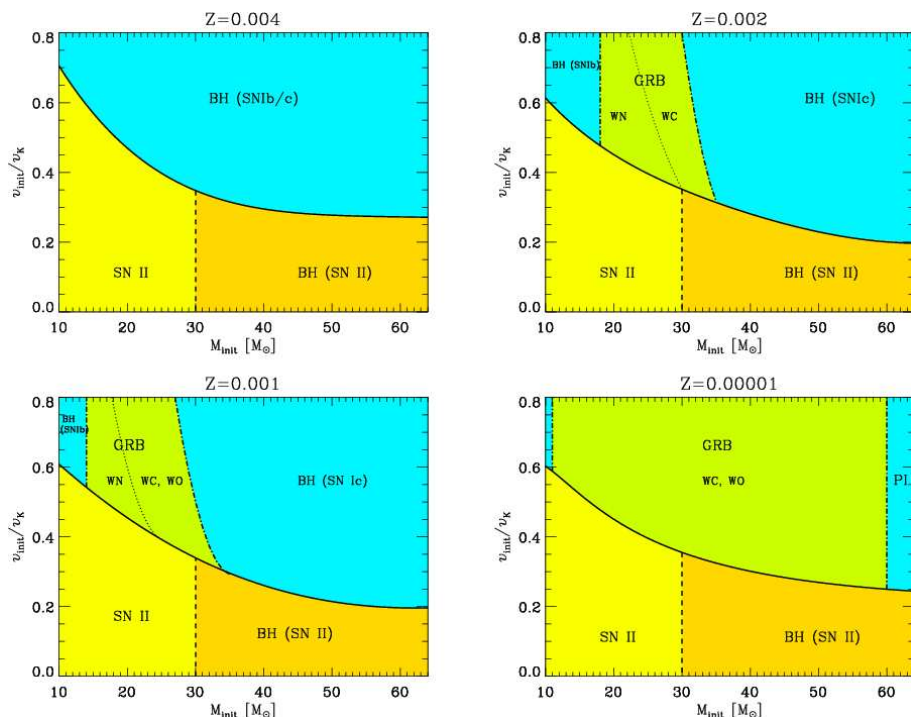
Figure 1.12 Different end scenarios for a set of stellar grids that have different progenitor masses, rotation velocities, and metallicities. WN, WC, and WO refer to types of Wolf-Rayets. Adapted from Yoon & Langer (2005).

would be reduced so much that a disc around the black hole and more importantly a GRB would not form. As the progenitor winds depend on the metallicity of the star and its environment (i.e., more metal more winds), studies showed that Wolf-Rayet stars that existed in low-metallicity environments ($Z < 0.3\,Z_\odot$; see also Fig. 1.12) were able to produce a GRB (Hirschi et al. 2005; Yoon & Langer 2005; Woosley & Heger 2006). This theoretically driven preference was consistent with concurrent observations of host galaxies, which suggested that long GRBs preferred low-metallicity environments (this is discussed thoroughly in Sect. 1.2.5) and lead to the standard collapsar model.

In the past three years it has become apparent that GRBs do not have to necessarily exist in regions of low-metallicity and metallicities can in fact be as large as solar (Levesque et al. 2010c; Krühler et al. 2012a; Elliott et al. 2013), which has opened again the question of how the collapsar model can work in a high-metallicity environment. Recent simulations that have looked at grids of rotating Wolf-Rayet populations have suggested that there is an extra (missing) braking mechanism that affects the rotation of a newly formed neutron star (Georgy et al. 2012). They relate this mechanism to either a strongly coupled magnetic field that prefers a low-metallicity environment or a moderate differential internal coupling, which does not dependent strongly on metalli-

city. Given the discovery of solar-metallicity GRB environments, it suggests there could be a moderate/weak internal coupling mechanism favouring a dependence on the mass and magnetic field of the progenitor.

1.2.5   Host Galaxy Population

History

Initial studies of long GRB host galaxies resulted in a unique sub-population of galaxies that were primarily of low mass, low metallicity, blue, and actively star forming (see, e.g., Fruchter et al. 1999; Le Floc'h et al. 2003; Berger et al. 2003; Christensen et al. 2004; Tanvir et al. 2004). This was consistent with the collapsar model, which required the presence of low metallicity systems to create a GRB (Hirschi et al. 2005; Yoon & Langer 2005; Woosley & Heger 2006).

Further work carried out with larger samples (e.g., Savaglio et al. 2009), showed again the same properties. However, they noted that long GRB hosts were no different to the normal population of star forming galaxies at the same redshifts and that their abundance is a result of the galaxy mass function. The galaxy mass function is the number density of galaxies per a given mass bin and usually has a Schechter-function shape ($N \propto M^{\alpha} e^{-M}$ where N is number and M is stellar mass; Schechter 1976), such that there are more low mass galaxies than high mass (see, e.g., Fontana et al. 2006). Recently it was also shown that galaxies with more star formation usually have lower global metallicities as a result of a fundamental metallicity relation and as long GRBs trace locations of star formation within the galaxy (Mannucci et al. 2011), we see the low-mass, low-metallicity systems.

Several host galaxies have been found that do not have the same properties as just noted and were usually associated with afterglows that were highly extincted (dark bursts). The dark bursts that exhibited highly extincted or no optical/near-infrared afterglow were associated with host galaxies that are defined as extremely red objects (ERO), which have huge amounts of dust and mass (e.g., Hashimoto et al. 2010; Hunt et al. 2011; Rossi et al. 2012; Svensson et al. 2012). In summary, long GRB host galaxies that were associated with dark bursts revealed that they were systematically more massive and red than the previous population localised with optically bright afterglows (e.g., Krühler et al. 2011a; Hjorth et al. 2012; Rossi et al. 2012). This correlation has also been observed in absorption lines of long GRB sight-lines that shows the stronger the absorption the larger the magnitudes and the extinction of the host galaxy (de Ugarte Postigo et al. 2012).

Finally, a few long GRBs have been found in environments with metallicities as large as solar or even super-solar (Krühler et al. 2012a; Savaglio et al. 2012), questioning the preferred properties of progenitor models and environments that can explain long GRBs.

The Current Picture

The research on long GRB host galaxies is still a growing field, with currently no consensus reached on exactly what properties they have, as a result of the variety of galaxies found harbouring GRBs. Therefore, in the following we outline the current view of GRB host galaxies using four samples: Savaglio et al. (SG09; 2009), Krühler et al. (KR11; 2011a), Mannucci et al. (MN11; 2011), and Perley et al. (PL13; 2013).

1. Stellar mass

   Despite initial investigations finding primarily low mass galaxies hosting GRBs, there have been several observations yielding high mass host galaxies. This was primarily a result of biased surveys, but which has now been investigated extensively in the past 2 years. As can be seen in Fig. 1.13, the stellar masses of long GRB hosts range from $10^7 \, M_\odot$ to $10^{12} \, M_\odot$, over a redshift range of $z = 0 - 4$ and have similar properties to normal field galaxies.

2. Star formation rates

   The star formation rates probed by GRB host galaxies cover a broad range of values across redshifts (10^{-2} to $10^2 \, M_\odot \, yr^{-1}$ Fig. 1.14) and vaguely follow a trend expected from normal field galaxies, where the star formation rate is larger for more massive galaxies, and vice versa. However, as it is expected for GRBs to trace star formation, the GRB host galaxies should have higher star formation rates when compared to normal field galaxies. This is currently not the case and there are two explanations: (i) a selection bias of GRBs, such that they depend on a host galaxy parameter, e.g., metallicity (Graham & Fruchter 2012; Perley et al. 2013), or (ii) a dependence on the fundamental metallicity relation, such that the lower the metallicity of the galaxy, the larger the star formation rate (e.g., Krühler et al. 2012b; Elliott et al. 2013).

3. Metallicity

   The ongoing debate of the connection of star formation rate and metallicity dependence has sparked a large investment of time in spectroscopy of GRB host galaxies to obtain the average host integrated metallicity or even the line-of-sight metallicity of the GRB. As a result of the possible line diagnostics that can be used to quantify the metallicity (Kewley & Ellison 2008), most detections have been at redshifts $z \lesssim 1$. The normal range for metallicity values is $Z \sim 0.01 - 0.5 \, Z_\odot$ (e.g., Savaglio et al. 2009; Graham & Fruchter 2012), but more recent observations have found a few cases of solar-metallicity galaxies (Fig. 1.15 and Levesque et al. (2010c); Krühler et al. (2012b); Elliott et al. (2013)), which would argue against a preference for low-metallicity environments. However, these galaxies are usually large and so metallicity dispersion would mean the integrated metallicities do not necessarily reflect the metallicity at the location of the GRB (Niino 2011). Given the limitations
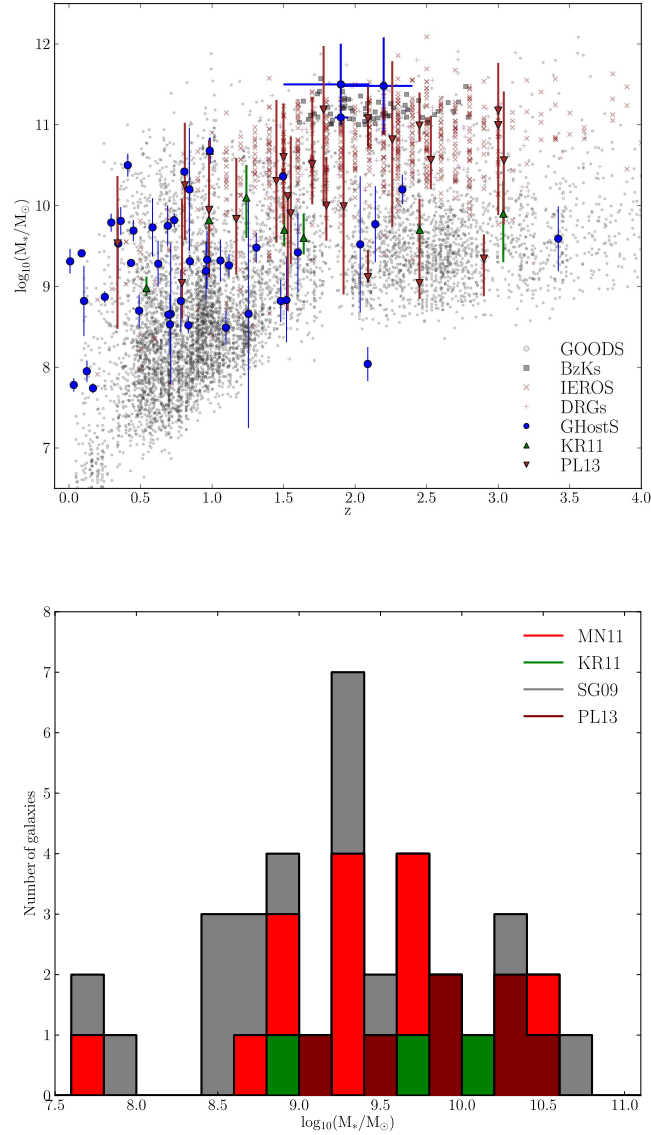
Figure 1.13 **Top**: Mass and redshift phase space of a selection of different types of galaxies. Light grey-circles are galaxies from the GOODS NICMOS survey (Conselice et al. 2011), grey-squares are BzK (colour) selected galaxies (Daddi et al. 2007a,b), light red-xs are high-redshift infrared extremely red objects (IEROs) (Yan et al. 2004), light maroon-crosses are distance red galaxies observed by *Spitzer* in the GOODS-S field (Papovich et al. 2006)[1], blue-circles are host galaxies obtained from (Savaglio et al. 2009) and the GRB Host Survey (`www.grbhosts.org`), upwards green triangles are dark GRB hosts (Krühler et al. 2011a), red-down-triangles are from Perley et al. (2013). **Bottom**: A stellar mass histogram of the GRB host galaxies.
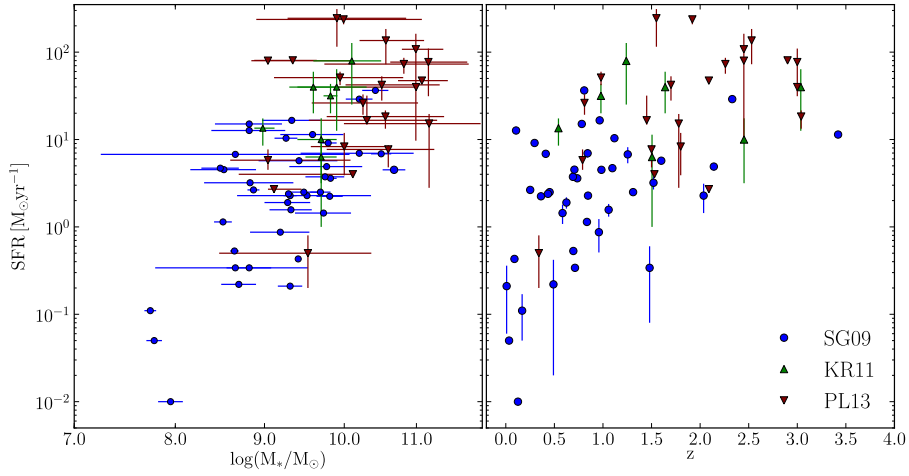
Figure 1.14 **Left**: Star formation rate plotted against the stellar mass of long GRB hosts. **Right**: The star formation rate as a function of redshift of the long GRB hosts used in the left panel.
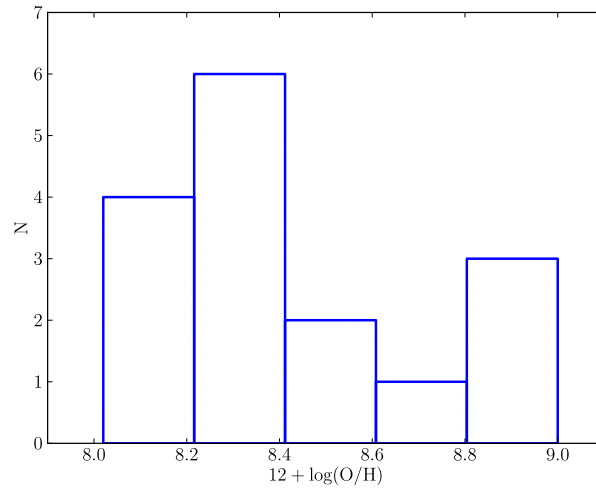
Figure 1.15 A histogram of host integrated metallicities obtained from Levesque et al. (2010d).

of spectroscopy and telescope mirror sizes, it is not an easy to task to measure or investigate in detail, the metallicity of a GRB host galaxy systematically across redshifts.

1.3   Long GRBs as Cosmological Tools

The luminous nature of long GRBs and their simple powerlaw spectra automatically makes them ideal tools for investigating the high redshift Universe ($z \sim 10$), especially in comparison to usual methods that involve Lyman-break and Lyman-α emitting galaxies (used consistently at $z \sim 4-6$). This unique property has lead to many authors utilising long GRBs as tools and we briefly outline a few examples of their usage in the following.

1. **Cosmic star formation history at high redshift**

   The spectroscopically confirmed association of long GRBs with the death of massive stars allows them to be used as tracers of star formation. At cosmological scales they can be used to estimate the cosmic star formation history (CSFH; $\dot{\rho}_*$) in the early Universe, i.e., $\dot{\rho}_* = \eta_{\mathrm{GRB}} \dot{\rho_{\mathrm{GRB}}}$, where η_{GRB} is a constant of proportionality. Despite many authors estimating the CSFH at high redshift, the connection of these two parameters is still an on going debate.

2. **Reionisation**

   Kistler et al. (2009) used the CSFH inferred from long GRBs to estimate the number of photons that must escape galaxies to ensure that the Universe is reionised. They find that a sufficient number of photons could escape from galaxies to account for the reionisation of the Universe. This conclusion has recently been built upon by using the non-detection of long GRB host galaxies at high redshift. These non-detections allow constraints to be placed on the high redshift galaxy luminosity function and, in turn, on the number of low-mass galaxies that exist at high redshift. These constraints still allow a large enough number of small galaxies to exist at high redshift to be the main contributors to the reionisation of the Universe (see, e.g., Trenti et al. 2012; Tanvir et al. 2012). Finally, recent work using a Gunn-Peterson (Gunn & Peterson 1965) trough in the absorption spectrum of GRB 130606A at a redshift of $z \sim 6$ has shown the Universe is still mostly ionised at redshifts of $z \sim 6$ (Chornock et al. 2013).

3. **Primordial Gaussianity**

   Maio et al. (2012) investigate the possibility of non-Gaussianities existing in the density field during the early stages of the Universe. Different Gaussianity models are used to estimate the CSFH and compared to the underlying long GRB rate. Large deviations are expected at $z > 6$ for different models. Therefore, when sample sizes are large enough the long GRB rate could be used to distinguish the type of Gaussianity.

4. **Population III stars**

   If population III stars end their lives as pair-instability supernovae then they would be detectable with current instrumentation, e.g., *Swift*. Therefore, the rate of these objects is estimated using the contribution of population III stars to the total CSFH. Bromm & Loeb (2006) conclude that 10% of the long GRBs detected above a redshift of $z > 5$ are from population III stars.

5. **Chemical evolution of the early Universe**

   Regions of hydrogen (Damped Lyman-α systems) or galaxies that lie along the line of sight of the long GRB emission result in absorption lines in the spectra of GRBs, which are located at the redshifted wavelength of the source. This facilitates measurements of chemical content at varying redshifts and has so far been possible to redshifts of $z \sim 6$ (Savaglio et al. 2012; Chornock et al. 2013).

   In summary, long GRBs are unique tools that cannot only be used to investigate their own properties, but also a wide range of other phenomena, easily reaching the early years of the Universe.

Chapter 2

Instrumentation, the GROND Sample and Simulations

2.1 *Swift*

The *Swift* (Gehrels et al. 2004) satellite is a NASA led multi-wavelength observatory for GRBs and other transient phenomena (Fig. 2.1). Launched in 2004, it was the very first satellite to have a dedicated slewing for transient targets and since its launch has gone beyond its expectations detecting up to 764 GRBs (2004 to May 2013). The rapid downlink of initial data and positional accuracy of arcseconds (see later sections) has allowed the ground-based community to react quickly to GRBs and find optical counterparts for the majority of cases. None of these achievements would be possible without the correct selection of instruments onboard, which we will outline in the following sections[1].

2.1.1 Burst Alert Telescope

The Burst Alert Telescope (BAT) is a large field of view γ-ray detector, with the primary aim of finding and localising GRBs to within radii of only a few arcminutes. The BAT consists of a coded mask and a solid state detector. The coded mask is an array of $\sim 54,000$ lead tiles, which in total has an area of $2.7\,\mathrm{m}^2$ and as a result, a field of view of $1.4\,\mathrm{sr}$. The detector has a total dimension of $(1.2 \times 0.6)\,\mathrm{m}^2$, made up of $\sim 30,000$ CdZnTe solid state detectors, each one being $(4 \times 4 \times 2)\,\mathrm{mm}^3$ (see Fig. 2.2). The final energy range is $15 - 150\,\mathrm{keV}$ with an energy resolution of $\frac{\Delta E}{E} \sim 5\%$ (Gehrels et al. 2004; Barthelmy et al. 2005). This makes it possible for both γ-ray light curves and spectra to be obtained.

The BAT searches continuously for GRBs and a trigger occurs if the observed flux within the detectors goes above a specific threshold, above the background. The trigger criteria are slightly more complex and, instead, a set of algorithms determine whether to

---

[1]We do not include a description of the Ultra-Violet Optical Telescope as no data are used within the thesis, we defer the reader to Gehrels et al. (2004).
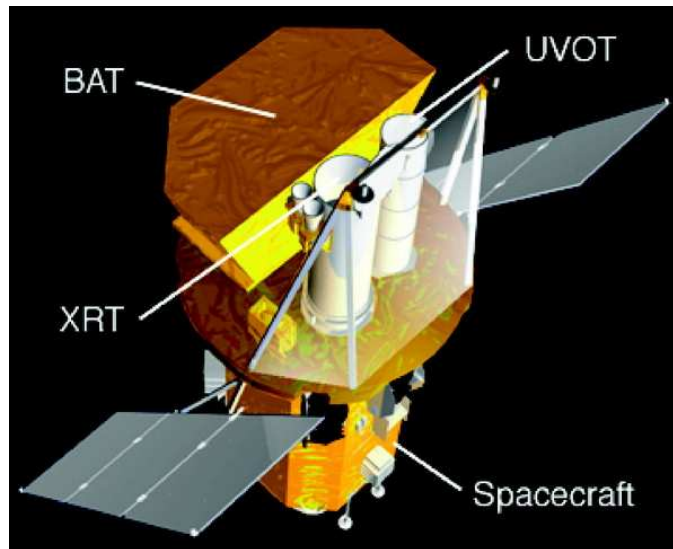
Figure 2.1 3D image of the NASA satellite *Swift* with the three instruments onboard labelled in white. Adapted from Gehrels et al. (2004).

count the event as a real trigger or not. The trigger usually depends upon the amplitude of the emission, duration of the emission, the region of detector illuminated, and the energy range covered (Gehrels et al. 2004). Once a trigger occurs and it is determined to be of interest, *Swift* will slew to the position to allow the other instruments to observe, so that better localisations, and X-ray and optical photometry can be obtained.

2.1.2   X-ray Telescope

The X-ray Telescope (XRT) uses a grazing incidence Walter 1 telescope (Fig. 2.3) to focus X-rays on to an XMM/EPIC MOS CCD. The CCDs have an image area of $600 \times 602 \, \text{pixel}^2$, which results in an effective area of $110 \, \text{cm}^2$, a field of view with a diamter of $11.5'$, a resolution of $18''$, and a spectral energy range from 0.2 to 10 keV. The energy resolution ranges from $\frac{\Delta E}{E} = 5 - 20\%$ depending on which energy range is considered. Also, the significance of charge trapping and surface losses cannot be ignored below 0.5 keV (Gehrels et al. 2004; Burrows et al. 2005).

The XRT has three possible readout modes, the choice of which depends on the type of object that is being observed. The possible modes are: (i) imaging mode, (ii) photon counting mode, and (iii) window timing mode. Imaging mode is used to determine positions of bright sources, whereby a single integration is taken and so does not allow spectroscopy (this is however flux limited). Windowed timing (WT) mode is designed to obtain high time resolution spectroscopy of the source when it is bright (~ 5 Crab), but this results in poor positional accuracy. Finally, photon counting (PC) mode is when accurate information about both the spectrum and position are needed and is usually
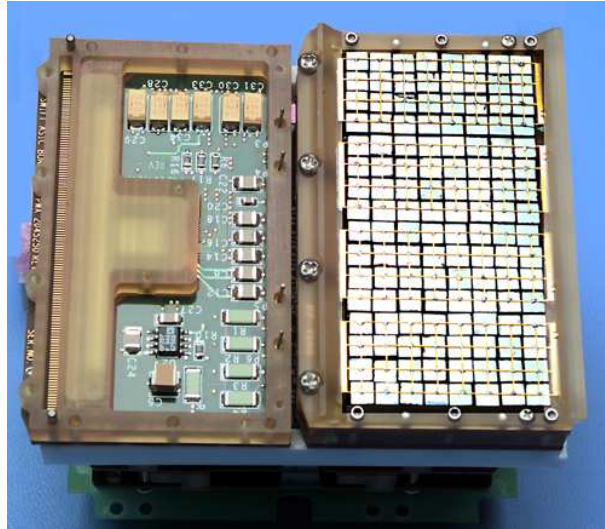
Figure 2.2 CdZnTe detector array of BAT on the right and on the left the detectors have been removed to show the power controllers. Adapted from Barthelmy et al. (2005).
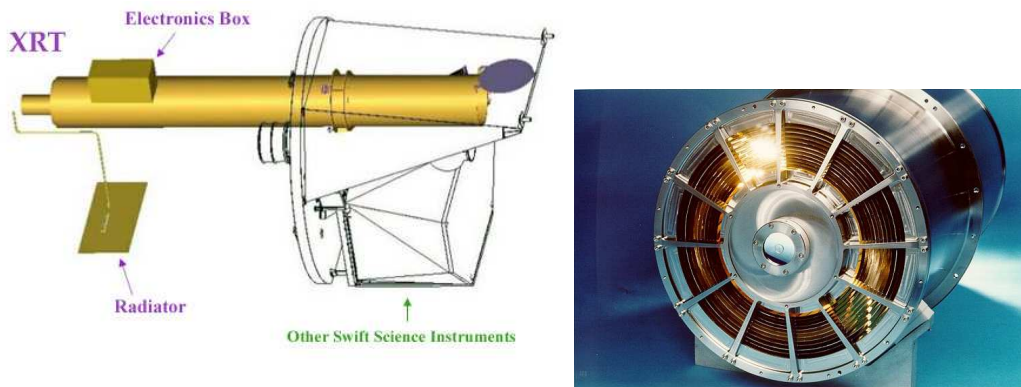
Figure 2.3 **Left**: 3D image of the *Swift* XRT in comparison to the satellite elements. Adapted from Burrows et al. (2000). **Right**: The Walter telescope unit that is used within the XRT. Adapted from Burrows et al. (2005).

used when sources have low fluxes (1-45 mCrab). In this thesis we will not distinguish between the PC and WT modes when they are used and imaging mode will no longer be of any relevance (Gehrels et al. 2004; Burrows et al. 2005).

2.1.3 Image Reduction

We obtain fully reduced data for the BAT and XRT from their respective online repositories. Therefore, no manual reduction is carried out. Data are regrouped to ensure that there are sufficient counts within a given spectral bin to allow χ^2 analysis (see Sect. 2.5.1). To do this we use the grappha task found in the standard HEAsoft packages[2].

2.1.4 GRB Coordinates Network

The aim of the GRB Coordinates Network (Barthelmy et al. 2000, GCN) is to make available GRB positions from γ-ray instruments to the astronomical community as fast as possible. This allows many other instruments to partake in multi-wavelengths observations and to also communicate their results via the GCN in real time, facilitating continued observing efforts if it is warranted (Fig. 2.4).

It is also possible to use the different arrival times, at each satellite, of the γ-rays to triangulate the position of the GRB and increase the precision of that position, in comparison to the position obtained from a single satellite. There currently exists such a network and it is called the Inter-Planetary Network (IPN) and currently consists of the following satellites: *WIND*, *2001 Mars Odyssey*, *INTEGRAL*, *RHESSI*, *Swift*, *MESSENGER*, *Suzaku*, *AGILE*, and *Fermi*[3].

2.2 *Fermi*

Fermi is a γ-ray space telescope led and launched by NASA in 2008, fitted with two instruments, the Large Area Telescope[4] and the Gamma-ray Burst Monitor. The science aims of *Fermi* are: (i) continue observing the diffuse γ-ray emission, (ii) continue observing unidentified sources originally seen by EGRET, (iii) understanding particle acceleration in active galactic nuclei, (iv) understanding GRBs and other transients, (v) investigating dark matter, and (vi) probe the early Universe using high energy γ-rays (Atwood et al. 2009).

The Gamma-ray Burst Monitor (Meegan et al. 2009, GBM) contains two different detectors. The first set of detectors are twelve thallium-activated sodium iodine detectors, which measure low-energy spectra in the range of $0.008 - 1\,\text{MeV}$ and also have the directional information for localisations (see Fig. 2.5). The second set are two bismuth

---

[2]http://heasarc.nasa.gov/lheasoft

[3]http://heasarc.gsfc.nasa.gov/docs/heasarc/missions/ipn.html

[4]We do not give detailed remarks on the Large Area Telescope as it plays no role in this thesis, we refer the reader to (Atwood et al. 2009).
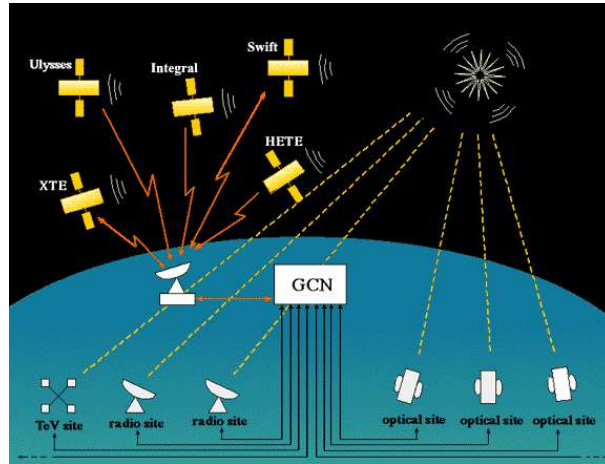
Figure 2.4 Schematic of the GCN, showing the initial detections of a GRB by the satellites and their positions being relayed to ground based instruments, which then further communicate their results. Credit to NASA.

germinate scintillation detectors that extend up to $40\,\mathrm{MeV}$ from $220\,\mathrm{keV}$, overlapping with the sodium detectors. Both detectors have their own sets of photomultiplier tubes that create an electronic signal from the scintillation light.

Three different modes are available for the GBM output: (i) CTIME, (ii) CSPEC, and (iii) time-tagged event. The CTIME data is the accumulated spectra from each detector and can be used for the triggering. The CSPEC is also accumulated spectra, but has a resolution of 128-channels rather than the 8-channels of the CTIME and is usually used to estimate fluences. The time-tagged event (TTE) data has high time resolution of $64\,\mathrm{ms}$, much better than CTIME ($4.096\,\mathrm{s}$) and CSPEC ($1.024\,\mathrm{s}$) (Meegan et al. 2009).

2.3   GROND

2.3.1   History & Overview

The Gamma-Ray burst Near-infrared Detector (Greiner et al. 2008a, GROND) is a seven channel imager that is currently mounted and operated at the Max-Planck-Gesellschaft/European Southern Observatory (MPG/ESO) 2.2 m telescope in La Silla (Chile, see Fig. 2.6). The primary aim of the instrument was to acquire fast as possible observations of GRBs, as soon as their prompt emission had been detected by γ-ray satellites (see Sect. 2.1 and 2.2). In this way, both accurate localisations and redshift estimates from spectral energy distributions (SED), could be acquired. Since its first light in April 2007 to January 2013, GROND has detected up to ~ 160 GRBs from redshifts of $z = 0.059$ (Olivares E. et al. 2012) to $z = 9.2$ (Cucchiara et al. 2011),
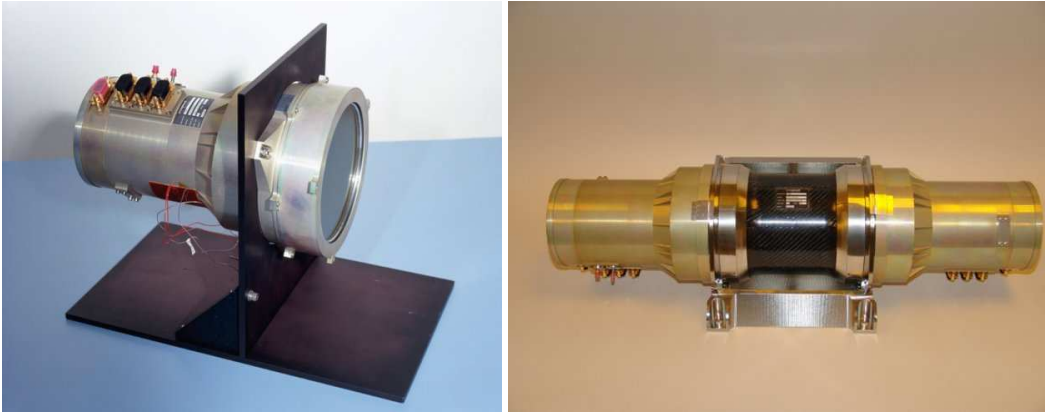
Figure 2.5 **Left**: GBM sodium detectors. **Right**: A picture of the GBM bismuth germinate scintillation detectors. Both adapted from Meegan et al. (2009).

yielding ~ 40 publications within the GRB field (e.g., Krühler et al. 2008; Greiner et al. 2009a; Küpcü Yoldaş et al. 2010; Greiner et al. 2011a; Elliott et al. 2012a; Sudilovsky et al. 2013). GROND is limited not only to GRBs and has observed many other transient/variable objects, such as X-ray binaries (Greiner et al. 2008b), tidal disruption events (Cappelluti et al. 2009), brown dwarfs (Goldman et al. 2010), black holes (Rau et al. 2011), neutron stars (Romani et al. 2012), and blazars (Ghisellini et al. 2013), to name but a few. GROND continues to operate in rapid response mode and we expect the total number of GRB detections to roughly double in the next 4 years.

2.3.2 Detector Design

The aim of GROND was to obtain SEDs of variable objects as a function of time. Therefore, it was required that GROND had to be able to take multi-band images simultaneously. To achieve this, a set of four optical $(2048 \times 2048\,\text{pixel}^2) \times 13.5\mu\text{m}$ charged coupled devices (CCDs) made of normal silicon and deep-depletion silicon, and three near-infrared (NIR) $1024 \times 1024\,\text{pixel}^2$ Rockwell HAWAII-1 arrays, in total, seven different bands were created. To ensure that simultaneity was possible the incoming telescope beam was split by utilising a set of dichroics. The first set of dichroics reflects short wavelengths of light to the four optical channels, but allows the longer wavelengths to continue to a fold mirror, which redirects the light to a collimator and then finally a NIR beam splitter (see Fig. 2.7). There is an extra fold mirror between the two sets of detectors as both must be cooled to two different temperatures to function. For this reason, both the optical and NIR detectors are connected to their own benches and are cooled differently by a cryostat. First, the NIR chips are cooled to a temperature of 65 K and the silicon CCDs are then reheated using resistance heaters to 165 K.

Given that the dichroics result in an identical 50% transmission wavelength between the adjacent bands, the cut-off wavelengths of the dichroics were chosen such that the
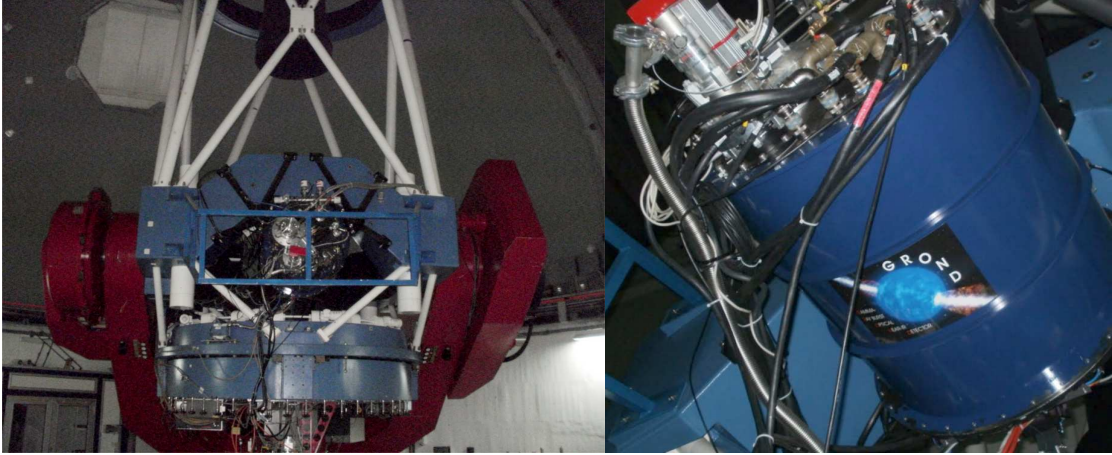
Figure 2.6 **Left**: 2.2 m MPG/ESO telescope located in the ESO La Silla Observatory, Chile. **Right**: GROND mounted at the 2.2 m MPG/ESO telescope, La Silla. The blue part of GROND is the shell of the cryostat.
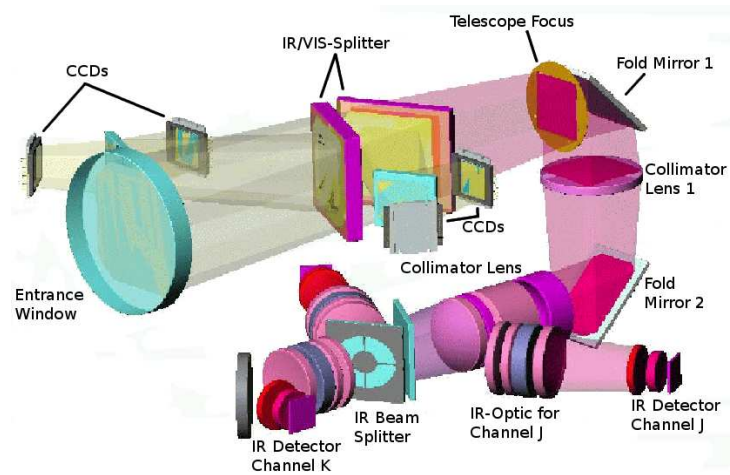
Figure 2.7 3D image of the internal schematics of GROND, which depicts the splitting of the telescope beam through the use of dichroics, resulting in the seven GROND bands. Adapted from Greiner et al. (2008a).
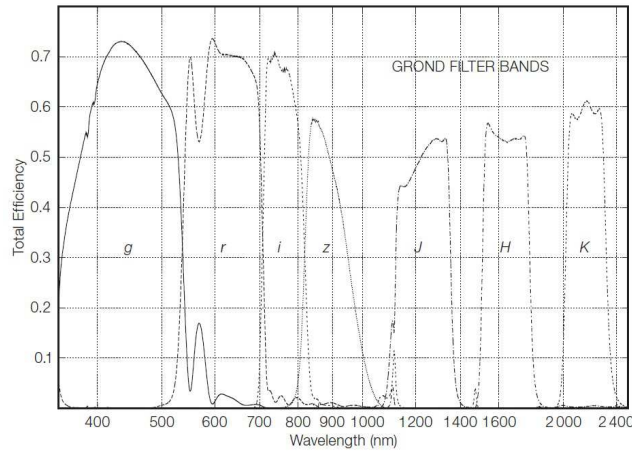
Figure 2.8 Transmission curves for all seven GROND filters, the four Sloan-like optical bands $g'r'i'z'$ and the three NIR Johnson-like bands JHK. Adapted from Greiner et al. (2008a).

four optical detectors matched (roughly) the Sloan filters (Aihara et al. 2011)[5]. The NIR channels are designed to be natively in the two micron survey (Skrutskie et al. 2006, 2MASS) bands of JHK. All of the seven band passes can be easily seen in Fig. 2.8.

The field of view (FOV) of a given instrument is dependent upon the telescopes focal length (17.6 m) and the size of the corresponding detector, which results in a FOV of $5.4 \times 5.4\,\mathrm{arcmin}^2$ for $g'r'i'z'$ and $10 \times 10\,\mathrm{arcmin}^2$ for JHK. The FOV of all channels is of sufficient size for normal GRB triggers that result in boxes with error circles of $\sim 1\,\mathrm{arcmin}$ and, in the majority of cases, the actual location is reasonably close to the centroid. Larger error boxes are also common, for which initial observations can only rely upon the NIR channels due to their naturally larger FOV.

The read out of the optical detectors is performed by the Fast Imager Electronic Readout Assembly (Beletic et al. 1998, FIERA), which has two readout speeds of fast (225 kHz) and slow (50 kHz) through two different ports for each channel. It is also possible for higher sensitivity in the bluer bands, whereby the $i'z'$ are read out twice, while the $g'r'$ bands only once. Images are stored within extensions of a single FITS[6] file and the corresponding details of the observation block are stored in the header of the FITS file. The NIR readout is carried out by the Infrared Detector High Speed Array Control and Processing Electronics (Meyer et al. 1998, IRACE). There is only a single readout mode suitable for science images, named IMODE. All the resulting images (JHK) are stored within one single FITS file and, again, the corresponding details in the FITS header. The use of these electronics requires calibration frames to be taken. On a daily basis we obtain details about the electronic readout noise (bias frames) and

---

[5]This is not exactly true for i', which must be corrected if comparisons with the SDSS are required.
[6]Flexible Image Transport System, the standard storage format within astronomy (Wells et al. 1981).

internal thermal noise (dark frames), and on a weekly basis we take images of constant flux (a) in the sky (skyflats) or (b) a light in the dome (dome flats), that describe the dependencies of the detectors on a whole. Bad pixels are also noted throughout the lifetime of GROND to ensure they are treated correctly in our analysis. Again, all of these images are stored in FITS files for further analysis.

2.3.3 Image Execution & Scheduling

As the telescope site is maintained by ESO, their VLT software[7] and other standards have been incorporated for the use of GROND and its interaction with the telescope.

Observations Blocks (Chavan et al. 2000, OB) contain the two vital properties of taking an exposure: (i) presetting the telescope, i.e., pointing to the correct location in the sky, placing the correct filter over the imager, or something equally valid for a mounted instrument, and (ii) the acquisition details, i.e., how long you want to integrate in each channel, the number of sky positions, etc. The OB will also contain other information for administrative use, e.g., OB name, Target name, Target ID, and all the details defined in the preset and acquisition. OBs are usually created using the Phase 2 Proposal Preparation[8]. In GROND nomenclature, the OB is named after the duration of the NIR exposure and the number of telescope dither positions (TDP). For example, an exposure of 4 minutes with 4 TDPs is named "4m4td". In fact the time taken to execute a complete integration in the optical channel is equal to the exposure time plus the readout time and is, for this example, 93 s. This is independent of the readout time. The NIR channels will integrate for 10 s each and so it is possible to fit six NIR integrations for every TDP (see Fig. 2.9 for a schematic of this OB type). Given the large sky background, especially in the NIR, the K channel has its own mirror that moves for each of the six integrations and is called a mirror dither position (MDP), which will facilitate a better subtraction of the sky background. There are several different OB constructions allowed, which are outlined in both the GROND instrument overview (Greiner et al. 2008a) and the GROND operation website[9]. In summary, the resulting FITS files will contain the science image, meteorological details of the observing site (airmass, seeing), time stamps and OB details, all of which will be used for correct reduction of the images at a later stage.

GROND is run in Rapid Response Mode (RRM), whereby a trigger to the telescope will cease any current observations for whichever instrument is currently mounted, and begin to observe the target of opportunity, which is most likely a GRB. Currently there are two other instruments mounted at the 2.2 m telescope: the Wide Field Imager (Baade et al. 1999, WFI) and the Fibre-fed Extended Range Optical Spectrograph (Kaufer et al. 1999, FEROS). To be as efficient as possible and to retain the data of the other observers, the semi-complete exposure is read out and not deleted when an RRM interrupt arrives. The creation of OBs for RRM and the schedule of OBs to be

---

[7]http://www.eso.org/projects/vlt/sw-dev
[8]https://www.eso.org/sci/observing/phase2/P2PPTool.html
[9]http://www.mpe.mpg.de/~jcg/GROND/operations.html
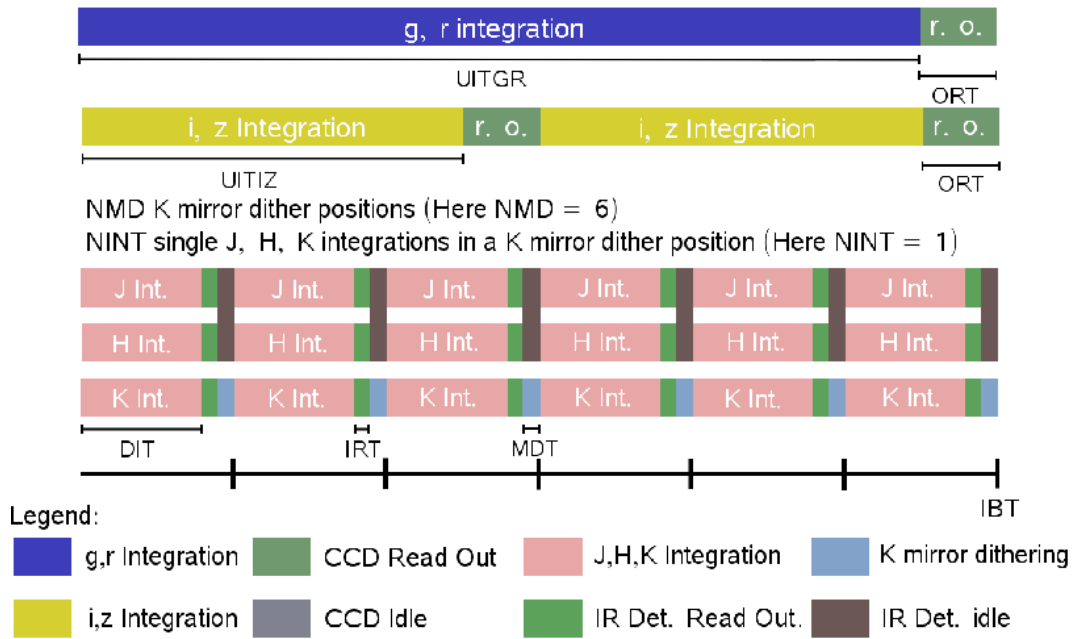
Figure 2.9 Schematic diagram of the integration and readout times for a single TDP in a 4m4td OB. As depicted the $i'z'$ bands can readout twice while the blue $g'r'$ bands continue to integrate. The K band has its own mirror that moves at each MDP, whereas, the JH bands remain idle in this movement. We note that the bars are not to the correct scale in time. Abbreviations; ORT: Optical Readout Time, UITIZ: Integration Time in $i'z'$, UITGR: Integration Time in $g'r'$, DIT: Integration Time in JHK, NINT: Number of JHK exposures in a single K mirror movement, NDIT: Number of co-added JHK exposures, NMD: Number of K Mirror Dithers, IRT: Infrared Readout Time, MDT: Mirror Dither Time. Adapted from Diploma Thesis of Thomas Krühler, TUM.

sent to the telescope is performed by the GROND Pipeline (Yoldaş et al. 2008). The GRB trigger is first received from the GCN and then a selection of criteria must be satisfied, primarily:

1. is the dome open,

2. is the target observable,

3. and is there a weather restriction.

Once the trigger initiates, the observation is no different to what was outlined previously. We primarily observe the afterglow of the GRB with GROND (see Chap. 3 for an example of prompt emission). The afterglow emission decays logarithmically with time, such that the OB type must be modified over time as well to ensure that we still retain enough depth in the image to get at least a 3σ detection. For example, we would begin with OBs of the 4m4td type and then gradually increase the exposure times to an 8m4td, then finally to a 20m4td. As the satellite determined position may not always be as accurate as needed for follow-up and as the afterglow is decaying, we must alert the community of our findings as soon as possible. This is especially important for larger telescopes (e.g., the European Southern Observatory's Very Large Telescope) for which time allocation is limited for GRB follow-up and so targets are usually only followed when positions of sub-arcsecond accuracy are obtained. To do this, we reduce the data on the fly utilising a suite of routines developed to process the raw images taken by GROND, which is outlined in the next section.

2.3.4 Image Reduction & Analysis

The data products obtained with GROND are processed using the GROND Pipeline (GP), developed by Krühler et al. (2008), which uses normal reduction and photometry routines within the astronomical community, primarily that of the Image Reduction and Analysis Facility (Tody 1993, IRAF) and Software for source Extraction `v2.8.6` (Bertin & Arnouts 1996, SExtractor). The code is written entirely in Python[10] and uses the IRAF wrapper PyRAF[11] `v1.1.1`. GP is split into three separate modules:

1. **Calibration Creation**

   For each band, master dark and bias frames are created to remove the effects from the detector. Also, master skyflat images are created to remove the pixel-to-pixel sensitivity and variations due to illumination over the entire image.

2. **Reduction & Combination**

   FITS images for each band and for each OB are desired to do analysis and so corrections for the initial file storage method and geometric effects must be carried

---

[10]`www.python.org`
[11]`http://www.stsci.edu/institute/software_hardware/pyraf`

out. In summary, the following is done to the images: (i) the optical images are split into single files rather being compiled in one FITS file and the NIR image is cut into three separate images, (ii) geometrical distortions that were caused by the focal reducer lenses of the NIR detectors are removed, (iii) the sky in the NIR images is subtracted, and (iv) each TDP is shifted and added, depending on the OB type that was used, to ensure a common overlap.

3. **Astrometry & Photometry**

   Using the telescope pointing information stored in the FITS header, a star catalogue is compared to the stars in the field of the science image. The catalogue used depends on the band and on the location of the sky and can be USNO A-2, USNO B1, DENIS, 2MASS, NOMAD, GSC22, or SDSS. The photometry module is carried out in two steps, first it uses the bright stars in the field to construct a point spread function (PSF) and secondly it calculates the flux within circular apertures for each object. Then the previously determined PSF is applied to the circular-aperture fluxes. Corrections are then made for the atmospheric extinction by knowing the airmass at the altitude it was observed. Finally, corrections for the Galactic extinction in the line of sight of the source are made with reddening values obtained from publicly available catalogues[12].

2.3.5   Image Subtraction

In some cases we detect an underlying host galaxy of the GRB, usually tens of days after the trigger, but this is highly dependent on redshift. Occasionally, the position of the afterglow with respect to the host galaxy can make it difficult to disentangle both features and so subtraction of the underlying host galaxy is required. Once the afterglow is no longer detected, we acquire a deep observation of the host galaxy and name this the template image. We now refer to the previous images taken of the afterglow as the science images. The overall pipeline for subtraction of the template from the science images was written specifically for this thesis. They are coded in Python using the same modules, as in GP, PyRAF and SExtractor.

For each of the science images, the template image is pixel aligned using *wcsregister*[13] and uncommon areas cut out using *imcopy*. Subtraction of the template from the science image is carried out using the high order transform of PSF and template subtraction package, HOTPANTS[14] v5.1.10b. HOTPANTS matches both the PSF and flux of the input science and template images (e.g., Alard 2000; Yuan & Akerlof 2008). This is done with a selection of PSF types and is carried out over sub-regions of the image. To obtain the best subtraction image, a grid of nine different PSF combinations and three box sizes are used. The best parameter set is chosen by finding the image with the smallest residuals in the box of a nearby star. Aperture photometry is carried out using *apphot*,

---

[12]http://irsa.ipac.caltech.edu/applications/DUST/
[13]Italics denote IRAF routines.
[14]www.astro.washington.edu/users/becker/hotpants.html
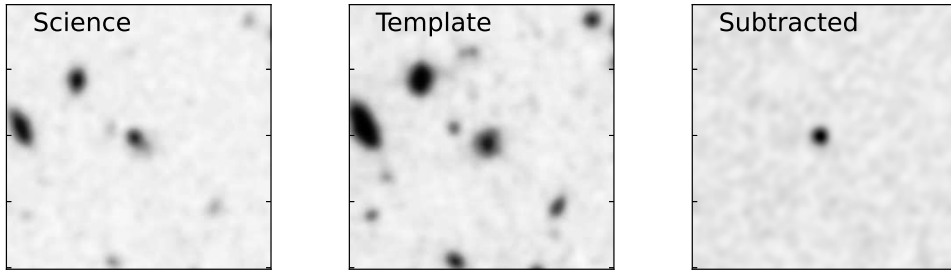
Figure 2.10 The left image shows a field that contains an afterglow as well as a host galaxy (science image), the middle image shows the host galaxy after the afterglow has faded away (template image), and the right image shows the result after subtracting the template from the science image. The images have been smoothed and scaled to give the best visual representation.

for an aperture the size of 3σ determined from the full width half maximum (FWHM). The FWHM of each image is obtained using SExtractor, from the narrowest 10% of stars. PSF photometry is carried out for the optical bands, $g'r'i'z'$, in the same manner as the GP. The corresponding uncertainties are calculated by adding in quadrature the corresponding noise of the source from the noise images output by HOTPANTS, where the noise image is a result of propagating the errors from the PSF kernel and template image and so can be treated in a Gaussian manner (see, e.g., Alard 2000). One example of before and after image subtraction can be seen in Fig. 2.10.

2.4 Other Instruments

There are a few other instruments relevant to this thesis and below is a quick summary of each:

a. GMOS

The Gemini Multi-Object Spectrograph (Hook et al. 2004, GMOS) is currently mounted on the 8 m Gemini North telescope, Mauna Kea (Hawaii), and can be used for imaging, long-, multi-, and integral-field spectroscopy. It has an array of three CCDs each of $(4068 \times 2048\,\mathrm{pixel}^2) \times 13.5\,\mu\mathrm{m}$, resulting in a field of view of $5.5 \times 5.5\,\mathrm{arcmin}^2$. The wavelength range is capable of going from $0.36 - 1.8\,\mu\mathrm{m}$ and has a resolving power of $R \sim 10000$.[15]

b. OSIRIS

The Optical System for Imaging and low Resolution Integrated Spectroscopy (Cepa et al. 2000, OSIRIS) is currently mounted on the 10.4 m Gran Telescopio Canarias,

---

[15]We obtain fully reduced spectra from all spectrographs and so do not outline the details of their reduction.

Roque de los Muchachos (La Plama). A series of tiny lenses allows ~ 3000 spectra to be acquired simultaneously for different locations in the sky. The spectrograph can reach resolutions of $R \sim 4000$ and covers a wavelength range of $1 - 2.4\,\mu$m. There is also an internal imaging camera that can be operated at the same time, using the same set or different filters.

c. WFI

The Wide Field Imager (Baade et al. 1999, WFI), currently mounted at the MPG/ESO 2.2 m telescope in La Silla (Chile). The WFI contains a $2000 \times 2000\,\mathrm{pixel}^2$ CCD and so a field of view of $34 \times 33\,\mathrm{arcmin}^2$. It is capable of observing in ~ 40 filters by the means of a filter wheel, usually in U, B, V and R. Reduction and photometry is done in a similar way as the GROND data.

d. WISE

The Wide-field Survery Explorer (Wright et al. 2010, WISE) is an infrared satellite surveying the sky in four filters centered at 3.4, 4.6, 12, and 22 μm. Reduced images and photometry are available via their online repositories.

e. X-shooter

The X-shooter (Vernet et al. 2011) is a multi-wavelength medium resolution spectrograph and is currently mounted on the 8 m UT2/Kueyen telescope, Paranal (Chile). It consists of three independent arms in the UVB, visual and NIR wavelength range, each with their own cross dispersed echelle spectrograph.

2.5   Fitting Models: Light Curves, SEDs & Galaxies

We require to fit models to the light curves and spectra of afterglows and the spectra of galaxies, which allows physical properties of them or their environment to be estimated. In the following we outline the common method of finding the best fit model and the specific models that we use.

2.5.1   Minimum χ^2 Fitting

First, a model is chosen that should physically represent the data and usually has n free parameters. If specific values are known they can be set as fixed parameters p. The best fit values are determined by minimising the following

$$\chi^2 = \sum_{i=1}^{N} \left(\frac{m_i - y_i}{\delta y_i} \right)^2 . \tag{2.1}$$

where m_i is the expected model value for the measured variable x_i, and y_i is the measured value for x_i. Even though the best fit returns the smallest χ^2 value, this does not necessarily reflect on how good the model used to fit the data is or give the uncertainty of each of the parameters. To determine if the fit is reliable the reduced-$\chi^2 = \chi^2/\mathrm{d.o.f.}$
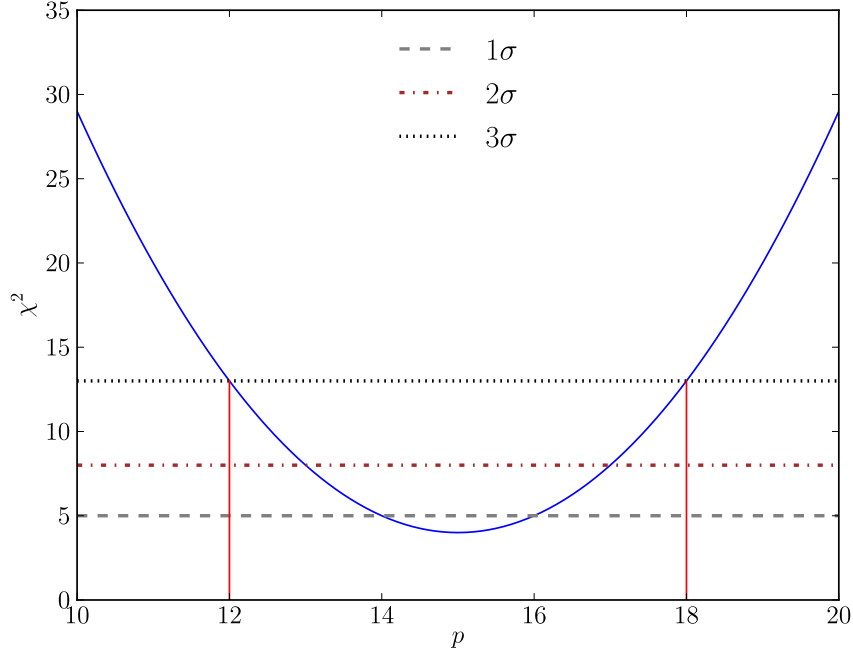
Figure 2.11 χ^2 contour for a dummy parameter p. The lines depict the 1σ (grey dashed), 2σ (brown dot-dashed), and 3σ (black dotted) confidence levels, which correspond to $\Delta\chi^2 = 1$, 3 and 9 for 1 free parameter. The 3σ levels in the x-axis space are depicted by the red-lines and so the best fit would be $p = 15 \pm 3$.

is calculated, where the degrees of freedom is, d.o.f. $= n - p - 1$. The most reliable fit should have a $\chi^2 = 1.0$ and other statistically reliable fits depend on n and p, for which the allowed reduced-χ^2 range can be found in statistical textbooks. The uncertainties of the best fit for a given parameter n_i are determined by looking for the $N\sigma$ difference in $\Delta\chi^2$ from the minimum χ^2 value. For example Fig. 2.11 shows a dummy χ^2 contour plot that shows the 1σ, 2σ, and 3σ uncertainties levels in $\Delta\chi^2$ space.

The method used to minimise the χ^2, by changing the free parameters, is a choice of the user and is usually freely available in public packages. The routines worth noting for this thesis are: (i) Minuit[16], a minimisation suite developed by CERN, (ii) Levenberg-Marquardt algorithms (LMA), and (iii) grid models, a brute force approach where one generates N-dimensional grids of parameters and fits them one by one. Unless specified, these are the techniques used throughout the thesis.

---

[16]http://wwwasdoc.web.cern.ch/wwwasdoc/minuit/minmain.html

2.5.2   GRB Light Curve Models

The fitting of GRB light curves is carried out by routines written in Python (Ph.D. Thesis of Thomas Krühler, TUM) that use the Minuit package developed by the particle physics community, with the python wrapper PyROOT `v6.1.0`[17]. The standard fireball theory predicts that we will observe a simple power law decay from the external shock (Chap. 1.2.3). However, this is not always the case and there may be other effects that contribute to the overall light curve at different times: two jets, supernovae bumps, underlying host galaxies, jet breaks and many others. The relevant light curve models to this thesis are listed below, where $F_\nu(t)$ is the flux for a fixed frequency ν at a time t.

1. Powerlaw

$$F_\nu(t) = F_{\nu,0}\left(\frac{t}{t_0}\right)^{-\alpha} \tag{2.2}$$

   where $F_{\nu,0}$ is the normalisation factor at t_0 and α is the temporal slope.

2. Broken powerlaw (Beuermann et al. 1999)

$$F_\nu(t) = F_{\nu,1}\left(\left(\frac{t}{t_1}\right)^{-\alpha_1 s_1} + \left(\frac{t}{t_1}\right)^{-\alpha_2 s_1}\right)^{\frac{-1}{s_1}} \tag{2.3}$$

   where $F_{\nu,1}$ is the normalisation factor at t_1, α_1 is the temporal slope for $t < t_1$, α_2 is the temporal slope for $t > t_1$ and s_1 is the smoothness, which describes how apparent the transition at the break time t_1 is (we note the that the powerlaws can switch in the time relation depending on the indices chosen).

3. Triple broken powerlaw (see, e.g., Li et al. 2012)

$$F_\nu(t) = F_{\nu,1}\left(F_\nu^{'}(t_1)^{-s_3} + F_\nu^{'}(t_2)^{-s_3} \times \left(\frac{t}{t_2}\right)^{\alpha_3}\right)^{-\frac{1}{s_3}} \tag{2.4}$$

   where $F_{\nu,1}$ is the normalisation factor at t_1, $F_\nu^{'}$ is the broken powerlaw function from Eqn. 2.3, and the other parameters α_i, s_i and t_i follow the same convention as the previous equations.

---

[17]`http://root.cern.ch/drupal/content/pyroot`
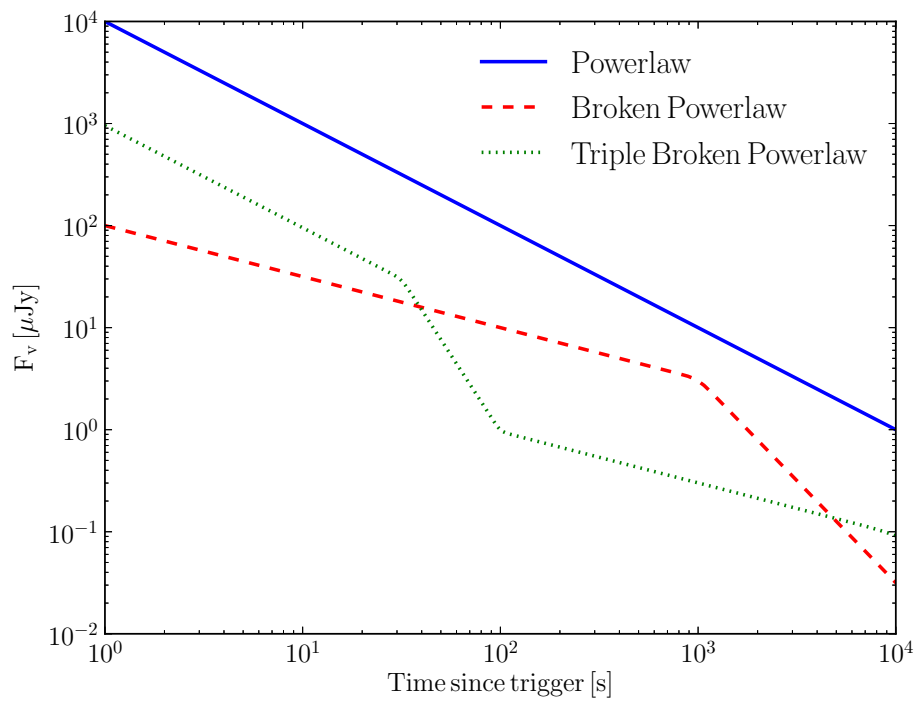
Figure 2.12 Afterglow flux plotted against time since the GRB trigger for each of the models described in Sect. 2.5.2.

2.5.3 GRB SED Models

We utilise two types of software to fit models to the SEDs of afterglows and prompt emission. The first routine is written in Python and is a wrapper for a modified version of the HyperZ v2.0 (Bolzonella et al. 2000) photometric redshift code[18]. HyperZ requires an input template of the expected SED that is trying to be fit, with a grid of all the possible free parameter combinations and is primarily used when only photometric data are available. The second is the X-ray Spectral-fitting program XSPEC v12.7.1 (Arnaud 1996), which also requires an input template but minimises using LMA. XSPEC is used when multi-wavelength data are available, i.e., γ-ray, X-ray and optical/NIR photometry, mainly because of its easy way of incorporating new instruments and user defined models. Both of these packages find the best fit using the minimum-χ^2 techniques outlined previously.

The expected SEDs of the prompt and the afterglow emission, predicted by the fireball model, are power laws, but they also include occasional slope changes as a result of the location of the characteristic frequencies (see Sect. 1.2.2). However, this is not always the case for the prompt emission, for which other models best reproduce the data and are commonly used despite not having any physical origin. Below we outline the possible models and adopt the notation that $F_t(\nu)$ is the flux for a given frequency ν at a fixed time t.

A. Prompt & Afterglow

   (a) Powerlaw

$$F_t(\nu) = F_{t,0} \left(\frac{\nu}{\nu_0} \right)^{-\beta} \tag{2.5}$$

   where $F_{t,0}$ is the flux normalisation at a given time t at the frequency ν_0 and β is the spectral index. We note that the photon index, p, is simply $p = \beta + 1$.

   (b) Broken powerlaw

$$F_t(\nu) = F_{t,1} \left(\left(\frac{\nu}{\nu_1} \right)^{-\beta_1} + \left(\frac{\nu}{\nu_1} \right)^{-\beta_2} \right) \tag{2.6}$$

   where $F_{t,1}$ is the flux normalisation at a given time t at the break frequency ν_1, and β_1 and β_2 are the spectral slopes above and below the break frequency.

B. Prompt

   (a) Cut-off powerlaw (Falcone et al. 2006)

$$F_t(\nu) = F_{t,0} \left(\frac{\nu}{\nu_0} \right)^{\beta} e^{-\frac{\nu(1+\beta)}{\nu_{\mathrm{peak}}}} \tag{2.7}$$

---

[18]http://webast.ast.obs-mip.fr/hyperz

where $F_{t,0}$ is the flux normalisation at a given time t and frequency ν_0, β is the spectral slope, and ν_{peak} is the peak frequency of the spectrum in $\nu F_t(\nu)$ space.

(b) Band function (Band et al. 1993)

$$
F_t(\nu) = \begin{cases} F_{t,1} \left(\frac{\nu}{\nu_1}\right)^{\beta_1+1} e^{-\frac{\nu}{\nu_c}} & \text{if } \nu < (\beta_1 - \beta_2)\,\nu_c \\ F_{t,1} \left(\frac{(\beta_1-\beta_2)\nu}{\nu_1}\right)^{\beta_1-\beta_2} \left(\frac{\nu}{\nu_1}\right)^{\beta_2+1} e^{-(\beta_1-\beta_2)} & \text{if } \nu > (\beta_1 - \beta_2)\,\nu_c \end{cases}
\tag{2.8}
$$

where $F_{t,1}$ is the normalisation for a give time t at the frequency ν_1, β_1 and β_2 are the spectral slopes and ν_c is the characteristic frequency.

We must also include other processes that affect the intrinsic slope of the SED:

1. Galactic dust reddening

   The dust from our Galaxy is along the line of sight of any observation taken from Earth and so any intrinsic property of an astrophysical source must be corrected. The wavelengths affected are primarily from the ultra-violet to the NIR, because dust reddening is more effective at smaller wavelengths. Several maps of the Galactic dust have been acquired over the years (e.g., Schlegel et al. 1998) and so the reddening value, $E(B-V)$, for a given direction can easily be obtained. The correction for each wavelength is different and is computed using the Milky Way extinction law (Pei 1992) of the form $f_\nu = A_\nu(\nu)/A_V$, where $A_V = E(B-V) \times R_V$ is the extinction in visual ($\sim 550\,\text{nm}$) and $R_V = 3.1$ for the Milky Way. The SED is then corrected by a multiplying function (Li et al. 2008) of

   $$
   f_{\text{Gal,Red}} = e^{-0.92 f_\nu A_V \frac{c}{\nu(1+z)}},
   \tag{2.9}
   $$

   where z is the redshift of the source (in the case of our Galaxy, $z = 0$).

2. Galactic gas absorption

   The column of gas in the line of sight of the source also absorbs light and happens primarily in the X-ray wavelengths. Again, there are several sources for which the quantity of Galactic gas can be obtained for a given position in the sky. The photo-electric cross-section, $\sigma(E)$, is then used to quantify the absorption in the following way (Balucinska-Church & McCammon 1992)

   $$
   f_{\text{Gal,Gas}} = e^{-N_H \sigma(E(1+z))},
   \tag{2.10}
   $$

   where N_H is the Galactic hydrogen column density, and $\sigma(E)$ includes the affects of He, C, N, O, Ne, Na, Mg, Al, Si, S, Cl, Ar, Ca, Cr, Fe, Co, and Ni, assuming solar abundances (again $z = 0$ for the Milky Way).

3. Host galaxy dust reddening

   Much like the Milky Way, there is dust within the host galaxy of the GRB (or astrophysical source), which dampens the emitted flux of the source. We correct for this using Eqn. 2.9. However, different extinction laws can be prescribed as they do not necessarily have to have the same dust profile as the Milky Way. We also employ dust laws of the Small and Large Magellanic Cloud types as described in (Pei 1992). The amount of dust in the host galaxy is a free parameter and it is obtained from the SED fitting.

4. Host galaxy gas absorption

   There exists also gas within the host galaxy and so the underlying absorption is corrected for by using Eqn. 2.10. The same gas law profile is assumed. However, the abundance of different elements in the host galaxy can be different to that of the Milky Way. This is a parameter that can be easily changed, but throughout this thesis they remain fixed at solar abundances. The quantity of gas is a free parameter that must be determined from the SED fitting.

5. Damped Lyman-α systems

   Throughout the Universe there exists concentrations of neutral hydrogen that cause absorption lines to appear within spectra of sources that sit behind the gas system. These systems are called Damped Lyman-α systems (for a review see, e.g., Wolfe et al. 2005, DLA) and can be correct for by (Totani et al. 2006)

$$f_{\text{Damped, Ly}-\alpha} = e^{-N_H \sigma_\alpha(\nu)(1+z_\alpha)\frac{c}{\nu(1+z)}} \tag{2.11}$$

   where N_H is the column density of the DLA, σ_α is the Lyman-α cross section, z_α is the DLA redshift and z is the source's redshift.

6. Lyman-α forest

   The Lyman-α forest is neutral intergalactic gas that lies between the observer and the emitting source. In the rest wavelength, the gas will absorb primarily at the Ly-α excitation (122 nm), and it is also possible for higher order excitations (Ly-β, 103 nm ; Ly-γ, 97.3nm, Ly-δ, 95 nm, etc). The wavelength 90.7 nm is the Lyman-limit, at which stage all the flux is absorbed and is usually named the Lyman-break. To include the wavelength averaged attenuation over an average line of sight, between the Ly-α and Ly-β series one would multiply the intrinsic flux by (Madau 1995; Faucher-Giguère et al. 2008)

$$f_{\text{Ly}-\alpha \, \text{Forest}} = 1 - \Delta\lambda_{\alpha-\beta} \int_{\lambda_\beta(1+z)}^{\lambda_\alpha(1+z)} e^{-1.8 \times 10^{-3}(1+z)^{3.92}} \mathrm{d}\lambda \tag{2.12}$$

   where z is the redshift of the source, λ_α and λ_β are the wavelengths of the Ly-α and β lines. The same calculation would be made for the other line series, however, Ly-α is the strongest and so we do not present the corrections for the remaining excitation.
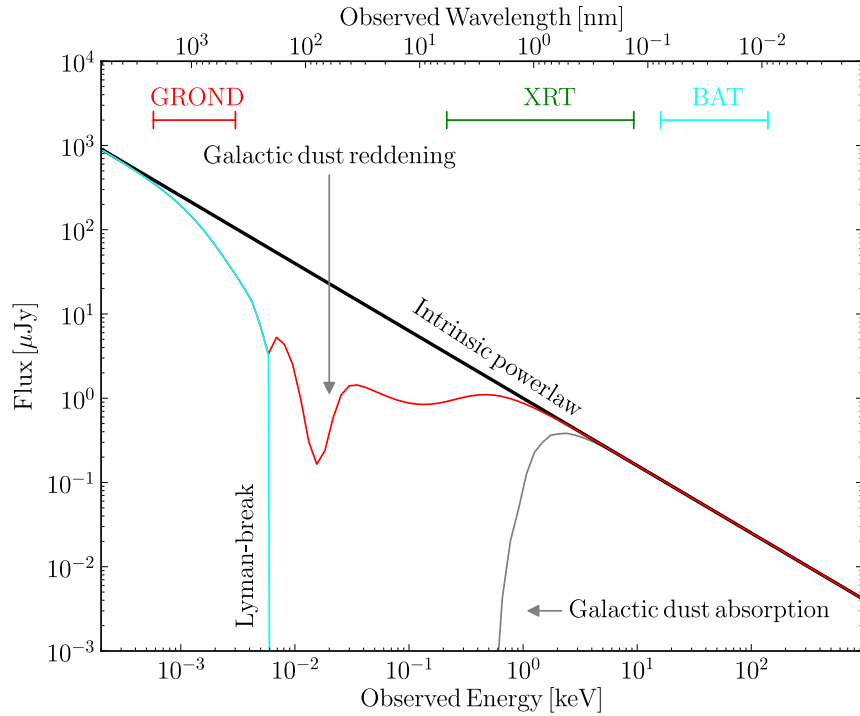
Figure 2.13 Synthesised GRB afterglow spectrum that has been constructed using the equations outlined in Sect. 2.5.3. The spectrum has an intrinsic power law with a spectral slope of $\beta = 0.8$, which has been influenced by (1) Galactic dust reddening of $A_V = 1.0\,\mathrm{mag}$, (2) Galactic dust absorption of $N_H = 1.0 \times 10^{22}\,\mathrm{cm}^{-2}$, (3) no host galaxy reddening, (4) no host galaxy dust absorption, (5) no intervening DLA, and (6) Lyman-α forest assuming the source is at a redshift of 1.0. The three bars at the top depict the energy ranges of GROND, XRT and BAT.

Fig. 2.13 depicts an intrinsic afterglow spectrum that has been affected by some of the processes listed.

2.5.4   Galaxy Models

Many GRB host galaxies have been discovered by GROND and fitting with SED models allows many properties of the host galaxy's stellar component to be determined, e.g., stellar mass, star formation rate, dust reddening and age. We utilise the Photometric Analysis for Redshift Estimate LePHARE `v2.2` (Arnouts et al. 1999; Ilbert et al. 2006) to find the best fit model, using the grid model approach. We use the publicly available set of galaxy templates of Bruzual & Charlot (2003). For these templates it is possible to change the star formation history, galaxy age, metallicity, dust reddening, and the attenuation law (see an example of templates in Fig. 2.14). The templates

of Bruzual & Charlot (2003) are created by using evolutionary population synthesis, which works in the following way:

1. First, for simplicity, it is assumed that whatever the star formation history of the galaxy is, it can be expanded into a series of instantaneous starbursts. This method is usually referred to as a simple stellar population.

2. An isochrone[19] at a given time t is generated for all types of stars based on their metallicity and mass, using stellar evolutionary tracks.

3. Spectra are generated for each location on the isochrone using stellar spectral libraries.

4. The initial mass function of the galaxy, which describes the fraction of stars that exist for a given mass out of the total available mass, is used to populate the galaxy with stars and weight the different spectra created at each isochrone.

5. The final SED is then constructed by adding up all the stellar spectra along the isochrone.

This methodology can be expressed fairly simply in the following way (Bruzual & Charlot 2003):

$$F_\lambda(t) = \int_0^t \psi\left(t - t'\right) S_\lambda\left(\eta\left(t - t'\right)\right) \, \mathrm{d}t', \tag{2.13}$$

where $S_\lambda\left(\eta\left(t - t'\right)\right)$ is the power radiated per unit wavelength per unit initial mass by an simple stellar population of age t' and metallicity $\psi\left(t - t'\right)$.

2.6 The GROND GRB Sample

To carry out statistical studies on GRBs requires samples that are both large enough to make statistically relevant deductions and also as statistically complete as possible, so that the deductions are not caused by any bias in the selection process. Therefore, many groups have compiled GRB samples based on different criteria. In this thesis we utilise the GROND sample. However, there are two other notable samples: (i) the Fynbo sample (Fynbo et al. 2009a), and (ii) the BAT6 sample (Salvaterra et al. 2012). The former is selected by using the same criteria outlined in Jakobsson et al. (2006), such that, (1) Swift detects a GRB with $T_{90\,Swift} > 2\,\mathrm{s}$, (2) the XRT position is released within 12 hours, (3) Galactic foreground extinction $< 0.5\,\mathrm{mag}$, (4) pole cut off $-70° < \delta < 70°$, (5) Sun-distance constraint $\delta_\odot > 55°$, and (6) there are no bright stars in the field, resulting in a long GRB sample size of 146 (March 2005 - September 2008; redshift completeness 53%). The BAT6 sample uses the same criteria, but requires that

---

[19]The line on a HR diagram, for which all the stars have the same age.
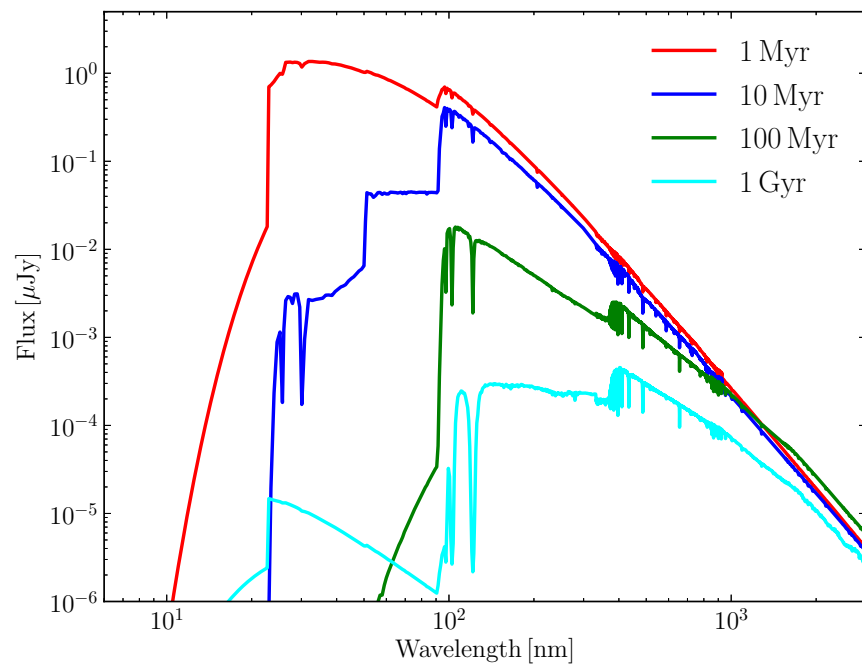
Figure 2.14 Four galaxy templates taken from Bruzual & Charlot (2003) that have been calculated assuming a metallicity fraction of $Z = 0.0001$, a Chabrier (2003) IMF, and Padova 1994 (`http://pleiadi.pd.astro.it`) stellar evolutionary tracks, but have four different ages as denoted in the legend.

the detected burst must have a photon flux of $P \geq 2.6\,\mathrm{photons\,s^{-1}\,cm^{-2}}$, yielding a total of 58 long GRBs (March 2005 - May 2011; redshift completeness 87%).

The GROND sample is selected by ensuring that (1) the GRB is a *Swift* trigger that had a detected X-ray afterglow, and (2) GROND observed the target within four hours after the trigger. The time selection was to ensure that there is a relatively high completeness level and also a large enough sample size, for which different completeness levels for different detection times for the most up to date GROND sample, can be seen in Fig. 2.15. The GROND sample criteria results in a long GRB sample of 39 and a short burst sample of 4, employing the *Swift* $T_{90} > 2\,\mathrm{s}$ definition.

The physical parameter of a GRB required for a statistical study defines the final completeness level of the sample. In our studies we are interested in the redshift distribution of the GRBs, i.e., the number of GRBs per redshift bin. Therefore, the number of bursts that have a measured redshift describes how complete the sample is, which is shown pictorially for all of the mentioned samples in Fig. 2.15. Each of these samples will grow in size over the next years, as long as the instrumentation remains in operation. However, the completeness levels rely heavily on the selection criteria, which is not necessarily controllable.

2.7   The First Billion Years Simulation

The First Billion Years (FiBY) project (Khochfar et al. in prep), is a suite of cosmological simulations primarily aimed at investigating the formation and evolution of the first galaxies (Fig. 2.16). The properties of the simulations are to be outlined in detail in future work (Dalla Vecchia et al. in prep), but are summarised in the following.

Each of the simulations uses a modified version of the `GADGET` code (Springel 2005), that utilises a smoothed particle hydrodynamic technique, developed for the Overwhelmingly Large Simulations project (Schaye et al. 2010).

In theory, star formation is believed to set in when gas exceeds a critical density and fragmentation begins. Therefore, within FiBY, above a density threshold of $n = 10\,\mathrm{cm^{-3}}$, star formation is described by a pressure law, or, equation of state, of the form $P \propto \rho^{\gamma}$, such that it reproduces the observed Kennicutt-Schmidt law (Kennicutt 1998), i.e., $\Sigma_{\mathrm{SFR}} \propto \Sigma_{\mathrm{gas}}$ where Σ is the surface density. The evolution of the resulting stellar populations, whether type II or III are followed throughout the simulation, whereby, the distinction is based on a simple metallicity cut. The mass distribution of the population II stars is described by a Chabrier initial mass function (IMF), and their respective metal enrichment by winds is determined from observed supernovae Ia/II yields (Wiersma et al. 2009). These stars live until a time determined from metallicity dependent lifetimes and then the resulting type of supernovae (Ia/II), which is mass dependent, causes thermal feedback, which is then injected into the surrounding medium (Johnson et al. 2013). The same process is carried out for population III stars, however, with a different IMF, of the Salpeter type, and different wind and supernovae (PISN) yields determined from the literature.
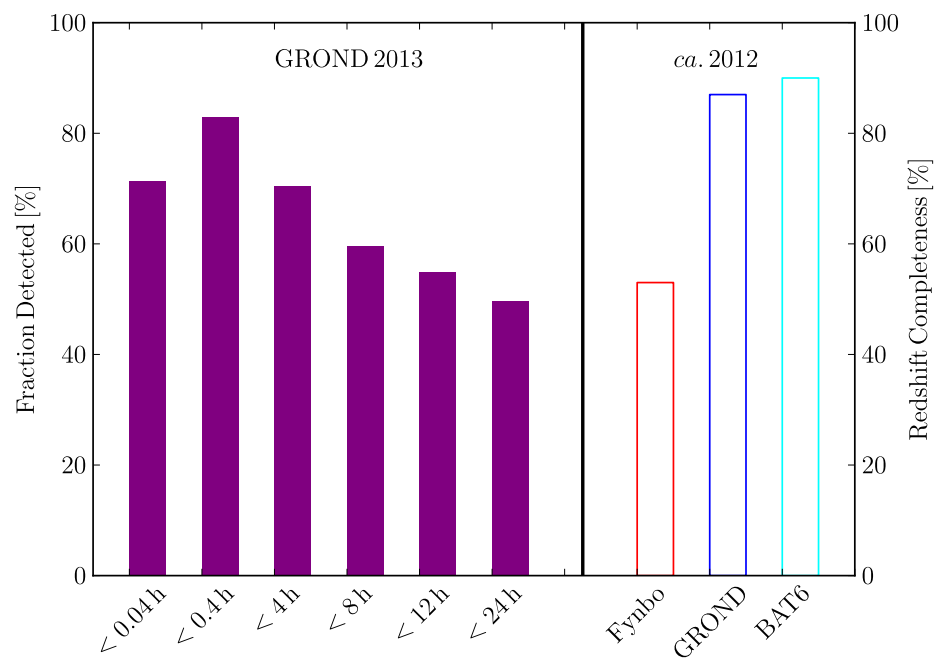
Figure 2.15 The left purple bars show the completeness fraction of the GROND 2013 sample (including short and long GRBs) for different follow-up times. The red, blue, and cyan bars on the right show the three different samples discussed in the text and their completeness levels based on redshift selection.
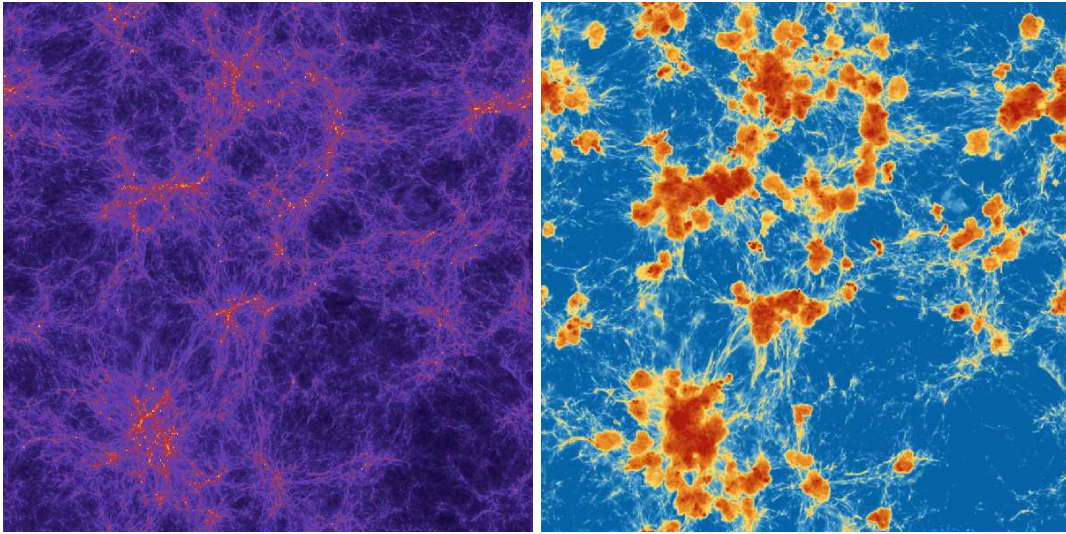
Figure 2.16 **Left**: Density map of a First Billion Years Project simulation, taken at a redshift slice of $z = 12$. The bright spots in the filament structures show the first stages of galaxy formation. **Right**: Temperature map of the same region of the density map, where the red colours are hotter than the blue colours. Images courtesy of Claudio Dalla Vecchia (2013).

The FiBY simulations have been modified from the `GADGET` code, so that it is possible to have line cooling in photoionisation equilibrium for a total of eleven elements (H, He, C, N, O, Ne, Mg, Si, S, Ca, and Fe), which is computed with CLOUDY `v07.02` (Ferland et al. 1999), along with a full non-equilibrium primordial chemistry network and molecular cooling functions for both H_2 and HD, following Schaye et al. (2010). These elements are incorporated into all of the feedback processes that have been outlined so far.

Finally, the process by which the intergalactic medium is heated and ionised is also computed for redshifts of $z > 6$. The period of reionisation is set to occur at a redshift of $z = 12$, based on measurements obtained from the WMAP (Komatsu et al. 2011). This process is outlined thoroughly in Johnson et al. (2013).

Chapter 3

Simultaneous optical/γ-ray wavelength observations of the γ-ray burst 121217A[1]

ABSTRACT

The mechanism that causes the prompt γ-ray emission from γ-ray bursts is still widely debated despite there being thousands of prompt detections. Multi-wavelength observations will help to investigate the possible underlying mechanisms. We observed the optical/NIR emission of the γ-ray burst 121217A during a prompt emission episode with *Swift*/BAT, *Swift*/XRT, *Fermi*/GBM, and the Gamma-Ray Burst Optical Near-infrared Detector and add it to the small sample of these kinds of bursts. Utilising the optical and X-ray light curves we determine Lorentz factors and radii of the prompt and deceleration periods, and compare broadband spectral energy distributions to those expected from the internal shocks models and other empirical relations. The optical emission exhibits a rebrightening of a factor of ~ 2, not as dramatic as those seen in bursts like the naked eye burst, and suggests the afterglow component from the first prompt period is dominating the emission. A powerlaw of slope $\beta = -0.4$ from the internal shock model can explain the spectral broadband spectral shape if self-absorption frequency $E_a < 10^{-5}\,\mathrm{keV}$ is included, and constrains the magnetic field to $B \sim 10^4\,\mathrm{G}$ for the afterglow determined $\Gamma_0 \sim 100$, $R \sim 10^{14}\,\mathrm{cm}$. However, at a redshift of $z = 3.0 \pm 0.2$, determined from the optical SED, the prompt powerlaw spectrum would require an extremely large gas column density $N_{\mathrm{H,X}} > 30 \times 10^{22}\,\mathrm{cm}^{-2}$. The alternative empirical Band model of $\beta_1 = -0.4$, $\beta_2 = -1.7$ and $E_{\mathrm{peak}} = 10\,\mathrm{keV}$, can explain the optical-γ slope and requires no modifications. We add γ-ray burst 121217 to the growing number of bursts that have optical coverage during their prompt emission and find that the internal shock model cannot be used to explain the observed optical emission completely.

---

[1]J. Elliott, J. Greiner, S. Schmidl, H.-F. Yu, D. Grupe, N. Gehrels, S. Oates, D. Gruber, and K. Cummings (2013), *A&A* in preparation.

3.1   Introduction

Ever since γ-ray bursts were first detected in the 1960s (Klebesadel et al. 1973, GRB), several satellites have been launched to expand our understanding of the underlying mechanism that caused them. The most notable are the instrument *BATSE* (Fishman et al. 1989) and the *Swift* (Gehrels et al. 2004) and *Fermi* satellites, which were launched in the periods of 1990-2008. They have collectively detected over thousands of long duration GRBs and acquired many prompt emission light curves and spectra. Even though this huge data set has answered many questions about the GRB phenomena, the underlying problem of the prompt emission mechanism remains elusive (for a review see Zhang 2012).

The standard model of a long-duration GRB foresees a compact object, formed by the collapse of a massive rapidly rotating star (Woosley 1993; Paczynski 1998; MacFadyen & Woosley 1999), that emits relativistic electron-positron fireballs with different Lorentz factors, in jets (Eichler et al. 1989; Narayan et al. 1992; Mészáros 2002). The currently favoured model of the prompt emission is the internal shock scenario (e.g., Rees & Meszaros 1994), whereby, these shells of different Lorentz factors cross one another causing relativistic shocks. Fermi acceleration (Fermi 1949) across the shock front then results in the electrons cooling in the form of synchrotron radiation (Sari et al. 1998), primarily at X-ray wavelengths, which is relativistically beamed into γ-rays (for a review see e.g., Mészáros 2002; Zhang & Yan 2011). Such a scenario allows easy comparison with observations by fitting powerlaws to the observed spectra, however, in the majority of cases the powerlaw does not fit the data well (Zhang & Yan 2011), especially in comparison to other empirical functions, e.g., the Band model (Band et al. 1993) or the high energy cut-off (e.g., Kaneko et al. 2006).

The Band model is completely empirical and currently there is no consensus on how the resulting spectrum is formed, where current theories involve for example, poynting-flux-dominated outflows (e.g., Zhang & Pe'er 2009) or a dissipative photosphere (e.g., Vurm et al. 2011). Therefore, it is crucial to obtain multi-wavelength studies of the GRB's prompt episode to see if the preferred models can be further constrained. This is not always possible, given the delay between the triggering of γ-ray telescopes and the slewing of optical instruments. Fortunately, however, there exists tens of fortuitous cases in which both the γ-ray emission and optical emission have been detected during the prompt period and can be divided to three possible scenarios: (i) a wide-field camera is observing the same field position as a satellite and so catches the optical emission simultaneously (e.g., 080319B Racusin et al. 2008; Bloom et al. 2009; Beskin et al. 2010), (ii) the prompt period is long enough that optical instruments slew in time to observe the prompt period (e.g., 990123, 080928, 110205A, 091024 Cucchiara et al. 2011; Gruber et al. 2011; Gendre et al. 2012; Zheng et al. 2012), (iii) there is a precursor to the main event so that optical instruments can slew in time (e.g., 041219A, 050820A, 061121 Blake et al. 2005; Genet et al. 2007; Page et al. 2007a). Only recently has it become possible to compile samples of bursts that exhibit optical emission during the prompt phase (Kopac et al. 2013), however, their heterogeneous selection means that

many more robust detections are required to reach significant completeness levels.

Despite the successful efforts to detect the optical emission during the prompt episode, there is still no consistent picture. Some GRB's optical emission traces that of the γ-ray emission, but is orders of magnitudes larger than expected by theory (e.g., 080319B), some do not trace the γ-ray emission (e.g., 050820A), and some are below what is expected (e.g., 061121). Given the difficulty of obtaining these optical wavelength measurements, especially in multiple filters, and the lack in number of test cases, more bursts of this type are require to find underlying systematics.

We add the *Swift/Fermi* burst GRB 121217A to this handful of cases, firstly by discussing its detections in Sect. 3.2. Secondly, we present the resulting light curves and spectra in Sect. 3.3, discuss the implications in Sect. 3.4 and then finally conclude in Sect. 3.5. Throughout we assume the standard notation of the GRB light curves and spectra of $F(\nu, t) \propto t^{-\alpha} \nu^{-\beta}$ and apply the mathematical representation of $Q_x = 10^x Q$. We adopt a ΛCDM cosmology with the following parameters $\Omega_\Lambda = 0.7$, $\Omega_\mathrm{M} = 0.3$, $H_0 = 73.0\,\mathrm{km\,s^{-1}\,Mpc^{-1}}$. Unless mentioned otherwise, all uncertainties are quoted to the 1σ level.

3.2 Observations

3.2.1 Swift

The Burst Alert Telescope (Barthelmy et al. 2005, BAT) mounted on *Swift* (Gehrels et al. 2004) was triggered by GRB 121217 on 17th December 2012 at $T_0 = 07{:}17{:}47$ UT (Siegel et al. 2012). *Swift* slewed immediately to the burst and the X-Ray Telescope (Burrows et al. 2005, XRT) began observing at $T_0 + 64.0\,\mathrm{s}$ until 15.6 days later (Evans et al. 2012). The BAT light curve was acquired from the *Swift* quick look data and the BAT spectrum was acquired from the *Swift* archive and can be seen in Fig. 3.1. The HEAsoft routines *batbinevt*, *bathotpix*, *batmaskwtevt*, *batbinevt*, *batupdatephakw*, and *batdrmgen* were used to generate the BAT PHA and RSP files from the event file in the standard manner. The XRT light curve (Fig. 3.2) was obtained from the XRT light curve repository (Evans et al. 2007, 2009) and the XRT spectral data from the public *Swift* archive. Each spectrum has been regrouped to ensure at least 20 counts per bin using the *grappha* task from the HEAsoft package using the response matrices from the CALDB v20120209.

The prompt emission exhibits two main emission periods separated by a quiescent period of $\sim 700\,\mathrm{s}$. Both peaks have similar durations of $\Delta t_\mathrm{Peak1} = 45\,\mathrm{s}$ and $\Delta t_\mathrm{Peak2} = 33\,\mathrm{s}$, and fluences (10-1000 keV) of $f_\mathrm{Peak1} = 4.8 \pm 0.6 \times 10^{-6}\,\mathrm{erg\,cm^{-2}}$ and $f_\mathrm{Peak2} = 3.3 \pm 0.4 \times 10^{-6}\,\mathrm{erg\,cm^{-2}}$, assuming a power-law with an exponential cut-off with powerlaw photon indices of $p_\mathrm{Peak1} = 1.20 \pm 0.12$ and $p_\mathrm{Peak2} = 1.29 \pm 0.14$ and peak energies of $E_\mathrm{pk,Peak1} = 264 \pm 75\,\mathrm{keV}$ and $E_\mathrm{pk,Peak2} = 184 \pm 56\,\mathrm{keV}$. The overall event has a $\Delta t_\mathrm{tot} = 780\,s$.
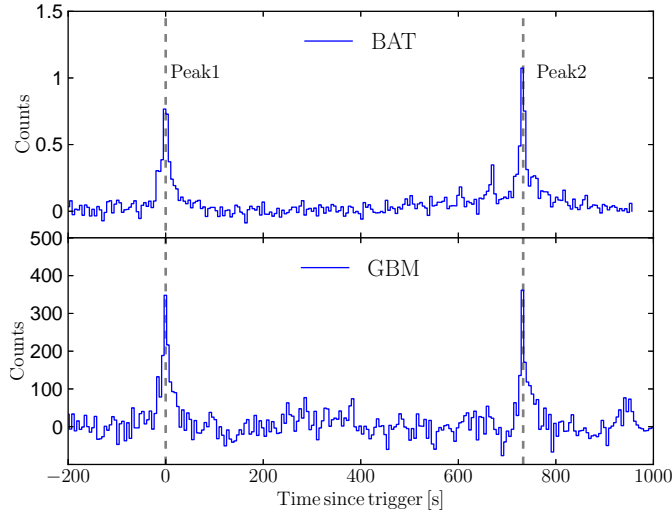
Figure 3.1 The γ-ray light curves of the two prompt episodes of GRB 121217A acquired with BAT and GBM (Sect. 3.2.1). The GBM triggered on the second peak which occurs at a time of $T_0 + 735\,s$, but has been shifted in this plot to coincide with the BAT T_0. Both light curves have been binned in time with a moving box of 5 seconds.

3.2.2 GBM

The *Fermi* Gamma-ray Burst Monitor (GBM; Atwood et al. 2009) was triggered by the second prompt emission of GRB 121217 on 17th December 2012 at 07:30:02 UT (Yu & Gruber 2012). Even though triggering was switched off during the first prompt emission, as it was moving through a region of high geomagnetic activity, it was still detected. The overall light curve is the same as that seen with BAT (Fig. 3.1). The GBM spectra were reduced in the standard manner using the *RMFIT* `v4.1BA` software package and the Response Generator *gbmrsp* `v2.0`. Fluences were determined using CSPEC data (time resolution of 4.096 s) and spectral fitting utilised time-tagged event data (time resolution of 64 ms).

3.2.3 GROND

The Gamma-Ray burst Optical Near-infrared Detector (Greiner et al. 2008a, GROND) began observing the field of GRB 121217A at $T = T_0 + 210\,s$ and located the optical counter part of GRB 121217 at R.A.(J2000) $= 10^h 14^m 50.4^s$, Dec.(J2000) $= -62°21'0\overset{''}{.}4$ (Elliott et al. 2012b) to an uncertainty of $0\overset{''}{.}5$. The first $500\,s$ of the acquired data does not have the optical counterpart within the field of view of the optical detectors, as a result of the XRT position being at the edge of the BAT error circle, and the time required to reposition the telescope. The follow up campaign lasted for 21 days until the afterglow was no longer detected. No underlying candidate host galaxy was discovered.
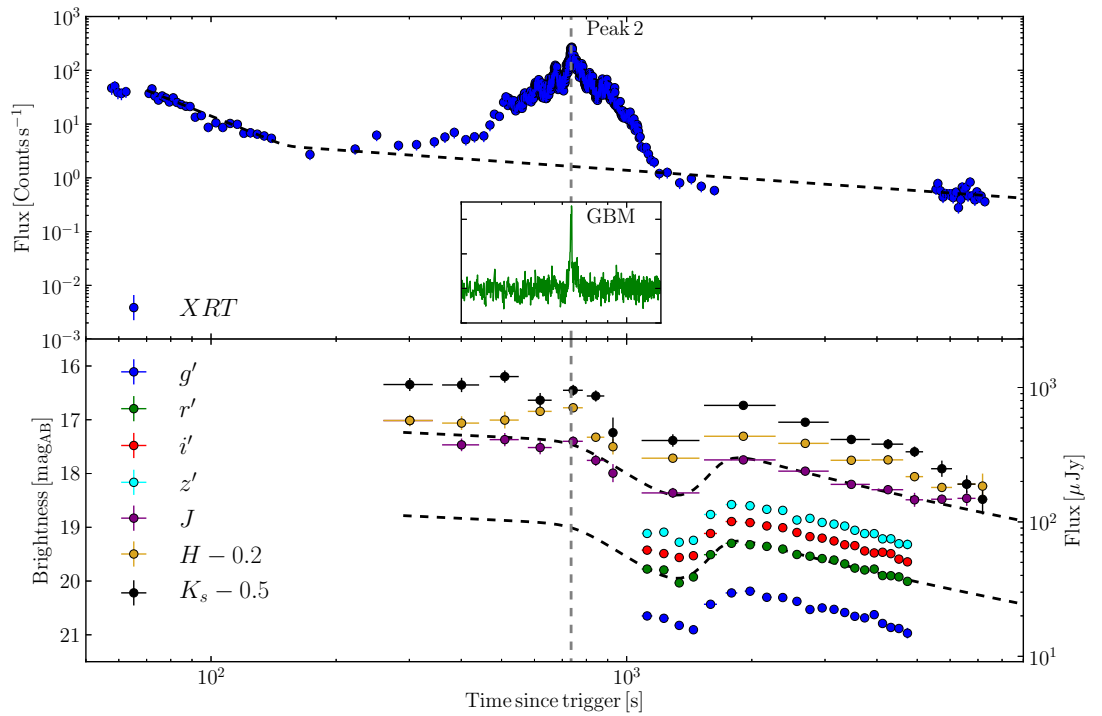
Figure 3.2 The X-ray (top) and optical (bottom) wavelength light curves of GRB 121217A, with the inset graph being the GBM prompt emission of the second peak. The canonical model of the X-ray emission can be seen as the black-dashed line in the top panel, where the flare simultaneous to the second prompt peak, has been excluded from the fit (Sect. 3.3.2). The black-dashed line in the lower panel is the best fit double broken power-law of the afterglow emission (Sect. 3.3.3). Only the observations with a time less than $T_0 + 10^4$ s have been included.

Image reduction and photometry of the GROND observations were carried out using standard IRAF tasks (Tody 1993) in the way outlined in Krühler et al. (2008) and Yoldaş et al. (2008). In brief, a point-spread function (PSF) was obtained from the bright stars within the field and applied to the afterglow. The absolute calibration of the optical photometry was achieved by observing a Sloan Digital Sky Survey (SDSS) field (Aihara et al. 2011) at R.A. (J2000) = $10^h 50^m 36.0^s$, Dec. (J2000) = $-21°36'00''$ and the GRB field consecutively, under photometric conditions. The NIR absolute calibration was obtained from the Two Micron Sky Survey (2MASS) stars (Skrutskie et al. 2006) within the field of the GRB. The magnitudes are corrected for a Galactic dust reddening of $E(B-V)^{\text{Gal}} = 0.368\,\text{mag}$ corresponding to an extinction of $A_V^{\text{Gal}} = 1.141\,\text{mag}$ for $R_V = 3.1$ (Schlegel et al. 1998).

3.3 Results

3.3.1 Redshift

A broadband spectral energy distribution was constructed from the GROND filters at a mid-time of $T_0 + 31.4\,\text{min}$, at which stage the optical counterpart is the afterglow component (see Sect. 3.3.3 for more details). Within the framework of the standard fireball model, external shocks emit synchrotron radiation, which is easily described by a powerlaw (Sari et al. 1998). These powerlaws are then modified by the GRB hosts intrinsic extinction and the GRBs redshift, which determines the position of the Lyman-break. To find the redshift and intrinsic host dust extinction we followed the prescription outlined in (Krühler et al. 2011b) and fit powerlaws over a grid of parameters consisting of: spectral slope $\beta = 0.01 - 2.00$ in steps of 0.01, host dust $A_V = 0.0 - 0.5\,\text{mag}$ in steps of 0.017, dust models (Milky Way, Large Magellanic Cloud and Small Magellanic Cloud), and redshift $z = 0.0 - 5.0$ in steps of 0.056. The best fit solution is determined from the minimum χ^2 value and the uncertainties from the corresponding χ^2 contours. We find a best-fit solution with $\chi^2/\text{d.o.f.} = 0.8/3$ for the Milky Way dust model, $\beta = 0.72 \pm 0.07$, $A_V = 0.10^{+0.07}_{-0.05}\,\text{mag}$, and $z = 2.97^{+0.11}_{-0.06}$ to at least the 3σ level (Fig. 3.3). The best-fits for the other dust models return consistent results and we observe no change larger than 3σ in the host dust requirement if 30% less of the Galactic dust reddening is used. From here on any fits requiring redshift will be set to zero for simplicity, but intrinsic dust absorption included.

3.3.2 X-ray Emission

We obtain the best-fit X-ray light curve from the *Swift* online catalogue (Evans et al. 2007, 2009), which determines the temporal slopes based on the type of classification that best fits the data, be it: canonical, one-break, no-breaks or undefined. By ignoring the flaring activity (Willingale et al. 2007) in the X-ray emission that occurs between $T_0 + 200\,\text{s}$ and $T_0 + 5715\,\text{s}$, the canonical afterglow reproduces the X-ray light curve the best (see Fig. 3.2) with $\chi^2 = 166/146$.
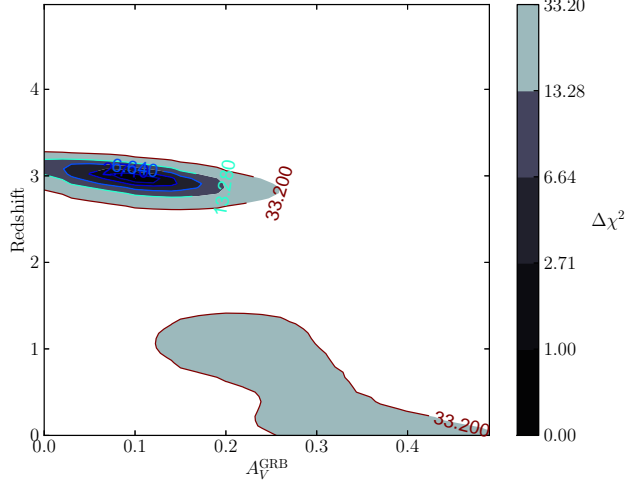
Figure 3.3 A contour plot of $\Delta\chi^2$ values for the range of host galaxy dust (A_V) and GRB redshift (z) parameters used in the fitting grid (Sect. 3.3.1), for the best-fit powerlaw ($\beta = 0.7$) and Milky Way dust model. The other dust model contour plots are not included, as they do not portray any different information.

Starting at $T_0 + 72\,\text{s}$, the X-ray light curve begins with a decaying power-law with a pre-flare temporal slope of $\alpha_{1,\text{X}} = 3.14 \pm 0.18$ and a spectral slope of $\beta_{1,\text{X}} = 1.11 \pm 0.01$, between $T_0 + 72\text{s}$ and $T_0 + 152\text{s}$. The steep decay is then followed by an increase in X-ray emission, where the peak flux is simultaneous to the second prompt emission peak. Both the flaring and second peak are discussed more thoroughly in Sect. 3.4.4. After the flaring activity, the X-ray becomes canonical again and begins to decay with an after-flare temporal slope of $\alpha_{2,\text{X}} = 0.54^{+0.05}_{-0.17}$ and spectral slope of $\beta_{2,\text{X}} = 0.92 \pm 0.06$. There is then a break at $t_{3,\text{b}} = T_0 + 2.6 \times 10^4\,\text{s}$, which steepens the decay to a final temporal slope of $\alpha_{3,\text{X}} = 1.38^{+0.06}_{-0.09}$ and spectral slope $\beta_{3,\text{X}} = 0.96 \pm 0.06$.

3.3.3 Optical/NIR Emission

The optical emission depicts no visible synchronous rebrightening before or after the second prompt emission and we defer the read to later discussions (Sect. 3.4.4). Therefore, we assume synchrotron emission from the reverse/forward shocks and fit a two broken power law, of the Beuermann et al. (1999) type, to GROND's 7 bands simultaneously. The best-fit solution seen in Fig. 3.2, has $\chi^2/\text{d.o.f.} = 166/115$, which is primarily large due to the noisy early and late NIR data, which upon removal can have a reduced-$\chi^2 \sim 1$. The optical emission begins with a shallow decay with a temporal slope of $\alpha_{\text{opt},1} = 0.15 \pm 0.03$ and then breaks at a time $T_0 + 750 \pm 19\,\text{s}$ to a temporal slope of $\alpha_{\text{opt},2} = 2.0 \pm 0.1$ with a smoothness $s_{\text{opt},12} = 8.0 \pm 1.5$. At a time of $\sim T_0 + 1450\,\text{s}$ the optical emission begins to rebrighten with $\alpha_{\text{opt},3} = -1.8 \pm 0.2$ until it reaches a maximum
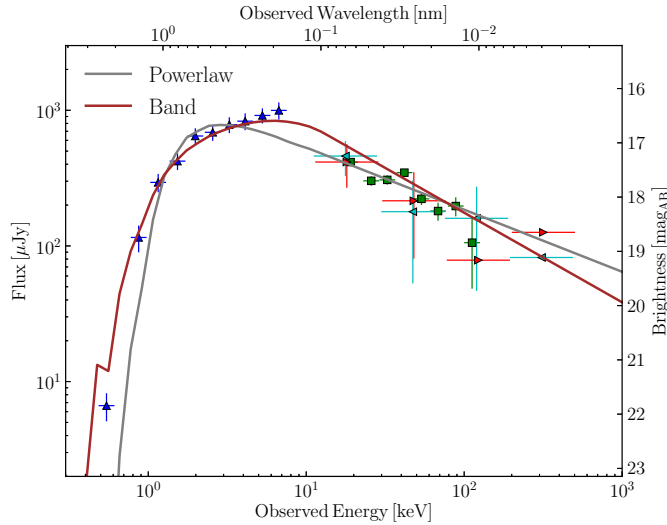
Figure 3.4 Broadband SED at the second prompt emission $(T_0 + 735\,\mathrm{s})$, composed of BAT (green squares), XRT (blue upward-triangles), and GBM detectors (red rightward-triangles and blue leftward-triangles, respectively). To make the plot more clear the data points have been rebinned in energy and the non-detections with the GBM/BGO are not included. The best-fit models for the powerlaw and Band models are depicted as the grey and red lines, respectively.

at $T_0 + 1669 \pm 10\,\mathrm{s}$, with a smoothness of $s_{\mathrm{opt},34} = 9.8 \pm 0.2$, and once again begins to decay with $\alpha_{\mathrm{opt},4} = 0.59 \pm 0.02$. The spectral slope remaining constant throughout with $\beta_{\mathrm{opt},34} = 0.72 \pm 0.07$.

3.3.4 Prompt Emission Broadband Spectrum

We construct a broadband SED at the time of the second prompt emission, occurring at a mid-time of $T_0 + (735 \pm 10)\,\mathrm{s}$, utilising the 3 GROND filters (JHK), *Swift*/BAT, *Swift*/XRT and *Fermi*/GBM (Fig. 3.4). A common time interval of 10 seconds has been used because this is the minimum integration time of the GROND/NIR images that were taken. The spectra from X-ray to γ-ray wavelengths were fit in XSPEC `v12.7.1` with a power-law (*pow*), cut-off power-law (*highecut*) and the band function (*grbm*) (both including and ignoring the NIR data) and each of the resulting parameters can be found in Table. 3.1 or are depicted in Fig. 3.4. For fits without NIR data included, we extrapolate each of the models to the NIR wavelengths ($\sim 1\,\mu\mathrm{m}$), as seen in Fig. 3.5.
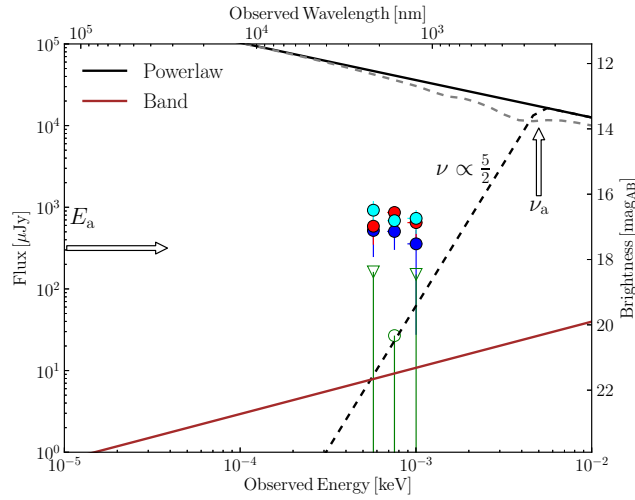
Figure 3.5 The extrapolation of the Band function (brown line) and the powerlaw (black line) models to the optical wavelength regime. The grey-dashed line denotes the effect of an extinction of $A_V \sim 0.1$ at a redshift of $z = 3$. The black dashed line shows the case-(I) scenario of synchrotron self-absorption and the corresponding lower limit for the energy break (E_a) denoted by the arrow. The blue-filled dots denote the total flux measured at the same time of the prompt emission ($T_0 + 735\,\mathrm{s}$) and the open-green triangles are with the expected afterglow flux subtracted, that were determined from the best fit temporal power law. The transparent cyan and red dots denote the fluxes measured at 759 and 769 seconds after the trigger, respectively. The energy break is discussed in Sect. 3.4.4.

Table 3.1 The best fit parameters for each spectral model.

Model	χ^2/d.o.f.	f^a	Parameter	Value
PL	370/340	0.01	β	0.46 ± 0.03
			$N_{\mathrm{H,X}}$ $[10^{22}\mathrm{cm}^{-2}]$	0.74 ± 0.10
PL^b	442/348	0.9	β	0.00 ± 0.02
			$N_{\mathrm{H,X}}$ $[10^{22}\mathrm{cm}^{-2}]$	0.21 ± 0.06
Band	308/338	55	β_1	-0.43 ± 0.07
			β_2	-1.66 ± 0.06
			E_{peak} [keV]	10 ± 212
			$N_{\mathrm{H,X}}$ $[10^{22}\mathrm{cm}^{-2}]$	0
Band^b	313/348	4.8	β_1	-0.79 ± 0.08
			β_2	-1.80 ± 0.16
			E_{peak} [keV]	50.1 ± 1.6
			$N_{\mathrm{H,X}}$ $[10^{22}\mathrm{cm}^{-2}]$	0.11 ± 0.07

Notes. $^{(a)}$ The ratio of the observed J flux to the expected J flux, i.e., $f = J_{\mathrm{obs}}/J_{\mathrm{exp}}$. $^{(b)}$Fits that have included the NIR channels. All fits have assumed a redshift of $z = 0$ for simplicity, see Sect. 3.3.1.

3.4 Discussion

3.4.1 High Latitude Emission: Deceleration Radius and Lorentz Factor of the First Prompt Peak

We consider the initial steep decay of the X-ray emission (Sect. 3.3.2), which is usually associated to high latitude emission (see e.g., Zhang et al. 2006) and compare the fitted values to the expected closure relations (Kumar & Panaitescu 2000). We find that $\alpha_{1,\mathrm{closure,X}} = 2 + \beta_{1,\mathrm{X}} = 3.11 \pm 0.01$ (c.f. $\alpha_{1,\mathrm{X}} = 3.14 \pm 0.18$) and therefore this period is consistent with being related to the prompt emission (i.e., high latitude emission) and not the afterglow component. We also calculated the closure relations for an afterglow component (e.g., Sari et al. 1998; Racusin et al. 2009), for $p > 2$ within a Wind/ISM environment for fast/slow cooling and find that they cannot reproduce the temporal slope α to at least 3σ.

Knowledge of the end time of the high latitude emission allows us to estimate the radius at which the γ-rays originate and the Lorentz factor of the shell. We place a limit on the radius at which this emission occurs (e.g. Lazzati & Begelman 2006; Mészáros 2006; Zhang et al. 2006), R_γ, with the following relation:

$$t_{\mathrm{tail}} \lesssim (1+z)\frac{2R_\gamma}{c}\frac{\theta_{\mathrm{jet}}^2}{2}. \tag{3.1}$$

where c is the speed of light, and θ_{jet} is the opening angle. Using the time at which there is a canonical jet break in the X-ray emission, at $t_{3,\mathrm{b}} = T_0 + 2.6 \times 10^4\,\mathrm{s}$ (Sect. 3.3.2),

the redshift $z = 3.0$ (Sect. 3.3.1) and the isotropic-equivalent energy $E \sim 10^{53}\,\mathrm{erg}$ (Sect. 3.2.1) from the first peak, we can estimate the opening angle as $\theta_\mathrm{j} = 3.3° \, (n_\gamma n_0)^{\frac{1}{8}}$ (Rhoads 1999), assuming that the γ-ray efficiency, $n_\gamma = 0.2$, and the ISM density, $n_0 = 1\,\mathrm{cm}^{-3}$. This opening angle results in a prompt emission radius of

$$R_\gamma \gtrsim \frac{2ct_\mathrm{tail}}{(1+z)\,\theta_\mathrm{j}} \gtrsim 1.2 \times 10^{14}\,\mathrm{cm}. \tag{3.2}$$

This value could be smaller by a factor of a few if the break in the X-ray light curve is not the jet break. The emission from the high latitude component is much brighter than the onset of the afterglow, that it is not seen until the canonical plateau phase begins, and so places an upper limit on the time (t_dec), and thus the radius (R_dec), at which deceleration of the shock begins. Utilising the fact that the tail emission ends at $T_0 + 152\,\mathrm{s}$, we constrain the the Lorentz factor, Γ, by applying Eqn. 6 of Zhang et al. (2006):

$$\Gamma_0 \gtrsim 125 \left(\frac{E_{\gamma,\mathrm{iso},52}\,(1+z)^3}{n_\gamma n t_\mathrm{peak}^3} \right)^{\frac{1}{8}} \gtrsim 40. \tag{3.3}$$

3.4.2 Optical Afterglow Rebrightening: Deceleration Radius and Lorentz Factor of the Second Prompt Peak

The optical afterglow-like component that is observed from $T_0 + 1670$ decays with a temporal slope of 0.59 ± 0.02, and depending on the dust model, has a spectral slope of $0.55 - 0.88$. These combinations are not consistent with the standard closure relations for either an ISM or Wind environment for any of the frequency ranges to the 3σ level. Assuming an ISM environment in the slow cooling regime, with a frequency located at $\nu_\mathrm{m} < \nu < \nu_\mathrm{c}$, would require that $\alpha = 1.58$, much steeper than that observed. The shallow decay of the afterglow could be attributed to an injection of energy, which is consistent with the X-ray flaring activity. Assuming an injection of the form $E \propto t^e$ (Panaitescu et al. 2006), the difference in slopes of $\Delta\alpha = 0.99$ would require that $e = 0.73$, in an ISM environment. Our assumption of an ISM environment is consistent with the X-ray emission from $T_0 + 72 - T_0 + 152\,\mathrm{s}$, which fits exactly the relations of high latitude emission in an ISM environment.

The rise time of the afterglow component, whether it be the forward or reverse shock, can be used to estimate the bulk Lorentz factor of the ejecta at the deceleration radius. We can treat this shell as a *thin shell*, as an association of the afterglow component with the first or second peak both result in an offset between the prompt emission and the afterglow emission. Using equation 3.3,

$$\Gamma_0' \gtrsim 92, \tag{3.4}$$

where any primed value is related to the second prompt emission. Therefore, the deceleration radius is,
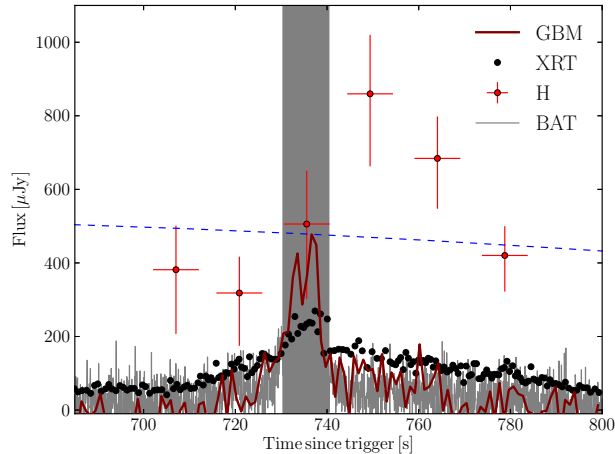
Figure 3.6 A high time resolution light curve of the second prompt emission of GRB 121217A, including BAT, GBM, XRT and the H band of GROND. The best fit afterglow light curve from Sect. 3.3.3 is shown by the dashed blue line. Even though in flux space it appears that there is a rebrightening, this is no where near as large as has been seen for other bursts (see, e.g., Racusin et al. 2008) and suggests the spectral component of the prompt emission is spectrally hard.

$$R'_{\text{dec}} = 2c\Gamma'^{2}_{0}t'_{\text{peak}} = 1.2 \times 10^{17}\,\text{cm}, \tag{3.5}$$

where we have assumed that the afterglow component is a result of the second peak, so $t'_{\text{peak}} = 934\,\text{s}$, and taken the same fixed parameters as outlined in the previous sections.

3.4.3 Lack of Optical Rebrightening?

The high time resolution light curve seen in Fig. 3.6, shows that there is a rebright-ening in the optical wavelengths by a factor of 2.7 ± 0.6, but this is delayed from the peak of the X-ray/γ-ray emission by a factor of $14 \pm 7\,\text{s}$. This rebrightening factor is incredibly small when compared to the rebrightening in the X-rays, which changes by a factor of ~ 100.

3.4.4 Internal Shock Model: Synchrotron Self-Absorption Frequency

The extension of the best fit powerlaw overpredicts the flux in the NIR wavelengths by a factor ~ 100 (Table 3.1) and would suggest the fireball model does not work. However, it is possible that the below $0.1\,\text{keV}$ there is a spectral break, which allows the powerlaw to become much harder. Following Shen & Zhang (2009) a spectral break can exist when the optical wavelength photons are being self-absorbed by the radiating

electrons and this occurs at the self-absorption frequency, $\nu'_{\rm a}$. We assume the case (I) scenario outlined in Shen & Zhang (2009), where the self-absorption frequency is $\nu'_{\rm m} < \nu'_{\rm a} < \nu'_{\rm p}$, assuming that $\nu'_{\rm m}$ is the minimum frequency allowed and $\nu'_{\rm p}$ is the maximum frequency allowed. These frequencies are set by properties of the initial fireball, mainly the emission radius, R'_{γ}, the Lorentz factor, Γ', and the magnetic field, B'. There is no visible spectral break in the prompt emission to define $\nu'_{\rm p}$ and so at this stage we can only set an upper limit of $\nu'_{\rm p} > 1000\,{\rm keV}$, with an emission of $f'_{\nu'_{\rm p}} = 4.9 \times 10^{-5}\,\mu{\rm Jy}$ assuming the best fit powerlaw. Using equation 10 from Shen & Zhang (2009), this would place a constraint on the self-absorption frequency of

$$\nu'_{\rm a} > 10^{19 - \frac{12.2}{2.5-\beta}} \left(\nu'^{-\beta}_{\rm p,19} \frac{f'_{\nu_{\rm p}}}{f'_{\nu_{\rm opt}}} \right)^{\frac{1}{2.5-\beta}} > 5.29 \times 10^{12}\,{\rm Hz} \tag{3.6}$$

and therefore,

$$E'_{\rm a} > 2.19 \times 10^{-5}\,{\rm keV}, \tag{3.7}$$

where the measured flux in the J band is $\nu'_{\rm opt} = 505\,\mu{\rm Jy}$, and can be seen pictorially in Fig. 3.5. This does not place a strong constraint on where the absorption frequency must lie, and would require higher or lower energy detections, however, it is still consistent with a break lying between the optical and X-ray wavelengths. If this was the case, the emission radius could be constrained, using Shen & Zhang (2009) equation 9,10 and A17, to

$$R'_{\gamma} = 350 \times 10^{14} \left(\frac{4}{1+z} \right)^{\frac{7}{4}} \Gamma'^{\frac{3}{4}}_{300} B'^{\frac{1}{4}}_{5}\,{\rm cm}, \tag{3.8}$$

at the optical frequency of $\nu'_{\rm opt} = 2.42 \times 10^{12}\,{\rm Hz}$. This value is much larger than those determined in other works (e.g., Shen & Zhang 2009) by a factor of ~ 10, and could suggest either a smaller Lorentz factor or magnetic fields. If we subtract an afterglow component, this reduces the J flux by a factor of $\sim \frac{1}{4}$ and so would change the above value by $R'_{\gamma} \propto f'^{\frac{1}{2}}_{\rm opt} \sim \frac{1}{2}$. Substituting the Lorentz factor (Eqn. 3.4) into Eqn. 3.8, results in an estimate of the required magnetic field of

$$B'_{5} = 0.2 R'^{4}_{\gamma,16}\,{\rm G}. \tag{3.9}$$

The rebrightening period of the X-ray emission around the second γ-ray peak is shown in Fig. 3.7, during which there exists several pulses and dips, and has a maximum peak at the same time as the prompt emission. Even though they peak at the same time, the length of the activity in the X-ray wavelengths is $t \sim 1000\,{\rm s}$, where as the prompt emission lasts for $t \sim 50\,{\rm s}$, at least 100 times longer (see also Fig. 3.2). We fit a powerlaw for the times at which the X-ray has bumpy features to obtain the spectral slope. We assume the best fit host galaxy gas absorption $N_{H,X} = 0.74 \times 10^{22}\,{\rm cm}^{-2}$ for the powerlaw fits, although this does not change the overall result.
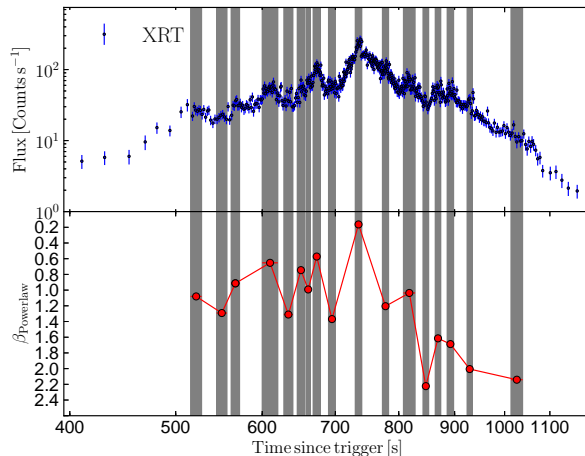
Figure 3.7 The top panel is a zoom in of the X-ray light curve during the second prompt emission that occurred at $t = T_0 + 735$ s. The low panel shows spectral index of the best fit powerlaw, β, in blue circles for a specific time slot shown by the grey shaded bars, using the best fit galactic gas from the complete prompt SED.

The powerlaw spectral index begins at ~ 1 and then approaches very flat values during each of the bumpy features and is the most flat at the time the prompt emission occurs, after which it becomes spectrally soft again, settling at ~ 2.0. Each of these bumps could be the result of slow shells (of low Lorentz Factors) causing internal shocks, which remain spectrally soft enough not to be observed in the prompt emission, and with a self-absorption frequency, would still show no signs of rebrightening in the optical wavelengths. Only when it becomes spectrally hard enough at $\beta \sim 1.0$ is it observable with the γ-ray detectors.

3.4.5 Testing the Band Model: Moving E-Peak

Initial fits of the Band function suggest that the flux predicted in the NIR wavelength overpredicts what is observed, however, once the expected flux from an afterglow component is subtracted it is consistent, as seen in Fig. 3.6. This would suggest that the afterglow component from the first prompt emission is dominating in the NIR bands, and so no prominent rebrightening is observed, as compared in the X-ray emission[2]. The rebrightening of the X-ray flares could also be interpreted within the framework of the Band model, assuming that the peak energy of the Band function is moving within the observable bands during the prompt emission. Unfortunately, it is not possible to carry out the same analysis used in Sect. 3.4.4, as the low number statistics per time

---

[2]We note that the same arguments work for the cut-off powerlaw model, and so neglect a discussion about it throughout the text.
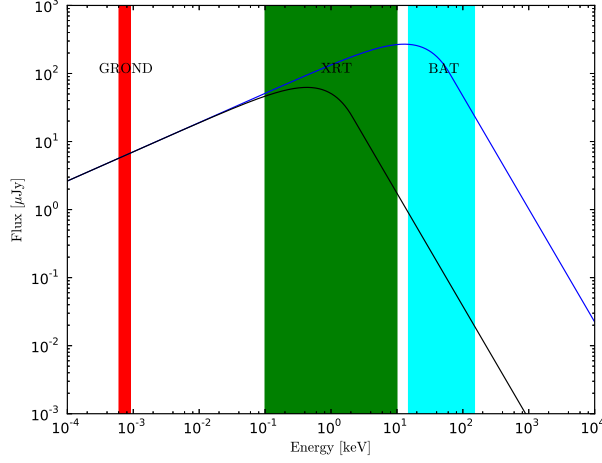
Figure 3.8 Two band functions with different peak energies. They show that as the peak energy moves to lower energies (black line) the flux in the γ-ray wavelengths decreases substantially that it would no longer be observable.

bin and the large number of free parameters do not allow the peak energy to be constrained. Therefore, we fit the time slice of the entire flare in the time range $T_0 + 1100$ s to $T_0 + 1384$ s with a band function, which results in a best fit of $\chi^2/\text{d.o.f.} = 562/533$ for $E_{\text{peak}} = 13.1 \pm 6.4$ keV, $\beta_1 = -1.25 \pm 0.04$, $\beta_2 = -2 \pm 113$, and assuming the best fit $N_{H,X}$ obtained from the best fit prompt SED. This would mean that for each energy injection observed in the X-ray emission, the E_{peak} is moving towards the X-ray wavelengths resulting in a flatter slope, and for the rest of the time it remains in a region not visible to us, such that there is no visible prompt emission. Also, there would not be a large contribution to the optical wavelengths, which would remain dominated by the initial afterglow component.

3.5 Conclusion

We observed the *Swift/Fermi* burst GRB 121217 from two satellites and one ground-based telescope, with five different instruments covering the optical/NIR, X-ray and γ-ray wavelengths during a secondary prompt emission period. The NIR emission exhibits no obvious rebrightening during this prompt episode, in contrast to cases such as the naked eye burst, and also its own X-ray emission which increases by a factor of a hundred. Allocating the NIR emission to an afterglow component of the first prompt period and subtracting its contribution would give the flux consistent with extrapolation from the prompt spectrum of the GRB.

Extrapolations of the internal shock model overestimate the expected flux, unless

self-absorption by the population of electrons is included, and allows the radius of the emission to be constrained to $R_\gamma \sim 350 \times 10^{14} \Gamma_{300}^{\frac{3}{4}} B_{\frac{1}{5}}^{5}$ cm and an estimate on the magnetic field of $B \sim 10^4$ G, using the high lattitude emission of the first prompt emission. However, all of the powerlaw models require that a large amount of gas exists in the host galaxy, which is unrealistic especially at a redshift of $z \sim 3$ (or anything > 1), suggesting that this is most likely not the correct model. On the other hand, the Band function and other variations (e.g., high energy cut-off) can reproduce the observed flux in the optical band remaining consistent throughout, requiring no other modifications.

Finally, the X-ray emission has several flaring episodes both prior and post to the prompt emission, showing that the central engine is active even after the initial prompt emission. The flaring can be explained as several small Lorentz factor shells that are not spectrally hard enough to be seen by the γ-ray detectors and that the self-absorption in the optical bands still dominates. It is also, possible to explain this within the Band framework, such that the peak energy E_{peak} of the spectrum is only within the observable wavelengths during the first and second prompt emission periods, giving a value of $E_{\text{peak}} \sim 13$ keV. Further observations of this type, especially in multiple filters, during the prompt emission of the GRB will help to further constrain the type of mechanism that can explain the origin of the Band model.

Chapter 4

The low-extinction afterglow in the solar-metallicity host galaxy of γ-ray burst 110918A[1]

ABSTRACT

Galaxies selected through long γ-ray bursts (GRBs) could be of fundamental importance when mapping the star formation history out to the highest redshifts. Before using them as efficient tools in the early Universe, however, the environmental factors that govern the formation of GRBs need to be understood. Metallicity is theoretically thought to be a fundamental driver in GRB explosions and energetics, but it is still, even after more than a decade of extensive studies, not fully understood. This is largely related to two phenomena: a dust-extinction bias, which prevented high-mass and thus likely high-metallicity GRB hosts from being detected in the first place, and a lack of efficient instrumentation, which limited spectroscopic studies, including metallicity measurements, to the low-redshift end of the GRB host population. The subject of this work is the very energetic GRB 110918A ($E_{\gamma,\mathrm{iso}} = 1.9 \times 10^{54}$ erg), for which we measure a redshift of $z = 0.984$. GRB 110918A gave rise to a luminous afterglow with an intrinsic spectral slope of $\beta = 0.70$, which probed a sight-line with little extinction ($A_V^{\mathrm{GRB}} = 0.16$ mag) and soft X-ray absorption ($N_{\mathrm{H,X}} = (1.6 \pm 0.5) \times 10^{21}$ cm^{-2}) typical of the established distributions of afterglow properties. However, photometric and spectroscopic follow-up observations of the galaxy hosting GRB 110918A, including optical/near-infrared (NIR) photometry with the Gamma-Ray burst Optical Near-infrared Detector (GROND) and spectroscopy with the Very Large Telescope (VLT)/X-shooter, reveal an all but average GRB host in comparison to the $z \sim 1$ galaxies selected through similar afterglows to date. It has a large spatial extent with a half-light radius of $R_{\frac{1}{2}} \sim 10$ kpc, the highest

stellar mass for $z < 1.9$ ($\log(M_*/M_\odot) = 10.68 \pm 0.16$), and an H$\alpha$-based star formation rate of SFR$_{\mathrm{H}\alpha} = 41^{+28}_{-16}\,\mathrm{M}_\odot\,\mathrm{yr}^{-1}$. We measure a gas-phase extinction of $A_V^{\mathrm{gas}} \sim 1.8\,\mathrm{mag}$ through the Balmer decrement and one of the largest host-integrated metallicities ever of around solar using the well-constrained ratios of [N II]/Hα and [N II]/[O II] ($12 + \log(\mathrm{O/H}) = 8.93 \pm 0.13$ and $8.85^{+0.14}_{-0.18}$, respectively). This presents one of the very few robust metallicity measurements of GRB hosts at $z \sim 1$, and establishes that GRB hosts at $z \sim 1$ can also be very metal rich. It conclusively rules out a metallicity cut-off in GRB host galaxies and argues against an anti-correlation between metallicity and energy release in GRBs.

4.1 Introduction

During their prompt emission, long GRBs are the brightest objects in the Universe, easily reaching isotropic-equivalent luminosities as high as $\sim 10^{54}\,\mathrm{erg\,s}^{-1}$. Their observed association with supernovae events (e.g., Galama et al. 1998; Hjorth et al. 2003; Stanek et al. 2003; Matheson et al. 2003; Della Valle 2011; Hjorth et al. 2012) has tightly linked them to the death of massive stars. The GRB itself is then believed to result from accretion of matter onto the newly formed, rapidly rotating black hole or compact object in the collapsar model (Woosley 1993; Paczynski 1998; MacFadyen & Woosley 1999). The lack of hydrogen and helium in the spectra of GRB supernovae classify them as type Ic, supporting the notion that GRB progenitors are likely Wolf-Rayet-like stars (for a review of supernova classifications see, e.g., Filippenko 1997). Given that these type of stars undergo vigorous mass loss from stellar winds, metallicity constraints ($Z < 0.3\,\mathrm{Z}_\odot$) on the progenitor are postulated to ensure that an accretion disk is still formed around the black hole (Hirschi et al. 2005; Yoon & Langer 2005; Woosley & Heger 2006).

The possible association of long GRBs with massive stars supported the idea that they could be used as complementary and independent tracers of star formation, especially at high redshifts ($z \gtrsim 4$), due to their very high luminosities (see, e.g., Daigne et al. 2006; Li 2008; Kistler et al. 2009; Ishida et al. 2011). However, to have full confidence in these studies the intrinsic evolutionary effects in long GRB production must be understood and the galactic environments preferred by the progenitor need to be quantified (e.g., Butler et al. 2010; Wang & Dai 2011; Salvaterra et al. 2012; Robertson & Ellis 2012; Elliott et al. 2012a). Of particular interest is the relation between the galaxies selected by GRBs and the star formation weighted population of field galaxies. To be direct and unbiased tracers of star formation, the relative rates of GRBs in galaxies of various physical properties should be the same in galaxies taken from samples that trace the global star formation density at a given redshift. Studies based on these galaxy samples are most commonly performed at $z \lesssim 1.5$, where the star formation of field galaxies is largely recovered by state-of-the-art, deep-field surveys.

Initial work showed that many long GRB host galaxies had a low mass, low metallicity, and blue colours and were actively star forming (see, e.g., Fruchter et al. 1999; Le Floc'h et al. 2003; Berger et al. 2003; Christensen et al. 2004; Tanvir et al. 2004).

This seemed directly in line with the requirements of the collapsar model. Further work carried out with larger samples (e.g., Savaglio et al. 2009) again showed similar characteristics. However, at a given mass and star formation rate (SFR), long GRB hosts were also found to be no different from the normal population of star-forming galaxies at the same redshift (Mannucci et al. 2011). Yet, these initial studies neglected the contribution from galaxies hosting dust-extinguished afterglows, often termed dark bursts (e.g., Perley et al. 2009; Greiner et al. 2011a). Galaxies hosting dark bursts are systematically more massive and have a higher dust content than the previously established population localised with optically bright afterglows (Krühler et al. 2011a; Hjorth et al. 2012; Rossi et al. 2012; Perley et al. 2013; Christensen et al. 2011; de Ugarte Postigo et al. 2012).

Despite the inclusion of this more evolved galaxy population, there are still fewer GRBs in massive galaxies than expected. This is based on their contribution to the overall SFR, at least for redshifts of $z < 1.5$ (Perley et al. 2013), which indicates that the GRB explosion mechanism is dependent on metallicity. It is, however, important to note that these conclusions are inferred indirectly through stellar mass as a metallicity proxy. In addition, while the photometric samples of GRB hosts have reached integrated number statistics of 100 and above (e.g., Hjorth et al. 2012; Perley et al. 2013), the most crucial measurement of gas-phase metallicity has only been performed in a handful of cases at $z \gtrsim 1$ (Levesque et al. 2010a; Krühler et al. 2012a).

Only a few host galaxies with substantial gas-phase metallicities around or above solar (e.g., Levesque et al. 2010b) that directly violate the proposed cut-off in galaxy metallicity have been observed to date. There is thus still lively debate in the literature about the nature of GRB hosts and their relation to the star formation weighted galaxy population as a whole (e.g., Niino 2011; Mannucci et al. 2011; Kocevski & West 2011; Graham & Fruchter 2012). The GRB hosts with high stellar mass and high global metallicity are hence of primary interest for GRB host studies as they directly probe this allegedly forbidden parameter space. A robust understanding of the galactic environments in which GRBs form would then add confidence to their use as cosmological probes beyond the limits of deep survey studies (e.g., Tanvir et al. 2012; Basa et al. 2012).

Here, we present spectroscopy and photometry of the host galaxy and afterglow of the luminous GRB 110918A, detected on the 18th of September 2011 at T_0=21:26:57 UT (Hurley et al. 2011). This burst had one of the highest fluences of any GRB observed over the last 20 years (together with GRB 021206; Wigger et al. 2008) and had the highest peak flux ever detected by *Konus-Wind* (Golenetskii et al. 2011; Frederiks & Pal'shin 2011, Frederiks et al. 2013 in prep.), located at a redshift of $z = 0.98$. The massive, metal-rich host galaxy and unobscured afterglow of GRB 110918A challenges the current view of the connection between local and global environments and allows us to investigate the preferred conditions for the formation of a long GRB.

The paper is arranged as follows: first we describe the observations carried out by both ground- and space-based instruments and their corresponding reduction in Sect. 4.2. Second, the resulting properties ascertained from the spectral energy distributions (SED) and spectra of the GRB and its host are described in Sect. 4.3. Fi-

nally, we discuss our findings and their implications for the population of long GRBs in Sect. 4.4 and conclude in Sect. 4.5. We adopt the convention that the GRB flux density is described by $F_\nu\,(t) \propto t^{-\alpha}\nu^{-\beta}$ and reported errors are at the 1σ confidence level, additionally, we assume a ΛCDM cosmology: $H_0 = 71\,\mathrm{km\,s^{-1}\,Mpc^{-1}}$, $\Omega_M = 0.27$ and $\Omega_\Lambda = 0.73$. We use a Chabrier (2003) initial mass function (IMF) and abundances throughout the text.

4.2 Observations and Data Reduction

4.2.1 Swift-XRT Spectra

At the time of the Interplanetary Network (IPN) trigger, *Swift* (Gehrels et al. 2004) was in both the South Atlantic Anomaly and Earth-occulted, and so no trigger (Krimm & Siegel 2011) was initiated in the Burst Alert Telescope (Barthelmy et al. 2005, BAT). However, the *Swift* X-ray telescope (Burrows et al. 2005, XRT) began observing the field of GRB 110918A (see Fig. 4.1) at $T_0 + 107.4\,\mathrm{ks}$ until $\sim 40\,\mathrm{d}$ later. The XRT spectrum shows no signs of spectral evolution, remaining with a constant hardness ratio of ~ 0.85 for its entire emission. We extracted a spectrum at the time interval of $T_0 + 140\,\mathrm{ks}$ to $T_0 + 250\,\mathrm{ks}$ to coincide with our optical/NIR wavelength observations (see Fig. 4.2). The XRT spectral data were obtained from the public *Swift* archive and regrouped to ensure at least 20 counts per bin in the standard manner, using the *grappha* task from the HEAsoft package with response matrices from CALDB `v20120209`. We assume a Galactic hydrogen column of $\mathrm{N_{H,X}^{Gal}} = 1.68 \times 10^{20}\,\mathrm{cm^{-2}}$ (Kalberla et al. 2005) in the direction of the burst.

4.2.2 GROND Optical/NIR Photometry

GROND (Greiner et al. 2008a), which is mounted at the MPG/ESO 2.2 m telescope at La Silla, Chile, began its follow-up campaign of GRB 110918A 29.2 hrs after the trigger simultaneously in the $g'r'i'z'JHK_s$ filters (Elliott et al. 2011). A mosaic of five pointings was carried out to cover the full IPN error box ($\sim 20'\times20'$), and the GRB optical afterglow candidate was detected at the location R.A. (J2000) $= 02^h10^m09.34^s$, Dec. (J2000) $= -27°06'19.7''$, in GROND's NIR chips, located just outside the IPN error box and consistent with the X-ray (Mangano et al. 2011) and optical (Tanvir et al. 2011) position with an uncertainty of $0.2''$. The GROND observations continued for over one month after the GRB trigger, and an underlying host was discovered (see also Oksanen et al. 2011). Deep images of 3600 s in the NIR and 4500 s in the optical were obtained with GROND of the host galaxy at $T_0 + 36.37\,\mathrm{d}$.

Image reduction and photometry of the GROND observations were carried out using standard Image Reduction and Analysis Facility tasks (IRAF; Tody 1993) in the way outlined in Krühler et al. (2008) and Yoldaş et al. (2008). In brief, a point-spread function (PSF) was obtained from the bright stars within the field and applied to the afterglow photometry. The absolute calibration of the optical photometry was achieved by observing a Sloan Digital Sky Survey (SDSS) field (Aihara et al. 2011) at R.A.
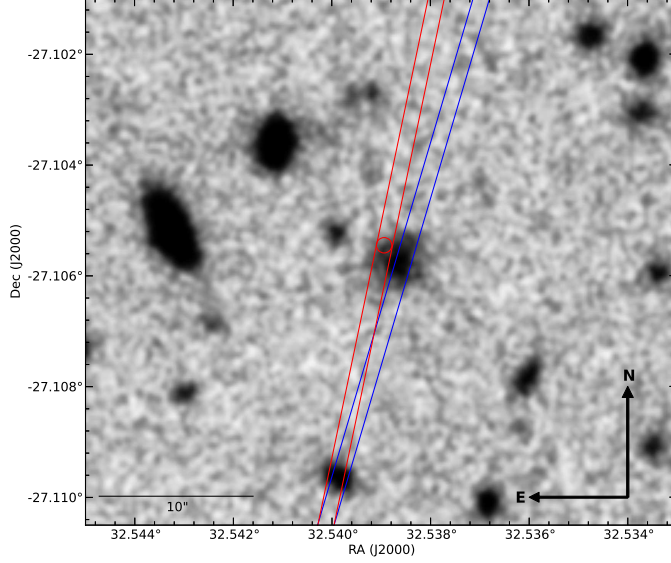
Figure 4.1 GROND 60-minute stacked i' band image of the GRB 110918A host galaxy. The slit arrangement used in the acquisition image is shown for both the OSIRIS afterglow spectrum (red line) and host spectrum (blue line).

(J2000) $= 01^h 40^m 00.0^s$, Dec. (J2000) $= -18°03'00.0''$ and the GRB field consecutively. The NIR absolute calibration was obtained from the Two Micron Sky Survey (2MASS) stars (Skrutskie et al. 2006) within the field of the GRB. As a result of the extension of the galaxy (see Fig. 4.1), an aperture size of $3.2''$ was used on the deep host galaxy images, within which the aperture flux flattened in a curve-of-growth analysis and the zero points were correspondingly corrected.

The scope of this paper does not involve a full analysis of the afterglow emission. However, afterglow flux measurements are required at certain time intervals to implement slit-loss corrections to the optical spectra and to determine the local extinction of the afterglow. Therefore, we only present the required data and direct the reader to future work for a full analysis of the afterglow[2]. For the slit-loss correction of the afterglow, we obtain the following brightnesses in the AB system (Oke & Gunn 1983) at a mid-time of $T_0 + 2.2$ d: $g' = 20.50 \pm 0.05$ mag, $r' = 20.20 \pm 0.04$ mag, $i' = 19.96 \pm 0.04$ mag, $z' = 19.83 \pm 0.07$ mag, $J = 19.46 \pm 0.09$ mag, $H = 19.04 \pm 0.10$ mag, $K_s = 18.66 \pm 0.19$ mag. The magnitudes are uncorrected for a Galactic dust reddening of $E(B - V)^{\mathrm{Gal}} = 0.020$ mag corresponding to an extinction of $A_V^{\mathrm{Gal}} = 0.062$ mag for $R_V = 3.1$ (Schlegel et al. 1998).

---

[2]The afterglow light curves are found in the Appendix.

4.2.3 WFI Optical Photometry

Further deep observations of the host galaxy were made 392 d after the trigger with the Wide Field Imager (Baade et al. 1999, WFI), which is also mounted on the MPG/ESO 2.2m telescope, in the standard broadband filters BB#B/123_ESO878 (B) and BB#U/150_ESO878 (U). Two sets of images were taken: the first on 25 October 2012, consisting of 1800 s in U and 600 s in B, and the second on 26 October 2012, consisting of 150 s in U and 75 s in B. A calibration field was obtained on 26 October 2012 in both the U and B filters, and the standard field SA113+158[3] was used as a primary calibrator. The photometry was carried out in the same way as the GROND images, and the magnitudes were converted into the AB system using the ESO magnitude converter[4].

4.2.4 WISE IR Photometry

The Wide-field Infrared Survey Explorer (Wright et al. 2010, WISE) All-Sky Source Catalogue[5] reveals a source at the position of the host galaxy of GRB 110918A, with an 11σ and 3σ detection in the $W1$ and $W2$ bands, which are centred at 3.4μm and 4.6μm, respectively. The *wmpro* magnitudes were used, which are the magnitudes retrieved from profile-fitting photometry (or the magnitude of the 95% confidence brightness) and converted into the AB system using the WISE conversion factors[6]. Galactic reddening corrections were made using the A_V^{Gal} conversions determined by Jarrett et al. (2012).

4.2.5 GMOS Optical Spectroscopy

The first spectrum of the afterglow was taken with the Gemini Multi-Object Spectrographs (Hook et al. 2004, GMOS) on the Gemini North telescope (Mauna Kea), starting at 12:52 UT on 20 September 2011, 1.6 d after the GRB trigger. Four exposures of 500 s each were obtained using the R400 grism and a $1''(\sim 8.0\,\mathrm{kpc}$ projected at $z = 0.984$) slit width. Two of the spectra were obtained with a central wavelength of $6000\,\text{Å}$ and the other two with $6050\,\text{Å}$ to cover the detector gaps. In addition, a spatial dither was used to cover the amplifier boundaries. The resulting spectrum covers the range $3930 - 8170\,\text{Å}$. We reduced the data with tasks within the Gemini.GMOS package and IRAF, `v1.11`, using flat field and arc lamp frames taken directly before and after the science image.

4.2.6 OSIRIS Optical Spectroscopy

The second spectrum of the afterglow was obtained using the Optical System for Imaging and low Resolution Integrated Spectroscopy (Cepa et al. 2000, OSIRIS) mounted on the 10.4 m Gran Telescopio Canarias (Roque de los Muchachos) starting at 13:00

---

[3]`www.eso.org/sci/observing/tools/standards/Landolt.html`

[4]`http://archive.eso.org/mag2flux`

[5]`http://irsa.ipac.caltech.edu`

[6]`http://wise2.ipac.caltech.edu/docs/release/allsky/expsup/sec4_4h.html`

UT on 21 September 2011, 2.2 d after the GRB trigger. Three exposures of 900 seconds each were taken using the R500B grism and a 1″slit width obtained at the parallactic angle. The resulting spectrum covers the range $4400 - 8700\,\text{Å}$. Data were reduced and calibrated using standard procedures in IRAF. The spectrum was flux calibrated using G157-34 as a standard star and the 1D spectrum was scaled to the GROND afterglow photometry to correct for slit losses (correction factor of ~ 1.9).

A spectrum of the host was obtained on 11 November 2011, $T_0 + 54.1$ d after the GRB trigger. A sequence of three 1200 s exposures was obtained with OSIRIS using the R1000R grism and a 1.0″ slit width, and covered the wavelength range of $5100\,\text{Å}$ to $10000\,\text{Å}$. The spectrum was flux calibrated using the standard star G191-B2B and corrected for slit losses by scaling the 1D spectrum to the photometry of the host galaxy obtained using GROND (correction factor of ~ 3.5).

4.2.7 X-Shooter Optical/NIR Spectroscopy

We further observed the host of GRB 110918A with the cross-dispersed echelle spectrograph X-shooter (Vernet et al. 2011) on the Very Large Telescope Kueyen (UT2). The X-shooter has three individual arms taking spectra simultaneously in the range of $3000\,\text{Å}$ to $5600\,\text{Å}$ (UVB arm), $5600\,\text{Å}$ to $10\,200\,\text{Å}$ (VIS arm), and $10\,200\,\text{Å}$ to $24\,800\,\text{Å}$ (NIR arm). Three different sets of observations were carried out on 17 December 2012, 07 January 2013, and 16 January 2013, respectively, with a position angle of $59°$ east of north. They consisted of a pair of nodded frames with exposure times of 1200 s in each of the UVB/VIS arms and 2×600 s in the NIR arm. The slit width was 1″.6, 1″.5, and 0″.9 yielding a resolution measured on arc lamp frames of $R \sim \lambda/\Delta\lambda = 3200$, 4900, and 5300 in the UVB, VIS, and NIR arm, respectively. The NIR slit includes a blocking filter for the K-band, which limited our effective wavelength coverage to $< 20\,500\,\text{Å}$ but provided lower background levels in the J- and H-band.

Each of the individual observations was reduced and wavelength- and flux-calibrated separately using standard procedures within the X-shooter pipeline `v2.0.0` (D'Odorico et al. 2006) supplied by ESO. The individual 2D frames were then stacked using variance weighting in a heliocentric reference frame, and the 1D spectra were extracted using an optimal extraction method. Given the extent of the target, slit losses are substantial. Similar to the OSIRIS and GMOS spectroscopy, we scaled the well-detected continuum of the X-shooter data to the available photometric host SED. The consistency between matching factors derived from different photometric data in the individual arms[7] provides confidence that the absolute flux calibration in the final X-shooter spectrum is accurate to better than $\sim 20\%$ over the full wavelength range of interest.

---

[7]We derive factors for the r'-, i'-, and z' -band data in the VIS arm of 3.1 ± 0.3, 2.8 ± 0.3, 2.8 ± 0.3, and 3.5 ± 0.4, 3.3 ± 0.3 for the J- and H-band in the NIR arm. The offset between the VIS and NIR arm is readily explained by the smaller slit width in the NIR arm.
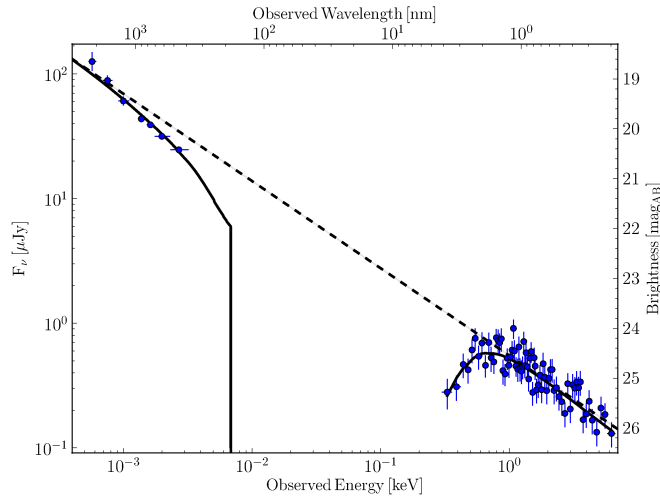
Figure 4.2 Broadband SED of GRB 110918A, including optical, NIR, and X-ray data. The SED was constructed using GROND data at a mid-time of $T_0 + 194\,$ks and X-ray data between $T_0 + 140\,$ks and $T_0 + 250\,$ks. The best-fit parameters for a power-law $(\chi^2/\text{d.o.f.} = 85/73)$ are: a spectral slope of $\beta = 0.70 \pm 0.02$, a hydrogen column density of $N_{H,X}^{GRB} = 1.56_{-0.46}^{+0.52} \times 10^{21}\,\text{cm}^{-2}$, and a line-of-sight extinction of $A_V^{GRB} = 0.16 \pm 0.06\,$mag, assuming SMC-like dust.

4.3   Results

4.3.1   The Afterglow Sight-Line: Dust, Star Formation Rate, and Gas

A broadband SED was constructed from the optical/NIR GROND photometry (see Sect. 4.2.2) at a mid-time of $T_0 + 194\,$ks and X-ray data between $T_0 + 140\,$ks and $T_0 + 250\,$ks. The SED was fit in a standard manner (e.g., Filgas et al. 2011a), assuming that the afterglow emission is well described by the standard synchrotron mechanism. The best-fit single power-law $(\chi^2/\text{d.o.f.} = 85/73)$ is shown in Fig. 4.2 with a spectral slope of $\beta = 0.70 \pm 0.02$, a hydrogen column density of $N_{H,X}^{GRB} = 1.56_{-0.46}^{+0.52} \times 10^{21}\,\text{cm}^{-2}$, and a line-of-sight extinction of $A_V^{GRB} = 0.16 \pm 0.06\,$mag, assuming a Small Magellanic Cloud- (SMC) like dust with $R_V = 2.93$ in the parametrisation of Pei (1992). Despite yielding an improved fit, a broken power-law model is not warranted as the number of free parameters increases $(\chi^2/\text{d.o.f.} = 83/71)$, implying that the improvement is not statistically significant. Nevertheless, the resulting parameters of the best-fit broken power-laws models that use different dust models are consistent with the uncertainties of the power-law values below the break at ~ 0.6 keV and do not alter our conclusions.

Using the procedure outlined by de Ugarte Postigo et al. (2012) with the two afterglow spectra obtained with GMOS $(T_0 + 1.6\text{d})$ and OSIRIS $(T_0 + 2.2\text{d})$, we detect the transition of several metal ions including Fe II, Mg II, and Mg I at a common redshift of $z = 0.984 \pm 0.001$ (see Tables 4.2 and 4.8), which is consistent with galactic winds or

star bursting periods (Fynbo et al. 2009a; Nestor et al. 2011; Christensen et al. 2011; Rodríguez Hidalgo et al. 2012). In comparison with a long GRB sample (de Ugarte Postigo et al. 2012), we find that it has stronger absorption features than 80% of the sample.

4.3.2 The Host's Stellar Component: Dust Attenuation, Star Formation Rate, and Stellar Mass

The host of GRB 110918A was detected in 11 different filters ranging from the ultraviolet to 4.5μm, yielding a well-sampled photometric SED (see Fig. 4.3 and Table 4.1). To estimate the global properties of the host galaxy, we employed standard techniques that use stellar population synthesis to estimate stellar masses, as outlined thoroughly in Ilbert et al. (2009). We constructed a grid of galaxy templates based on the models taken from Bruzual & Charlot (2003) over a wide parameter space consisting of a range of ages $(0-1.35 \times 10^9 \mathrm{yr})$, star formation histories $(\propto e^\tau, \tau = 0.1, 0.3, 1, 2, 3, 5, 10, 15, 30)$, reddening values $(E(B-V) = 0-0.4\,\mathrm{mag})$, a single attenuation law (starburst; Calzetti et al. 2000) and metallicities $(Z = 0.004, 0.008, 0.02)$. Emission lines were also included, whereby the emission lines were estimated from the predicted UV luminosity and converted to a SFR using Kennicutt (1998). For each template, an SED was constructed for the filters required and a χ^2 was calculated using the Photometric Analysis for Redshift Estimate routines, LePHARE [8] $\mathtt{v2.2}$ (Arnouts et al. 1999; Ilbert et al. 2006). The best-fit template was the one that gave the minimum χ^2, and the corresponding uncertainties for each parameter were obtained from the grid of χ^2 values. Systematic uncertainties of up to an average of $0.2-0.3\,\mathrm{dex}$ are expected in the stellar mass value due to the adopted stellar population models and extinction laws (see, e.g., Krühler et al. 2011a, and references therein). The filter response curves for the $W1$ and $W2$ bands were obtained from Wright et al. (2010) and for the U and B bands from the ESO web pages[9]. The results of the best-fit template, which had a $\chi^2/\#\,\mathrm{Bands} = 5.4/11$, had the following parameters: a mass of $\log_{10}\left(\frac{\mathrm{M}_*}{\mathrm{M}_\odot}\right) = 10.68 \pm 0.16$, an SED SFR of $\mathrm{SFR_{SED}} = 66^{+50}_{-30}\,\mathrm{M}_\odot$, a reddening of $E(B-V)^\mathrm{stars} = 0.26 \pm 0.15\,\mathrm{mag}$, and a starburst age of $\tau = 0.7^{+1.4}_{-0.4}\,\mathrm{Gyr}$.

4.3.3 The Host's Gas-Phase Component: Dust Extinction, Star Formation Rate, and Metallicity

The first host spectrum of GRB 110918A was obtained with OSIRIS/GTC in the optical wavelength range ~ 50 days after the trigger, and the one second was obtained with X-shooter more than 460 days post trigger. The X-shooter spectrum extends our spectral coverage to the NIR and thus to the wavelength range, where important tracers of SFR and metallicity are located. In summary, we clearly detect the Hα and Hβ transition from the Balmer series, as well as the forbidden transitions of [O II]($\lambda\lambda$3726,

---

[8] `www.cfht.hawaii.edu/~arnouts/LEPHARE/lephare.html`
[9] `www.eso.org/sci/facilities/lasilla/instruments/wfi/inst/filters`
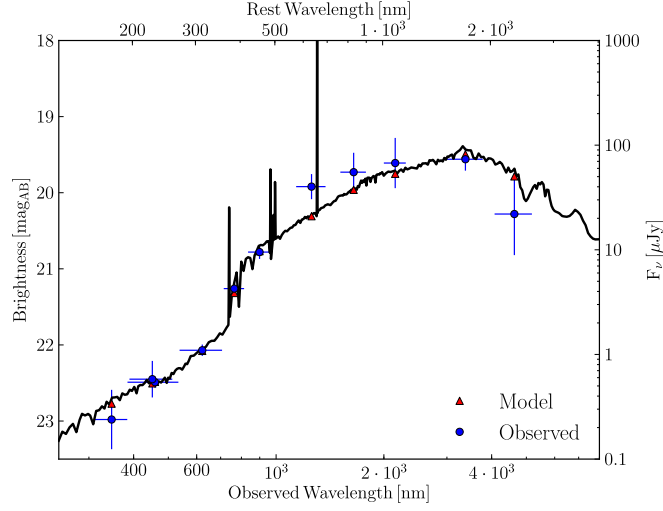
Figure 4.3 SED of the host of GRB 110918A obtained using GROND, WFI and WISE data, amounting to 11 filters: $UBg'r'i'z'JHK_sW1W2$ from left to right. The best-fit spectrum is depicted in black.

Table 4.1 Host galaxy magnitudes.

Filter	Instrument	Magnitude	Uncertainty
		$(\mathrm{mag_{AB}})$	$(\mathrm{mag_{AB}})$
U	WFI	22.98	0.25
B	WFI	22.45	0.16
g'	GROND	22.49	0.15
r'	GROND	22.07	0.05
i'	GROND	21.26	0.06
z	GROND	20.78	0.06
J	GROND	19.92	0.11
H	GROND	19.73	0.17
K_s	GROND	19.61	0.22
$W1$	WISE	19.56	0.10
$W2$	WISE	20.28	0.36

Notes. Corrected for Galactic foreground reddening. The observations in $g'r'i'z'JHK_s$ were obtained 36.37 d after the burst. The UB observations were obtained 392 d after the burst. The $W1$ and $W2$ photometry were obtained prior to the burst by the WISE Survey.

3729) and [N II](λ6584). The emission lines corresponding to [O III]($\lambda\lambda$4959,5007) are cosmologically redshifted to regions of low sensitivity for both OSIRIS and X-shooter and are thus not detected.

The velocity profile of the emission lines is clearly resolved by our X-shooter data and spans approximately $500\,\mathrm{km\,s^{-1}}$ in velocity space (see Fig. 4.9). It displays a conspicuous two-humped profile, with the two peaks of the emission lines separated by $200\,\mathrm{km\,s^{-1}}$. However, we do not observe a spatial tilt in the line shape, as would have been expected from a largely rotationally supported galaxy (unless it is face on), and both peaks appear at the same spatial position in the 2D spectrum. Line fluxes were measured by numerically integrating the available data and cross-checked with fitting Gaussians. Both procedures return consistent values; from the X-shooter spectrum, we measure global[10] emission-line fluxes of $f_{[\mathrm{OII}]} = (19.0 \pm 3.1)\times 10^{-17}\mathrm{erg\,s^{-1}\,cm^{-2}}$, $f_{\mathrm{H}\beta} = (9.5 \pm 1.9)\times 10^{-17}\mathrm{erg\,s^{-1}\,cm^{-2}}$, $f_{\mathrm{H}\alpha} = (47.8 \pm 4.9)\times 10^{-17}\mathrm{erg\,s^{-1}\,cm^{-2}}$ and $f_{[\mathrm{NII}]} = (15.3 \pm 3.3)\times 10^{-17}\mathrm{erg\,s^{-1}\,cm^{-2}}$. The OSIRIS spectrum yields $f_{[\mathrm{OII}]} = (20.0 \pm 2.8)\times 10^{-17}\mathrm{erg\,s^{-1}\,cm^{-2}}$, which is fully consistent with the X-shooter value.

Assuming the case B recombination (Osterbrock 1989) and using the standard values for electron density ($10^2\,\mathrm{cm^{-3}} \lesssim n_\mathrm{e} \lesssim 10^4\,\mathrm{cm^{-3}}$) and temperature ($T_\mathrm{e} \sim 10^4\,\mathrm{K}$), the Balmer ratio of H$\alpha$/H$\beta$ implies an $E(B-V)^\mathrm{gas} = 0.57^{+0.24}_{-0.22}$ or visual extinction $A_V^\mathrm{gas} = 1.8^{+0.8}_{-0.7}$ mag towards the star-forming regions assuming a Milky-Way-like extinction law[11]. This is the luminosity-weighted reddening/extinction of the gas phase. This value is typically found to be a factor of around two larger than the stellar $E(B-V)^\mathrm{stars}$ from the photometric SED model (e.g., Calzetti et al. 2000), which is consistent with our measurements for GRB 110918A. The Hα line flux implies an SFR of $\mathrm{SFR}_{\mathrm{H}\alpha} = 41^{+28}_{-16}\,\mathrm{M}_\odot\,\mathrm{yr^{-1}}$, following Kennicutt (1998) with a Chabrier (2003) IMF.

Using the different emission-line ratios, we can measure the gas-phase metallicity of the galaxy hosting GRB 110918A (see e.g., Kewley & Ellison 2008, for an extensive summary on those techniques). At $z \sim 1$, we are limited to the diagnostic ratios based on Hα, [O II], and [N II]. When the ratio of [N II] and Hα is used as a metallicity tracer, uncertainties in the reddening or chromatic slit losses are not going to affect the overall results because the respective lines are located very close in wavelength space. However, [N II]/Hα saturates at high metallicities ([N II]/H$\alpha\sim$ 0.3), while [N II]/[O II] does not. The final uncertainties are thus comparable in both indicators, and we measure $12 + \log(\mathrm{O/H})_\mathrm{N2H\alpha} = 8.93\pm0.13$ and $12 + \log(\mathrm{O/H})_\mathrm{N2O2} = 8.85^{+0.14}_{-0.18}$ using the formulation of Nagao et al. (2006). Different calibrations of the strong-line diagnostics yield $12 + \log(\mathrm{O/H})_\mathrm{N2H\alpha} = 8.63\pm0.08$ (Pettini & Pagel 2004) or $12 + \log(\mathrm{O/H})_\mathrm{N2O2} = 8.86^{+0.10}_{-0.14}$ (Kewley & Dopita 2002). The inherent systematic uncertainty of typically 0.1-0.2 dex (e.g., Nagao et al. 2006; Kewley & Ellison 2008) has not been included. These measurements imply metallicities between 0.9 and 1.7 times solar. All physical parameters of the galaxy hosting GRB 110918A are summarized in Table 4.2.

---

[10]Here and in the following, the error includes both the statistical error of the measurement and the error in slit-loss correction.

[11]Different local extinction laws yield comparable results, as there is little difference in the wavelength range of the Hα and Hβ Balmer lines.

Table 4.2 Physical parameters of the galaxy hosting GRB 110918A

Quantity	Unit/Method	Value
$E(B-V)^{\mathrm{GRB}}$	mag	0.05 ± 0.02
$N_{\mathrm{X,H}}^{\mathrm{GRB}}$	$10^{21}\,\mathrm{cm}^{-2}$	$1.56^{+0.52}_{-0.46}$
$\mathrm{EW}_{\mathrm{rest}}^{\mathrm{GRB}}$	(Å) Mg II(2796, 2803)	6.0
$\mathrm{SFR}_{\mathrm{[OII]}}^{\mathrm{GRB}}$	$\mathrm{M}_\odot\,\mathrm{yr}^{-1}$	2.3 ± 0.7
Stellar Mass	$\log(M_*/M_\odot)$	10.68 ± 0.16
Half-light radius	kpc	10
$E(B-V)^{\mathrm{stars}}$	mag	0.26 ± 0.15
$\mathrm{SFR}_{\mathrm{SED}}$	$\mathrm{M}_\odot\,\mathrm{yr}^{-1}$	66^{+50}_{-30}
τ	Gyr	$0.7^{+1.4}_{-0.4}$
$SFR_{H\alpha}$	$\mathrm{M}_\odot\,\mathrm{yr}^{-1}$	41^{+28}_{-16}
$E(B-V)^{\mathrm{gas}}$	mag	$0.57^{+0.24}_{-0.22}$
12+log(O/H)	[N II]/H$\alpha^{(a)}$	8.93 ± 0.13
12+log(O/H)	[N II]/H$\alpha^{(b)}$	8.63 ± 0.08
12+log(O/H)	[N II]/[O II]$^{(a)}$	$8.86^{+0.10}_{-0.14}$
12+log(O/H)	[N II]/[O II]$^{(c)}$	$8.85^{+0.14}_{-0.18}$

Notes. All values use a Chabrier IMF and take into account the statistical uncertainty of the measurements, as well as the uncertainty in the slit-loss and dust-correction factor if applicable. [a] Following Nagao et al. (2006). [b] Following Pettini & Pagel (2004). [c] Following Kewley & Dopita (2002).

4.4 Discussion

4.4.1 Host Galaxy Identification

We have used absorption lines from metal ions in the afterglow spectrum (see also Fynbo et al. 2009a for an extensive sample) and forbidden/recombination lines from the host galaxy to determine the redshift of the GRB (see also Krühler et al. 2012b), but it is in principle possible that the GRB lies at a higher redshift. To investigate if the host galaxy of GRB 110918A has been misidentified, we calculate the commonly used p-value, $p(m) = 1 - \exp\left(-\pi r_i^2 \sigma\left(\leq m\right)\right)$, which is the probability of finding a galaxy of magnitude m (or brighter) overlapping the GRB within an effective radius r_i, assuming that galaxies are Poisson distributed throughout the sky (Bloom et al. 2002). This neglects any type of galaxy clustering; however, recent work indicates that GRB locations do not preferentially lie in areas of strong galaxy overabundances (Cucchiara et al. 2012; Sudilovsky et al. 2013). The number of galaxies brighter than m per square arcsecond is given by σ, taken from Bloom et al. (2002) and calculated from the work of Hogg et al. (1997).

The burst location of GRB 110918A is seen to be offset from the bright centroid of the host by 12 kpc. However, in comparison to the half-light radius of the host galaxy, $R_{\frac{1}{2}} = 10.6$ kpc, the offset is consistent with the long GRB population, which has a median offset of $R_{\text{offset}}/R_{\frac{1}{2}} \sim 1$ (Bloom et al. 2002). We follow Bloom et al. (2002) and set $r_i = 2 \times R_{\frac{1}{2}} = 2.66''$. Synthetic R_C-band (Bessell 1979) photometry of the GRB 110918A host galaxy is calculated using the best-fit galaxy template taken from Sect. 4.3.2. Using the AB-to-Vega conversions given in Rossi et al. (2012) results in $R_C = 21.7\,\text{mag}_{\text{Vega}}$. This yields a probability of chance association of $p = 0.01$, making this galaxy highly likely the host of GRB 110918A.

The non-detection of the Lyman forest above $\sim$4500 Å implies a strong upper limit of $z < 2.7$. Therefore, using our knowledge of the strength of spectral features in GRB environments and their distribution (de Ugarte Postigo et al. 2012), we can estimate the likelihood of the GRB having occurred between redshift 1.0 and 2.7 and yet not having detectable absorption lines at the redshift of the host in its spectrum. We calculated the detection limits for Mg II and C IV doublets as described by de Ugarte Postigo et al. (2012) and found that the lines would have to be weaker than 99.7% of a normal long GRB sample to have happened at a redshift between 1 and 2.7. Furthermore, the properties of the absorber (strong Mg II absorption and vigorous star formation, see Sect. 4.3.1), are very common in other afterglow observations and do not indicate a different physical nature. Combining the arguments presented above, we consider the redshift of the GRB and, accordingly, the physical association between the GRB and the host GRB galaxy, robust.

4.4.2 Host Environment in the Context of the GRB-Host Population

The mass-metallicity relation of field galaxies (e.g., Tremonti et al. 2004) has been studied in depth to high redshift (Savaglio et al. 2005; Erb et al. 2006; Yabe et al. 2012).
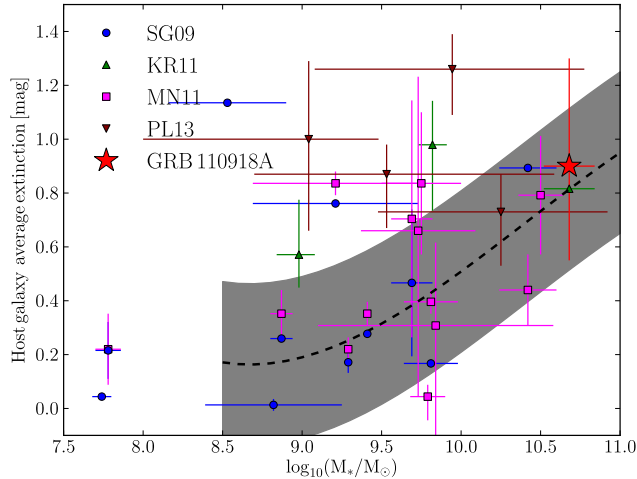
Figure 4.4 Average line-of-sight extinction of the host galaxy vs. the stellar mass. Values from SG09 and MN11 have been converted from $E(B-V)^{\text{gas}}$ to $E(B-V)^{\text{stars}}$ using the relation from Calzetti et al. (2000). The dotted-black line is the polynomial fit determined by Garn & Best (2010), and the grey region denotes the uncertainty of 0.3 dex.

Similarly, the dust content of a given galaxy is also well known to correlate with stellar mass (e.g., Garn & Best 2010; Zahid et al. 2013). To illustrate the behaviour for GRB hosts, we show the average host galaxy extinction versus the stellar mass of the host galaxy alongside the correlation determined by Garn & Best (2010) in Fig. 4.4. The GRB hosts are taken from Savaglio et al. (2009, SG09), Mannucci et al. (2011, MN11), Krühler et al. (2011a, KR11), and Perley et al. (2013, PL13) and converted to a Chabrier IMF, if need be. The correlation of Garn & Best (2010) has been determined from SDSS galaxies with $z < 0.7$, and so we limited our GRB sample to galaxies with $z < 1.0$. GRB hosts follow the distribution obtained from field galaxies well, with a possible excess of dusty systems at stellar masses of $10^{9-10}\,M_\odot$. Given the inherent systematic difficulties of determining the dust reddening in galaxies and the heterogeneous selection of targets (in particular, the KR11 and PL13 samples were initially selected to contain a lot of dust), this trend should not be over-interpreted. What seems clear is that the host of GRB 110918A is at the high end of the distribution of stellar masses for GRB hosts and there is no strong discrepancy between GRB-selected galaxies and field galaxies in the relation between their dust content and stellar mass.

Secondly, we plot the host's stellar mass vs. the GRB's line-of-sight extinction in Fig. 4.5. Perley et al. (2013) have highlighted that throughout the covered galaxy-mass scale there is a very tight correlation between stellar-mass and sight-line extinction probed by the GRBs. Quite surprisingly, this correlation between afterglow dust and

galaxy mass is found to be stronger than for any other physical property of the galaxy (PL13). From Fig. 4.5 it can be seen that hosts selected due to high afterglow extinction (green, KR11; brown PL13) have systematically more massive and dust-extinguished sight lines than the optically selected hosts (blue, SG09). Outliers to this trend, such as GRB 061222A or GRB 100621A, have already been noted (e.g., Krühler et al. 2011a; Perley et al. 2009). They were within blue, low-mass galaxies that were locally strongly extinguished along the line of sight. GRB 110918A is the first example of a dust-poor line-of-sight with a galaxy mass at the high-end of the distribution (i.e., $\log_{10}\left(\frac{M_*}{M_\odot}\right) >$ 10.5). While in principle, cases like GRB 110918A would be easy to identify (bright afterglow, easy localisation, bright host), no comparable example has been reported in the literature to date.

The host of GRB 110918A shows host-integrated extinction ($A_V^{\mathrm{stars}} = 0.90\,\mathrm{mag}$) that is similar to galaxies of a similar mass range (e.g., $M_* > 10^{10}\,\mathrm{M_\odot}$ in Fig. 4.4 and $M_* > 4 \times 10^9\,\mathrm{M_\odot}$ in Fig. 15 of Perley et al. (2013) have an $A_V^{\mathrm{stars}} \gtrsim 1.0\,\mathrm{mag}$). However, in comparison to the systems of similar mass, GRB 110918A exhibits at least ten times less extinction along the GRB line-of-sight. Therefore, it is possible that: (i) the geometry of dust within the host of GRB110918A is more patchy than homogeneous in comparison to the rest of the massive GRB host population, in agreement with the example of GRB 100621A and 061222A, whereby clumpy dust was one explanation for having a highly extinguished afterglow within an unobscured galaxy (Krühler et al. 2011a; Perley et al. 2013), or (ii) the progenitor had enough time to destroy local dust from its UV emission (see Perley et al. 2013 and references therein).

4.4.3 Fundamental Metallicity Relation

The difference between galaxies of long GRBs and that of normal star forming field galaxies is an ongoing debate. We have derived estimates for the mass, metallicity, and SFR of the host of GRB 110918A, which facilitates comparing this galaxy with respect to normal star forming galaxies through the fundamental metallicity relation (FMR; Mannucci et al. 2011). The plane of the FMR was derived from star forming SDSS galaxies in the mass range $9.2 < \log_{10}\left(\frac{M_*}{M_\odot}\right) < 11.4$ and is described by

$$12 + \log(O/H) = 8.90 + 0.47 \times (\mu_{0.32} - 10), \qquad (4.1)$$

where $\mu_{0.32} = \log_{10}\left(M_*/M_\odot\right) - 0.32 \times \log\left(\mathrm{SFR/M_\odot yr^{-1}}\right)$. Using the SED-determined mass and the H_α-determined SFR, the metallicity from the FMR is $12 + \log(O/H) = 8.98 \pm 0.08$, in agreement with the metallicity from the N II/H_α line ratio of $12 + \log(O/H) = 8.93 \pm 0.13$. The method used in our metallicity estimate is the same as the one used by MN11 to construct the FMR in order to ensure a direct comparison. The estimated errors are based purely on the uncertainties of the mass and SFR, and any systematic uncertainties from the method used to fit the stellar mass have been ignored.

The agreement in the characteristic properties of the host galaxy of GRB 110918A with the FMR (see Fig. 4.6) shows that the host galaxy has no deficit of metals in
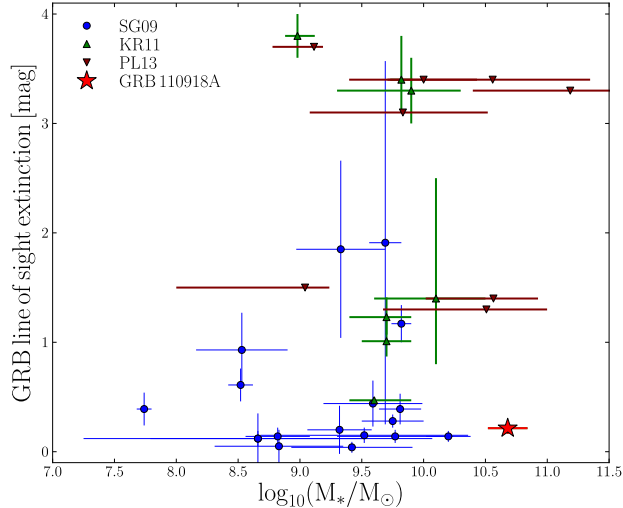
Figure 4.5 GRB line-of-sight A_V^{GRB} plotted against the stellar mass of the host galaxy. The extinction values have been obtained from Kann et al. (2006), Kann et al. (2010), Greiner et al. (2011a), Schady et al. (2012), and Perley et al. (2013).

comparison to normal field galaxies, which is in line with the conclusions of SG09, MN11, KR11, and Michałowski et al. (2012). This illustrates that the mass and SFR of a GRB-selected galaxy, at least for this one event, can be used as a fair proxy for the metallicity, even in the solar or super-solar regime.

4.4.4 Metallicity and Long GRB Progenitors

Many authors have attributed the fact that most long GRB host galaxies exhibit low metallicities as the result of an environmental preference, rather than the effect of the FMR (e.g., Modjaz et al. 2008; Graham & Fruchter 2012; Perley et al. 2013). This dependence on metallicity has also led to the prediction that the lower the progenitor metallicity, the larger the angular momentum and thus the higher the energy output ($E_{\gamma,\mathrm{iso}}$) of the GRB (MacFadyen & Woosley 1999). Initial studies indeed showed an anti-correlation between these two quantities (Stanek et al. 2006), together with a cut-off metallicity above which long GRBs (for $z < 0.2$) are no longer created, i.e., $Z < 0.15\,Z_\odot$. However, more recent studies, which include long GRBs at cosmological redshifts and exclude sub-luminous GRBs (Wolf & Podsiadlowski 2007; Levesque et al. 2010d), indicate that there is no clear anti-correlation between metallicity and the GRB's energy output, as shown in Fig. 4.7. The prompt emission of GRB 110918A yielded an energy output of $E_{\gamma,\mathrm{iso}} = 1.9 \times 10^{54}$ erg (Frederiks & Pal'shin 2011) within the top 2% of the GRB population (Amati et al. 2008, Frederiks et al. 2013). This
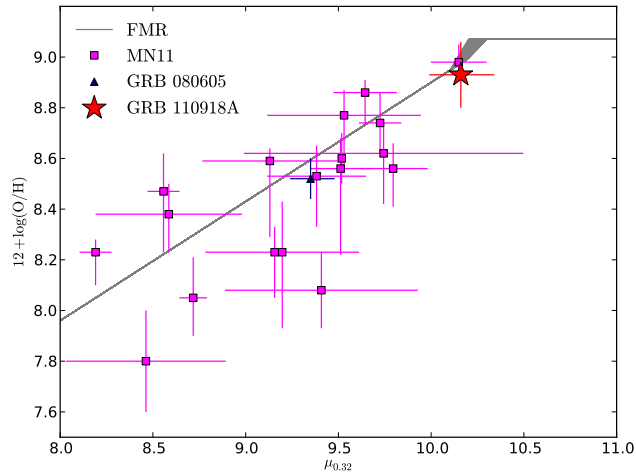
Figure 4.6 Metallicity determined from the fundamental metallicity relation (taken from MN11) vs. the parametric quantity $\mu_{0.32}$, plotted in grey for a range of SFRs (SFR $= 0 - 100\,\mathrm{M_\odot yr^{-1}}$). Real quantities are plotted for MN11 (magenta squares), GRB 080605 (Krühler et al. 2012a, cyan upward-pointing triangle), and GRB 110918A (red). The host of GRB 110918A is well described by the SDSS-determined FMR.
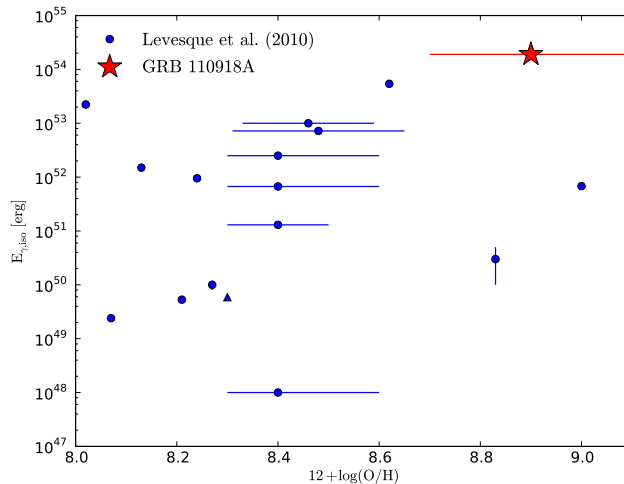
Figure 4.7 Isotropic-equivalent energy release in γ-rays of GRBs plotted against the gas-phase metallicity of the host galaxy. Blue data are taken from Levesque et al. (2010d).

makes GRB 110918A one of the most energetic long GRBs yet observed and its host one of the most metal-rich galaxies, in contradiction to the idea of a correlation between $E_{\gamma,\text{iso}}$ and metallicity.

Recently, Perley et al. (2013) performed an extensive photometric study of host galaxies selected from a sample of dark bursts, limiting the selection biases present in previous works. However, while the inclusion of dark GRB hosts increases the consistency of GRB hosts with the star formation weighted sample of field galaxies, there is still a clear lack of high-mass galaxies at $z \lesssim 1.5$. Associating the galaxy mass with metallicity, this provides indirect evidence for a metallicity effect in GRB hosts. A similar conclusion was reached based on a comparison of long GRB hosts with supernovae hosts (Graham & Fruchter 2012), namely, that long GRB hosts show a strong preference for lower metallicity environments relative to other populations of star forming galaxies, with a metallicity cut-off of $Z < 0.5\,Z_\odot$. This cut-off is not consistent with the host galaxy of GRB 110918A, even if metallicity dispersions of $\sim 0.3\,\text{dex}$ are considered (Niino 2011).

4.5 Conclusion

We observed the afterglow of GRB 110918A and its associated host galaxy and obtained photometry and spectroscopy of both. The extensive follow-up campaign has allowed us to measure the afterglow sight-line extinction, along with the attenuation of the galaxy's stellar and gas-phase component. We further derive the host's integrated

SFR, stellar mass, and gas-phase metallicity. In summary, this burst has revealed the following properties with respect to the long GRB population:

1. The SED-determined stellar mass of $\log_{10}(M_*/\mathrm{M}_\odot) = 10.68 \pm 0.16$ makes the host of GRB 110918A one of the most massive galaxies selected by a GRB at $z \sim 1$.

2. GRB 110918A is the first relatively unobscured afterglow ($A_V^{\mathrm{GRB}} = 0.16\,\mathrm{mag}$) that has been detected in a very massive host galaxy, suggesting either that the geometry of dust is more clumpy than homogeneous or that local dust has been destroyed by the progenitor.

3. The optical/NIR spectrum reveals a solar metallicity environment ($0.9 - 1.7\,\mathrm{Z}_\odot$, depending on the chosen diagnostic), making it one of the most metal-rich long GRB host galaxies found yet.

4. Using the fundamental metallicity relation and the measured SFR, stellar mass, and metallicity, we show that the host of GRB 110918A is no different from star-forming galaxies selected through their own stellar light.

5. The large energy output from the γ-ray emission of GRB 110918A and the large metallicity content of the host galaxy are in strong contradiction with the existence of an anti-correlation between energy output of the GRB and environmental metallicity.

6. Finally, the solar abundance of metals contradicts a cut-off for host galaxies of $Z < 0.5\,\mathrm{Z}_\odot$, even if a chemical dispersion of $\sim 0.3\,\mathrm{dex}$ existed.

4.A The Afterglow Light Curve

The afterglow of GRB 110918A was imaged for over 40 days after the trigger with GROND in the $g'r'i'z'JHK_S$ bands (outlined in Sect. 4.2.2). Using the deep observations of the host, the underlying contribution from the host galaxy was subtracted implementing the High Order Transform of PSF and Template Subtraction package, HOTPANTS[12] `v5.1.10b`. The resulting afterglow light curve can be seen in Fig. 4.8, while the raw data can be found in Tables 4.4 and 4.5 and the host subtracted data in Tables 4.6 and 4.7. The standard stars used in $g'r'i'z'$ for relative calibration can be found in Table 4.3.

4.B The Afterglow's Sight-Line Spectrum

The spectra obtained with GMOS and OSIRIS (see Sect. 4.2.6) reveal many absorption lines of gas along the line-of-sight toward the afterglow, specifically of the following

---

[12]`http://www.astro.washington.edu/users/becker/hotpants.html`

Table 4.3 Optical reference stars.

R.A.	Dec.	g'	r'	i'	z'
(J2000)	(J2000)	mag$_{AB}$	mag$_{AB}$	mag$_{AB}$	mag$_{AB}$
02:10:16.65	-27:06:22.7	19.85 ± 0.03	19.64 ± 0.03	19.53 ± 0.04	19.54 ± 0.04
02:10:11.56	-27:04:53.9	20.28 ± 0.03	19.86 ± 0.03	19.72 ± 0.04	19.72 ± 0.05
02:10:13.25	-27:07:04.0	19.82 ± 0.03	19.48 ± 0.03	19.30 ± 0.03	19.27 ± 0.04
02:10:12.62	-27:08:12.2	20.83 ± 0.04	19.37 ± 0.03	17.96 ± 0.03	17.27 ± 0.03

Table 4.4 GROND photometric data $g'r'i'z'$.

$T_{mid} - T_0$	Exposure	g'	r'	i'	z'
s	s	mag$_{AB}$	mag$_{AB}$	mag$_{AB}$	mag$_{AB}$
193892	691	20.43 ± 0.04	20.15 ± 0.02	19.92 ± 0.04	19.80 ± 0.07
194311	1526	20.39 ± 0.04	20.16 ± 0.03	19.93 ± 0.03	19.73 ± 0.08
194724	699	20.42 ± 0.03	20.18 ± 0.02	19.92 ± 0.04	19.80 ± 0.06
204203	683	20.48 ± 0.03	20.25 ± 0.02	20.05 ± 0.03	19.87 ± 0.06
204615	1508	20.48 ± 0.03	20.25 ± 0.02	20.02 ± 0.03	19.84 ± 0.06
205025	689	20.51 ± 0.03	20.28 ± 0.02	20.02 ± 0.03	19.89 ± 0.06
214526	693	20.56 ± 0.03	20.33 ± 0.02	20.09 ± 0.04	19.98 ± 0.06
215017	1674	20.56 ± 0.04	20.33 ± 0.02	20.11 ± 0.03	19.90 ± 0.07
215504	700	20.56 ± 0.05	20.32 ± 0.03	20.12 ± 0.04	19.91 ± 0.07
290361	691	21.09 ± 0.02	20.81 ± 0.02	20.66 ± 0.03	20.40 ± 0.06
290775	1519	21.11 ± 0.03	20.88 ± 0.03	20.65 ± 0.04	20.44 ± 0.06
291188	693	21.09 ± 0.03	20.83 ± 0.02	20.62 ± 0.03	20.44 ± 0.05
381456	1727	21.60 ± 0.02	21.30 ± 0.02	21.06 ± 0.03	20.96 ± 0.05
553350	1732	22.19 ± 0.04	21.96 ± 0.03	21.59 ± 0.06	21.30 ± 0.07
725709	1727	22.62 ± 0.05	22.46 ± 0.05	22.02 ± 0.09	21.54 ± 0.10
981853	3455	22.89 ± 0.06	22.76 ± 0.07	22.02 ± 0.09	21.60 ± 0.09
1507300	5327	23.09 ± 0.07	22.84 ± 0.08	22.05 ± 0.07	21.75 ± 0.09

Notes. All magnitudes have been corrected for Galactic foreground reddening. No correction has been made to subtract the flux contribution from the underlying host galaxy.

Table 4.5 GROND photometric data JHK_s.

$T_{mid} - T_0$	Exposure	J	H	K_s
s	s	$\mathrm{mag_{AB}}$	$\mathrm{mag_{AB}}$	$\mathrm{mag_{AB}}$
126393	82	18.93 ± 0.08	18.76 ± 0.08	....
194337	1579	19.40 ± 0.09	19.18 ± 0.12	18.84 ± 0.15
204643	1560	19.50 ± 0.08	19.19 ± 0.12	18.90 ± 0.16
215045	1726	19.58 ± 0.10	19.35 ± 0.12	18.84 ± 0.15
290803	1571	19.78 ± 0.09	19.64 ± 0.12	18.90 ± 0.16
381482	1773	20.21 ± 0.10	19.73 ± 0.16	19.03 ± 0.16
553375	1779	20.53 ± 0.14	20.17 ± 0.17	19.25 ± 0.19
725734	1774	20.82 ± 0.16	20.43 ± 0.21	19.64 ± 0.19
981879	3455	21.08 ± 0.15	20.59 ± 0.18	19.56 ± 0.28
1507330	5379	20.77 ± 0.12	20.65 ± 0.16	19.50 ± 0.27

Notes. All magnitudes have been corrected for Galactic foreground reddening. No correction has been made to subtract the flux contribution from the underlying host galaxy.

Table 4.6 GROND host-subtracted photometric data $g'r'i'z'$.

$T_{mid} - T_0$	Exposure	g'	r'	i'	z'
193892	691	20.48 ± 0.04	20.14 ± 0.02	19.93 ± 0.02	19.87 ± 0.03
194724	699	20.52 ± 0.03	20.08 ± 0.03	19.93 ± 0.03	19.86 ± 0.04
204203	683	20.46 ± 0.04	20.16 ± 0.02	20.02 ± 0.02	19.88 ± 0.05
205025	689	20.51 ± 0.04	20.26 ± 0.02	20.03 ± 0.03	19.91 ± 0.04
214527	693	20.65 ± 0.03	20.28 ± 0.02	20.13 ± 0.03	20.05 ± 0.03
215504	700	20.63 ± 0.04	20.30 ± 0.02	20.18 ± 0.03	20.14 ± 0.04
290776	1519	20.99 ± 0.04	20.70 ± 0.03	20.52 ± 0.03	20.43 ± 0.04
381457	1727	21.67 ± 0.03	21.31 ± 0.02	21.14 ± 0.03	21.05 ± 0.04
553350	1732	22.43 ± 0.04	22.04 ± 0.03	21.89 ± 0.04	21.75 ± 0.05
725709	1727	23.09 ± 0.05	22.65 ± 0.04	22.53 ± 0.06	22.51 ± 0.06
981853	3455	23.78 ± 0.06	23.30 ± 0.06	23.31 ± 0.10	23.03 ± 0.28
1507300	5327	> 24.80	> 24.15	> 22.84	> 22.01

Notes. All magnitudes have been corrected for Galactic foreground reddening.

Table 4.7 GROND host subtracted photometric data JHK_s.

$T_{mid} - T_0$	Exposure	J	H	K_s
s	s	mag$_{AB}$	mag$_{AB}$	mag$_{AB}$
126444	393	18.74 ± 0.05	18.47 ± 0.07	....
193921	745	19.42 ± 0.06	19.04 ± 0.05	....
194338	790	....	....	18.92 ± 0.08
194751	752	19.54 ± 0.06	19.25 ± 0.06	....
204231	736	19.35 ± 0.06	19.39 ± 0.06	....
204643	780	....	....	19.05 ± 0.07
205052	742	19.48 ± 0.06	19.29 ± 0.06	....
214555	746	19.59 ± 0.06	19.45 ± 0.08	....
215045	863	....	....	19.17 ± 0.07
215531	753	19.49 ± 0.06	19.30 ± 0.06	....
290803	1571	20.12 ± 0.08	19.80 ± 0.07	> 18.93
381482	1773	20.67 ± 0.10	20.22 ± 0.08	> 19.34
553375	1779	> 20.48	> 20.91	> 18.44
725734	1774	> 20.71	> 20.55	> 18.91
981879	3455	> 20.80	> 20.80	> 18.44
1507329	5379	> 20.77	> 20.49	> 19.09

Notes. All magnitudes have been corrected for Galactic foreground reddening.
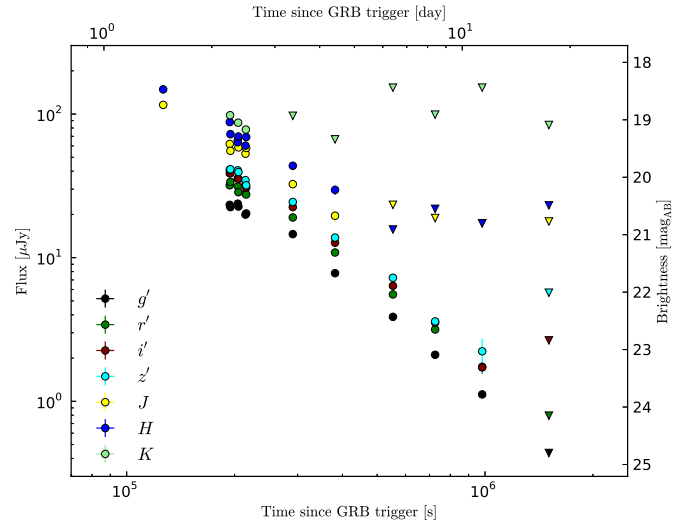
Figure 4.8 Afterglow light curve of GRB 110918A obtained with the 7-channel imager GROND (host subtracted).

species: Fe II (2344,2374,2382,2586,2600), Mg II (2803,2796), Mg I (2853), and Ca II (3935,3970). The equivalent widths of the metals are listed in Table 4.8.

4.C   The Host's Emission Lines

Two spectra of the host galaxy were obtained with OSIRIS and X-shooter (see Sect. 4.3.3), showing the following emission lines: Hα and Hβ transitions from the Balmer series and also forbidden transitions of [O II] and [N II] (only [O II] emission was detected with OSIRIS, and so for consistency only the X-shooter emission lines are shown). All of the 2D spectral images and 1D Gaussian fits can be seen in Fig 4.9.

91
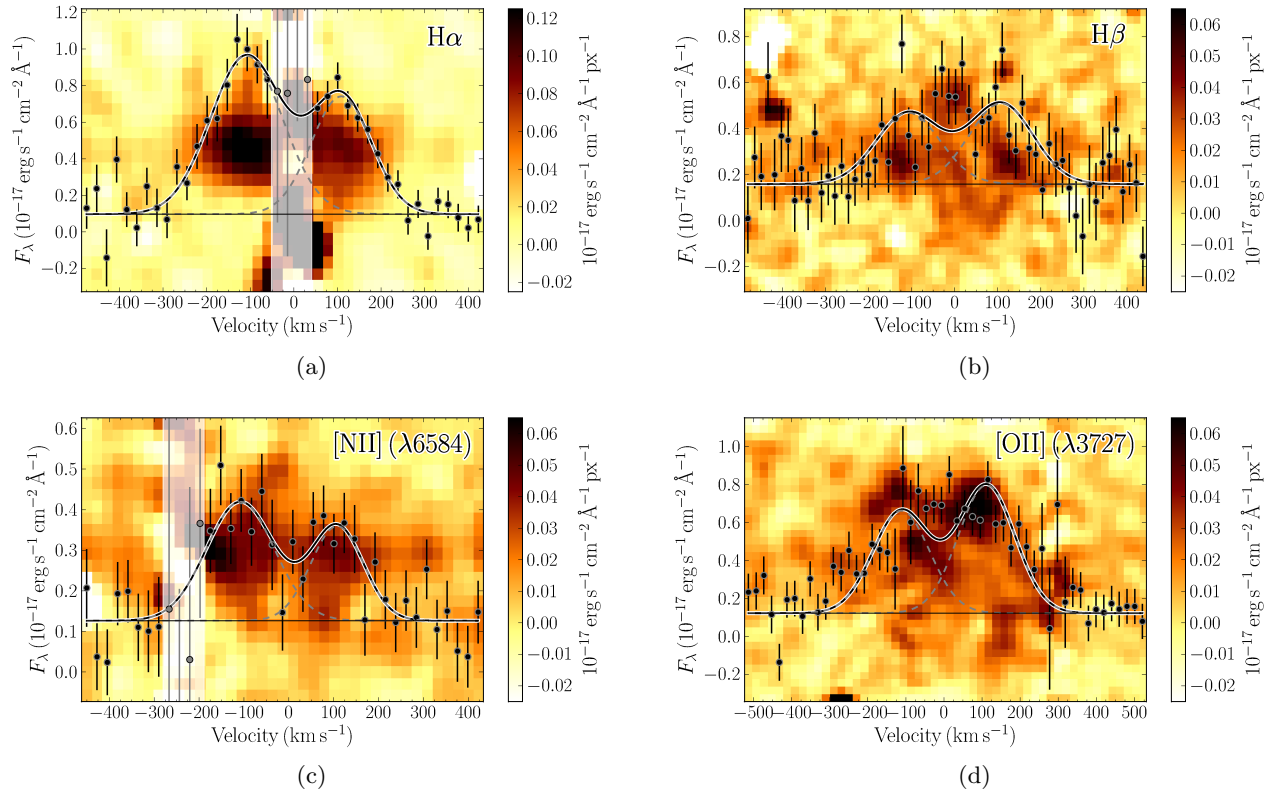
Figure 4.9 2D spectra of the host of GRB 110918A depicting four different emissions ([N II], [O II], Hα, Hβ). Overplotted is our Gaussian fit, where areas that overlay telluric lines are shown in white and excluded from the fit. All the values presented are raw values and do not include slit-loss or extinction corrections. Each image has been smoothed in both pixel directions for presentation purposes. **(a)**: The Balmer series transition Hα. **(b)**: The Balmer series transition Hβ. **(c)**: The forbidden transition [N II]. **(d)**: The forbidden transition [O II].

Table 4.8 Equivalent widths measured for the absorption lines of the afterglow.

λ_{obs}	Feature	Contaminants	$\mathrm{EW_{obs}}$	$\mathrm{EW_{rest}}$	z
Å					
4650.4	Fe II2344.2	Fe II*2345.0	4.3 ± 0.4	2.2 ± 0.2	0.9838
4713.4	Fe II2374.5†	....	....	....	0.9850
4720.5	....	Fe II*2381.5	8.4 ± 0.6	4.2 ± 0.3	....
4727.2	Fe II2382.8†	....	....	....	0.9389
5132.7	Fe II2586.7	Mn II2594.5	3.7 ± 0.4	1.9 ± 0.2	0.9843
5157.7	Fe II2600.2	Mn II2696.7, Fe II*2586.7	6.3 ± 0.5	3.2 ± 0.2	0.9836
5547.3	Mg II2796.4†	....	....	....	0.9837
5540.8	....	....	11.9 ± 0.4	6.0 ± 0.2	....
5560.1	Mg II2803.5†	....	....	....	0.9833
5660.2	Mg I2853.0	....	4.3 ± 0.4	2.2 ± 0.2	0.9840
7806.1	Ca II3934.8	....	4.0 ± 0.5	2.0 ± 0.2	0.9839
7877.6	Ca II3969.6	....	3.3 ± 0.6	1.7 ± 0.3	0.9845

Notes. Redshift was determined for those lines with no contaminants. † Blended lines.

Chapter 5

The long γ-ray burst rate and the correlation with host galaxy properties[1]

ABSTRACT

To answer questions on the start and duration of the epoch of reionisation, periods of galaxy mergers and properties of other cosmological encounters, the cosmic star formation history, $\dot{\rho}_*$ or CSFH, is of fundamental importance. Using the association of long-duration gamma-ray bursts (LGRBs) with the death of massive stars and their ultra-luminous nature ($> 10^{52}\mathrm{erg\,s^{-1}}$), the cosmic star formation history can be probed to higher redshifts than current conventional methods. Unfortunately, no consensus has been reached on the manner in which the LGRBs rate, $\dot{\rho}_{grb}$ or LGRBR, traces the CSFH, leaving many of the questions mentioned mostly unexplored by this method. Observations by the gamma-ray burst near-infrared detector (GROND) over the past 4 years have, for the first time, acquired highly complete LGRB sample. Driven by these completeness levels and new evidence of LGRBs also occurring in more massive and metal rich galaxies than previously thought, the possible biases of the $\dot{\rho}_{grb}$-$\dot{\rho}_*$ connection are investigated over a large range of galaxy properties. The cosmic star formation history is modelled using empirical fits to the galaxy mass function and galaxy star formation rates. Biasing the CSFH by means of metallicity cuts, mass range boundaries, and other unknown redshift dependencies of the form $\dot{\rho}_{grb} \propto \dot{\rho}_*(1 + z)^{\delta}$, a $\dot{\rho}_{grb}$ is generated and compared to the highly complete GROND LGRB sample. It is found that there is no strong preference for a metallicity cut or fixed galaxy mass boundaries and that there are no unknown redshift effects ($\delta = 0$), in contrast to previous work which suggest values of $Z/\mathrm{Z}_\odot \sim 0.1 - 0.3$. From the best-fit models obtained, we predict that $\sim 1.2\%$ of the LGRB burst sample exists above $z = 6$. The linear relationship between $\dot{\rho}_{grb}$ and $\dot{\rho}_*$ suggested by our results implies that redshift biases present in previous

---

LGRB samples significantly affect the inferred dependencies of LGRBs on their host galaxy properties. Such biases can lead to, for example, an interpretation of metallicity limitations and evolving LGRB luminosity functions.

5.1 Introduction

Long-duration gamma-ray bursts (LGRBs) are among the most luminous and energetic events to occur in our Universe. First signalled by their prompt high energy emission (observer frame γ-rays; e.g., Narayan et al. 1992), pinpointing regions of star formation irrespective of host galaxy luminosity, they are then followed by a longer wavelength and longer lasting afterglow (X-ray through to radio; e.g, Cavallo & Rees 1978; Goodman 1986; Paczynski 1986; Mészáros 2002) from which precise positions, redshifts and host galaxy abundance measurements can be obtained. Such high luminosities allow LGRBs to be detected to high redshifts making them powerful probes of the early Universe. As early as 1993, they were thought to have been the result of the core-collapse of a massive star, under the mechanism named the *collapsar model* (Woosley 1993; Paczynski 1998; MacFadyen & Woosley 1999). Given strong evidence of an association of a LGRB to a supernova (SN) in 1998, (Galama et al. 1998, SN1998bw) and first conclusive spectroscopic confirmation of SN2003dh associated with GRB 030329 (Stanek et al. 2003; Matheson et al. 2003), the connection of most LGRBs with the core-collapse of massive stars is now unquestionable (for a review, see e.g., Woosley & Bloom 2006).

As a result of the collapsar model's connection to the death of massive stars and the small distances that the progenitors travel away from their birth location in their relatively short lives, LGRBs can be used to trace the star formation rate of their host environment. Combined with the fact that LGRBs have been spectroscopically confirmed to be a cosmological phenomena (see e.g., Metzger et al. 1997b), they could be used to trace the cosmic star formation history (CSFH; $\dot{\rho}_*$). The advantage of using LGRBs rather than conventional methods based on Lyman-break galaxies (LBGs) and Lyman-α emitters (LAEs) (e.g., Rafelski et al. 2011), is that their immense luminosities allow them to be detected up to very high redshifts, e.g., z = 6.7 (Greiner et al. 2009a), 8.2 (Tanvir et al. 2009) and 9.2 (Cucchiara et al. 2011). Therefore, the CSFH-LGRB rate (LGRBR) connection has been investigated from as early as 1997 (see e.g., Totani 1997; Wijers et al. 1998).

Knowing the CSFH to such high redshifts is of fundamental importance for studying galaxy evolution. The current picture of the CSFH (see e.g., Madau et al. 1996; Hopkins & Beacom 2006; Li 2008; Kistler et al. 2009) is that there is a steady increase of star formation from $z = 0$ to $z = 1$ followed by a plateau up to redshift $z \sim 4$. However, the shape of the CSFH above $z = 4$ remains highly uncertain, where it could continue to plateau (Kistler et al. 2009), drop off (Li 2008) or even increase (Daigne et al. 2006).

The achievement of constraining the CSFH to high redshifts would allow many questions about the Universe to be answered, with one of the most sought after being: "when did reionisation occur?". The reionisation of the Universe is the period when

the first objects radiated enough energy to ionise the neutral hydrogen and from recent experimental observations, based on the SDSS and WMAP, is believed to lie in the redshifts range $\sim 6 - 15$ (e.g., Shin et al. 2008; Becker et al. 2001; Page et al. 2007b). However, it is currently not clear what the predominant sources of UV radiation were that reionised the Universe. A few examples of the possible ionising sources are supernovae (e.g., Johnson & Khochfar 2011), population III stars (e.g., Ciardi et al. 2003), quasars (e.g., Ricotti & Ostriker 2004), X-ray binaries (e.g., Power et al. 2009) and stars (e.g., Srbinovsky & Wyithe 2007). To study such questions at high redshift an understanding of the relationship between the CSFH and LGRBR would be incredibly valuable. However one obstacle that plagues the CSFH-LGRB rate connection is whether or not LGRBs are biased tracers of star formation. The question of biasing was first introduced because core-collapse models could not generate a LGRB without the progenitor system having low-metallicity ($\approx 0.3\,Z_\odot$; e.g., Hirschi et al. 2005; Yoon & Langer 2005; Woosley & Heger 2006). Also, it was noticed that the LGRBR was flatter at higher redshifts than the CSFH and that LGRBs were typically found in low-mass, low-metallicity galaxies (see e.g., Le Floc'h et al. 2003; Savaglio et al. 2009; Svensson et al. 2010; Mannucci et al. 2011). The difference in the LGRBR and CSFH, suggested in previous papers, can be understood if cosmic metallicity thresholds, evolving LGRB luminosity distributions (e.g., the progenitor evolves with redshift; Virgili et al. 2011), evolving stellar initial mass functions (Wang & Dai 2011) or sample selection effects (see e.g., Coward et al. 2008; Lu et al. 2012) are included.

A significant hindrance of the analysis of the CSFH-LGRBR connection is the number of LGRBs with no redshift measurement, i.e., redshift incompleteness. For a redshift to be measured, high precision localisations ($\sim 0.5''$) are required for follow-up spectroscopy. Since the advent of the *Swift* satellite (Gehrels et al. 2004), a survey telescope equipped with a GRB alert telescope (BAT), an X-ray telescope (XRT) and a ultraviolet/optical telescope (UVOT), there have been over 600 GRB detections in the past 7 years. The combination of large sky coverage of the BAT and the (near-) instantaneous follow-up with the XRT and UVOT, high precision localisations have been achievable, which were not as common in the preceding era. Accompanying this, the number of robotic ground-based follow-up telescopes has increased, allowing GRBs to be seen minutes and even seconds (Page et al. 2009) after they trigger the BAT. However, despite such efforts it has only been possible to obtain redshifts for $\sim 30\%$ of GRBs in comparison to the high success (84%) of X-ray detections[2].

Such a low redshift completeness is the result of: large uncertainties in the GRB localisations, weather, the GRB does not fit the redshift follow-up program criteria and GRB sky location, to name but a few. This biasing can become so complex, that it is not always so simple to remove from the sample considered, but none the less has been tried before (e.g., Coward et al. 2008). Consequently, many groups have been trying to improve the completeness levels of their statistics. One such instrument has been set to this task, the gamma-ray burst optical near-infrared (NIR) detector (GROND; Greiner

---

[2]Taken from the *Swift* GRB tables; `http://heasarc.nasa.gov/docs/swift/archive/grb_table/stats/`

et al. 2008a). This multi-channel imager mounted at the 2.2m MPG/ESO telescope at La Silla (Chile) has operated for the past 4 years as an automated GRB afterglow follow-up instrument. The robotic nature of GROND has allowed it to significantly increase the afterglow detection rate ($\sim 98\%$) for all LGRBs observed within 4 hours of the trigger. Due to the reduced attenuation from gas and dust at observer frame NIR wavelengths, GROND's multi-band capabilities in combination with its rapid-response allows photometric redshifts to be determined when spectroscopic observations were not possible or fruitless (i.e., redshift desert, low signal-to-noise). This has facilitated, for the first time, highly complete GRB redshift samples.

Only recently have highly complete samples been used to show that GRBs that exhibit no afterglow are primarily the result of these GRBs originating in a galaxy of high extinction (Greiner et al. 2011a). These *dark bursts* (see also Fynbo et al. 2009a; Cenko et al. 2009; Perley et al. 2009) are usually not included in GRB host follow-up programs due to poor localisations. New evidence has shown that GRBs with heavily dust-extinguished afterglows exist in systematically more massive galaxies (Krühler et al. 2011a), thus originally biasing our opinion on host galaxies. Furthermore, it has been seen before that not all GRB host galaxies fit the picture of low-mass, low-metallicity (see e.g., Levesque et al. 2010c; Hashimoto et al. 2010; Savaglio et al. 2012) and that some can occur in extremely dust extinguished galaxies (Levan et al. 2006; Berger et al. 2007; Hashimoto et al. 2010; Hunt et al. 2011, Rossi et al. 11), which are also usually associated with large metallicities.

In this work we investigate, simultaneously, the effect of mass ranges and metallicity cuts placed on the CSFH and its effects on the CSFH-LGRBR connection with the recently available and highly redshift-complete sample of Greiner et al. (2011a). The paper is outlined as follows. The CSFH and LGRBR models are explained in Sect. 5.2. The description of individual LGRBs and their properties are discussed in Sect. 5.3. The implementation of the model with the data is presented in Sect. 5.4. The LGRB host property results and differences to other studies are discussed in Sect. 5.5. In Sect. 5.6 we discuss the caveats of our approach and make predictions on the LGRB distribution and CSFH at high redshifts, and summarise our conclusions in Sect. 5.7. A ΛCDM cosmology has been assumed throughout this paper ($\Omega_\Lambda = 0.7$, $\Omega_M = 0.3$, $H_0 = 73.0 \, \mathrm{km \, s^{-1} \, Mpc^{-1}}$).

5.2 Cosmic Star Formation History & LGRB Rate Models

The aim of this work is to compare LGRB number densities generated by models, that vary with regards to their host galaxy characteristics, to an observed LGRB number density. To do this, the CSFH is converted to a LGRBR utilising a conversion factor, η_{grb} (i.e., from the stars in a given galaxy how many will produce a LGRB that is then observed by a given instrument). The number density is then calculated by numerical integration. The whole process is outlined in the next section and is divided in the following way:

A. **CSFH Model**

1. The CSFH is formulated from empirically constrained models of galaxy star formation rates (Sect. 5.2.1) and galaxy mass functions (Sect. 5.2.2).

2. Restrictions are implemented in the CSFH model (Sect. 5.2.5) on such things as: galaxy mass ranges (Sect. 5.2.2), galaxy metallicities (Sect. 5.2.3) and red-dead galaxies (Sect. 5.2.4).

B. **LGRBR Model**

1. An initial mass function for stars is chosen (Sect. 5.2.6), which will be used for η_{grb}.

2. A LGRB luminosity function is chosen to model the samples that will be investigated and implemented in η_{grb} (Sect. 5.2.7).

3. The LGRB number density is calculated using numerical integration and the conversion factor η_{grb} (Sect. 5.2.8).

5.2.1 Star Formation Rate

During a galaxy's evolution, its gas supply will go through two distinct phases named the *source* and *sink*. The source phase is the inflow (accretion) of cold gas due to the halo's potential well, and the sink phase is the consumption/loss of gas by production of stars and outflows. These two processes occur constantly during the evolution of a galaxy with different weighting, e.g., at redshift 2 it is still possible to have cold accretion on to massive galaxies (see e.g., Khochfar & Silk 2009b). However, it has been shown via simulations that galaxies will reach a steady state between these two phases (Bouche et al. 2010) and that the SFR can be considered to be solely dependent on the inflow of cold gas. It is this process that is believed to result in the SFR "sequence", i.e., the relationship between the star formation rate and stellar mass, M_*, of a galaxy. This sequence is seen to obey the following relationship (Bouche et al. 2010):

$$SFR\left(M_*, z\right) = 150\left(M_*/10^{11}M_\odot\right)^{0.8}\left(\frac{1+z}{3.2}\right)^{2.7}\mathrm{M_\odot yr^{-1}}. \tag{5.1}$$

The main drawbacks of this formulation are that it is only fit up to redshifts of $z = 2$ (for a model that can account for high redshift observations of the SFR stellar mass relation, see Khochfar & Silk 2011) and that it is built from average stellar masses. This results in a spread of $\sim 0.3\,\mathrm{dex}$. The final model is compared to data in Sect. 5.2.5.

5.2.2 Galaxy Mass Function

The galaxy mass distribution function (GMF) is commonly described by a Schechter function (Schechter 1976). However, as galaxies evolve they accrete more gas and create more stars, thus modifying the number density of galaxies at a given mass for a specific

Table 5.1 Galaxy mass function parameters taken from Fontana et al. (2006).

M_0^*	M_1^*	M_2^*	α_0^*
11.16	0.17±0.05	-0.07± 0.01	-1.18

α_1^*	ϕ_0^*	ϕ_1^*
-0.082±0.033	0.0035	-2.20±0.18

redshift (e.g., Khochfar & Silk 2009a). Therefore, a redshift evolving GMF, as measured from the GOODS-MUSIC field (Fontana et al. 2006), is used in this paper (similarly to Young & Fryer 2007; Belczynski et al. 2010):

$$\phi\left(\mathcal{M}, z\right) = \phi^*\left(z\right) \ln\left(10\right) \left[10^{\mathcal{M}-M^*(z)}\right]^{1+\alpha^*(z)} e^{-10^{\mathcal{M}-M^*(z)}}, \tag{5.2}$$

where $\mathcal{M} = \log_{10}\left(M_*/M_\odot\right)$, M_* is the stellar mass of the galaxy and the parametric functions obey:

$$\phi^*\left(z\right) = \phi_0^*\left(1 + z\right)^{\phi_1^*}$$
$$\alpha^*\left(z\right) = \alpha_0^* + \alpha_1^* z$$
$$M^*\left(z\right) = M_0^* + M_1^* z + M_2^* z^2$$

The parameter values are given in Table 5.1. Given that the above GMF is modelled on flux limited surveys, we note that methods have been used to calculate missing galaxies by mass-to-light ratios. Secondly, the empirical fits are also only applicable for redshifts, $z < 4$. See Fontana et al. (2006) for full details on the galaxy selection and GMF fitting.

5.2.3   Mass-Metallicity Relation

As galaxies evolve and stars form, they pollute the galaxy with metals through stellar winds, supernovae and other forms of feedback and therefore can mediate the inflow and collapse of gas. A mass-redshift dependent metallicity empirically fit relation, ϵ, is assumed throughout this paper, taken from Savaglio et al. (2005), of the form[3]:

$$\epsilon\left[\text{O/H}\right] = \epsilon\left(M_*, t_H\right) = -7.5903 + 2.5315 \log M_*$$
$$-0.09649 \log^2 M_* + 5.1733 \log t_H$$
$$-0.3944 \log^2 t_H - 0.0403 \log t_H \log M_* \tag{5.3}$$

where M_* is the stellar mass and t_H the Hubble time measured in 10^9 years. The relation is taken to be true over the redshift range we investigate (up to $z \approx 12$), but has been noted that it is difficult to reconcile for $z > 3.5$ (Maiolino et al. 2008)

---

[3]The conversions $\epsilon\left[O/H\right] + 12 = \epsilon\left[Z/Z_\odot\right] + 8.69$, (Savaglio 2006) and $t_H = \frac{(1+z)^{-1.5}}{1.4\sqrt{\Omega_\Lambda}H_0}$ are used throughout this paper.

5.2.4   Galaxy Downsizing

Massive galaxies in the redshift regime of $z \sim 1 - 3$ have been seen to have little (passively evolving) or no (dead) star formation (Cimatti et al. 2004; Labbé et al. 2005; Daddi et al. 2005; Kong et al. 2006). Observationally, more massive galaxies are seen to cease star formation first and this has been coined downsizing. The mechanism to explain this process is believed to be caused by the quenching of star formation by active galactic nuclei (AGN; e.g., Croton et al. 2006), galaxy mergers (e.g. Springel 2005), temperature thresholds (e.g., Dekel & Birnboim 2006) or gravitational heating (e.g., Khochfar & Ostriker 2008), but the relative importance is still unclear. It is possible to experimentally constrain the quenching stellar mass, M_Q, above which no star formation is occurring. This is also seen to evolve strongly with redshift in the following manner (Bundy et al. 2006):

$$M_Q(z) = M_Q^0 (1 + z)^{3.5}, \tag{5.4}$$

where M_Q^0 is the local ($z \sim 0$) quenching mass. A value of $\log_{10}\left(M_Q^0/M_\odot\right) = 10.9 \pm 0.1$ (Villar et al. 2011) is assumed throughout.

5.2.5   Cosmic Star Formation History

Given the previous models, it is possible to model the cosmic star formation history. This is simply the integration of the individual galaxy SFRs over the GMF. As our aim was to also investigate varying characteristics of galaxies that contribute to the CSFH, we include the following free parameters: metallicity upper limit, ϵ_L, and stellar mass upper and lower limits, M_1, M_2. This results in a CSFH of the form,

$$
\begin{aligned}
\dot{\rho} &= \int_{M_1}^{M_2} \zeta(z)\,\gamma(M_*, z, \epsilon_L)\, SFR(M_*, z)\, \phi(M_*, z)\, \mathrm{d}M_* \\
&= \dot{\rho}(z, \epsilon_L, M_1, M_2) \tag{5.5}
\end{aligned}
$$

where the metallicity and downsizing constrains γ and ζ respectively, are defined by the following relations:

$$\gamma(M_*, z, \epsilon_L) = \begin{cases} 1 & \text{if } \epsilon(M_*, z) < \epsilon_L \\ 0 & \text{if } \epsilon(M_*, z) \geq \epsilon_L \end{cases} \tag{5.6}$$

$$\zeta(z) = \begin{cases} 1 & \text{if } M_Q(z) > M_* \\ 0 & \text{if } M_Q(z) \leq M_* \end{cases} \tag{5.7}$$

The form of the above two step-functions (Eqns. 5.6 and 5.7) could be different. For example, Wolf & Podsiadlowski (2007) implemented a metallicity cut-off of not only step-functions, but power laws and broken power laws. Their results show that they cannot currently discriminate between the form the metallicity cut can take. Secondly, it has been seen observationally that the quenching mass is not a single cut-off but a
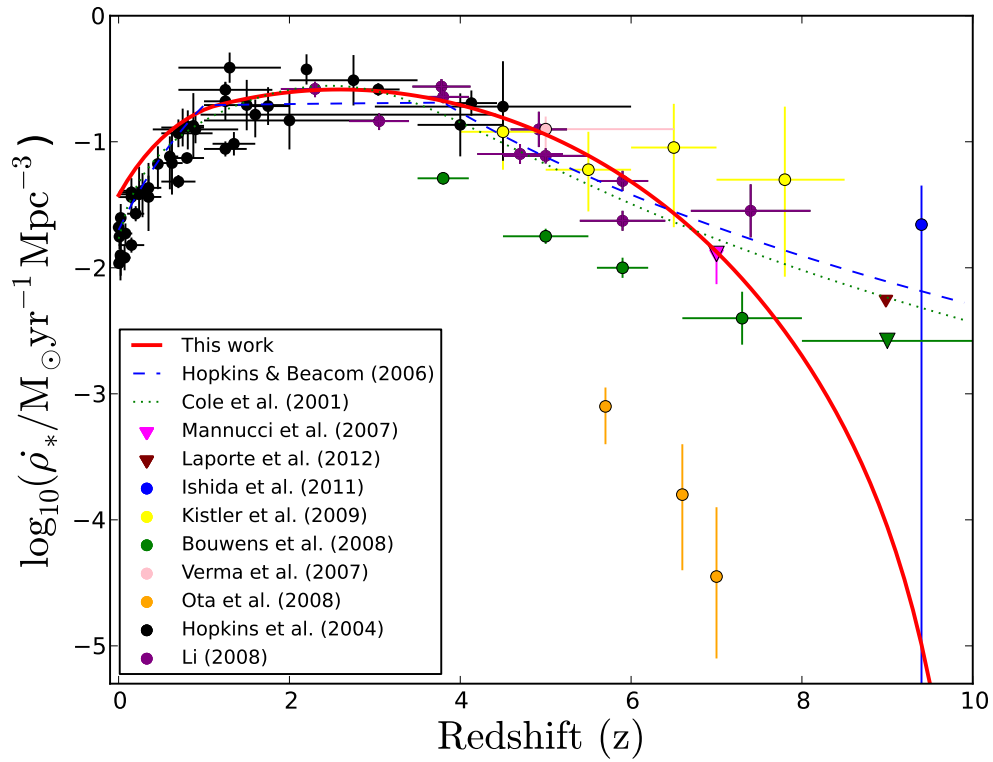
Figure 5.1 The cosmic star formation history given by the model in Eqn. 5.5 using no metallicity limit (i.e., no ϵ_{L}) and $(\mathcal{M}_1\mathcal{M}_2) = (7, 12)$ (bold-red line), and two empirical fits (green-dotted and blue-dashed lines). The data are denoted in the legend.

smooth function of mass (e.g., Kong et al. 2006), however, the knowledge of this trend is also not well known. Therefore, for simplicity both are chosen to be implemented as step-functions.

The numerically integrated model, presented in Fig. 5.1, is compared to data from Hopkins (2004) and Li (2008), and to two empirical fits from Hopkins & Beacom (2006) and Cole et al. (2001). The behaviour of the three curves is similar, peaking between redshift 2 and 3 and becoming negligible above redshift 7. A goodness of fit of our model to the data yields a $\chi^2/\text{d.o.f.} = 36/50$. There is a small overproduction of stars at low redshift in comparison to the data, which can be lowered by reducing the quenching mass, M_Q^0. However, there is a range of possible quenching masses that could be used and still give a good fit to the experimental data. As a result, it was opted to use the local quenching mass given by Villar et al. (2011). It is noted that this parameter could also have been left free in our analysis, however, simulations we ran using no quenching mass gave the same results that are outlined in Sect. 5.5.

The important difference between the approach used in this paper to others is that the form of the model in Eqn. 5.5 allows freedom for the mass and metallicity of the contributing host galaxies. Also, as we are interested in the low-redshift range ($z < 3$), we can remove the freedom of the parameters of the individual models incorporated (e.g., Eqn. 5.1.).

5.2.6   Initial Mass Function

Previously, it was mentioned that different types of initial mass functions (IMFs) have been used to explain the current LGRBR-CSFH connection. Currently there is no consensus on the correct IMF to be used: Salpeter (Salpeter 1955), Scalo (Scalo 1986), Kroupa (Kroupa 2001) or Chabrier (Chabrier 2003), and is still a lively debated issue (see Bastian et al. 2010). A commonly chosen IMF is the Salpeter IMF and is used throughout this work:

$$\psi(m) = m^{-\alpha}, \tag{5.8}$$

where m is the star mass and $\alpha = 2.35$. We note that the collapsar model requires the formation of a black hole and this only applies to the high end mass of stars ($> 30\text{M}_\odot$). The main difference between possible IMFs is at the low-mass end, and therefore any IMF chosen would have been viable as long as it was redshift independent. We do not consider an evolving IMF (top heavy; see e.g., Davé 2008; Weidner et al. 2011), but similar studies have been done utilising this type (e.g., Wang & Dai 2011).

5.2.7   GRB Luminosity Function

The LGRB luminosity function (LF) can take on many forms, for example: Schechter functions, broken power-laws, log-normal functions and normal functions (Gaussian function). Throughout this paper a normal function has been used (see e.g., Bastian et al. 2010; Belczynski et al. 2010) of the form:

Table 5.2 GRB Luminosity Function best-fit parameters.

Sample	$\log_{10}\left(L_{\mathrm{c}}/\mathrm{erg\,s}^{-1}\right)$	σ_L	n_*	$\chi^2/\mathrm{d.o.f.}$
S	51.33	0.97	10.89	0.63/4
P	51.74	0.93	13.19	5.56/5
UL1	51.06	0.87	23.48	0.52/3
UL2	51.11	0.92	22.95	0.39/3

$$\phi\left(L\right) = n_* e^{(L-L_{\mathrm{c}})/2\sigma_L^2}, \tag{5.9}$$

where $L = \log\left(L_{iso}/\mathrm{erg\,s}^{-1}\right)$. One of the fits to our data can be seen in Fig. 5.2, and the best-fits for all the samples considered (see Sect. 5.3) can be found in Table 5.2. The total fraction of LGRBs seen by a specific instrument, then takes the form:

$$f\left(z\right) = \frac{\int_{L_{\mathrm{limit}(z)}}^{\infty} \phi\left(L\right)\mathrm{d}L}{\int_{-\infty}^{\infty} \phi\left(L\right)\mathrm{d}L}. \tag{5.10}$$

The luminosity limit, $L_{\mathrm{limit}(z)}$, of the sample can be calculated using the luminosity distance, D_L, of the form $L_{\mathrm{limit}} = 4\pi D_L^2 F_{\mathrm{limit}}$. By taking F_{limit} to be the lowest luminosity of the sample (see Sect. 5.3), results in the following flux limit: $F_{\mathrm{limit}} = 1.08 \cdot 10^{-8}\,\mathrm{erg\,s}^{-1}\,\mathrm{cm}^{-2}$. This flux limit is essentially the limiting flux of the BAT on board the *Swift* satellite.

It is also possible that the LGRB LF is a function of redshift. A redshift dependence would imply that there is a change in the LGRB explosion mechanism throughout redshift or that the progenitor mass distribution, or mode (single, binary), is changing. This has been investigated previously by Salvaterra & Chincarini (2007) and Campisi et al. (2010) who both come to the conclusion that a non-evolving LF is possible, but requires a metallicity cut to reproduce the observed LGRB distribution (for metallicity cuts see Sect. 5.4). On the contrary to this, Butler et al. (2010) rule out an evolving luminosity function to the 5σ level using *Swift* data. To increase the simplicity of the modelling, we assumed that the mechanism was redshift independent and that the progenitor was of a constant type. For a discussion on implications of these assumptions, see Sect. 5.6.3.

5.2.8   Long Gamma-Ray Burst Rate

Given the CSFH model formulated in the previous section, we now consider which population of galaxies contribute to the observed LGRBR. To do this, six parameters have to be considered; (i) the co-moving volume; (ii) the instruments limiting flux, that affects how many LGRBs of a given luminosity can actually be detected; (iii) a LGRB probability, that transforms the number of stars being formed to the number of LGRBs being produced; (iv) proportionality relation of the CSFH-LGRB rate, to

include any further dependencies unaccounted for in our model; (v) the fraction of the sky observable by the instrument; (vi) and the length of time the instrument has been running. The total detectable LGRB rate for a given instrument in a redshift bin (z_1, z_2) is then simply:

$$N(z_1, z_2) = \eta_{\mathrm{grb}} \int_{z_1}^{z_2} \frac{f(z)\,\dot{\rho}(z, \epsilon_L, M_1, M_2)\,(1+z)^{\delta}\,\frac{\mathrm{d}V}{\mathrm{d}z}}{(1+z)}\,\mathrm{d}z, \tag{5.11}$$

where $\frac{\mathrm{d}V}{\mathrm{d}z} = 4\pi D_{\mathrm{com}}^2(z)\,\frac{\mathrm{d}D_{\mathrm{com}}(z)}{\mathrm{d}z}$, D_{com} is the co-moving distance, η_{grb} is the probability of stars resulting in a LGRB and then detected by an instrument, and δ is the power of proportionality for the CSFH to LGRBR (see e.g., Bromm & Loeb 2006; Yoon et al. 2006; Daigne et al. 2006; Young & Fryer 2007; Wolf & Podsiadlowski 2007; Salvaterra & Chincarini 2007; Kistler et al. 2009; Campisi et al. 2010; Qin et al. 2010; Butler et al. 2010; Wanderman & Piran 2010; Belczynski et al. 2010; Virgili et al. 2011; de Souza et al. 2011; Wang & Dai 2011; Ishida et al. 2011). The LGRB probability can be parameterised as (explained similarly in Bromm & Loeb 2006):

$$\eta_{\mathrm{grb}} = \Delta T\,\Delta\Omega\,\eta_{\mathrm{coll}}\,\eta_{\mathrm{BH}}\,\eta_{\mathrm{time}}\,\eta_{\mathrm{X-ray}}\,\eta_{\mathrm{redshift}}\,\eta_{\mathrm{other}}, \tag{5.12}$$

where ΔT is the length of observations, $\Delta\Omega$ is the solid angle of the observable sky and the remaining parameters are discussed in the following paragraphs.

As mentioned, LGRBs are likely associated with black holes produced by the collapse of stars above a specific progenitor mass, M_{BH}, and is quantified in the following way:

$$\eta_{\mathrm{BH}} = \frac{\int_{M_{\mathrm{BH}}}^{M_{\mathrm{max}}} \psi(m)\,\mathrm{d}m}{\int_{M_{\mathrm{min}}}^{M_{\mathrm{max}}} m\psi(m)\,\mathrm{d}m}, \tag{5.13}$$

where M_{min} and M_{max} are the minimum and maximum star masses considered in our model respectively. Secondly, GRBs are believed to be jets of collimated matter, as a result of breaks observed in afterglow light curves. This means that only a small fraction of bursts are visible to the observer, quantified by η_{coll}.

The last four probabilities, η_{time}, $\eta_{\mathrm{X-ray}}$, η_{redshift} and η_{unknown} are a result of our sample selection criteria, outlined in the next section. They are the probability of detecting an optical-NIR afterglow less than 4 hours after a GRB trigger, the probability of detecting an X-ray afterglow, the probability of detecting a redshift, and any unknown probabilities respectively.

Finally, the parameter δ includes further dependencies between the CSFH and LGRBR not accounted for by our model. This parameter is the same utilised in Kistler et al. (2009), where it is used to incorporate effects that are not known, i.e., a black-box approach. We employ the same idea, so that a non-zero δ would imply we are missing an effect in our CSFH modelling. One example is an evolving LGRB LF or an evolving stellar IMF. It is now possible to formulate a LGRB number density distribution for a redshift bin through the use of a modelled cosmic star formation history, which can then

be compared to an experimental data set. We would like to note that the empirically calibrated relations used in the model are only verified for redshifts $z < 4$, and could differ at higher redshifts. To investigate the implications of this on our final results, we manually modify the CSFH at redshifts $z > 3$ in Sect. 5.6.2.

5.3 Data Samples

5.3.1 Gamma-ray Burst Sample

Our LGRB sample is taken from Greiner et al. (2011a), which unlike previous studies, is highly complete in terms of optical/NIR afterglow detection rates and measured redshifts. Greiner et al. (2011a) chose the sample by selecting GRBs that have been detected by GROND within 4 hours after the *Swift* BAT trigger and that exhibited an X-ray afterglow. This selection results in a sample of 43 GRBs: 39 LGRBs and 4 short GRBs (believed to be associated with the merger of 2 neutron stars or a neutron star-black hole system; Belczynski et al. 2006). The 39 LGRB sample contains 31 spectroscopic redshifts, 6 photometric redshift measurements (3 of which are upper limits) and 2 with no optical/NIR afterglow detections and thus no redshift measurements. For more details on the burst sample and individual bursts, see Greiner et al. (2011a).

As mentioned previously, it is only LGRBs that are believed to trace the death of massive stars, and so the short-GRBs were not considered in our analysis. The LGRB sample was then subdivided into; spectroscopic **(S)**: bursts with spectroscopic redshift (31/39); photometric **(P)**: spectroscopic sample including photometric redshifts (34/39); upper limit 1 **(UL1)**: photometric sample including upper limit photometric redshifts (36/39); and upper limit 2 **(UL2)**: upper limit sample including a possible redshift measurement (37/39). This subdivision was introduced for two reasons. Firstly, to see if the results changed when having a single method (spectroscopic) of redshift identification compared to multiple types of redshift identification (spectroscopic and photometric). Secondly, the upper limits were included to get as close to a 100% redshift-detected-sample as possible. All the samples cover a range of $z = 0$ to $z = 6.7$, and the P, UL1 and UL2 samples cover $z = 0$ to $z = 9.2$. Any bias in the redshift distribution, i.e., possible deficits in the high redshift regime and effects of selecting bursts followed by GROND < 4 hours after the trigger, has been investigated by Greiner et al. (2011a). This was carried out by comparing the sample to one of twice the size (Fynbo et al. 2009a), with a completeness at the time of 50%, utilising a Kolmogorov-Smirnov test. This showed that the difference at high-z was statistically insignificant and at the 1σ level, both samples could be drawn from the same underlying distribution. For information on individual bursts see Table 5.3 and for the property-distributions see Figs. 5.2, 5.3 and 5.4.

5.3.2 LGRB Properties

For each burst the measurement of a redshift and luminosity is required for the modelling of the CSFH-LGRBR, which will be discussed in Sect. 5.2. Redshifts for
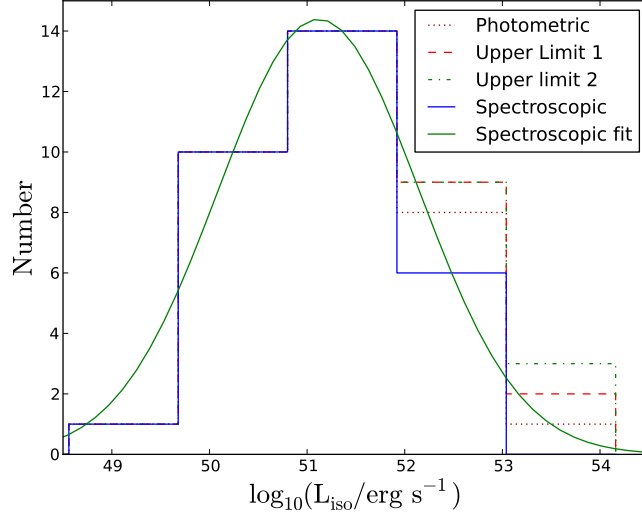
Figure 5.2 Number density of the luminosities for all of the subsamples considered. The bold line depicts an example best-fit normal-Gaussian to the spectroscopic sample. Bin sizes are chosen for presentation of the data.

Figure 5.3 Luminosity-redshift space of all the subsamples considered. The dashed line depicts the flux limit, found by fitting the spectroscopic distribution, $F_{\mathrm{limit}} = 1.08 \cdot 10^{-8}\,\mathrm{erg\,s^{-1}\,cm^{-2}}$ (see Sect. 5.2.7). Bin sizes are chosen for presentation of the data.
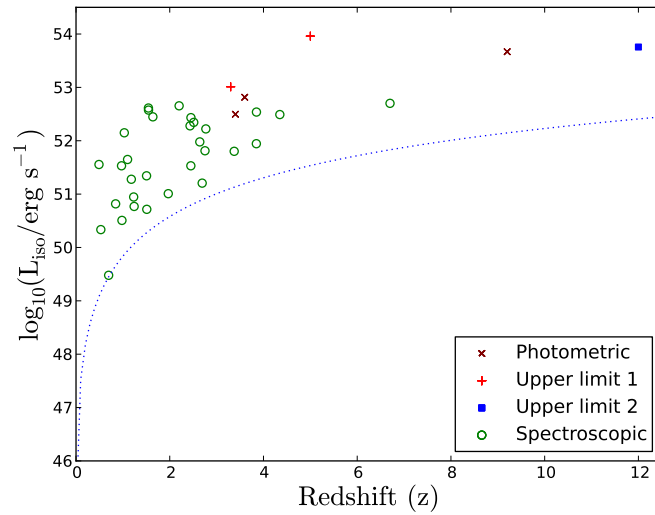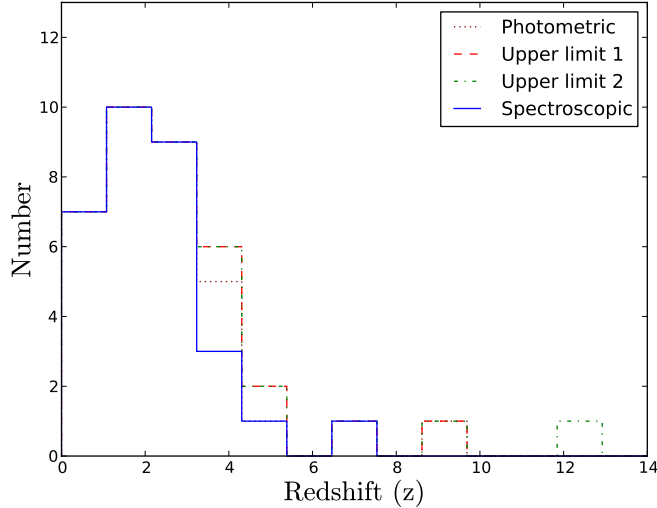
Figure 5.4 Number density of the redshifts for all of the subsamples considered. Bin sizes are chosen for presentation of the data.

all of the samples were obtained from the table compiled by Greiner et al. (2011a) and the luminosities were calculated from the isotropic energy (E_{iso}) and the duration of the burst over which 90% of the flux is released (T_{90}), using the standard relation of $L_{\text{iso}} = E_{\text{iso}} (1 + z) / T_{90}$ (Bloom et al. 2001). The E_{iso} and T_{90} for each burst was obtained from fits to the prompt emission taken from the extension of Butler et al. (2007, from here NB11)[4]. For bursts with photometric or upper limit redshifts an E_{iso} was calculated via the same procedure described in Bloom et al. (2001). One of the following energy spectra, $\phi(\text{E})$, was used based on the best-fit to the LGRB's BAT spectra:

$$
\phi(E) = \begin{cases} K_A \left(\frac{E}{A}\right)^{\alpha} & \text{Power Law (PL)} \\[3em] K_A \left(\frac{E}{A}\right)^{\alpha} e^{\frac{-E(2+\alpha)}{E_{\text{peak}}}} & \text{Cut-off Power Law (CPL)} \end{cases} , \qquad (5.14)
$$

(see e.g. Sakamoto et al. 2008) where K_A is the normalisation at $E = A\,\text{keV}$ in units of photons $\text{keV}^{-1}\,\text{cm}^{-2}\text{s}^{-1}$, E_{peak} is the peak energy in the cut-off power-law spectrum, i.e., in $E^2\phi(E)$ space, and α is the spectral slope. Utilising the best-fit model, the K-corrected E_{iso} is calculated via[5]:

---

[4]http://astro.berkeley.edu/~nat/swift/

[5]For BAT it is assumed $E_1 = 15\,\text{keV}$ and $E_2 = 150\,\text{keV}$, but we rescale similar to NB11 to the range of, $E_1 = 1\,\text{keV}$ to $E_2 = 10^4\,\text{keV}$

$$E_{\mathrm{iso}} = \Delta t \frac{4\pi D_L^2}{1+z} \int_{E_1/(1+z)}^{E_2/(1+z)} E\phi\left(E\right)\,\mathrm{d}E, \tag{5.15}$$

where D_L is the luminosity distance, z the redshift, and Δt the time over which the spectra is fit (a time-integrated spectra).

Table 5.3: The properties of the GROND Dark Burst samples.

Burst	z^a	$\log_{10}\left(\frac{E_{\mathrm{iso}}}{\mathrm{erg}}\right)$	T_{90}	Prompt Model^b				
				Name	α	E_{peak}	K_A	Δt
			(s)			(keV)	ph keV^{-1}cm^{-2}s^{-1}	(s)
100316B$^{\mathrm{S,P,UL1,UL2}}$	1.180 (1)	51.57	4.3	...	...	...	...	...
091127$^{\mathrm{S,P,UL1,UL2}}$	0.490 (2)	52.36	9.6	...	...	...	...	...
091029$^{\mathrm{S,P,UL1,UL2}}$	2.752 (3)	52.84	40.0	...	...	...	...	...
091018$^{\mathrm{S,P,UL1,UL2}}$	0.971 (4)	51.88	4.4	...	...	...	...	...
090926B$^{\mathrm{S,P,UL1,UL2}}$	1.24 (5)	52.52	126.4	...	...	...	...	...
090814A$^{\mathrm{S,P,UL1,UL2}}$	0.696 (6)	51.30	113.2	...	...	...	...	...
090812$^{\mathrm{S,P,UL1,UL2}}$	2.452 (7)	53.89	99.8	...	...	...	...	...
090519$^{\mathrm{S,P,UL1,UL2}}$	3.85 (8)	53.76	81.8	...	...	...	...	...
090313$^{\mathrm{S,P,UL1,UL2}}$	3.375 (9)	53.11	90.2	...	...	...	...	...
090102$^{\mathrm{S,P,UL1,UL2}}$	1.547 (10)	53.65	30.7	...	...	...	...	...
081222$^{\mathrm{S,P,UL1,UL2}}$	2.77 (11)	53.17	33.5	...	...	...	...	...
081121$^{\mathrm{S,P,UL1,UL2}}$	2.512 (12)	53.08	19.4	...	...	...	...	...
081029$^{\mathrm{S,P,UL1,UL2}}$	3.848 (13)	53.48	169.1	...	...	...	...	...
081008$^{\mathrm{S,P,UL1,UL2}}$	1.968 (14)	52.83	199.3	...	...	...	...	...
081007$^{\mathrm{S,P,UL1,UL2}}$	0.529 (15)	50.89	5.6	...	...	...	...	...
080913$^{\mathrm{S,P,UL1,UL2}}$	6.7 (16)	52.72	8.2	...	...	...	...	...
080805$^{\mathrm{S,P,UL1,UL2}}$	1.505 (17, 18)	52.99	111.8	...	...	...	...	...
080804$^{\mathrm{S,P,UL1,UL2}}$	2.20 (19, 18)	53.94	61.7	...	...	...	...	...
080710$^{\mathrm{S,P,UL1,UL2}}$	0.845 (20, 18)	52.69	139.1	...	...	...	...	...
080707$^{\mathrm{S,P,UL1,UL2}}$	1.23 (21, 18)	52.07	30.3	...	...	...	...	...
080605$^{\mathrm{S,P,UL1,UL2}}$	1.640 (22, 18)	53.31	19.6	...	...	...	...	...
080520$^{\mathrm{S,P,UL1,UL2}}$	1.545 (23, 18)	52.68	3.0	...	...	...	...	...
080413B$^{\mathrm{S,P,UL1,UL2}}$	1.1 (24, 18)	52.17	7.0	...	...	...	...	...
080413A$^{\mathrm{S,P,UL1,UL2}}$	2.433 (25, 18)	53.41	46.7	...	...	...	...	...

Table 5.3: The properties of the GROND Dark Burst samples.

Burst	z^a	$\log_{10}\left(\frac{E_{\text{iso}}}{\text{erg}}\right)$	T_{90}	Prompt Model[b]				
				Name	α	E_{peak}	K_A	Δt
			(s)			(keV)	ph keV^{-1}cm^{-2}s^{-1}	(s)
080411[S,P,UL1,UL2]	1.03 (26, 18)	53.60	58.3	...	...	...	...	...
080330[S,P,UL1,UL2]	1.51 (27)	52.13	66.1	...	...	...	...	...
080210[S,P,UL1,UL2]	2.641 (28, 18)	53.06	43.9	...	...	...	...	...
080129[S,P,UL1,UL2]	4.349 (29)	53.42	45.6	...	...	...	...	...
071031[S,P,UL1,UL2]	2.692 (30)	52.91	187.2	...	...	...	...	...
071010A[S,P,UL1,UL2]	0.98 (31)	51.56	22.4	...	...	...	...	...
070802[S,P,UL1,UL2]	2.45 (32)	52.16	14.7	...	...	...	...	...
090429B[P,UL1,UL2]	9.2 (33)	53.42	5.8	CPL	$-0.69^{+0.91}_{-0.76}$	$46.17^{+6.53}_{-10.72}$	0.059	7.55
081228[P,UL1,UL2]	3.4 (34)	52.43	3.8	PL	$-1.99^{+0.31}_{-0.35}$	...	0.028	4.44
080516[P,UL1,UL2]	3.6 (35)	52.98	6.8	PL	$-1.78^{+0.26}_{-0.28}$	...	0.039	7.83
091221[UL1,UL2]	$< 3.3^d$	54.21	69.0	PL	$-1.62^{+0.06}_{-0.06}$	...	0.043	101.31
090904B[UL1,UL2]	$< 5.0^d$	54.94	58.2	PL	$-1.58^{+0.08}_{-0.08}$	...	0.105	86.40
100205A[UL2]	12.0^e	54.2	32.76	PL	$-1.73^{+0.29}_{-0.31}$	...	0.008	41.40

Notes. [a] If not mentioned otherwise, the redshift is taken from Greiner et al. (2011a). [b] Both the prompt best-fit model and parameters are taken from NB11. They are only listed if the E_{iso} was calculated manually. [c] S: Spectroscopic, P: Photometric, UL1: Upper limit 1, UL2: Upper limit 2. [d] These upper limits are treated as being the actual redshift value. [e] Value taken from between $11 < z < 13.5$, (Cucchiara et al. 2010).

References. All references are taken from Greiner et al. (2011a, Table 2). (1) Vergani et al. (2010); (2) Cucchiara et al. (2009); (3) Chornock et al. (2009b); (4) Chen et al. (2009); (5) Fynbo et al. (2009b); (6) Jakobsson et al. (2009); (7) de Ugarte Postigo et al. (2009a); (8) Thoene et al. (2009); (9) Chornock et al. (2009a); de Ugarte Postigo et al. (2010); (10) de Ugarte Postigo et al. (2009b); (11) Cucchiara et al. (2008); (12) Berger & Rauch (2008); (13) D'Elia et al. (2008); (14)

D'Avanzo et al. (2008); (15) Berger et al. (2008); (16) Greiner et al. (2009b); (17) Jakobsson et al. (2008b); (18) (Fynbo et al. 2009a); (19) Thoene et al. (2008b); (20) Perley et al. (2008); (21) Fynbo et al. (2008a); (22) Jakobsson et al. (2008d); (23) Jakobsson et al. (2008a); (24) Vreeswijk et al. (2008); (25) Thoene et al. (2008c); (26) Thoene et al. (2008a); (27) Malesani et al. (2008); Guidorzi et al. (2009); (28) Jakobsson et al. (2008c); (29) Greiner et al. (2009b); (30) Ledoux et al. (2007); Fox et al. (2008); (31) Prochaska et al. (2007a); (32) Prochaska et al. (2007b); Elíasdóttir et al. (2009); (33) Tanvir (2010); (34) Afonso et al. (2008); Krühler et al. (2011b); (35) Filgas et al. (2008).

5.4 Methodology

We moved through a 3D parameter space, consisting of mass ranges, metallicity upper limits and proportionality relations (i.e., δ), in small step sizes and at each step compared the modelled LGRBR produced to our sample, using least χ^2 statistics to asses the goodness of fit. The parameter details and methodology used are explained in the next sections.

5.4.1 Fixed Parameters

The parameters ΔT, $\Delta \Omega$ and η_{grb} in Eqn. 5.11 were assumed to be independent of redshift and luminosity. The values used can be found in Table 5.4, but are discussed briefly in the following paragraphs.

The length of time of GROND observations (covered by our sample), $\Delta \mathrm{T}$, is 3.5 years (September 2007 - March 2010) and the solid angle of the BAT detector is $\Omega_{4\pi}^{Swift} = \frac{\Omega^{Swift}}{4\pi} = 0.11$ (Barthelmy et al. 2005). Therefore, for GROND, $\Omega_{4\pi}^{\mathrm{GROND}} = \Omega_{4\pi}^{\mathrm{La\,Silla}} \cdot \Omega_{4\pi}^{Swift} = 0.077$ (i.e., the probability that the LGRB is observable to GROND after it has been detected by *Swift*).

The LGRB probability, η_{GRB}, is related to η_{BH} and η_{coll}. For the first of these parameters, see Eqn. 5.13, we assume the mass above which a BH can form is taken to be $\mathrm{M_{BH}} \geq 30 \mathrm{M}_\odot$, over the possible mass range considered of $M_{\min} = 0.1 - M_{\max} = 100\,\mathrm{M}_\odot$ in a Salpeter IMF, following the prescription used in Yoon et al. (2006).

The final parameter to be fixed is the collimation factor, η_{coll}, being derived from the jet opening angle. The latter usually ranges between 1°-10° (Frail et al. 2001; Cenko et al. 2010) implying a collimation factor range of $1.5 \times 10^{-4} - 1.52 \times 10^{-2}$ (utilising $\eta_{\mathrm{coll}} = 1 - \cos \theta_{\mathrm{jet}}$; Frail et al. 2001). A median value of $\theta_{\mathrm{jet}} = 5°$, $\eta_{\mathrm{coll}} = 3.8 \times 10^{-3}$ is assumed throughout.

5.4.2 Investigated Parameters

There are four parameters which were varied simultaneously to investigate which combination of these best agree with the observed LGRB rate. The parameters were: galaxy mass lower and upper limits ($\mathcal{M}_1, \mathcal{M}_2$) respectively, metallicity upper limit (ϵ_L), the proportionality power (δ) and the missing GRB probability, η_{other}, all of which can be found in Eqn. 5.11. As before, the parameter ranges investigated can be found in Table 5.4 and are briefly explained below.

Approximately 80% of LGRB hosts are thought to lie within a mass range of $10^{9.4}\mathrm{M}_\odot$ to $10^{9.6}\mathrm{M}_\odot$ (Savaglio et al. 2009). To test this hypothesis, a mass range boundary can be applied to the CSFH. This is done by moving the values of M_1 and M_2 to a central value, by equal step sizes, i.e., $(\mathcal{M}_1, \mathcal{M}_2) = (7, 12)...(7 + \Delta\mathcal{M}, 12 - \Delta\mathcal{M})$. The initial boundaries are chosen to be close to the limits of that of the GOODS-Field survey and are the same as adopted by Belczynski et al. (2010). The step size is set to $\Delta\mathcal{M} = 0.05$.

The LGRB collapsar model requires a metallicity threshold to result in a LGRB. Also, LGRB host surveys show a similar preference for low-metallicity, as is indicated

Table 5.4 Summary of model parameters used in Eqn. 5.11.

Parameter	Value or Range	Step size	Fixed
η_{coll}	3.8×10^{-3}	...	y
η_{time}	0.14 (1)	...	y
η_{X-ray}	0.57 [a]	...	y
$\eta_{redshift}$	const.[b]	...	y
$\Delta\Omega$	0.077	...	y
ΔT	3.5	...	y
$M_{\mathrm{BH}}/\mathrm{M}_\odot$	30.0	...	y
$M_{\mathrm{min}}/\mathrm{M}_\odot$	0.1	...	y
$M_{\mathrm{max}}/\mathrm{M}_\odot$	100	...	y
$(\mathcal{M}_1, \mathcal{M}_2)$	$(7, 12)...(7 + \Delta\mathcal{M}, 12 - \Delta\mathcal{M})$	0.05	n
$\epsilon_{\mathrm{L}}/\mathrm{Z}_\odot$	0.1 - 1.8	0.05	n
δ	0 - 2.9	0.1	n
η_{other}	...	...	n

Notes. [a] Product of fraction of GRBs followed by XRT (2) and number of GRBs with an X-ray afterglow (3). [b] Calculated based on the sample used, i.e., sub-sample size / full-sample size.

References. (1) Greiner et al. (2011a); (2) `http://heasarc.nasa.gov/docs/swift/archive/grb_table/stats/`; (3) `http://www.mpe.mpg.de/~jcg/grbgen.html`

Table 5.5 Median metallicities and masses for different LGRB host galaxy programs.

Survey	Z	δ_Z^a	$\log_{10}(M_*/M_\odot)$	$\delta_\mathcal{M}^a$
	$(Z_\odot)$	dex		dex
Svensson et al. (2010)	0.54	0.65	9.12	1.84
Savaglio et al. (2005)	0.26	0.12	9.32	0.75
Mannucci et al. (2011)	0.61	0.30	9.33	0.64
Rau et al. (2010)[b]	0.13	0.62	...	...
Krühler et al. (2011a)	...	...	9.76	0.38

Notes. [a] Standard deviation. [b] Damped Lyman-α systems at $z \sim 2$.

in Table 5.5 where we give the median metallicities and masses of host galaxies from different surveys. Therefore, the metallicity upper limit, i.e., the galaxy metallicity below which the galaxy contributes to the CSFH, is set to range from $0.1 - 1.8\,Z_\odot$ (the latter value being the limit at which the cuts stop affecting the CSFH in the model considered for the mass range chosen) with a step size of $\Delta Z = 0.05\,Z_\odot$.

As mentioned previously, it is possible that there are other effects not considered by our model or one of the assumptions that we made may be inaccurate. This uncertainty is quantified by the parameter δ. This black-box approach was carried out by Kistler et al. (2009), who found a value of $\delta = 1.5$, which could be explained by metallicity cuts or an evolving luminosity function. As we have included metallicity effects and mass ranges, a positive value of δ would imply that (i) the LGRB LF is non-evolving, (ii) the stellar IMF is different to that considered in our model or (iii) the progenitor system is incorrect. To allow for a range of possibilities, δ is varied from 0 to 2.9 in steps of $\Delta\delta = 0.1$.

The final parameter we consider free is η_{other}, obtained from Eqn. 5.11. As a result of its unknown nature, it will be determined from the model fitting that is described in Sect. 5.4.3. Unlike the static parameters described in the Sect. 5.4.1, the parameters described in this section are redshift and mass dependent. Different combinations of these parameters can produce similar outcomes, i.e., a degeneracy and each parameter can have an effect on the other. For example, when the mass range is brought inwards, for each redshift, it will limit also the metallicities, as galaxies grow they will produce more metals. The only way to see which combination is preferred is to look for the best-fit to the data in a systematic approach. The effect of changing each parameter individually is depicted in Figs. 5.5, 5.6 and 5.7.

5.4.3 Modelling

The 3D parameter space is to be investigated in a brute-force approach, in the following steps:

1. The selected samples are first binned in log-luminosity space with a bin size of
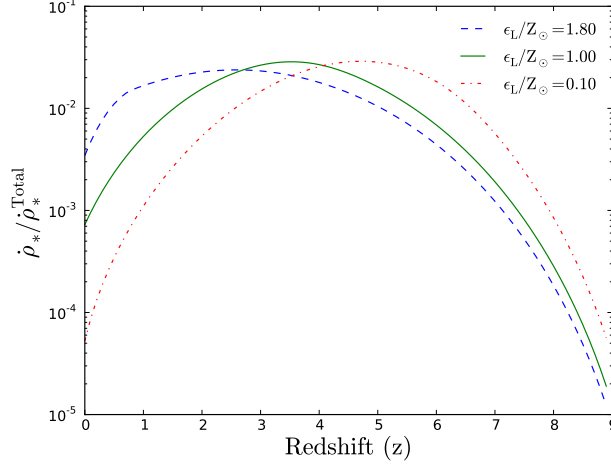
Figure 5.5 The resulting CSFH model when using different metallicity upper limits. Blue-dashed: $\epsilon_L = 1.8$, green-bold: $\epsilon_L = 1.0$ and red-dash-dotted: $\epsilon_L = 0.1$. Each curve utilises $(\mathcal{M}_1, \mathcal{M}_2) = (7, 12)$ and $\delta = 0$. The normalisation, $\dot{\rho}_*^{Total}$, is the integrated CSFH from redshift $z = 0 - \infty$.

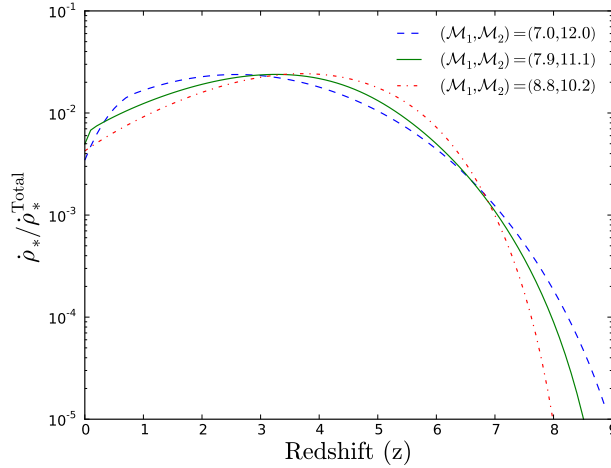Figure 5.6 The resulting CSFH model when using different mass ranges. Blue-dashed: $(\mathcal{M}_1, \mathcal{M}_2) = (7, 12)$, green-bold: $(\mathcal{M}_1, \mathcal{M}_2) = (7.9, 11.1)$, red-dash-dotted: $(\mathcal{M}_1, \mathcal{M}_2) = (8.8, 10.2)$. Each curve utilises $\epsilon_L = 1.8$ and $\delta = 0$. The normalisation, $\dot{\rho}_*^{Total}$, is the integrated CSFH from redshift $z = 0 - \infty$.
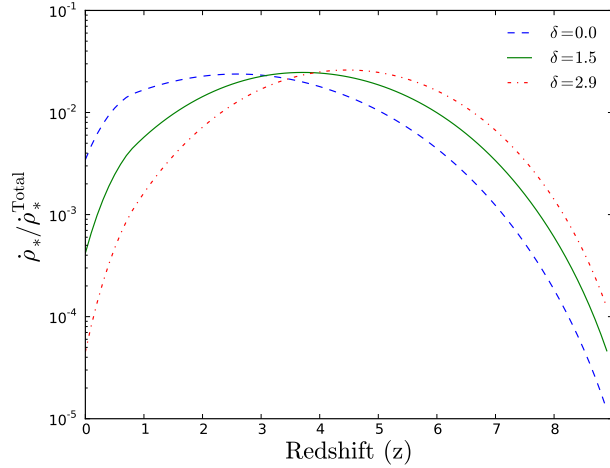
116

Figure 5.7 The resulting CSFH model when using different power dependences. Blue-dashed: $\delta = 0$, green-bold: $\delta = 1.5$, red-dash-dotted: $\delta = 2.9$. Each curve utilises $\epsilon_{\mathrm{L}} = 1.8$, $(\mathcal{M}_1, \mathcal{M}_2) = (7, 12)$. The normalisation, $\dot{\rho}_*^{Total}$, is the integrated CSFH from redshift $z = 0 - \infty$.

$\log\left(L/\mathrm{erg\,s}^{-1}\right) = 0.5$ for the spectroscopic and photometric samples, and 1.0 for the upper limit 1 and upper limit 2 samples (see e.g., Fig. 5.2).

2. A non-evolving LGRB LF (Eqn. 5.9) is then fit to the luminosity distribution (corresponding to each sample) using a least squares algorithm taken from the *SciPy*[6] library.

3. The chosen sample is then binned in redshift space (bin sizes; spectroscopic: 1.74, photometric: 1.87, upper limit 1: 1.6, upper limit 2: 2.0) where bin sizes are chosen to ensure a limited number of bins ($> 80\%$) have zero counts.

4. The LGRB number density model (Eqn. 5.11) is then calculated utilising a given (M_1, M_2), δ, ϵ_{L} and LGRB LF determined in step 2, using the same redshift bin sizes as in the previous step, i.e., $N(z_1, z_2)$.

5. η_{other} is calculated by taking the median value of the ratio of the binned data to the expected model data (a median is favoured as the high-z bins contain low counts and can dominate the slope of the best-fit).

6. The data is then compared to the model predictions using a least χ^2-test of the form, $\chi^2 = \sum \frac{(x_{\mathrm{expected}} - x_{\mathrm{observed}})^2}{\delta x_{\mathrm{observed}}}$. The count errors are assumed to be Poisson distributed.
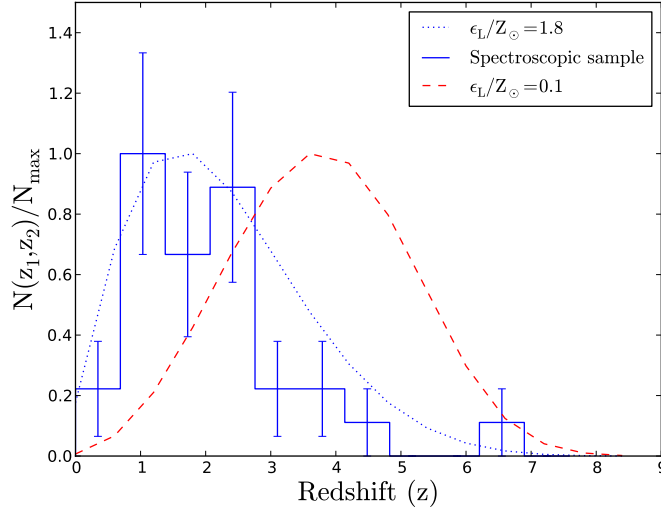
---

[6]http://www.scipy.org/

Figure 5.8 Examples of LGRBR models in comparison to the spectroscopic sample. The blue-solid line is spectroscopic sample, the blue-dashed is the model with input parameters $\delta = 0$, $\epsilon_L = 1.8$, $(\mathcal{M}_1, \mathcal{M}_2) = (7, 12)$ and the red-dashed line is the same but with a metallicity limit of $\epsilon_L = 0.1$. All three histograms are normalised to their peak value to highlight their main differences.

7. This is then repeated for all of the parameters in the 3 dimensional space described in Table 5.4.

An example of the binned data and the corresponding LGRB rate models for two metallicity constraints can be seen in Fig 5.8.

5.4.4   Summary of Assumptions

To summarise, the assumptions made throughout this section are:

- LGRBs produce an X-ray afterglow and are collimated.

- LGRBs are formed via the single progenitor collapsar model from stars above a mass of $30\,\mathrm{M}_\odot$.

- A Salpeter IMF between $0.1 - 100\,\mathrm{M}_\odot$, is assumed.

- LGRBs have a static normal (Gaussian) luminosity function.

- Galaxies obey a redshift-evolving mass function.

- Galaxies lie on the mass-metallicity relation.

118

- Downsizing is described by an evolving quenching mass (mass upper limit).

5.5 Results

Given the methodology outlined in Sect. 5.4, a LGRB number distribution was generated utilising a 3D parameter space consisting of metallicity limits, mass ranges and missing redshift effects. These models were then compared to the different samples described in Sect. 5.3.1, of varying completeness levels, and the best-fit results were determined using a least χ^2 test.

5.5.1 Parameter Spaces

The results of the fits can be seen in Figs. 5.9a, 5.9b, 5.10a and 5.10b. Each figure depicts the contour plot for metallicity vs mass of the best-fit values for $\delta = 0$ (upper panels). For all of the distributions investigated, the best-fit δ was zero and so only a single contour plot is displayed. For clarity to the reader, the best-fit χ^2 for all δ values considered is shown (see lower panels). All the best-fit values can be found in Table 5.6. The zero value of δ implies that there are no missing redshift effects in the modelling that has been used (this is discussed further in Sect. 5.6).

The four samples, S, P, UL1 and UL2 show a preference for a CSFH-LGRBR connection with no strong global metallicity restrictions. The S and P samples show that no mass range limitations for the host galaxies are preferred. The UL1 and UL2 samples show a preference for the metallicity limits $\epsilon_L = 1.7\,Z_\odot$ and $1.75\,Z_\odot$ and the mass ranges $(\mathcal{M}_1, \mathcal{M}_2) = (8.0, 11.0)$ and $(7.15, 11.85)$ respectively. These limits are very lax in comparison to the normal measured results of $\epsilon_L \leq 0.3\,Z_\odot$ (see e.g., Yoon et al. 2006; Salvaterra & Chincarini 2007; Campisi et al. 2010; Virgili et al. 2011) and the range of $(\mathcal{M}_1, \mathcal{M}_2) = (9.4, 9.6)$ (Savaglio et al. 2009), and are interpreted as no limit. The predominant difference in our best-fit model compared to previous studies in this area is a result of the differences in the peak of the redshift number distribution whereby previous samples usually peaked at $z \sim 4$, and required a metallicity cut-off (see Fig. 5.8). As we are comparing this to an experimental data set, the way in which a sample is selected is very important (this is discussed in more detail in the next section). We note that there is no acceptable fit to the S sample to the 1% level, but is included for completeness. Also, there are models present in the contour plot that are still acceptable fits at the 1% level for the following metallicity ranges and mass boundaries: $(\mathcal{M}_1, \mathcal{M}_2) = (7, 12) - (7.8, 11.2)$ and $\epsilon_L/Z_\odot = 1.65 - 1.8$, $(\mathcal{M}_1, \mathcal{M}_2) = (7.95, 11.05) - (8.05, 10.95)$ and $\epsilon_L/Z_\odot = 1.65 - 1.8$, $(\mathcal{M}_1, \mathcal{M}_2) = (7, 12) - (8.25, 10.75)$ and $\epsilon_L/Z_\odot = 1.45 - 1.8$, for the P, UL1 and UL2 samples respectively (1% acceptance boundaries are depicted as bold-black lines in Figs.5.9b, 5.10a and 5.10b).
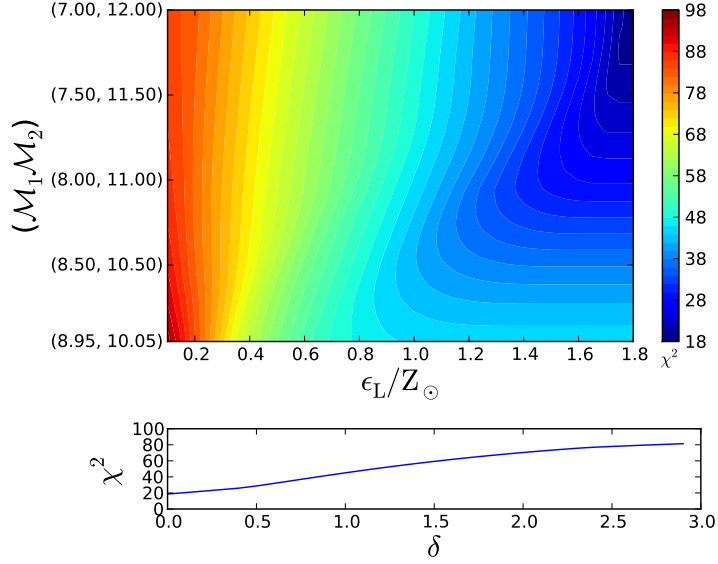
(a) Spectroscopic (S) Sample, d.o.f.= 3.
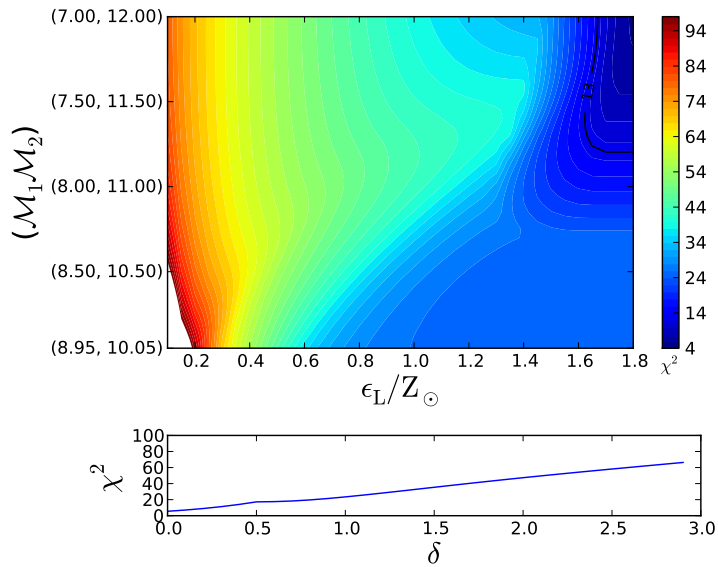
(b) Photometric (P) Sample, d.o.f.= 4.

Figure 5.9 The best-fit plots for each sample investigated. **Top Panels**: The χ^2 contour plot for $\delta = 0$, white areas denote χ^2 values much larger than the colour scale shown. Only the contour of $\delta = 0$ is displayed as the fits begin to get worse when δ starts to increase. The black lines denote the maximum χ^2 to be an acceptable fit to the 1% level. **Bottom Panels**: The χ^2 values for all of the best-fits in δ space, depicting the worst fits for progressively increasing δ.

120
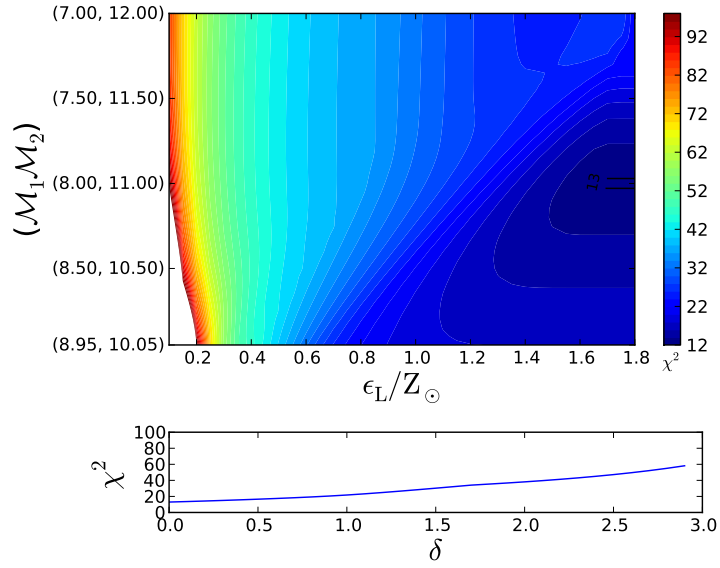
(a) Upper limit 1 (UL1) Sample, d.o.f.= 5.
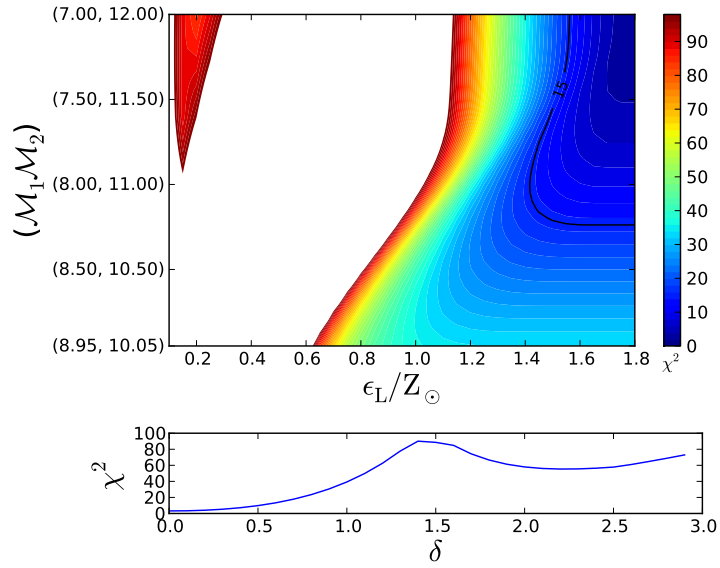
(b) Upper limit 2 (UL2) Sample, d.o.f.= 5.

Figure 5.10 Continuation of Fig. 5.9

Table 5.6 Best-fit properties of all the redshift samples.

Sample	$\epsilon_{\rm L}$	$\mathcal{M}_1$	$\mathcal{M}_2$	$\eta_{\rm other}$*	χ^2/d.o.f.	a
	$\rm Z_\odot$	$\log_{10}\left(\frac{\rm M}{\rm M_\odot}\right)$	$\log_{10}\left(\frac{\rm M}{\rm M_\odot}\right)$	$\times 10^3$		$\rm M_\odot\,yr^{-1}Mpc^{-3}$
S	1.80	7.00	12.00	2.5 ± 1.7	18.65/3	0.063
P	1.80	7.00	12.00	3.6 ± 2.6	4.81/4	0.050
UL1	1.70	8.00	11.00	7.0 ± 3.2	12.98/5	0.013
UL2	1.75	7.15	11.85	4.1 ± 1.9	2.19/5	0.032
$\rm S^m$	1.80	7.00	12.00	2.5 ± 1.7	18.49/3	0.063
$\rm P^m$	1.80	7.00	12.00	3.6 ± 0.7	6.92/4	0.050
$\rm UL1^m$	1.70	8.00	11.00	6.3 ± 1.7	12.86/5	0.013
$\rm UL2^m$	1.75	7.15	11.85	4.1 ± 0.5	4.12/5	0.032

Notes: $^{(*)}$ Errors are the standard deviation of the first 3 bins. The δ-parameter has a value of zero for all of the best fits. $^{(m)}$ Models with a user modified CSFH.

5.5.2 Completeness Levels

The differences observed between these results and that of previous work can be explained by the redshift completeness of the samples that have been considered. To generate samples of complete redshift, the common approach is to take LGRBs that are above a specific luminosity value (luminosity cut). Such a method assumes that for all LGRBs above the chosen luminosity cut, the probability of measuring the LGRB redshift is equal and independent of redshift. A luminosity cut in itself is a perfectly acceptable thing to do as one can implement the same choices in the model that is used by placing the same luminosity cuts in Eqn. 5.9. However, as it has been mentioned previously, redshift follow-up is not a consistent process. Ground-based programs are usually biased towards following potentially interesting GRBs (i.e., at high-z), and measurements are easier to attain in the case of the more luminous, quickly detected bursts with smaller telescopes. There remains a large gap, both from the spectroscopic desert in the redshift range $z = 1-2$ (see e.g., Steidel et al. 2004), but also in the mid-range redshift $z = 2-3$ as the LGRB is not visible to the smaller telescopes and the time is not always allocated for such bursts on the large telescopes. Over the past few years, this has begun to change and all types of LGRB are being targeted for follow-up, leading to highly complete samples, much like the one in this paper. For a LGRBR that is biased to galaxies with an $\epsilon_{\rm L} = 0.1$, the LGRB number density would need to peak at redshift 4 (see Fig. 5.8). Placing luminosity cuts on the sample in this paper, it can be seen that the redshift peak remains in the range 1-3 (see Fig. 5.11) and even very large cuts cannot place it in the redshift bin of 4. We also note that for the S sample no acceptable fit was found, to the 1% level, to fulfil a null hypothesis, in comparison to the other three samples. This is in agreement with the argument presented, as 2/3 photometric redshifts and 1 upper limit lie in the redshift $z \sim 3$, which are excluded from the spectroscopic sample.

5.6   Discussion

The possible connection between the CSFH and LGRBR was investigated utilising a model of the CSFH and a 3D parameter space of: mass ranges, metallicity limits and proportionality laws. This was used in combination with a highly complete LGRB redshift measured sample.

5.6.1   LGRB Probability

To calculate the LGRB probability parameter, η_{grb} (Eqn. 5.12), we made a priori assumptions about several values (e.g., black hole mass and jet collimation). However, the parameters taken from the literature that influence the probability of a star forming a GRB have a possible range of acceptable values (see Sect. 5.4.1). Due to the inclusion in our calculation of η_{grb} of a normalisation parameter, η_{other}, a change in the physical parameters η_{coll} (and thus θ_{coll}) and η_{BH} (and thus M_{BH}) would not change the shape of the resulting LGRBR distribution, since the value η_{grb} would counteract changes in η_{coll} and η_{BH}. Assuming that we have included all the LGRB probabilities and thus $\eta_{\mathrm{other}} = 1$, the resulting changes in θ_{coll} and M_{BH} can be quantified by:

$$M'_{\mathrm{BH}} = \left[\frac{-(\alpha + 1)}{\eta_{\mathrm{other}}} \int_{M_{\mathrm{BH}}}^{M_{\mathrm{max}}} \psi\left(m\right) \mathrm{d}m + M^{-(\alpha+1)} \right]^{\frac{1}{(\alpha+1)}} \tag{5.16}$$

$$\theta'_{\mathrm{coll}} = \cos^{-1}\left(1 - \frac{\eta_{\mathrm{coll}}}{\eta_{\mathrm{other}}} \right). \tag{5.17}$$

The rescaled values for all the samples investigated can be found in Table 5.7 and show two extreme cases: (i) large progenitor masses and (ii) small jet opening angles, for which the first property relies on the LGRB collapsar mechanism. The values of (i) and (ii) were initially chosen to be $M_{\mathrm{BH}} = 30 M_{\odot}$ and $\theta_{\mathrm{jet}} = 5°$ respectively (see Sect. 5.4). For a LGRB to occur, we required the formation of a BH which we assume forms a progenitor above a specific mass, M_{BH}. Such large masses of the progenitor imply that LGRBs form from direct collapse to a BH rather than SN fall back under the collapsar model (see e.g., Heger et al. 2003). Smaller jet opening angles of $\sim 1°$, as mentioned previously, are possible but would have effects on, for example, the derived collimated energies of LGRBs (see e.g., Racusin et al. 2009).

Despite the fact that we have considered these parameters separately, it is also equally valid to tune each value at once to give the same final results. To improve upon this, each probability parameter must be measured to more precision before the CSFH can be used to constrain any single one of them. Finally, it is also possible that one of these parameters could also evolve with redshift, but as $\delta = 0$ was shown to be the best-fit in Sect. 5.5, this again is unlikely to be the case.

Table 5.7 Redshift and LGRB probability predictions.

Sample	$5 < z < 6$	$6 < z < 8$	$z > 8$	${\theta'_{\mathrm{coll}}}^*$	${M_{\mathrm{BH}}}^*$
	%	%	%	°	M$_\odot$
S^N	3.7	1.2	0.0169	0.98 ± 0.36	99.88 ± 36.78
S^M	2.7	0.1	0.0002	0.98 ± 0.36	99.88 ± 36.78
P^N	3.7	1.2	0.0169	0.82 ± 0.30	99.91 ± 36.76
P^M	5.6	3.4	0.0030	0.82 ± 0.30	99.91 ± 36.76
UL1^N	4.9	1.3	0.0050	0.58 ± 0.21	99.95 ± 36.77
UL1^M	7.8	9.3	8.0831	0.60 ± 0.22	99.95 ± 36.77
UL2^N	3.7	1.2	0.0147	0.75 ± 0.28	99.93 ± 36.76
UL2^M	6.9	6.9	2.3077	0.75 ± 0.28	99.93 ± 36.76

Notes. $^{(N)}$ Normal CSFH model (Eqn. 5.5) using the best-fit properties given in Table 5.6. $^{(M)}$ Modified CSFH model (Eqn 5.18) using the best-fit properties given in Table 5.6. $^{(*)}$ Uncertainties are given as 1σ deviations, as the propagated errors of Eqn. 5.16 and Eqn. 5.17 are dominated by $1/\eta^2_{\mathrm{other}}$ and are thus underestimated.

5.6.2 High-z Predictions of the CSFH

Galaxy detection drops off very quickly with higher redshifts due to instrumental limitations making LGRBs complementary probes to studying high-z star formation, provided we understand the relation between the LGRBR and the CSFH. As a result of the empirically determined models outlined in Sect. 5.2 being limited to redshifts $z < 3$ and the possibility that the CSFH flattens out at at high redshift, we modify the CSFH model to a linear function for redshifts of $z > 3$ (similar to Daigne et al. 2006):

$$\dot{\rho}(z) = \begin{cases} \dot{\rho}(z) & \text{if } z \leq 3 \\ \dot{\rho}(z = 3) - az & \text{if } z > 3 \end{cases}, \tag{5.18}$$

where a is a constant to be determined. The parameter a is set to vary from the slope of the CSFH at $z = 3$ and is increased to a flat distribution over the range $\log_{10}\left(a/M_\odot \, yr^{-1} Mpc^{-3}\right) = 0.4 - 2.5$. Each parameter fit was then compared to each LGRB sample and the best-fit a can be found in Table 5.6 and the resulting change in the best-fit CSFH can be seen in Fig. 5.12.

All of the samples show no preference for a CSFH flattening at high redshift except the upper limit 1 distribution, which shows a preference for a CSFH that remains constant with evolving redshift. However, the $\Delta\chi^2$ between the modified and unmodified CSFH is 0.12, and so both are still feasible solutions. Overall, the other three samples show no preference for a flattening in the CSFH at higher redshifts. This is in contradiction to the work by Kistler et al. (2009), who showed that CSFH would be higher than thought, utilising the *Swift* LGRB sample and a single high-z LGRB. As discussed in Sect. 5.5.2, this is understood as being a result of the extended efforts of
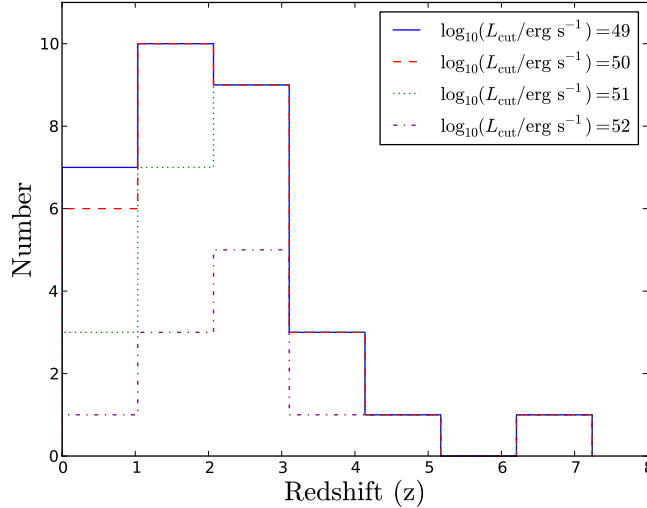
Figure 5.11 LGRB redshift number distribution. Each distribution depicts the sample after LGRBs below a specific luminosity limit are removed. It can be seen the redshift peak remains in the range 1-3.

measuring redshifts of LGRBs for $z > 6$. Also, work carried out by Daigne et al. (2006) show that they required a CSFH that increased with redshift. However, this would imply higher star formation rates at the early stages of the Universe, which are not seen observationally or with simulations. Due to this unphysical nature, they propose that the LGRB mechanism is evolving with redshift. Again, due to the preference of $\delta = 0$ in our studies, our analysis suggests that there is no evolution of the LGRB mechanism required.

Given the best-fit models the total fraction of LGRBs that exist in each redshift range is predicted for each distribution analysed (values can be found in Table 5.7). A fraction of $\sim 1.2\%$ of the LGRB population existing $z > 6$ is calculated, similar to the value of $\sim 1\%$ from (Campisi et al. 2010), within the error of Greiner et al. (2011a) who predict $5.5 \pm 2.8\%$ for $z > 5$ and consistent with other works (Perley et al. 2009; Fynbo et al. 2009a). While this sounds like a small fraction, it is much larger than the corresponding fractions for AGN/QSO (Willott et al. 2010).

5.6.3 Summary of Results and Limitations

It had been previously thought that the LGRB host sample was biased to a specific range of masses with low metallicity. We find acceptable fits for a mass range of $10^7 - 10^{12} M_\odot$, which would suggest that the LGRB rate is a sensitive measure of the faint- and massive-end of the mass function of galaxies. We note that the proportions of
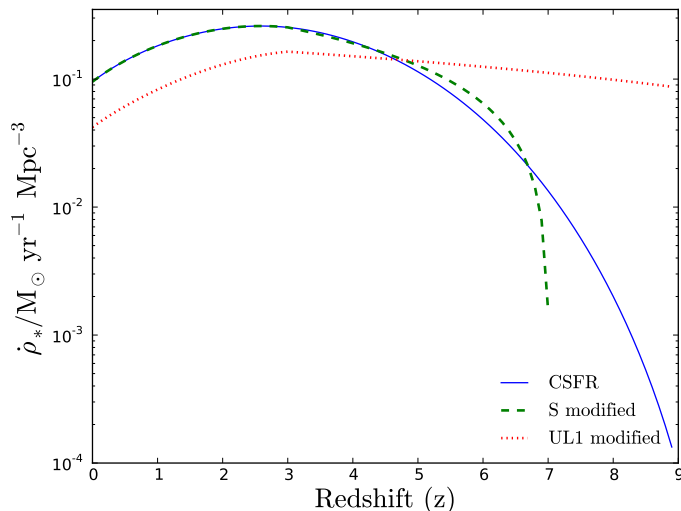
Figure 5.12 The bold-blue line is the CSFH model described by eqn (5.5). The green-dashed and the red-dotted lines depict the best-fit modified CSFH for the S and UL1 distributions respectively.

galaxies are determined by the specified GMF and the quenching mass, both described in Sect. 5.2. The high mass range is in good agreement with Krühler et al. (2011a), who show that by selecting hosts based on high extinction more massive galaxies were found. On the contrary, the GMF would imply there are more missing low-mass galaxies and that LGRBs are selecting star forming regions, with no biases. Secondly, the results of Sect. 5.5.1 also show that there is no strong, $\sim 0.1 - 0.3\,\mathrm{Z_\odot}$ metallicity preference for the host galaxy at the 95% redshift-complete level. It should be noted that this is a global metallicity and does not reflect directly on the LGRB model itself, but on the properties of the LGRB hosts as a whole. Other types of cuts have been implemented where metallicity dispersion is also considered (Niino 2011; Wolf & Podsiadlowski 2007), however, as our model solution requires no cuts at all, this would not affect the outcome. Thirdly, the δ parameter chosen to quantify any effects not considered within our model favours a value of zero. Such a result implies the following: (i) the stellar IMF need not be evolving, (ii) the LGRB LF is also redshift independent and (iii) the progenitor system is consistent throughout all redshifts considered.

In summary, the results show that LGRBs are occurring in any type of galaxy (the galaxy number density obeying an evolving GMF of full mass range), with no strong metallicity limits. The only requirement is that there is star formation occurring, in agreement with simulations that suggest LGRB host galaxies preferentially have high specific star formation rates (e.g., Courty et al. 2007; Mannucci et al. 2011) and observational evidence that LGRBs primarily occur in regions of high star formation

(Fruchter et al. 2006).

As with any model there are limitations. For low redshifts ($z < 3$) we had used empirically calibrated models, that allowed the freedom of their parameters to be removed (see e.g., Eqns. 5.1, 5.2, 5.3 or 5.4). To make reliable judgements at high redshifts ($z > 3$), further observations able to study these relations at higher redshift are needed or other techniques used such as, Monte Carlo Markov Chain (e.g., Virgili et al. 2011), Principal Component Analysis (e.g., Ishida et al. 2011), or simulations introduced into our model (e.g., Campisi et al. 2010; de Souza et al. 2011; Ishida et al. 2011). Another important consideration is the assumptions and simplifications made at the beginning of the modelling, i.e., the stellar IMF, the LGRB luminosity function, the LGRB explosion mechanism and the GMF. Many of the parameters kept constant could also be left free.

The form of the stellar IMF, at present, is still a lively debated issue and could be modified by changing the slope (α), the change over short time scales and also the change over redshift (top-heavy; see Sect. 5.2.6). Any of these changes would result in a modification of the following models that use an IMF for their determination: SFR (Sect. 5.2.1), GMF (Sect. 5.2.2) and the LGRBR probability (Sect. 5.2.7). For example, Wang & Dai (2011) show that the CSFH-LGRBR connection requires no constraints if a redshift dependent stellar IMF is used. For our given framework we require no evolution of the IMF, however, any big changes to the form of the stellar IMF would require deeper analysis.

Secondly, the luminosity function of the LGRB was assumed to take the form of a normal (Gaussian function). There are many other forms, as mentioned previously, such as Schechter functions, log-normals and redshift dependent functions that could be utilised. Again, each one implies different physics, and will naturally influence the final result.

The minimum mass of a star to form a BH was set to $M_{\mathrm{BH}} \geq 30\,\mathrm{M}_\odot$, as the collapsar model was assumed for LGRB creation. However, there is a range of possible lower range masses (Nomoto et al. 2010) and also secondary mechanisms for BHs to generate a LGRB, for example SN-fallback (for a review see Fryer et al. 2007). There are also different types of progenitor systems (other than a WR) that are thought to be possible to generate a LGRB, e.g., NS-White Dwarf binaries (Thompson et al. 2009), Helium-Helium binaries (Fryer & Heger 2005), Quark stars (Ouyed et al. 2005), Be/Oe stars (Martayan et al. 2010; Eldridge et al. 2011), blue-stragglers (Woosley & Heger 2006) and red-giants (Eldridge et al. 2011). Different mechanisms have been investigated before, but not in combination with the parameters of this paper (see Young & Fryer 2007).

Finally, the primary difference of the studies of this paper is the redshift completeness of the distribution. The normal way of improving completeness levels is to choose LGRBs above a specific luminosity to compensate for the limitations of the detector at increasing redshift. However, redshift measurements are not only dependent on the brightness of the afterglow, and follow-up of GRBs is not always consistent for many reasons: LGRB sky positioning, weather, satellite location and localisation precision, to name but a few. Secondly, until recently, many follow-up programs were interested in

very low and very high redshift GRBs. Such a biasing in combination with the redshift desert, results in a deficit, in the $z \sim 1-5$ range, that is not easily removed by luminosity selections (for an analysis of removing selection criteria see Coward et al. 2008). These deficits can strongly bias the results and give different interpretations of metallicity cuts and evolving LGRB LFs (see Sect. 5.5.2). Rather than improving completeness levels by cuts (e.g., luminosity, time criteria), Bayesian inference or other methods, incompleteness should be reduced by utilising programs with consistent LGRB follow-up. Such programs would require no selection biasing of GRB triggers for redshift or host follow-up. This is definitely not an easy aim and is not always possible with current telescope over-subscription, but many programs have already shown that completeness is an important criterion (see e.g., Fynbo et al. 2008b; Greiner et al. 2011a; Krühler et al. 2011a).

In summary, the CSFH-LGRBR connection has a large number of free parameters that are co-dependent in several ways, especially if redshift dependencies are incorporated. As a result, each parameter cannot be treated independently and should always be considered contemporaneously, in a systematic way. Since the extrapolation of the individual parameters to higher redshifts is very difficult to determine, the most direct way of improving the uncertainties is primarily a systematic follow-up of all redshifts, that would benefit from a GRB mission which has a substantially larger detection rate than *Swift* (e.g., GRIPS; Greiner et al. 2011b).

5.7   Conclusion

The association of LGRBs with the death of massive stars has presented many new opportunities for utilising them as high redshift tools. One possibility is using the LGRB rate to trace the CSFH to unprecedented redshifts, which is usually challenging by conventional methods. To reach such a goal, the manner in which the LGRB rates traces the CSFH needs to be known, whether it is dependent on galactic properties or not (e.g., galaxy stellar mass, metallicity or stellar initial mass functions). In this work we have studied whether any type of dependence is required, given new evidence of LGRBs occurring in more massive galaxies than had been previously thought in combination with highly complete redshift measured LGRB samples (up to 95% complete).

Using a highly complete sample we find best-fit solutions that show no preference for a strong metallicity or stellar mass constraints. These results imply that the LGRB population has no preference on the global properties of their host galaxy other than it has active star formation. We also show that our initial model does not require additional redshift dependences and, therefore, implying that there is no redshift dependence required in the LGRB probability or luminosity function.

The best-fit CSFH models are modified at redshifts > 3 to linear functions to investigate the possibility that the CSFH flattens out. The least χ^2 of the four modified models shows no preference for a flattening of star formation at high redshift. This is in contradiction with some other LGRB studies, but the exact form of the CSFH at high redshifts is still not settled. We predict that above $z = 6$, $\sim 1.2\%$ of all LGRBs

exist, which is in agreement with recent simulations (Campisi et al. 2010) and statistical studies (Perley et al. 2009; Fynbo et al. 2009a; Greiner et al. 2011a).

Our results show that sample biasing and completeness levels of distributions are of essential importance and cannot always be recovered in the standard methods. Such completeness can only be achieved by consistent follow-up of LGRBs with no preference (or bias) on what LGRB is followed. Once unknown (and hard to quantify) biases are introduced, they can have dramatic changes to the interpretation of the data.

Chapter 6

First Billion Years Simulation 2: Populating γ-ray bursts at $z > 5$[1]

ABSTRACT

The association of long γ-ray bursts (LGRB) with the death of massive stars and luminosities reaching $10^{54}\,\mathrm{erg\,s^{-1}}$ make them ideal probes of the high redshift cosmic star formation history (CSFH). However, the way in which the two depend on one another is still an on going debate. We utilise the high resolution cosmological First Billion Years 2 (created and run by the Theoretical Modelling of Cosmological Structures group) suite of simulations to investigate the connection between the LGRB rate (LGRBR) and the CSFH for redshifts of $z > 5$. We populate stellar particles in the simulation with black holes utilising modified Monte-Carlo techniques and determine if a LGRBR is formed based on stellar age, metallicity and stellar mass. A LGRBR is then determined from the populated LGRBs and compared to the LGRBR expected from the simulation's CSFH. We find that the populated LGRBR can match well the internal CSFH-LGRBR with a constant offset of $N_{\mathrm{Populated}} \propto N_{\mathrm{CSFH}}$ throughout redshift. The connection depends heavily on the prescriptions used for stellar ages, but is constant throughout redshift that it has no functional relevance. A redshift dependence of the form $(1 + z)^{\delta=1.5}$ is not reproducible by the mass-metallicity-age selection of the populated LGRBR, suggesting that simple environmental effects would not explain such a feature. Further studies that include a physical reasoning for the luminosity function of LGRBRs would possibly shed light on this. LGRBs are seen to be simple tracers of the CSFH at high redshifts $z > 5$ when compared consistently within a simulation, which encourages more detections of high redshift LGRBs in the future.

6.1   Introduction

Reaching luminosities as high as $10^{53}\,\mathrm{erg\,s^{-1}}$ makes long gamma-ray bursts (LGRBs) the brightest objects in the Universe during their emission. With such an unexcelled brightness, LGRBs are the perfect tool for investigating the high redshift Universe.

The association of LGRBs with the death of massive stars (Galama et al. 1999; Stanek et al. 2003; Hjorth et al. 2003; Matheson et al. 2003) facilitates their use as star formation tracers. However, before this connection can be used routinely and robustly, the way in which they trace one another must be known accurately. This has lead many authors to investigate the differences, if any, between the LGRB rate (LGRBR) and the cosmic star formation history (CSFH) (e.g., Wijers et al. 1998; Bromm & Loeb 2006; Daigne et al. 2006; Li 2008; Butler et al. 2010; Wanderman & Piran 2010). Early studies showed an overabundance of LGRBs at higher redshifts than that inferred from the CSFH (e.g., Daigne et al. 2006) and suggested the cause was an environmental bias of the LGRB progenitor. However, since then, this bias has taken many forms. Firstly, a metallicity bias such that galaxies below a given metallicity ($Z < 0.3\,\mathrm{Z_\odot}$) contribute to forming LGRBs (e.g., Kistler et al. 2009; Robertson & Ellis 2012), which was supported by host galaxy samples, which showed a surplus of low-mass, low-metallicity galaxies (e.g., Le Floc'h et al. 2003; Christensen et al. 2004; Savaglio et al. 2009). Secondly, an unknown redshift dependence parametrised by a powerlaw, δ, which could be the result of the underlying explosion mechanism or the LGRB number distribution/luminosity function (e.g., Salvaterra et al. 2012) changing with redshift. Thirdly, a redshift dependent initial mass function (e.g., Wang & Dai 2011), and finally a result of selection biases (Coward et al. 2008) or luminosity cuts placed on the LGRB distribution (Elliott et al. 2012a).

Theoretical predictions of lower-metallicity LGRBs being more probable and a deficit of massive, metal-rich host galaxies (e.g., Graham & Fruchter 2012; Perley et al. 2013), has lead to metallicity cut-offs being the most favoured explanation. However, increasing observations of solar/super-solar metallicity galaxies makes it difficult to reconcile (e.g., Levesque et al. 2010c; Krühler et al. 2012b; Elliott et al. 2013).

Given the lack of robust host galaxy integrated metallicity measurements (especially above $z \sim 1$) and sight-light measurements of metallicity at the location of the LGRB, make it difficult to investigate any dependences that may exist and near-impossible to identify any evolution. In contrast, the ease of use of cosmological simulations has improved over recent years that it is becoming more common to use them to make predictions about LGRBs (e.g., Campisi et al. 2011), their environment (e.g., Pontzen et al. 2010; Artale et al. 2011), and their influence on the Universe (e.g., Maio et al. 2012). Despite this achievement, the mass-resolution and chemical complexity of current simulations make it difficult to create LGRBs at the singularity level and dependent on its environment in a reliable manner.

We first introduce the simulation we use for our study in Sect. 6.2. Section 6.3 outlines the methods used to generate a LGRB based on its environment and how we calculate the LGRBR and CSFH. The results are then displayed in Sect. 6.4. We then

discuss the implications of our findings in Sect. 6.5 and conclude in Sect. 6.6.

6.2   Simulations

The First Billion Years (FiBY) project (Khochfar et al. in prep), is a suite of cosmological simulations primarily aimed at investigating the formation and evolution of the first galaxies. The code was modified and the simulations run by the Theoretical Modelling of Cosmological Structures (TMoX) group. The properties of the simulations are to be outlined in detail in future work (Dalla Vecchia et al. in prep), but the highlights are noted in the following.

Each simulation is based on a modified smoothed particle hydrodynamic code, `GADGET` (Springel 2005), developed for the Overwhelmingly Large Simulations project (Schaye et al. 2010). The code was modified in five major ways: (i) line cooling in photoionisation equilibrium for a total of eleven elements (H, He, C, N, O, Ne, Mg, Si, S, Ca, and Fe), which is computed with `CLOUDY v07.02` (Ferland et al. 1999), (ii) metal enrichment from supernovae and stellar winds, and thermal feedback from supernovae (for full details see Johnson et al. 2013), (iv) a full non-equilibrium primordial chemistry network and molecular cooling functions for both H_2 and HD, following Schaye et al. (2010), and (v) chemical enrichment from population III stars that allows the pollution fraction for each one of the eleven elements mentioned, to be known.

Within the simulation we cannot resolve individual stars, but in fact can resolve stellar populations with a stellar mass resolution of $10^5 \, M_\odot$. We refer to these systems as star particles throughout the text (there exist also gas particles and dark matter particles, but we neglect any mention of these throughout the text).

We only refer to the simulation used in this work. The simulation adopts the cosmological constants from the Wilkinson Microwave Anisotropy Probe (WMAP; Komatsu et al. 2009), i.e., $\Omega_m = 0.265$, $\Omega_b = 0.0448$, $\Omega_\Lambda = 0.735$, $H_0 = 71 \, \text{kms}^{-1}\text{Mpc}^{-1}$, and $\sigma_8 = 0.81$ and includes dark matter and gas. It was started at a redshift of $z = 127$ and finished at a redshift of $z \sim 6$. It has a co-moving box size of 16 Mpc and a smoothed-particle-hydrodynamics particle density of 342^3.

6.3   Model & Methodology

In this work we want to obtain two things: (i) generate and count the number of black holes (BH) that could result in a LGRB that have been created in star particles within a high resolution cosmological simulation, and (ii) compare this calculated LGRBR to the one inferred from the simulation's CSFH. We construct a semi-analytical model which uses the output from a simulation created and run by the TMoX group. We outline the methodology in the following:

A. **LGRB Population**

1. Find a star particle and define it as a population type-II (Pop II) or type-III (Pop III) star using a cut-off metallicity of Z_{cut}.

2. Select an IMF (Sect. 6.3.1) and populate stars with a given mass using a Monte-Carlo method (Sect. 6.3.1), until the total mass of the star particle is used.

3. Ascertain whether this star results in a LGRB by looking at the age of the star particle (Sect. 6.3.3) and the mass-metallicity plane (Sect. 6.3.2).

4. Add up the total number of LGRBs per redshift bin to get the populated LGRBR.

B. **CSFH-LGRBR**

1. Calculate the CSFH for the given simulation box, ρ_*.

2. Convert the CSFH into a LGRBR using the same assumptions as in the GRB creation steps (Sect. 6.3.4).

6.3.1 Initial Mass Function

The initial mass function (IMF) quantifies how many stars per stellar mass bin are created during star formation (for a complete overview see Bastian et al. 2010) and is quantified mathematically in the following way

$$\psi\left(m\right) \propto m^{-\alpha}\left(1+z\right)^{\beta}, \tag{6.1}$$

where α depends on the adopted IMF and β describes the redshift evolution. The IMF for Pop II stars is only usually measured for nearby clusters and local resolved stellar populations (Bastian et al. 2010). At higher redshifts, it is only inferred from integrated galaxy properties or other methods (see, e.g., Davé 2008). There is still no current consensus on whether the IMF varies with redshift or environment. A directly measured IMF is currently incomprehensible for Pop III stars and is usually constrained from simulations or theory (for a review, see, e.g., Bromm & Larson 2004). However, the IMF of Pop II and III stars differ substantially and so at this stage we employ a strict metallicity cut of $Z = 10^{-5}$ (e.g., Frebel et al. 2007), for which above this limit the star particle is designated a Pop II star and below a Pop III star (throughout our analysis we consider only Pop II stars and consider Pop III in later work). Throughout the text we adopt a Salpeter (Salpeter 1955) IMF ranging from $0.1 - 100\,\mathrm{M}_\odot$ ($\alpha = 2.35$ and $\beta = 0$, see Fig. 6.1) that is constant with redshift.

Simulated masses of each potential GRB are generated using the Monte-Carlo Alias method (Kronmal & Peterson 1979). This method requires the creation of a cumulative distribution of the probability distribution (in our case the stellar IMF). Then a randomly drawn value from zero to one is used to define at which interval the probability would lie and, therefore, the underling x value (in our case stellar mass m). This procedure is carried out until all of the star particles mass is allocated. Given that there is a lower bound at which no BH can result in a GRB within the stellar explosion models we consider (see Sect. 6.3.2), we remove the total mass attributed to these stars to decrease the total processing time.
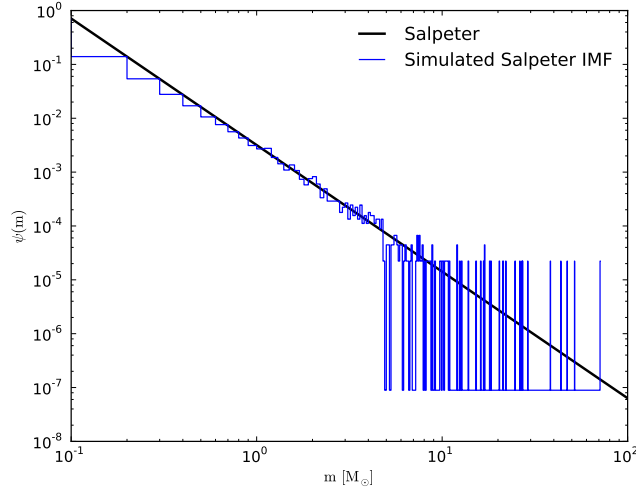
Figure 6.1 The fraction of stars plotted against the stellar mass for a Salpeter IMF is shown in black.The blue lines depict the simulated masses using the Monte-carlo Alias method (see Sect. 6.3.1)

6.3.2   Progenitor Mass-Metallicity

The collapsar model, that describes how a viable LGRB BH forms, usually requires lower metallicity environments to ensure that angular momentum is retained and a disc is formed (e.g., Hirschi et al. 2005). Techniques that include this effect when creating LGRBs are often applied to global properties of the host galaxy, rather than the LGRB itself (e.g., Hao & Yuan 2013). As the capabilities of FiBY allow us to obtain the metallicity of the star particles, we can place direct constraints on each LGRB itself. We employ a mass-metallicity relation based on grid simulations of Wolf-Rayet stars (Georgy et al. 2009) that result in a LGRB-BH, which is depicted in Fig. 6.2. We consider star particles that lie within the LGRB-BH region (navy) as viable LGRBs, whereas the star particles that lie in the separate part of the phase-space (light blue) regions will explode to another class of compact object that is outlined more thoroughly in Georgy et al. (2009).

6.3.3   Progenitor Age

We have assumed a Wolf-Rayet type progenitor and thus a star that has a short lifetime in comparison to the normal stellar population. Therefore, we remove star particles that are too old to still host young stars, so that we do not generate an overabundance of LGRB progenitors. We take the death ages of different Wolf-Rayet types from a grid of stellar explosion models (Georgy et al. 2012). We use an average death age upper limit of $10^{5.56}$ yr, but given the uncertainty of the models this could
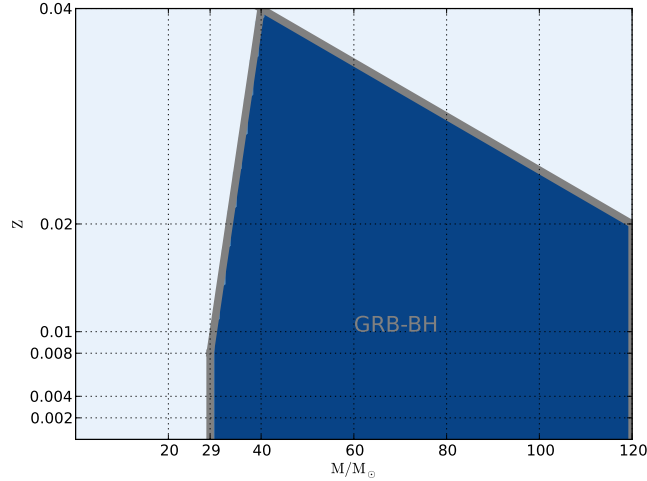
Figure 6.2 The metallicity fraction plotted against the mass of a grid of Wolf-Rayet progenitor stars taken from Georgy et al. (2009). The navy shaded region bounded by grey lines depicts the mass-metallicity region in which a GRB will occur.

vary by $\pm 2\,\mathrm{dex}$, however, this should not alter our main conclusions and is discussed in Sect. 6.5.1. When calculating the CSFH-LGRBR, we cannot place constraints on stellar lifetimes in the same manner as just outlined. Instead we incorporate a limit on the age through the use of an analytical expression for stellar age as a function of mass. The lifetime of a star, τ, for a given mass m is (Kodama 1997; Romano et al. 2005):

$$\tau\left(m\right) = \begin{cases} 50 & \text{if } \mathrm{m/M_\odot} \leqslant 0.56 \\ \frac{0.344 - \sqrt{1.790 - 0.2232(7.764 - \log_{10} m)}}{0.1116} & \text{if } 0.56 < \mathrm{m/M_\odot} \leqslant 6.6 \\ 1.2 m^{-1.85} + 0.003 & \text{if } \mathrm{m/M_\odot} > 6.6 \end{cases} \qquad (6.2)$$

6.3.4   CSFH-LGRBR Relation

We determine the CSFH of the FiBY simulations in the standard manner. In brief, we calculate the total mass of stellar particles (and star forming gas particles for a consistency check) for each redshift slice and compute the rate in change of stellar mass to the previous redshift slice, $\dot{m}_*$. The final CSFH, $\dot{\rho}_*$, is obtained by normalising $\dot{m}_*$ to the box size of the simulation.

The inferred association of the death of massive stars with LGRBs allows LGRBs to be used as proxies of massive star formation, assuming that the difference between birth and death of the star is less than the Hubble flow (i.e., $\tau_{\mathrm{death}}/\tau_{\mathrm{Hubble}} \sim 10^{-5}$). On a cosmological scale, LGRBs can be used as a tracer of the CSFH via the following equation (see Elliott et al. 2012a and references therein):

$$N\left(z_1, z_2\right) = \eta_{\mathrm{grb}} \int_{z_1}^{z_2} \frac{f\left(z\right) \dot{\rho_*}\left(z\right)\left(1+z\right)^{\delta} \frac{\mathrm{d}V}{\mathrm{d}z}}{\left(1+z\right)}\,\mathrm{d}z, \qquad (6.3)$$

where $N\left(z_1, z_2\right)$ is the total number of LGRBs between the redshifts z_1 and z_2, $\frac{\mathrm{d}V}{\mathrm{d}z} = 4\pi D_{\mathrm{com}}^2\left(z\right)\frac{\mathrm{d}D_{\mathrm{com}}(z)}{\mathrm{d}z}$, D_{com} is the co-moving distance, η_{grb} is the probability of stars resulting in a LGRB, and δ is the power of proportionality (i.e., intrinsic redshift evolution) for the CSFH to LGRBR. The LGRB probability can be parametrised as

$$\eta_{\mathrm{grb}} = \eta_{\mathrm{other}} \frac{\int_{M_{\mathrm{BH}}}^{M_{\mathrm{max}}} \psi\left(m\right)\tau\left(m\right)\,\mathrm{d}m}{\int_{M_{\mathrm{min}}}^{M_{\mathrm{max}}} m\psi(m)\tau\left(m\right)\,\mathrm{d}m}, \qquad (6.4)$$

where M_{min} and M_{max} are the minimum and maximum star masses considered in our model respectively. We note that we do not include a LGRB luminosity function, nor any corrections based on instrument limitations, as we are comparing directly the simulation's CSFH-LGRBR to the LGRBR ascertained from populating LGRBs within the simulation, i.e., $\eta_{\mathrm{other}} = 1$.

6.4 Results

6.4.1 CSFH of the Simulation

The CSFH of the FiBY simulation is shown in Fig. 6.3. We compare it to several values obtained from the literature, determined from star-forming field galaxies (Mannucci et al. 2007; Bouwens et al. 2008; Li 2008), Lyman-break galaxies (Laporte et al. 2012; Zheng et al. 2012), Ly-α emitters (Ota et al. 2008), and LGRBs (Kistler et al. 2009; Ishida et al. 2011) that reach a redshift of $z \sim 10$. Both the simulation CSFH and the measured distribution are seen to be consistent throughout redshift. Also, the calculation using star and gas particles results in the same trend, showing consistency within the simulation itself. From here we only use the star particle determined CSFH.

6.4.2 LGRBR of Populated LGRBs

The number rate of LGRBs can be seen in Fig. 6.4 Top. The production of LGRBs does not start until $z \sim 12$, at which point the metallicity enrichment is large enough to classify the star particles as Pop II rather than Pop III. The rate then increases by a factor of a thousand as it reaches a redshift of $z \sim 6$, showing a similar behaviour to that of the CSFH depicted in Fig. 6.3.

Fig. 6.4 Middle shows the fractional effect that the mass-metallicity selection has on star-particles that become LGRB-BHs. As expected from galactic evolution, metallicity pollution becomes important as the redshift becomes lower and affects the LGRBR primarily at a redshift of $z \sim 5.5$, dampening it by up to 20%. Given the resolution
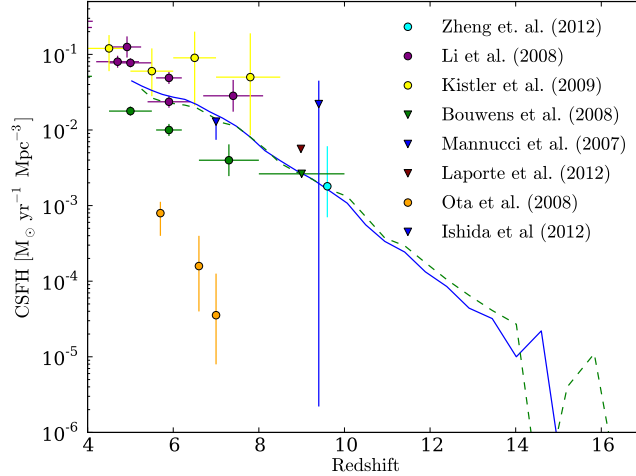
Figure 6.3 Cosmic star formation history of the FiBY simulation using star particle's stellar mass (green dashed line) or star-forming/gas particles (blue-line). Each of the data points are CSFH measurements obtained from the literature and are in good agreement with the simulation.

of FiBY, the metallicity constraint is not the same as placing constraints on the entire host galaxy (Elliott et al. 2012a), but rather on the properties of the progenitor stellar population. However, in comparison to the stellar lifetime constraint, depicted in Fig. 6.4 Bottom, the effect is minuscule. The stellar lifetime constraint reduces the overall rate by a factor of ~ 1000, even by redshifts as early as $z \sim 10$. Even so, the fractional change caused by the stellar lifetime selection is fairly constant throughout redshift that this would not affect greatly our results and is discussed in more detail in Sect. 6.5.1.

6.4.3   CSFH-LGRBR of the Simulation

The CSFH determined LGRBR is shown in Fig. 6.5 and is plotted alongside the LGRB population distribution described in Sect. 6.4.2. Both distributions can be seen to follow the same trend and have similar orders of magnitude. This suggests that the LGRBR has no dependence on redshift, at least for the redshift range of $z > 5$, but is discussed more in Sect. 6.5.2. Even though no evolution may take place, the absolute value of the distributions are highly dependent on the LGRB lifetime, imposed in our methodology and can change by several orders of magnitude (we discuss its influence in Sect. 6.5.1). Also, there is a noticeable difference at the higher redshifts ($z > 12$), but this is highly dependent on the Pop III or Pop II metallicity cut-off, Z_{cut}.
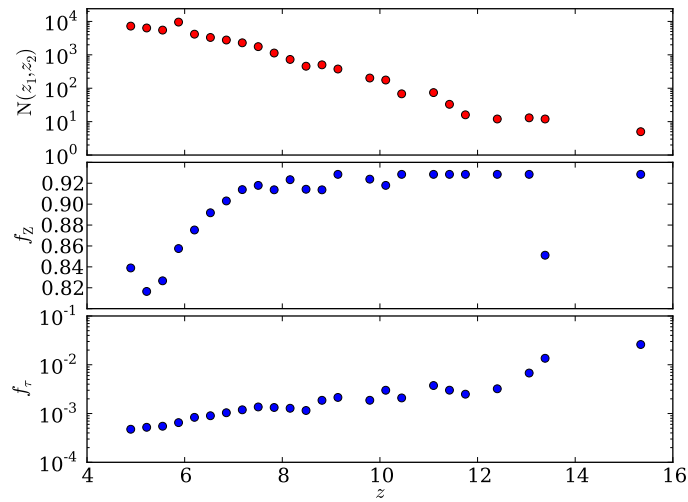
Figure 6.4 **Top**: Number of LGRBs per redshift bin, which was determined from the total number of populated BHs that could successfully become LGRBs. **Middle**: The ratio of the number of LGRBs including the Georgy et al. (2009) metallicity constraints to the number of LGRBs without the metallicity constraints. **Bottom**: The ratio of the number of LGRBs including the age constraint from Georgy et al. (2012) to the number of LGRBs without including the age constraint (metallicity constraints have been included for both of these).
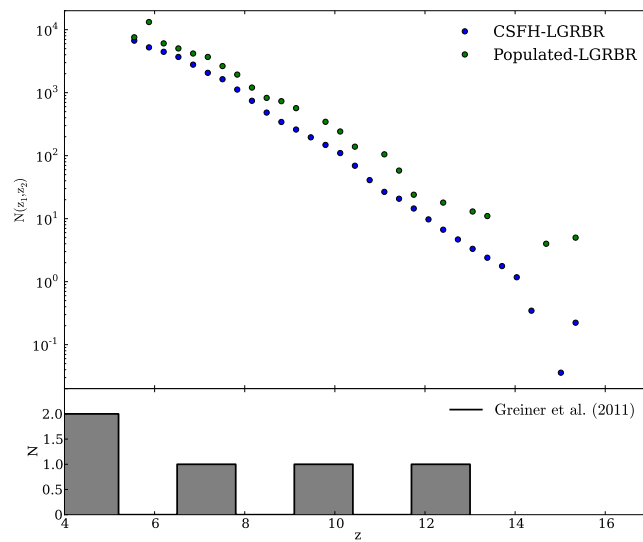
Figure 6.5 **Top**: LGRBR calculated from the populated LGRBs is denoted by the green circles and the CSFH-LGRBR of the simulation is denoted by the blue circles. Both show the same behaviour and even have similar values throughout redshift, however, this is highly dependent upon the chosen age restriction and the corresponding functional form (this is discussed more in Sect. 6.5.1). **Bottom**: The measured GRB number distribution taken from the Greiner et al. (2011a) upper limit 2 sub-sample (see Elliott et al. 2012a), which has a redshift completeness of 95%.

6.5 Discussion

6.5.1 Stellar Age Prescriptions

We already noted in Sect. 6.4.3 that the effect of changing the prescription for stellar lifetimes is non-trivial and can easily change the absolute LGRBR by a factor of ~ 100. For a comparison, we adopt the formalism of (Copi 1997; Hao & Yuan 2013) such that the stellar lifetime is defined as $\log_{10} \tau(m) = 10 - 3.6 \log_{10} m + (\log_{10} m)^2$. We plot the ratio of the populated LGRBR ($N_{\mathrm{Populated}}$) over the simulation CSFH-LGRBR (N_{CSFH}), in Fig. 6.6 for both of the stellar lifetime prescriptions. We then fit a simple straight line of $y = ax + c$ to the ratio excluding any measurements above a redshift of $z > 14$. Both lines can be seen to be straight, with no apparent gradient in either of the analytical expressions used. The main difference is a constant offset, with values of ~ 500 for Copi (1997), and ~ 1 for Kodama (1997), in comparison to the populated LGRBR.

In addition, we modified the age limit used for the populated LGRBR to match the age value defined in both of the analytical expressions ($\sim 10^{6.8}$ yr), but no visible change in the results is seen. It is not surprising that there exists a discrepancy in the ratio of the two lines as there is a large number of assumptions that go both into the CSFH-LGRBR conversion and the determination of the stellar lifetime formalism. However, we are primarily interested in how both distributions evolve with redshift rather than their absolute values. Therefore, both curves are in good agreement and display no evolution in the redshifts of $z = 5 - 13$ (we discuss the effects of evolutionary changes and other biases in the next section).

6.5.2 Redshift Evolution and Metallicity

To see the effects of a redshift dependence, we modify the δ-value in Eqn. 6.3 to $\delta = 1.5$ (Kistler et al. 2009) and plot the ratio of the resulting CSFH-LGRBR to the one without any evolution in Fig. 6.7 (i.e., $\delta = 0$). It can be seen that if a redshift dependence existed between the CSFH and the LGRBR, they would begin to deviate from one another towards the higher redshifts and the ratio of the CSFH-LGRBR to the populated LGRBR would require a much sharper slope of ~ 10 in comparison to slope of ~ 0 we obtain. Our result of no redshift evolution is not by construction, as we require a mass-metallicity selection to define a LGRB, which does in fact evolve with redshift (specifically the metallicity). These results show that if a dependence of $\delta = 1.5$ could be included, it would not be reproducible by environmental effects alone.

Secondly, to test the effects of metallicity cut-offs of host galaxies, we apply the formula outlined in Langer & Norman (2006):

$$\Psi(m, Z_{\mathrm{cut}}) = \frac{\hat{\Gamma}\left(\alpha_1 + 2, Z_{\mathrm{cut}}^{\beta} 10^{0.15 \beta z}\right)}{\Gamma(\alpha_1 + 2)}, \qquad (6.5)$$

where $\hat{\Gamma}$ is the incomplete gamma function, Γ is the gamma function, $\beta = 2$, $\alpha_1 = -1.16$
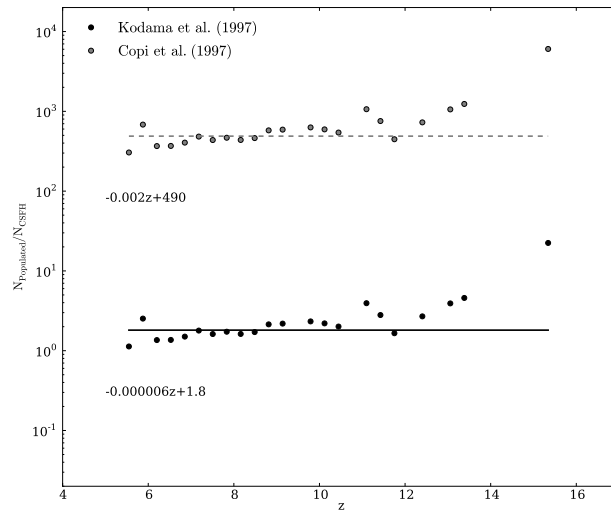
Figure 6.6 Ratio of the populated LGRBR to the CSFH-LGRBR, for the two different analytical expressions used for the stellar lifetimes (black and grey dots). The lines are fits to the ratio of the form $y = ax + c$ and show that $a \sim 0$ for both, and $c \sim 1$ for Kodama (1997) and $c \sim 500$ for Copi (1997).
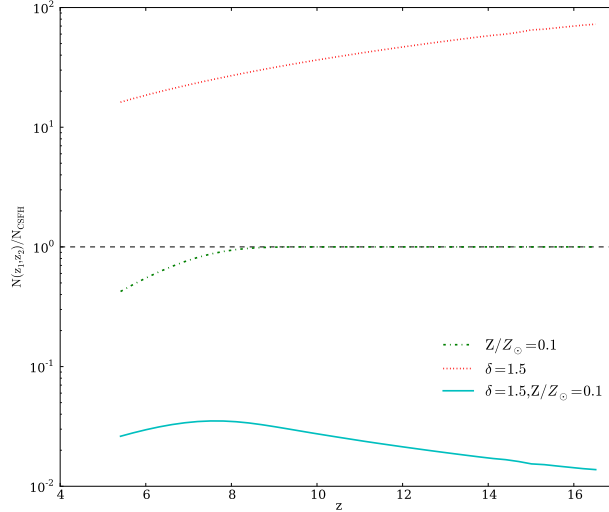
Figure 6.7 Ratio of modified CSFH-LGRBRs to the unmodified CSFH-LGRBR determined in Sect. 6.4.3. The red dashed line is when an evolution in redshift of $\delta = 1.5$ is included, the green dot-dashed line is when a cut-off host metallicity of $Z = 0.1\,Z_\odot$ is incorporated (Salvaterra & Chincarini 2007), and the cyan line is a combination of both of these effects.

and Z_{cut} is the metallicity cut-off. We note that this is not the only formalism that can be used, but is one of the most common. This factor is then included in the integral of Eqn. 6.3 and is shown in Fig. 6.7. It can be seen that the effect of metallicity only becomes important at $z \sim$ 8.0 as the Universe begins to pollute itself substantially and a downturn in the number of LGRBs is visible.

To compare this analytical metallicity cut-off, we carried a similar cut-off, but within the simulation itself. This is done by removing the mass of star particles that had a metallicity of $Z > 0.1\,Z_\odot$ when calculating the CSFH and, in turn, the CSFH-LGRBR. In comparison to the populated LGRBR, the metallicity limited CSFH-LGRBR produces less LGRBs by a factor of ~ 5. However, this comparison can be considered to be too naive as the metallicity cut-off used is very similar to the mass-metallicity constraints used to define a LGRB. A more robust method of placing metallicity cut-offs on the host galaxy, within the simulation, would be to calculate an average metallicities of the star particles that are gravitationally bound to one another. This is planned in future work.
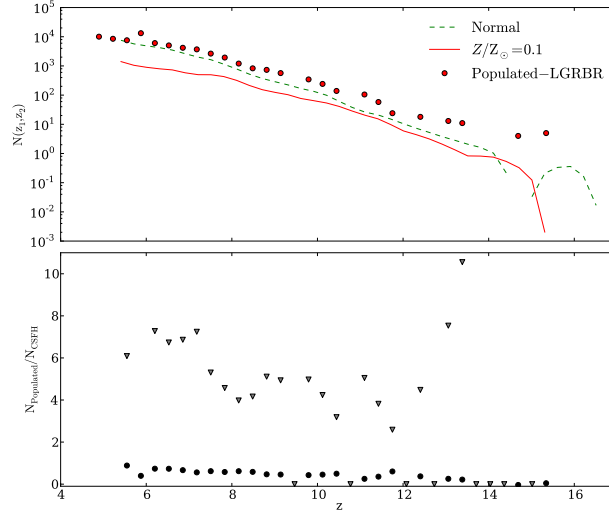
Figure 6.8 **Top**: Dots are the populated LGRBR and the two lines are the CSFH-LGRBRs. The green-dashed line is the same one shown in Fig. 6.5, but the red line is for a cut-off metallicity on the star particles of $0.1\,Z_\odot$. **Bottom**: Ratio of the populated LGRBR to the CSFH-LGRBR. Grey-up triangles are the metallicity constrained populated LGRBR and black dots are unmodified populated LGRBR. The star particle cut-off metallicity of $Z = 0.1\,Z_\odot$ is incorporated, but is most likely an overestimate given a more correct approach would involve taking the average value of the surrounding, gravitationally bound star particles.

6.6   Conclusion

Low number statistics of LGRBs, their environment, and host galaxy properties throughout redshift, i.e, $z \sim 0 - 10$, makes it difficult to draw conclusions on the progenitors underlying mechanism. We utilise a high-resolution cosmological simulation with advanced treatment of chemical processes to generate LGRBs based on their stellar mass, age, and local environment. We come to the following conclusions:

1. LGRB environmental metallicity only starts to play a role at $z \sim 6$ and can depreciate the rate of LGRBs by $\sim 20\%$.

2. Stellar lifetimes of stars has a dramatic effect on the absolute number of LGRBs, but does not have any evolutionary dependence.

3. LGRBR determined from populated LGRBs in comparison to the LGRBR inferred from the CSFH of the simulation, trace one another without a strong redshift dependence.

4. Redshift evolution of the type $\delta = 1.5$ would not be possible with simple environmental selection effects alone.

As the sophistication of cosmological simulations improve they open up a new avenue for investigating LGRBs at high redshift, while we wait for the samples to increase in size.

Chapter 7

Summary and Outlook

This thesis has showed how long GRBs can be used as tools to investigate a range of properties, from the prompt emission of GRBs, to the CSFH. The multi-wavelength capabilities of GROND and its rapid response, make it one of, if not, the most important detectors to acquire data on the prompt emission of GRBs. Only recently has it been possible to start compiling samples of these observations to make statistical conclusions on the mechanism. However, despite this progress, the samples remain heterogeneous, such that more observations, akin to GRB 121217A, are required. High time resolution and signal-to-noise are also needed, which sometimes is only possible with state-of-the-art detectors and telescopes. This again is difficult given the limited time available for programmes at telescopes such as the VLT, but it has become feasible in the recent years (e.g., PI: Elliott, ESO VLT/UT4/HAWK-I Proposal, Periods 88 and 91).

The question of the preferred environments of long GRBs was opened again by the host galaxy of GRB 110918A, which contains solar quantities of metals. This is one of the most robust measurements of metallicities at $z \sim 1$ and shows the potential of the detectors mounted at ESO-like facilities. However, more observations of this type are required; not only of host-integrated quantities, but measurements of metallicities at different locations of the host galaxy. This would allow measurements of both metallicity gradients and line-of-sight GRB metallicities, finally closing the debate about long GRB environments. To carry out statistically relevant samples, consistently throughout redshift, is a difficult task and is only becoming possible with the introduction of integrated field units and multi-wavelength spectrographs.

Estimates of the CSFH at high redshift are of utmost importance for such things as galaxy evolution and for investigating the causes of the reionisation of the Universe. We demonstrate that long GRBs can be used to replace conventional methods that utilise Lyman-break galaxies, however, the limited number of long GRBs at high redshift make it difficult to make constrained estimates. The number of high redshift detections should increase over the coming years, but with the possibility of *Swift* no longer functioning in the near future, the systematically large positional errors of *Fermi* and the IPN, and no confirmed replacement in the near-future, makes the detection of these high redshift GRBs even more unlikely.

The ease use of cosmological simulations allow us to investigate, in a self-consistent manner, the current ideas of long GRBs and their environments, without necessarily requiring high redshift detections. We show preliminary work that compares a semi-analytical long GRB rate to the CSFH within a simulation, which showcases the potential of this type of study. We plan further research that will take advantage of the high resolution simulation, FiBY, to investigate the following: (i) to see if the clustering of long GRBs, based on the prescribed IMF, are statistically different that they can be used to determine the IMF, (ii) to find which type of galaxies long GRBs reside in, their metallicity dispersions, and the resulting observations that they would result in, and (iii) to find a semi-analytical model that can explain the underlying long GRB luminosity function that is a result of environmental factors, such as metallicity or rotational velocity. Such predictions could be tested by the upcoming next generation missions, such as the *James Web Telescope*, the Extremely Large Telescope or the Large Synoptic Survey Telescope.

Bibliography

Afonso, P., Kruehler, T., Greiner, J., & Klose, S. 2008, GRB Coordinates Network, 8752, 1

Aihara, H., Allende Prieto, C., An, D., et al. 2011, ApJS, 193, 29

Alard, C. 2000, A&AS, 144, 363

Amati, L., Guidorzi, C., Frontera, F., et al. 2008, MNRAS, 391, 577

Arnaud, K. A. 1996, in ASPCS, Vol. 101, Astronomical Data Analysis Software and Systems V, ed. G. H. Jacoby & J. Barnes, 17

Arnouts, S., Cristiani, S., Moscardini, L., et al. 1999, MNRAS, 310, 540

Artale, M. C., Pellizza, L. J., & Tissera, P. B. 2011, MNRAS, 415, 3417

Atwood, W. B., Abdo, A. A., Ackermann, M., et al. 2009, ApJ, 697, 1071

Baade, D., Meisenheimer, K., Iwert, O., et al. 1999, The Messenger, 95, 15

Balucinska-Church, M. & McCammon, D. 1992, ApJ, 400, 699

Band, D., Matteson, J., Ford, L., et al. 1993, ApJ, 413, 281

Barthelmy, S. D., Barbier, L. M., Cummings, J. R., et al. 2005, Space Sci. Rev., 120, 143

Barthelmy, S. D., Cline, T. L., Butterworth, P., et al. 2000, in AIP Conf. Proc. Ser, Vol. 526, Gamma-ray Bursts, 5th Huntsville Symposium, ed. R. M. Kippen, R. S. Mallozzi, & G. J. Fishman, 731–735

Basa, S., Cuby, J. G., Savaglio, S., et al. 2012, A&A, 542, A103

Bastian, N., Covey, K. R., & Meyer, M. R. 2010, ARA&A, 48, 339

Becker, R. H., Fan, X., White, R. L., et al. 2001, AJ, 122, 2850

Belczynski, K., Holz, D. E., Fryer, C. L., et al. 2010, ApJ, 708, 117

Belczynski, K., Perna, R., Bulik, T., et al. 2006, ApJ, 648, 1110

Beletic, J. W., Gerdes, R., & Duvarney, R. C. 1998, Experimental Astronomy, 8, 13

Beloborodov, A. M. 2010, MNRAS, 407, 1033

Berger, E., Cowie, L. L., Kulkarni, S. R., et al. 2003, ApJ, 588, 99

Berger, E., Fox, D. B., Cucchiara, A., & Cenko, S. B. 2008, GRB Coordinates Network, 8335, 1

Berger, E., Fox, D. B., Kulkarni, S. R., Frail, D. A., & Djorgovski, S. G. 2007, ApJ, 660, 504

Berger, E. & Rauch, M. 2008, GRB Coordinates Network, 8542, 1

Bertin, E. & Arnouts, S. 1996, A&AS, 117, 393

Beskin, G., Karpov, S., Bondar, S., et al. 2010, ApJL, 719, L10

Bessell, M. S. 1979, PASP, 91, 589

Beuermann, K., Hessman, F. V., Reinsch, K., et al. 1999, A&A, 352, L26

Blake, C. H., Bloom, J. S., Starr, D. L., et al. 2005, Nature, 435, 181

Blandford, R. D. & Znajek, R. L. 1977, MNRAS, 179, 433

Bloom, J. S., Frail, D. A., & Sari, R. 2001, AJ, 121, 2879

Bloom, J. S., Kulkarni, S. R., & Djorgovski, S. G. 2002, AJ, 123, 1111

Bloom, J. S., Perley, D. A., Li, W., et al. 2009, ApJ, 691, 723

Bolzonella, M., Miralles, J.-M., & Pelló, R. 2000, A&A, 363, 476

Bouche, N., Dekel, A., Genzel, R., et al. 2010, ApJ, 718, 1001

Bouwens, R. J., Illingworth, G. D., Franx, M., & Ford, H. 2008, ApJ, 686, 230

Bromm, V. & Larson, R. B. 2004, ARA&A, 42, 79

Bromm, V. & Loeb, A. 2006, ApJ, 642, 382

Bruzual, G. & Charlot, S. 2003, MNRAS, 344, 1000

Bundy, K., Ellis, R. S., Conselice, C. J., et al. 2006, ApJ, 651, 120

Burrows, D. N., Hill, J. E., Nousek, J. A., et al. 2005, Space Sci. Rev., 120, 165

Burrows, D. N., Hill, J. E., Nousek, J. A., et al. 2000, in SPIE Conf. Ser, Vol. 4140, SPIE Conf. Ser., ed. K. A. Flanagan & O. H. Siegmund, 64–75

Butler, N. R., Bloom, J. S., & Poznanski, D. 2010, ApJ, 711, 495

Butler, N. R., Kocevski, D., Bloom, J. S., & Curtis, J. L. 2007, ApJ, 671, 656

Calzetti, D., Armus, L., Bohlin, R. C., et al. 2000, ApJ, 533, 682

Campisi, M. A., Li, L.-X., & Jakobsson, P. 2010, MNRAS, 407, 1972

Campisi, M. A., Maio, U., Salvaterra, R., & Ciardi, B. 2011, MNRAS, 418, 500

Cappelluti, N., Ajello, M., Rebusco, P., et al. 2009, A&A, 495, L9

Cavallo, G. & Rees, M. J. 1978, MNRAS, 183, 359

Cenko, S. B., Frail, D. A., Harrison, F. A., et al. 2010, ApJ, 711, 641

Cenko, S. B., Kelemen, J., Harrison, F. A., et al. 2009, ApJ, 693, 1484

Cepa, J., Aguiar, M., Escalera, V. G., et al. 2000, in SPIE Conf. Ser, Vol. 4008, SPIE Conf. Ser, ed. M. Iye & A. F. Moorwood, 623–631

Chabrier, G. 2003, PASP, 115, 763

Chavan, A. M., Silva, D. R., Boarotto, C., et al. 2000, in SPIE Conf. Ser, Vol. 4010, SPIE Conf. Ser, ed. P. J. Quinn, 81–89

Chen, H.-W., Helsby, J., Shectman, S., Thompson, I., & Crane, J. 2009, GRB Coordinates Network, 10038, 1

Chornock, R., Berger, E., Fox, D. B., et al. 2013, ArXiv e-prints, 1306.3949

Chornock, R., Perley, D. A., Cenko, S. B., et al. 2009a, GRB Coordinates Network, 8994, 1

Chornock, R., Perley, D. A., & Cobb, B. E. 2009b, GRB Coordinates Network, 10100, 1

Christensen, L., Fynbo, J. P. U., Prochaska, J. X., et al. 2011, ApJ, 727, 73

Christensen, L., Hjorth, J., & Gorosabel, J. 2004, A&A, 425, 913

Ciardi, B., Ferrara, A., & White, S. D. M. 2003, MNRAS, 344, L7

Cimatti, A., Daddi, E., Renzini, A., et al. 2004, Nature, 430, 184

Cline, T. L., Butterworth, P. S., Stilwell, D. E., et al. 1997, IAU Circ., 6593, 1

Cline, T. L., Desai, U. D., Klebesadel, R. W., & Strong, I. B. 1973, ApJL, 185, L1

Cole, S., Norberg, P., Baugh, C. M., et al. 2001, MNRAS, 326, 255

Conselice, C. J., Bluck, A. F. L., Buitrago, F., et al. 2011, MNRAS, 413, 80

Copi, C. J. 1997, ApJ, 487, 704

Costa, E., Feroci, M., Frontera, F., et al. 1997, IAU Circ., 6572, 1

Courty, S., Björnsson, G., & Gudmundsson, E. H. 2007, MNRAS, 376, 1375

Coward, D. M., Guetta, D., Burman, R. R., & Imerito, A. 2008, MNRAS, 386, 111

Croton, D. J., Springel, V., White, S. D. M., et al. 2006, MNRAS, 365, 11

Cucchiara, A., Fox, D., Levan, A., & Tanvir, N. 2009, GRB Coordinates Network, 10202, 1

Cucchiara, A., Fox, D. B., Cenko, S. B., & Berger, E. 2008, GRB Coordinates Network, 8713, 1

Cucchiara, A., Fox, D. B., Tanvir, N. R., et al. 2010, GRB Coordinates Network, Circular Service, 10374, 1 (2010), 374, 1

Cucchiara, A., Levan, A. J., Fox, D. B., et al. 2011, ApJ, 736, 7

Cucchiara, A., Prochaska, J. X., Zhu, G., et al. 2012, MNRAS, 426, 2078

Daddi, E., Alexander, D. M., Dickinson, M., et al. 2007a, ApJ, 670, 173

Daddi, E., Dickinson, M., Morrison, G., et al. 2007b, ApJ, 670, 156

Daddi, E., Renzini, A., Pirzkal, N., et al. 2005, ApJ, 626, 680

Daigne, F., Rossi, E. M., & Mochkovitch, R. 2006, MNRAS, 372, 1034

Dar, A. & de Rújula, A. 2004, Physics Reports, 405, 203

D'Avanzo, P., D'Elia, V., & Covino, S. 2008, GRB Coordinates Network, 8350, 1

Davé, R. 2008, MNRAS, 385, 147

de Souza, R. S., Yoshida, N., & Ioka, K. 2011, A&A, 533, A32

de Ugarte Postigo, A., Fynbo, J. P. U., Thöne, C. C., et al. 2012, A&A, 548, A11

de Ugarte Postigo, A., Goldoni, P., Thöne, C. C., et al. 2010, A&A, 513, A42

de Ugarte Postigo, A., Gorosabel, J., Fynbo, J. P. U., Wiersema, K., & Tanvir, N. 2009a, GRB Coordinates Network, 9771, 1

de Ugarte Postigo, A., Jakobsson, P., Malesani, D., et al. 2009b, GRB Coordinates Network, 8766, 1

Dekel, A. & Birnboim, Y. 2006, MNRAS, 368, 2

D'Elia, V., Covino, S., & D'Avanzo, P. 2008, GRB Coordinates Network, 8438, 1

Della Valle, M. 2011, International Journal of Modern Physics D, 20, 1745

Dermer, C. D., Böttcher, M., & Chiang, J. 1999, ApJL, 515, L49

Djorgovski, S. G., Kulkarni, S. R., Bloom, J. S., & Frail, D. A. 1999, GRB Coordinates Network, 289, 1

D'Odorico, S., Dekker, H., Mazzoleni, R., et al. 2006, in SPIE Conf. Ser., Vol. 6269

Drenkhahn, G. & Spruit, H. C. 2002, A&A, 391, 1141

Eichler, D., Livio, M., Piran, T., & Schramm, D. N. 1989, Nature, 340, 126

Eldridge, J. J., Langer, N., & Tout, C. A. 2011, MNRAS, 414, 3501

Elíasdóttir, Á., Fynbo, J. P. U., Hjorth, J., et al. 2009, ApJ, 697, 1725

Elliott, J., Greiner, J., Khochfar, S., et al. 2012a, A&A, 539, A113

Elliott, J., Kruehler, T., Klose, S., et al. 2011, GRB Coordinates Network, 12366, 1

Elliott, J., Krühler, T., Greiner, J., et al. 2013, ArXiv e-prints, 1306.0892

Elliott, J., Schmidl, S., & Greiner, J. 2012b, GRB Coordinates Network, 14091, 1

Erb, D. K., Shapley, A. E., Pettini, M., et al. 2006, ApJ, 644, 813

Evans, P. A., Beardmore, A. P., Page, K. L., et al. 2009, MNRAS, 397, 1177

Evans, P. A., Beardmore, A. P., Page, K. L., et al. 2007, A&A, 469, 379

Evans, P. A., Goad, M. R., Osborne, J. P., & Beardmore, A. P. 2012, GRB Coordinates Network, 14090, 1

Falcone, A. D., Burrows, D. N., Lazzati, D., et al. 2006, ApJ, 641, 1010

Faucher-Giguère, C.-A., Prochaska, J. X., Lidz, A., Hernquist, L., & Zaldarriaga, M. 2008, ApJ, 681, 831

Ferland, G., van Hoof, P., Verner, D., et al. 1999, Cloudy: Numerical simulation of plasmas and their spectra, astrophysics Source Code Library

Fermi, E. 1949, Physical Review, 75, 1169

Filgas, R., Greiner, J., Schady, P., et al. 2012, A&A, 546, A101

Filgas, R., Greiner, J., Schady, P., et al. 2011a, A&A, 535, A57

Filgas, R., Krühler, T., Greiner, J., et al. 2011b, A&A, 526, A113

Filgas, R., Kupcu-Yoldas, A., Greiner, J., et al. 2008, GRB Coordinates Network, 7740, 1

Filippenko, A. V. 1997, ARA&A, 35, 309

Fishman, G. J., Meegan, C. A., Wilson, R. B., et al. 1994, ApJS, 92, 229

Fishman, G. J., Meegan, C. A., Wilson, R. B., et al. 1989, in Bull. Am. Astron. Soc., Vol. 21, Bull. Am. Astron. Soc., 860

Fontana, A., Salimbeni, S., Grazian, A., et al. 2006, A&A, 459, 745

Fox, A. J., Ledoux, C., Vreeswijk, P. M., Smette, A., & Jaunsen, A. O. 2008, A&A, 491, 189

Frail, D. A., Kulkarni, S. R., Sari, R., et al. 2001, ApJL, 562, L55

Frebel, A., Johnson, J. L., & Bromm, V. 2007, MNRAS, 380, L40

Frederiks, D. & Pal'shin, V. 2011, GRB Coordinates Network, 12370, 1

Fruchter, A. S., Levan, A. J., Strolger, L., et al. 2006, Nature, 441, 463

Fruchter, A. S., Thorsett, S. E., Metzger, M. R., et al. 1999, ApJL, 519, L13

Fryer, C. L. & Heger, A. 2005, ApJ, 623, 302

Fryer, C. L., Mazzali, P. A., Prochaska, J., et al. 2007, PASP, 119, 1211

Fryer, C. L., Woosley, S. E., & Hartmann, D. H. 1999, ApJ, 526, 152

Fynbo, J. P. U., Jakobsson, P., Prochaska, J. X., et al. 2009a, ApJS, 185, 526

Fynbo, J. P. U., Malesani, D., Jakobsson, P., & D'Elia, V. 2009b, GRB Coordinates Network, 9947, 1

Fynbo, J. P. U., Malesani, D., & Milvang-Jensen, B. 2008a, GRB Coordinates Network, 7949, 1

Fynbo, J. P. U., Prochaska, J. X., Sommer-Larsen, J., Dessauges-Zavadsky, M., & Møller, P. 2008b, ApJ, 683, 321

Galama, T. J., Vreeswijk, P. M., van Paradijs, J., et al. 1998, Nature, 395, 670

Galama, T. J., Vreeswijk, P. M., van Paradijs, J., et al. 1999, A&AS, 138, 465

Garn, T. & Best, P. N. 2010, MNRAS, 409, 421

Gehrels, N., Chincarini, G., Giommi, P., et al. 2004, ApJ, 611, 1005

Gendre, B., Atteia, J. L., Boër, M., et al. 2012, ApJ, 748, 59

Genet, F., Daigne, F., & Mochkovitch, R. 2007, A&A, 471, 1

Georgy, C., Ekström, S., Meynet, G., et al. 2012, A&A, 542, A29

Georgy, C., Meynet, G., Walder, R., Folini, D., & Maeder, A. 2009, A&A, 502, 611

Ghisellini, G., Nardini, M., Tagliaferri, J., G., et al. 2013, MNRAS, 428, 1449

Goldman, B., Marsat, S., Henning, T., Clemens, C., & Greiner, J. 2010, MNRAS, 405, 1140

Golenetskii, S., Aptekar, R., Frederiks, D., et al. 2011, GRB Coordinates Network, 12362, 1

Goodman, J. 1986, ApJL, 308, L47

Graham, J. F. & Fruchter, A. S. 2012, ApJ, submitted (arXiv:1211.7086)

Greiner, J., Bornemann, W., Clemens, C., et al. 2008a, PASP, 120, 405

Greiner, J., Krühler, T., Fynbo, J. P. U., et al. 2009a, ApJ, 693, 1610

Greiner, J., Krühler, T., Klose, S., et al. 2011a, A&A, 526, A30

Greiner, J., Krühler, T., McBreen, S., et al. 2009b, ApJ, 693, 1912

Greiner, J., Mannheim, K., Aharonian, F., et al. 2011b, Experimental Astronomy, 116

Greiner, J., Sala, G., & Kruehler, T. 2008b, The Astronomer's Telegram, 1577, 1

Gruber, D., Krühler, T., Foley, S., et al. 2011, A&A, 528, A15

Guidorzi, C., Clemens, C., Kobayashi, S., et al. 2009, A&A, 499, 439

Gunn, J. E. & Peterson, B. A. 1965, ApJ, 142, 1633

Hao, J.-M. & Yuan, Y.-F. 2013, ArXiv e-prints, 1305.5165

Hashimoto, T., Ohta, K., Aoki, K., et al. 2010, ApJ, 719, 378

Heger, A., Fryer, C. L., Woosley, S. E., Langer, N., & Hartmann, D. H. 2003, ApJ, 591, 288

Hirschi, R., Meynet, G., & Maeder, A. 2005, A&A, 443, 581

Hjorth, J., Malesani, D., Jakobsson, P., et al. 2012, ApJ, 756, 187

Hjorth, J., Sollerman, J., Møller, P., et al. 2003, Nature, 423, 847

Hogg, D. W., Pahre, M. A., McCarthy, J. K., et al. 1997, MNRAS, 288, 404

Hook, I. M., Jørgensen, I., Allington-Smith, J. R., et al. 2004, PASP, 116, 425

Hopkins, A. M. 2004, ApJ, 615, 209

Hopkins, A. M. & Beacom, J. F. 2006, ApJ, 651, 142

Hunt, L., Palazzi, E., Rossi, A., et al. 2011, ApJL, 736, L36

Hurley, K., Golenetskii, S., Aptekar, R., et al. 2011, GRB Coordinates Network, 12357, 1

Ilbert, O., Arnouts, S., McCracken, H. J., et al. 2006, A&A, 457, 841

Ilbert, O., Capak, P., Salvato, M., et al. 2009, ApJ, 690, 1236

Ishida, E. E. O., de Souza, R. S., & Ferrara, A. 2011, MNRAS, 418, 500

Jakobsson, P., de Ugarte Postigo, A., Gorosabel, J., et al. 2009, GRB Coordinates Network, 9797, 1

Jakobsson, P., Fynbo, J. P. U., Malesani, D., Hjorth, J., & Milvang-Jensen, B. 2008a, GRB Coordinates Network, 7757, 1

Jakobsson, P., Fynbo, J. P. U., Vreeswijk, P. M., & de Ugarte Postigo, A. 2008b, GRB Coordinates Network, 8077, 1

Jakobsson, P., Levan, A., Fynbo, J. P. U., et al. 2006, A&A, 447, 897

Jakobsson, P., Vreeswijk, P. M., Malesani, D., et al. 2008c, GRB Coordinates Network, 7286, 1

Jakobsson, P., Vreeswijk, P. M., Xu, D., & Thoene, C. C. 2008d, GRB Coordinates Network, 7832, 1

Jarrett, T. H., Masci, F., Tsai, C. W., et al. 2012, AJ, 144, 68

Johnson, J. L., Dalla, V. C., & Khochfar, S. 2013, MNRAS, 428, 1857

Johnson, J. L. & Khochfar, S. 2011, ApJ, 743, 126

Kalberla, P. M. W., Burton, W. B., Hartmann, D., et al. 2005, A&A, 440, 775

Kaneko, Y., Preece, R. D., Briggs, M. S., et al. 2006, ApJS, 166, 298

Kann, D. A., Klose, S., & Zeh, A. 2006, ApJ, 641, 993

Kann, D. A., Klose, S., Zhang, B., et al. 2010, ApJ, 720, 1513

Kaufer, A., Stahl, O., Tubbesing, S., et al. 1999, The Messenger, 95, 8

Kennicutt, Jr., R. C. 1998, ARA&A, 36, 189

Kewley, L. J. & Dopita, M. A. 2002, ApJS, 142, 35

Kewley, L. J. & Ellison, S. L. 2008, ApJ, 681, 1183

Khochfar, S. & Ostriker, J. P. 2008, ApJ, 680, 54

Khochfar, S. & Silk, J. 2009a, MNRAS, 397, 506

Khochfar, S. & Silk, J. 2009b, ApJL, 700, L21

Khochfar, S. & Silk, J. 2011, MNRAS, 410, L42

Kistler, M. D., Yüksel, H., Beacom, J. F., Hopkins, A. M., & Wyithe, J. S. B. 2009, ApJL, 705, L104

Klebesadel, R. W., Strong, I. B., & Olson, R. A. 1973, ApJL, 182, L85

Kocevski, D. & West, A. A. 2011, ApJL, 735, L8

Kodama, T. 1997, PhD thesis, PhD thesis, Institute of Astronomy, Univ. Tokyo, (1997)

Komatsu, E., Dunkley, J., Nolta, M. R., et al. 2009, ApJS, 180, 330

Komatsu, E., Smith, K. M., Dunkley, J., et al. 2011, ApJS, 192, 18

Kong, X., Daddi, E., Arimoto, N., et al. 2006, ApJ, 638, 72

Kopac, D., Kobayashi, S., Gomboc, A., et al. 2013, ArXiv e-prints, 1305.6897

Kouveliotou, C., Meegan, C. A., Fishman, G. J., et al. 1993, ApJL, 413, L101

Krimm, H. A. & Siegel, H. v. M. 2011, GCN Report, 350, 1

Kronmal, R. & Peterson, A. 1979, in 1979 Winter Simulation Conference, IEEE (New York, NY, USA: IEEE), 269–80, 1979 Winter Simulation Conference, 3-5 Dec. 1979, San Diego, CA, USA

Kroupa, P. 2001, MNRAS, 322, 231

Krühler, T., Fynbo, J. P. U., Geier, S., et al. 2012a, A&A, 546, A8

Krühler, T., Greiner, J., Schady, P., et al. 2011a, A&A, 534, A108

Krühler, T., Küpcü Yoldaş, A., Greiner, J., et al. 2008, ApJ, 685, 376

Krühler, T., Malesani, D., Milvang-Jensen, B., et al. 2012b, ApJ, 758, 46

Krühler, T., Schady, P., Greiner, J., et al. 2011b, A&A, 526, A153

Kulkarni, S. R., Frail, D. A., Wieringa, M. H., et al. 1998, Nature, 395, 663

Kumar, P. & Panaitescu, A. 2000, ApJL, 541, L51

Küpcü Yoldaş, A., Greiner, J., Klose, S., Krühler, T., & Savaglio, S. 2010, A&A, 515, L2

Labbé, I., Huang, J., Franx, M., et al. 2005, ApJL, 624, L81

Langer, N. & Norman, C. A. 2006, ApJL, 638, L63

Laporte, N., Pelló, R., Hayes, M., et al. 2012, A&A, 542, L31

Lazzati, D. & Begelman, M. C. 2006, ApJ, 641, 972

Lazzati, D., Covino, S., Gorosabel, J., et al. 2004, A&A, 422, 121

Le Floc'h, E., Duc, P.-A., Mirabel, I. F., et al. 2003, A&A, 400, 499

Ledoux, C., Jakobsson, P., Jaunsen, A. O., et al. 2007, GRB Coordinates Network, 7023, 1

Levan, A., Fruchter, A., Rhoads, J., et al. 2006, ApJ, 647, 471

Levesque, E. M., Berger, E., Kewley, L. J., & Bagley, M. M. 2010a, AJ, 139, 694

Levesque, E. M., Kewley, L. J., Berger, E., & Zahid, H. J. 2010b, AJ, 140, 1557

Levesque, E. M., Kewley, L. J., Graham, J. F., & Fruchter, A. S. 2010c, ApJL, 712, L26

Levesque, E. M., Soderberg, A. M., Kewley, L. J., & Berger, E. 2010d, ApJ, 725, 1337

Li, A., Liang, S. L., Kann, D. A., et al. 2008, ApJ, 685, 1046

Li, L. 2008, MNRAS, 388, 1487

Li, L., Liang, E.-W., Tang, Q.-W., et al. 2012, ApJ, 758, 27

Longair, M. S. 1994, High energy astrophysics. Volume 2. Stars, the Galaxy and the interstellar medium.

Lu, R.-J., Wei, J.-J., Qin, S.-F., & Liang, E.-W. 2012, ApJ, 745, 168

MacFadyen, A. I. & Woosley, S. E. 1999, ApJ, 524, 262

Madau, P. 1995, ApJ, 441, 18

Madau, P., Ferguson, H. C., Dickinson, M. E., et al. 1996, MNRAS, 283, 1388

Maio, U., Salvaterra, R., Moscardini, L., & Ciardi, B. 2012, MNRAS, 426, 2078

Maiolino, R., Nagao, T., Grazian, A., et al. 2008, A&A, 488, 463

Malesani, D., Fynbo, J. P. U., Jakobsson, P., Vreeswijk, P. M., & Niemi, S.-M. 2008, GRB Coordinates Network, 7544, 1

Mangano, V., Sbarufatti, B., Evans, P. A., & Krimm, H. A. 2011, GRB Coordinates Network, 12364, 1

Mannucci, F., Buttery, H., Maiolino, R., Marconi, A., & Pozzetti, L. 2007, A&A, 461, 423

Mannucci, F., Salvaterra, R., & Campisi, M. A. 2011, MNRAS, 439

Martayan, C., Zorec, J., Frémat, Y., & Ekström, S. 2010, A&A, 516, A103

Matheson, T., Garnavich, P. M., Stanek, K. Z., et al. 2003, ApJ, 599, 394

Mazets, E. P., Golenetskii, S. V., Ilinskii, V. N., et al. 1981, Ap&SS, 80, 3

Meegan, C., Lichti, G., Bhat, P. N., et al. 2009, ApJ, 702, 791

Mészáros, P. 2002, ARA&A, 40, 137

Mészáros, P. 2006, Reports on Progress in Physics, 69, 2259

Metzger, M. R., Cohen, J. G., Chaffee, F. H., & Blandford, R. D. 1997a, IAU Circ., 6676, 3

Metzger, M. R., Djorgovski, S. G., Kulkarni, S. R., et al. 1997b, Nature, 387, 878

Meyer, M., Finger, G., Mehrgan, H., Nicolini, G., & Stegmeier, J. 1998, in SPIE Conf. Ser, Vol. 3354, SPIE Conf. Ser, ed. A. M. Fowler, 134–138

Michałowski, M. J., Kamble, A., Hjorth, J., et al. 2012, ApJ, 755, 85

Modjaz, M., Kewley, L., Kirshner, R. P., et al. 2008, AJ, 135, 1136

Nagao, T., Maiolino, R., & Marconi, A. 2006, A&A, 459, 85

Narayan, R., Paczynski, B., & Piran, T. 1992, ApJL, 395, L83

Nestor, D. B., Johnson, B. D., Wild, V., et al. 2011, MNRAS, 412, 1559

Niino, Y. 2011, MNRAS, 417, 567

Nomoto, K., Tanaka, M., Tominaga, N., & Maeda, K. 2010, New Astronomy Review, 54, 191

Oke, J. B. & Gunn, J. E. 1983, ApJ, 266, 713

Oksanen, A., Schaefer, B., Harlingten, C., & Templeton, M. 2011, GRB Coordinates Network, 12458, 1

Olivares E., F., Greiner, J., Schady, P., et al. 2012, A&A, 539, A76

Osterbrock, D. E. 1989, Astrophysics of gaseous nebulae and active galactic nuclei

Ota, K., Iye, M., Kashikawa, N., et al. 2008, ApJ, 677, 12

Ouyed, R., Rapp, R., & Vogt, C. 2005, ApJ, 632, 1001

Paciesas, W. S., Meegan, C. A., Pendleton, G. N., et al. 1999, ApJS, 122, 465

Paczynski, B. 1986, ApJL, 308, L43

Paczynski, B. 1998, ApJL, 494, L45

Page, K. L., Willingale, R., Bissaldi, E., et al. 2009, MNRAS, 400, 134

Page, K. L., Willingale, R., Osborne, J. P., et al. 2007a, ApJ, 663, 1125

Page, L., Hinshaw, G., Komatsu, E., et al. 2007b, ApJS, 170, 335

Panaitescu, A., Mészáros, P., Gehrels, N., Burrows, D., & Nousek, J. 2006, MNRAS, 366, 1357

Papovich, C., Moustakas, L. A., Dickinson, M., et al. 2006, ApJ, 640, 92

Pei, Y. C. 1992, ApJ, 395, 130

Perley, D. A., Cenko, S. B., Bloom, J. S., et al. 2009, AJ, 138, 1690

Perley, D. A., Chornock, R., & Bloom, J. S. 2008, GRB Coordinates Network, 7962, 1

Perley, D. A., Levan, A. J., Tanvir, N. R., et al. 2013, ApJ, submitted (arXiv:1301.5903)

Pettini, M. & Pagel, B. E. J. 2004, MNRAS, 348, L59

Piran, T. 1999, Physics Reports, 314, 575

Pontzen, A., Deason, A., Governato, F., et al. 2010, MNRAS, 402, 1523

Power, C., Wynn, G. A., Combet, C., & Wilkinson, M. I. 2009, MNRAS, 395, 1146

Prilutskii, O. F. & Usov, V. V. 1975, Ap&SS, 34, 395

Prochaska, J. X., Perley, D. A., Modjaz, M., et al. 2007a, GRB Coordinates Network, 6864, 1

Prochaska, J. X., Thoene, C. C., Malesani, D., Fynbo, J. P. U., & Vreeswijk, P. M. 2007b, GRB Coordinates Network, 6698, 1

Qin, S.-F., Liang, E.-W., Lu, R.-J., Wei, J.-Y., & Zhang, S.-N. 2010, MNRAS, 406, 558

Racusin, J. L., Karpov, S. V., Sokolowski, M., et al. 2008, Nature, 455, 183

Racusin, J. L., Liang, E. W., Burrows, D. N., et al. 2009, ApJ, 698, 43

Rafelski, M., Wolfe, A. M., & Chen, H.-W. 2011, ApJ, 736, 48

Rau, A., Greiner, J., Elliott, J., & Olivares E, F. 2011, The Astronomer's Telegram, 3365, 1

Rau, A., Savaglio, S., Krühler, T., et al. 2010, ApJ, 720, 862

Rees, M. J. & Meszaros, P. 1994, ApJL, 430, L93

Rhoads, J. E. 1997, ApJL, 487, L1

Rhoads, J. E. 1999, ApJ, 525, 737

Ricotti, M. & Ostriker, J. P. 2004, MNRAS, 352, 547

Robertson, B. E. & Ellis, R. S. 2012, ApJ, 744, 95

Rodríguez Hidalgo, P., Wessels, K., Charlton, J. C., et al. 2012, MNRAS, 427, 1801

Romani, R. W., Filippenko, A. V., Silverman, J. M., et al. 2012, ApJL, 760, L36

Romano, D., Chiappini, C., Matteucci, F., & Tosi, M. 2005, A&A, 430, 491

Rossi, A., Klose, S., Ferrero, P., et al. 2012, A&A, 545, A77

Sakamoto, T., Barthelmy, S. D., Barbier, L., et al. 2008, ApJS, 175, 179

Salpeter, E. E. 1955, ApJ, 121, 161

Salvaterra, R., Campana, S., Vergani, S. D., et al. 2012, ApJ, 749, 68

Salvaterra, R. & Chincarini, G. 2007, ApJL, 656, L49

Sari, R., Piran, T., & Narayan, R. 1998, ApJL, 497, L17

Savaglio, S. 2006, New Journal of Physics, 8, 195

Savaglio, S., Glazebrook, K., & Le Borgne, D. 2009, ApJ, 691, 182

Savaglio, S., Glazebrook, K., Le Borgne, D., et al. 2005, ApJ, 635, 260

Savaglio, S., Rau, A., Greiner, J., et al. 2012, MNRAS, 420, 627

Scalo, J. M. 1986, Fund. Cosmic Phys., 11, 1

Scarsi, L. 1997, in Data Analysis in Astronomy, ed. V. Di Gesu, M. J. B. Duff, A. Heck, M. C. Maccarone, L. Scarsi, & H. U. Zimmerman, 65–78

Schady, P., Dwelly, T., Page, M. J., et al. 2012, A&A, 537, A15

Schaye, J., Dalla Vecchia, C., Booth, C. M., et al. 2010, MNRAS, 402, 1536

Schechter, P. 1976, ApJ, 203, 297

Schlegel, D. J., Finkbeiner, D. P., & Davis, M. 1998, ApJ, 500, 525

Schulze, S., Klose, S., Björnsson, G., et al. 2011, A&A, 526, A23

Shen, R.-F. & Zhang, B. 2009, MNRAS, 398, 1936

Shin, M.-S., Trac, H., & Cen, R. 2008, ApJ, 681, 756

Siegel, M. H., Barlow, B. N., Burrows, D. N., et al. 2012, GRB Coordinates Network, 14089, 1

Skrutskie, M. F., Cutri, R. M., Stiening, R., et al. 2006, AJ, 131, 1163

Soderberg, A. M., Chakraborti, S., Pignata, G., et al. 2010, Nature, 463, 513

Springel, V. 2005, MNRAS, 364, 1105

Srbinovsky, J. A. & Wyithe, J. S. B. 2007, MNRAS, 374, 627

Stanek, K. Z., Gnedin, O. Y., Beacom, J. F., et al. 2006, Acta Astronomica, 56, 333

Stanek, K. Z., Matheson, T., Garnavich, P. M., et al. 2003, ApJL, 591, L17

Steidel, C. C., Shapley, A. E., Pettini, M., et al. 2004, ApJ, 604, 534

Stern, B. E. & Poutanen, J. 2004, MNRAS, 352, L35

Sudilovsky, V., Greiner, J., Rau, A., et al. 2013, A&A, in press (arXiv:1302.6362)

Svensson, K. M., Levan, A. J., Tanvir, N. R., Fruchter, A. S., & Strolger, L.-G. 2010, MNRAS, 405, 57

Svensson, K. M., Levan, A. J., Tanvir, N. R., et al. 2012, MNRAS, 421, 25

Tanvir, N. R. 2010, in AIP Conf. Proc. Ser., Vol. 1279, AIP Conf. Proc. Ser., ed. N. Kawai & S. Nagataki, 32–39

Tanvir, N. R., Barnard, V. E., Blain, A. W., et al. 2004, MNRAS, 352, 1073

Tanvir, N. R., Fox, D. B., Levan, A. J., et al. 2009, Nature, 461, 1254

Tanvir, N. R., Levan, A. J., Fruchter, A. S., et al. 2012, ApJ, 754, 46

Tanvir, N. R., Wiersema, K., Levan, A. J., Greiss, S., & Gaensicke, B. 2011, GRB Coordinates Network, 12365, 1

Thoene, C. C., De Cia, A., Malesani, D., & Vreeswijk, P. M. 2008a, GRB Coordinates Network, 7587, 1

Thoene, C. C., de Ugarte Postigo, A., Vreeswijk, P. M., Malesani, D., & Jakobsson, P. 2008b, GRB Coordinates Network, 8058, 1

Thoene, C. C., Jakobsson, P., De Cia, A., et al. 2009, GRB Coordinates Network, 9409, 1

Thoene, C. C., Malesani, D., Vreeswijk, P. M., et al. 2008c, GRB Coordinates Network, 7602, 1

Thompson, T. A., Kistler, M. D., & Stanek, K. Z. 2009, ArXiv e-prints, 0912.0009

Tody, D. 1993, in ASPCS, Vol. 52, Astronomical Data Analysis Software and Systems II, ed. R. J. Hanisch, R. J. V. Brissenden, & J. Barnes, 173

Totani, T. 1997, ApJL, 486, L71

Totani, T., Kawai, N., Kosugi, G., et al. 2006, PASJ, 58, 485

Tremonti, C. A., Heckman, T. M., Kauffmann, G., et al. 2004, ApJ, 613, 898

Trenti, M., Perna, R., Levesque, E. M., Shull, J. M., & Stocke, J. T. 2012, ApJL, 749, L38

van Eerten, H. J. & MacFadyen, A. I. 2012, ApJ, 751, 155

Vedrenne, A. & Jean-Luc, G. 2009, Gamma-Ray Bursts: The brightest explosions in the Universe

Vedrenne, G. 1981, Royal Society of London Philosophical Transactions Series A, 301, 645

Vergani, S. D., D'Avanzo, P., Malesani, D., et al. 2010, GRB Coordinates Network, 10495, 1

Vernet, J., Dekker, H., D'Odorico, S., et al. 2011, A&A, 536, A105

Villar, V., Gallego, J., Pérez-González, P. G., et al. 2011, ApJ, 740, 47

Virgili, F. J., Zhang, B., Nagamine, K., & Choi, J.-H. 2011, MNRAS, 417, 3025

Vreeswijk, P. M., Thoene, C. C., Malesani, D., et al. 2008, GRB Coordinates Network, 7601, 1

Vurm, I., Beloborodov, A. M., & Poutanen, J. 2011, ApJ, 738, 77

Wanderman, D. & Piran, T. 2010, MNRAS, 406, 1944

Wang, F. Y. & Dai, Z. G. 2011, ApJL, 727, L34

Waxman, E., Kulkarni, S. R., & Frail, D. A. 1998, ApJ, 497, 288

Weidner, C., Kroupa, P., & Pflamm-Altenburg, J. 2011, MNRAS, 412, 979

Wells, D. C., Greisen, E. W., & Harten, R. H. 1981, A&AS, 44, 363

Wiersema, K. 2013, ArXiv e-prints, 1302.2083

Wiersema, K., Curran, P. A., Krühler, T., et al. 2012, MNRAS, 426, 2

Wiersma, R. P. C., Schaye, J., Theuns, T., Dalla Vecchia, C., & Tornatore, L. 2009, MNRAS, 399, 574

Wigger, C., Wigger, O., Bellm, E., & Hajdas, W. 2008, ApJ, 675, 553

Wijers, R. A. M. J., Bloom, J. S., Bagla, J. S., & Natarajan, P. 1998, MNRAS, 294, L13

Willingale, R., O'Brien, P. T., Osborne, J. P., et al. 2007, ApJ, 662, 1093

Willott, C. J., Delorme, P., Reylé, C., et al. 2010, AJ, 139, 906

Wolf, C. & Podsiadlowski, P. 2007, MNRAS, 375, 1049

Wolfe, A. M., Gawiser, E., & Prochaska, J. X. 2005, ARA&A, 43, 861

Woosley, S. E. 1993, ApJ, 405, 273

Woosley, S. E. & Bloom, J. S. 2006, ARA&A, 44, 507

Woosley, S. E. & Heger, A. 2006, ApJ, 637, 914

Wright, E. L., Eisenhardt, P. R. M., Mainzer, A. K., et al. 2010, AJ, 140, 1868

Yabe, K., Ohta, K., Iwamuro, F., et al. 2012, PASJ, 64, 60

Yan, H., Dickinson, M., Eisenhardt, P. R. M., et al. 2004, ApJ, 616, 63

Yoldaş, A. K., Krühler, T., Greiner, J., et al. 2008, in AIP Conf. Proc. Ser., Vol. 1000, AIP Conf. Proc. Ser., ed. M. Galassi, D. Palmer, & E. Fenimore, 227–231

Yoon, S.-C. & Langer, N. 2005, A&A, 443, 643

Yoon, S.-C., Langer, N., & Norman, C. 2006, A&A, 460, 199

Young, P. A. & Fryer, C. L. 2007, ArXiv Astrophysics e-prints

Yu, D. & Gruber, D. 2012, GRB Coordinates Network, 14094, 1

Yuan, F. & Akerlof, C. W. 2008, ApJ, 677, 808

Zahid, H. J., Yates, R. M., Kewley, L. J., & Kudritzki, R. P. 2013, ApJ, 763, 92

Zeh, A., Klose, S., & Hartmann, D. H. 2004, ApJ, 609, 952

Zeh, A., Klose, S., & Kann, D. A. 2006, ApJ, 637, 889

Zhang, B. 2012, in AIP Conf. Proc. Ser., Vol. 1505, AIP Conf. Proc. Ser., ed. F. A. Aharonian, W. Hofmann, & F. M. Rieger, 88–100

Zhang, B., Fan, Y. Z., Dyks, J., et al. 2006, ApJ, 642, 354

Zhang, B. & Pe'er, A. 2009, ApJL, 700, L65

Zhang, B. & Yan, H. 2011, ApJ, 726, 90

Zheng, W., Shen, R. F., Sakamoto, T., et al. 2012, ApJ, 751, 90

Acknowledgments

In the following I would like to thank the people that made it possible for me to carry out a Ph.D., survive during it, and ensure I did not end up in an early grave.

I thank my supervisor, Jochen Greiner, for giving me the opportunity to carry out my studies at the MPE and his encouragement and guidance throughout the past three years. Although, I have the feeling that he may have preferred that I stay in Chile forever. I appreciate the constant help and support from my thesis committee, Sandra Savaglio and Sadegh Khochfar, who answered all my questions regardless of how stupid they may have been. Many thanks to Christa Ingram and Birgit Boller for making the endless German bureaucracy seem so easy.

My colleagues who suffered alongside me; Robert Filgas - despite looking evil and being mean we all know you're really.... evil and mean, Felipe Olivares - where does such a small person put all that alcohol!?, Patricia Schady - the only British person who doesn't like tea, Vladimir Sudilovsky - please don't put fly eggs under my door, David Gruber - lets not make any more ping-pong hats, Thomas Krühler - how do you manage to do everything that extra bit better?, Karla Varela - its the emergency-help-cord not the light switch, Mohit Tanga - has anyone seen Mohit?, Alex (not David) Kann - you are a human encyclopaedia, Sebastian Schmidl - we have the unluckiest shifts together, David Yu - give me some more fish balls!, and Arne Rau - you really do love your Prius.

My friends who put up with my good and bad sides; Bhaskar Agarwal - it fascinates me in how many ways you can cross **the** line, Guido Aviisati - I've never seen someone appreciate Nuts as much as you, Chervin Laporte - the only person who would literally murder someone if they hurt his fingers, Claudio Dalla Vecchia - extrema!, and Ilona and Jan-Peter - why won't you take Bhaskar off our hands?

I thank my parents for their support in all aspects of my life, my father, Gerard Elliott - you have many life encouraging stories that usually involve a "bag of wank" and my mother, Anne Elliott - you retain the skill of being only person that can still consistently embarrass me.

I am indebted to all the staff at La Silla who all helped me keep my sanity during my GROND shifts. Especially Javier and Pablo, who ensured my mate-addiction was met during my stays. Not to mention Regis and Timo who shared my confinement - yet they got shorter sentences. Also, Greg and Amaury who generously fed me copious amounts of wine and fondue at the mountain.

I reserve a special thanks to my girlfriend who I love dearly, Alessia Longobardi, who had to put up with all of my crap in the past year. But seriously, you thanked your cats in your masters thesis!?